Modulating Photophysical Properties of Dye-loaded Gold Nanoparticles through Plasmon-Molecule Coupling

Atikur Rahman

A thesis submitted for the partial fulfilment of the
Degree of Doctor of Philosophy

Institute of Nano Science and Technology
Knowledge City, Sector 81, SAS Nagar 140306, Punjab, India.

Indian Institute of Science Education and Research Mohali
Knowledge City, Sector 81, SAS Nagar, Manauli PO, Mohali 140306, Punjab, India.

August 2022

Dedicated to

My Parents and Brothers

Declaration

The work presented in this thesis has been carried out by me under the guidance of Prof. Prakash P. Neelakandan at the Institute of Nano Science and Technology (INST), Mohali. This work has not been submitted in part or in full for a degree, a diploma, or a fellowship to any other university or institute. Whenever contributions of others are involved, every effort is made to indicate this clearly, with due acknowledgement of collaborative research and discussions. This thesis is a bonafide record of original work done by me and all sources listed within have been detailed in the bibliography.

Atikur Rahman

In my capacity as the supervisor of the candidate's thesis work, I certify that the above statements by the candidate are true to the best of my knowledge.

Prakash P. Neelakandan

Acknowledgements

First and foremost, I praise **Allah s.w.t**, **The Almighty**, **the Most Beneficent** *and* **Merciful**, *the Creator of the Universe, for providing me with the patience, courage, and zeal in order to accomplish my Ph.D. thesis work.*

At this moment of accomplishment, I would like to express my heartfelt gratitude to my esteemed supervisor **Prof. Prakash P. Neelakandan**, *for his constant guidance, patience, encouragement and motivation which gave me enormous strength to complete this work successfully. I am grateful to him for teaching me how to appreciate science, to conduct research, to communicate ideas, and to have envision for the future. He has not only been an excellent teacher and mentor, but also a valuable moral support on a personal level, always open to scientific discussions and listening to my problems. It is indeed a rare privilege to work under his valuable guidance and supervision.*

I would like to thank my Ph.D. monitoring committee members **Prof. Asish Pal** *and* **Dr. Asifkhan Shanavas**, *for their valuable time, insightful comments, and encouragement.*

I am very thankful to **Prof. Amitava Patra**, *Director INST, for providing excellent infrastructure to carry out our research work. I wish to express my special thanks to the founder Director of INST,* **Prof. A. K. Ganguli**, *and ex-officiating Director,* **Prof. H. N. Ghosh**, *and the esteemed Faculty of INST for the guidance and affectionate conversation during this course of time. I also extend my acknowledgments for the financial assistance from the UGC, New Delhi, in the form of Junior Research Fellowship (JRF) and Senior Research Fellowship (SRF) during my Ph.D. tenure.*

I would like to thank all my collaborators whom I have worked with throughout the years: **Prof. H. N. Ghosh**, **Dr. Asifkhan Shanavas**, **Dr. Pranjali Yadav**, **Dr. Navneet Kaur,** **Mr. Tanmay Goswami** *and* **Ms. Priyanka Sharma**. *You each have an amazing and rare talent to think about science and you have been an incalculable help to me during my time at INST.*

My sincere gratitude to all the members of **PPN** *group, both past and present,* **Dr. Praveen Kumar**, **Dr. Nidhi Naithani**, **Dr. Sharad Asthana**, **Dr. Khalid Naim**, **Ms. Sanchita Shah**,

ABBREVIATIONS

SP	Surface plasmons
LSP	Localized surface plasmons
PSP	Propagating surface plasmons
LSPR	Localized surface plasmon resonance
CT	Charge transfer
2D	Two-dimensional
g	Rate of energy transfer between light and matter
κ	Escape rate of light from system
γ	Loss rate of polarization of matter
SERS	Surface-enhanced Raman spectroscopy
PEF	Plasmon-enhanced fluorescence
k_{nr}	Non-radiative decay rate
MEF	Metal-enhanced fluorescence
SMD	Single-molecule detection
RIU	Refractive index unit
NIR	Near-infrared
PDT	Photodynamic therapy
ROS	Reactive oxygen species
ISC	Intersystem crossing
$^1O_2$	Singlet oxygen
MNPs	Metal nanoparticles
BODIPY	4,4'-difluoro-4-bora-3a,4a-diaza-s-indacene

OLEDs	Organic light-emitting diodes
DSSCs	Dye-sensitized solar cells
NLOs	Nonlinear optics
HR-TEM	High-resolution transmission electron microscopy
DLS	Dynamic light scattering
EDX	Energy dispersive X-ray
FESEM	Field emission scanning electron microscopy
NMR	Nuclear magnetic resonance
COSY	Correlation spectroscopy
DOSY	Diffusion ordered spectroscopy
FRET	Förster resonance energy transfer
TCSPC	Time-correlated single-photon counting
TA	Transient absorption
AIE	Aggregation-induced emission
ACQ	Aggregation-caused quenching
Φ_f	Fluorescence quantum yield
Φ_Δ	Singlet oxygen quantum yield
SPR	Surface plasmon resonance
SE	Stimulated emission
LUMO	Lowest unoccupied molecular orbital
LED	Light-emitting diode
ICP-MS	Inductively coupled plasma-mass spectrometry

ABSTRACT

Plasmon-Molecule Coupling
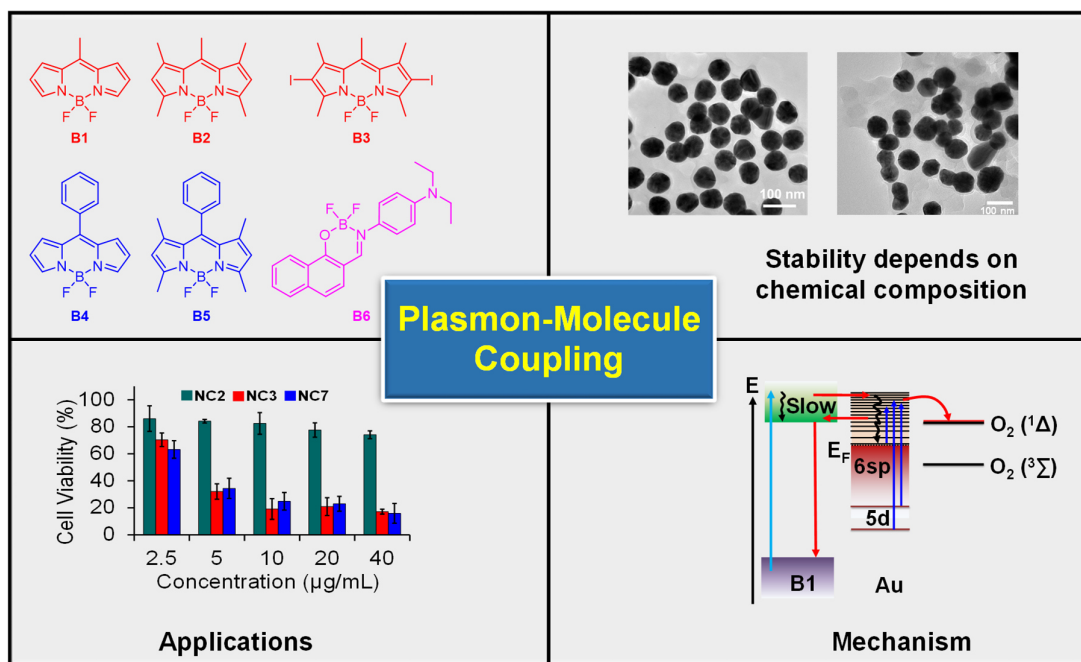
Metal nanoparticles (MNPs) exhibiting surface plasmon resonance (SPR) properties can interact with the oscillating dipoles of organic molecules in a pronounced manner. Molecules which absorb light near to the SPR absorption peak of MNPs can induce changes in the photophysical and electronic properties of MNPs due to plasmon-molecule interactions. These interactions can also increase or decrease the field incident on the dye molecule and perturb their electronic transitions. Plasmon-molecule interactions are governed by several factors such as the spectral overlap between the molecular and plasmonic resonance, chemical composition and concentration of the dye molecule, shape and size of MNPs and the distance between MNPs and dye molecule. If the coupling interactions are weak, various surface-enhanced phenomena are known to arise whereas strong coupling often results in the formation of hybrid 'plexcitonic' states. Irrespective of the strength of the coupling interactions, the optical properties of the hybrid systems are markedly different from those of their constituents.

Plasmon-molecule coupled systems have incredible potential in materials science and biology. Several literature reports exemplify their utility as ultrafast switches, bistable devices, modulators, sensors, photocatalysts and biological imaging agents. A limited number of examples are also known wherein molecule-plasmon interactions have been utilized in

photodynamic therapy (PDT) although the mechanistic details of such systems are generally overlooked. Motivated by these facts, we aim to study systematically the photophysical properties of a series of nanocomposites with the objective of understanding the underlying mechanism of plasmon-molecule interactions. We chose gold nanoparticles and organoboron compounds for our investigations because of the low toxicity and tuneable absorption profile of gold nanoparticles and the luminescence features of the dye molecules.

Chapter 1 focuses on literature review of plasmon-molecule interactions from fundamentals to applications. We have briefly discussed surface plasmons, excitons, and their interactions in terms of coupling strength. Further, various types of plasmon-molecule coupled systems and their applications have been discussed. Finally, the recent advancements in plasmon-molecule interactions for applications in PDT have been discussed, highlighting the importance of mechanism which will help in the development of new plasmon-molecule coupled systems.

Chapter 2 describes the synthesis and characterization of dye molecules as well as their nanocomposites. NMR spectroscopy revealed that various supramolecular interactions between the individual components play a key role in the formation of stable nanocomposites. We studied the effect of structural variations in the dye molecules **B1**-**B5** on nanocomposite formation and it was observed that sterically bulky molecule destabilizes the nanocomposites. Further, the dye molecule **B6** containing a stimuli-responsive group was employed so as to study the effect of immediate environment on the photophysical properties. We also synthesized a multi-chromophoric nanocomposite containing two dye molecules in order to study the impact of interaction between the two molecules on the photophysics of the nanocomposites.

Chapter 3 discusses the photophysical properties of all the nanocomposites. The nanocomposite formation resulted in major changes in the photophysical properties of their components: bathochromic shifts were observed in the absorption maxima of the dye molecules and gold nanoparticles whereas the fluorescence of the dye molecules was completely quenched. On the other hand, in the multi-chromophoric nanocomposite, Förster resonance energy transfer (FRET) was observed to occur between the two dye molecules on the surface of gold nanoparticles. This opened up radiative pathways and made this nanocomposite moderately fluorescent. In the case of the dye **B6** wherein the absorption overlap was minimal with gold nanoparticles but a significant overlap was observed between the fluorescence of **B6** and the absorption of gold nanoparticles, plasmon-enhanced luminescence was observed. Further, we observed that chemical structure of dye molecules

had a significant effect on the photostability and photosensitization properties of the nanocomposites. Thus, our findings highlight the importance of spectral overlap between dye molecule and gold nanoparticles on plasmon-molecule coupling.

Chapter 4 focuses on the potential application of the synthesized nanocomposites as photosensitizers for PDT. Ultrafast spectroscopy was used to map the excited state processes in the nanocomposites and our investigations revealed hot electron migration from dyes **B1-B3** to gold nanoparticles. Further, the nanocomposites exhibited enhanced plasmonic lifetimes which resulted in an increase in singlet oxygen generation upon plasmonic photoexcitation. However, we observed a reversal in the direction of hot electron migration from gold nanoparticle to dye molecule **B6** which resulted in enhanced luminescence. Further, the nanocomposites were found to be photostable and biocompatible and thus were utilized as photocytotoxic agents against cancer cells and luminescence imaging agents.

Contents

xvii

Chapter 1

Plasmon-Molecule Interactions: From Basics to Applications

1.1. Introduction.

The rational design of devices capable of harnessing and manipulating light-matter interactions and their fundamental investigation at the nanometre scale level has long been a significant focus of scientific research interest.[1–4] Because they can emphasize and bait optical energy in subwavelength spatial regions, plasmon-molecule coupled systems are perfect for this application.[5,6] Plasmon-molecule interaction refers to the interactions between the surface plasmons of noble metal nanostructures and the excitons of organic molecules. Plasmon-molecule interactions have received a lot experimental and theoretical attention due to their wide range of applications in surface-enhanced Raman spectroscopy[7–9], plasmon-enhanced fluorescence[10,11], plasmon-enhanced solar light harvesting and photocatalysis[12–15], and ultrasensitive chemical and biological sensors[16–19]. This chapter covers the basics of surface plasmons, excitons, their interactions with organic molecules, and their various applications, followed by an overview of the thesis.

1.2. Surface Plasmons.

Surface plasmons (SP) or plasmons are the coherent and collective oscillations of free surface electrons at a metal-dielectric interface that are excited by incident photons of light.[20] Surface plasmons of metal nanoparticles interact with illuminating light to generate a hybrid particle recognized as the surface plasmon polariton. Although surface plasmons have been known since 1957 by R. H. Ritchie[20], their importance has grown since the early 2000s when H. A. Atwater explored their application in sensors and electronics.[21] Depending on the morphology of the metallic structure, these surface plasmons are classified as localized surface plasmons (LSPs) and propagating surface plasmons (PSPs)[22,23] (Figure 1.1). PSPs are excited on metal surfaces at frequencies larger than the wavelength of incident light, and these plasmonic oscillations propagate for 10 to 1000 of micrometres along the metal surface.[24] LSPs are confined charge density oscillating on the surface of metallic nanostructures. LSPs are excited on the surface of metal nanostructures with a smaller

frequency than the electron mean free path within the material and the incident light wavelength.[25] Localized surface plasmon resonance (LSPR) occurs when the frequency of free electron oscillations matches the frequency of the electric field component of incident light, resulting in a sufficient enhancement of the localized electromagnetic field. The frequency of LSPR of a metal nanostructure can be tuned by changing the shape and size of the nanostructures as well as the dielectric constant of the surrounding medium.[26–29] This electromagnetic field enhancement also results in various surface-enhanced phenomena that may be studied using multiple spectroscopic techniques. Several studies discuss the advancement of plasmonic nanostructures to confine surface plasmons in design and nanofabrication, with applications in biosensors[30], nanolasers[31], light-emitting diodes[32,33], solar cells[34,15], nanophotonics[35,36], nano-optics[37,38], etc.
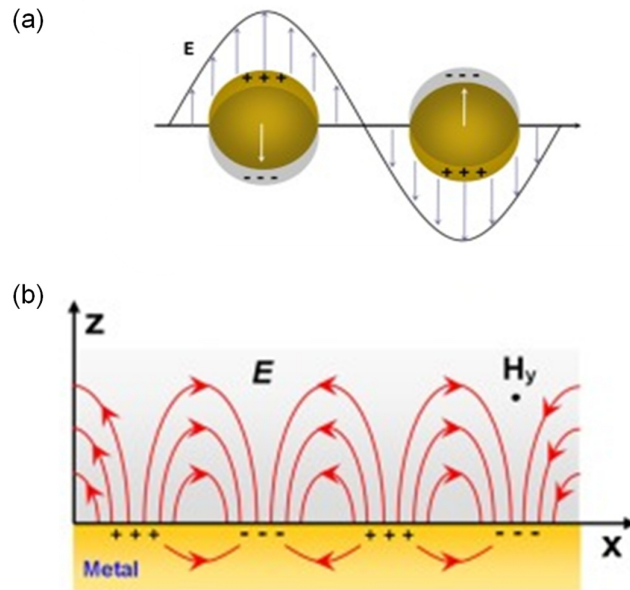
Figure 1.1. Schematic illustration for the mechanism of (a) localized surface plasmons (LSPs) and (b) propagating surface plasmons (PSPs). Reproduced with permission from ref. [39].

1.3.   Excitons.

In 1931 and 1932, Frenkel and Peierls, respectively, introduced the concept of excitons as "excitation waves".[40,41] An exciton is a quasi-particle that is electrically neutral and is composed of an electron and a hole pair held together in a bound state by Coulomb force. Excitons generally exist in various materials, such as semiconductors and insulators. Depending on the coupling strength of the electron-hole pair, they are further categorized as Frenkel and Mott-Wannier excitons.[42,43] Frenkel excitons are formed when an electron and a

hole bind by a strong coulombic force of the same order as the unit cell size (Figure 1.2a). Frenkel excitons, which have binding energies of 0.2-1.2 eV[44], are found in aggregates of organic molecules, conjugated polymers, and molecular crystals. Frenkel excitons can also be sub-divided into two categories based on the spin states of the bound electron-hole pairs: short-lived singlet excitons and long-lived triplet excitons.[45] Charge transfer excitons (CT excitons) are a form of Frenkel exciton that is highly delocalized and has low oscillator strengths. CT excitons are coulombically bound electron-hole pairs on opposite sides of a heterojunction interface in different materials. On the contrary, Mott-Wannier excitons typically exist in semiconductors with binding energies much lower than the thermal energy (kT ~ 26 meV) at room temperature.[46,47] Wannier excitons have weaker oscillator strengths as compared to Frenkel excitons. They also have large Bohr radii, delocalizing over 10 to 1000 atoms.[48] Wannier excitons are observed in 2D semiconductors such as transition metal dichalcogenides. They have exciton binding energies of 0.5 V[49] and are delocalized across several unit cells in the 2D sheet (Figure 1.2b). However, molecular excitons are a synonym for Frenkel excitons in a molecular crystal system. When a molecule absorbs a quantum of energy, the electron moves to the lowest empty molecular orbital and the hole to the highest occupied molecular orbital; this bound excited electron-hole state is known as a molecular exciton.[50,51] Many fascinating properties arise from molecular excitons with nanosecond lifetimes, such as exciton transfer or energy transfer from one to another molecule where the molecular excitons have proper energetic overlap with the absorbance of another molecule.
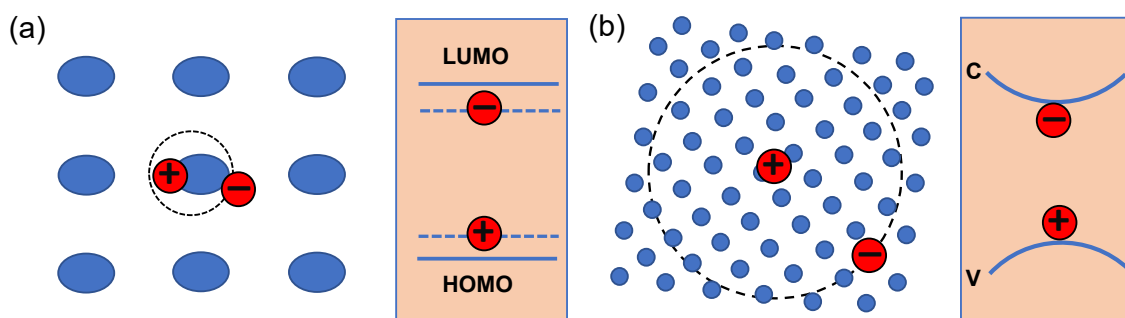
Figure 1.2. Schematic of (a) Frenkel and (b) Mott-Wannier excitons.

1.4.   Coupling between LSPs and Excitons.

The interaction between plasmons and excitons is known as plexcitons which are polaritonic in nature.[52,53] When the LSPR of a metal nanostructure matches to the molecular frequency, energy is exchanged between plasmons and excitons. Further, plexcitons are divided into two types based on Dicke's hypothesis: strong and weak coupling.[54,55] The

integration strength of the separate sub-systems, i.e., excitons and metal plasmons, determines weak and strong coupling in a plexciton system.

When the energy transfer between the light and the exciton is more significant than their average dissipation, a strong plexciton coupling is achieved. Because of the strong coupling, the wave function is also perturbed. Furthermore, this results in a new hybrid state that lacks the distinct properties of either original system.[56] This strong coupling leads to several interesting phenomena that have applications in various fields. Furthermore, the strong coupling can create a hybrid state, which is associated with Fano resonance[57], found in many materials. Rabi splitting[58] refers to the strong coupling process in a microcavity system, that is associated with splitting the peak with distinct coupling intensities. Quantum coherent oscillation can be achieved via such strong coupling, which has applications in quantum information processing.[59] As strong coupling can change the electromagnetic environment of a fluorophore, it can be utilized to alter the reaction rate of various chemical transformations.[60,61] The strong coupling of superconducting qubit and microwave can be used for a variety of applications such as routers, photon detectors[62], single-photon switches[63], and so on.

In the case of weak coupling, matter and the optical field can be thought of as distinct entities that merely exchange energy.[64] For the weakly coupled systems, plasmons and excitons' electromagnetic wave functions and modes remain unperturbed. Still, the electromagnetic field of plasmon interacts with the excitonic dipole moment. A weak coupling system exhibits many well-known phenomena such as increased radiation rate, absorption cross-sections, and energy exchange between excitons and plasmons.[65] Such weak coupling is caused by plasmonic enhancement of the local electromagnetic field near the excitonic material and Förster -type coulombic interactions.

A schematic illustration of weak and strong coupling is shown in Figure 1.3. The main difference between these two couplings is in their energy dissipation channels. The LSP mode, on the other hand, is dissipated through radiative losses and ohmic losses associated with the metal nanoparticle. The comparison of the two regimes of strong and weak coupling is defined by g - the rate of energy transfer between light and matter, κ - the escape rate of light from system and γ - the loss rate of polarization of matter. Weak and strong coupling is said to occur when g << γ, κ and g >> γ, κ, respectively.[66] The main divergence of these two couplings is that the strong coupling resembles reversible spontaneous emission[67], whereas the weak coupling gives irreversible spontaneous emission.[65] Furthermore, this irreversible spontaneous emission can be suppressed or enhanced, making it attractive for applications

like promoting absorption, surface-enhanced phenomena, fluorescence enhancement, and fluorescence quenching. Many reviews have been thoroughly documented to understand the coupling of light-matter from a quantum perspective view for both weak and strong coupling and their applications.[65,68]
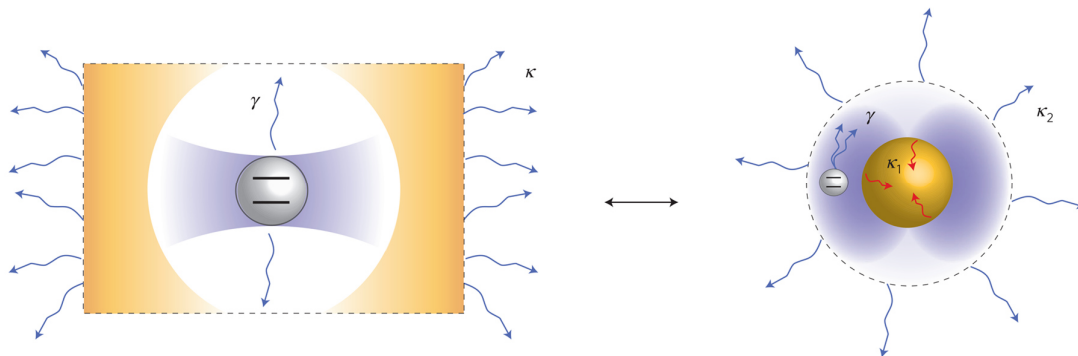
Figure 1.3. Weak and Strong Coupling. The analogy between an atom in a single-mode leaky cavity (left) and an atom inside the local field of a resonant LSP mode is supported by a metal nanoparticle (right). Reproduced with permission from ref. [69].

Plasmon-molecule coupling arises from the interaction of a dye molecule with the surface plasmons on metal nanostructures.[6] It can also be classified as strong or weak coupling depending on the magnitude of the coupling between plasmons and organic molecules, as described earlier. It is known that organic chromophores behave like oscillating dipoles, and metal surfaces can respond to the oscillating dipole, thereby resulting in modified optical properties. The electric field felt by a chromophore will be affected by its interactions with the metal surface and the interaction of light with the metal surface. These interactions can increase or decrease the field incident on the chromophore and perturb the electronic transitions. Further, metal nanostructures exhibiting LSPR properties can interact with dyes more pronouncedly forming the hybrid states with unique photophysical properties. Furthermore, the conjugation of metal nanostructures with other materials such as biomolecules, semiconductor nanocrystals, and organic molecules allows tuning their photophysical properties.

1.5.   Various types of Plasmon-Molecule Interactions.

The interaction of dyes with several metallic nanostructures such as colloidal nanoparticles, nanoshells, nanorods, etc., has been studied. Based on these studies, it is generally accepted that the interaction between the metal nanostructures and organic dyes is

governed by the overlap of the LSPR peak of metal nanostructures and the dyes. The concentration of the dyes and the distance between nanomaterial and the dye molecules are also crucial in governing the optical properties. Three types of interactions between the localized plasmons and organic molecules have been reported as shown in Figure 1.4. (a) If the absorption of the plasmon and the molecules do not overlap, it leads to a coupling effected through changes in the refractive index. The adsorption of dye molecules on nanoparticles increases the refractive index of the nano-environment surrounding the nanomaterial resulting in a decrease in the Coulombic restoring force that acts on free electrons. The reduced restoring force thus leads to red-shifted plasmon resonance. (b) If the absorption of the plasmon and the molecules overlap, it results in plasmon-molecule resonance coupling whereby hybrid states are created. The plasmon-molecular resonance coupling can be very strong resulting in drastic changes in the plasmonic and molecular absorption properties. (c) When the molecule and the plasmon have overlapping absorption and fluorescence, the emission intensity of the fluorophores is remarkably enhanced. The enhancement in fluorescence can be explained based on the increase in the excitation rate due to the local electric field enhancements and the increase in the radiative emission rate caused by the increased local densities of photonic states. A detailed understanding of these three types of plasmon-molecule interactions is discussed in the following section.
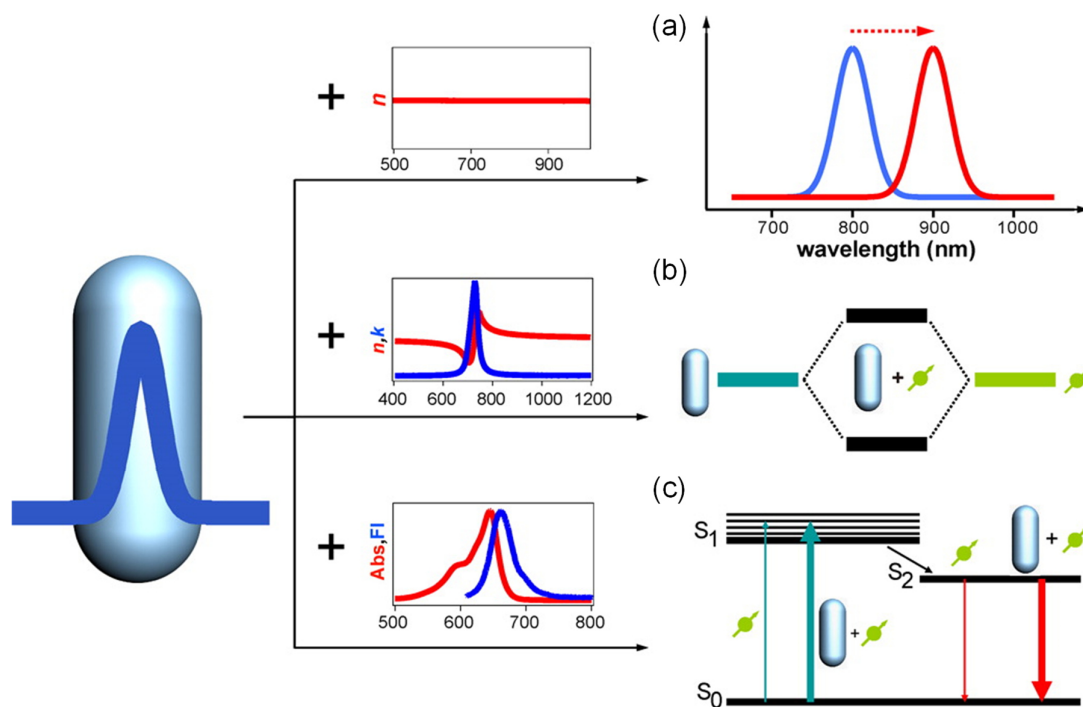
Figure 1.4. Illustration of the three types of plasmon-molecule interactions. (a) Adsorption of molecules without absorption induces a plasmon shift. (b) Resonance coupling occurs between metal nanostructures and adsorbed molecules with strong absorption. (c) Fluorescence enhancement occurs when fluorophores are adjacent to metal nanostructures. Reproduced with permission from ref. [6].

1.5.1. Adsorption.

In the first situation, the absorption spectra of organic dyes do not overlap with plasmon absorption, or dye electronic absorption energies are far away from plasmon resonance energies (Figure 1.4a). Dye adsorption increases the refractive index of the nano-environment around the metal nanostructures. Therefore, an additional induced polarisation charges accumulate around the nanostructures in the presence of external electromagnetic excitation. Furthermore, it increases the screening of the Coulombic restoring force, which acts on free electrons in metal nanostructures. Therefore, the restoring force is reduced. Due to the wavelength-independent nature of refractive index, it results in a red shift in the localized plasmon resonance. This plasmon-molecule interaction lies at the heart of the widely known refractive index sensors. The refractive index sensitivities of metal nanostructures are the key parameters determining the sensor's sensing ability. When the refractive index of the medium is increased by a factor of one, the plasmon peak shifts towards longer wavelength. More polarization charges accumulating around nanostructures

result in stronger Coulombic restoring force screening and larger plasmon resonance red shifts. The ability of metal nanostructures to polarize charge is determined by the local electromagnetic field distribution. The charge polarization of the nanomaterial is driven by the sizes and shapes of the metal nanostructures. Therefore, the refractive index sensitivity is significantly associated with these parameters. It is crucial to understand the key factors that influence the refractive index sensitivity of metal nanostructures to realize the full potential of plasmonic sensors. These plasmon-molecule interactions of metal nanostructures and non-absorbing organic molecules can aid in assessing the essential structural and plasmonic properties and understanding the fundamental aspects of refractive index sensitivities of metal nanostructures.

1.5.2. Resonance Coupling.

When the absorption of molecules overlaps with the absorption of LSPR of metal nanostructures in the second scenario, resonance coupling occurs (Figure 1.4b). The refractive index of molecules which absorb an intense light has both real and imaginary components. The real parts of the refractive index alter abruptly near the molecular absorption peak. Due to the refractive index alteration, the plasmon shifts are much more prominent when molecules are adsorbed on metal nanostructures. This resonance coupling can also be explained from another aspect. The local field adjacent to the surface of metal nanostructures is strongly enhanced when plasmon resonances are excited, with a field intensity enhancement factor of six orders of magnitude. When molecular absorption energy matches the plasmon resonance energy, the molecular transition will effectively couple with the LSPR of metal nanostructures via a local electric field. This coherent plasmon-molecule resonance coupling is found to be incredibly strong, affecting plasmonic and molecular absorption properties and forming the hybrid states and anti-crossing patterns on the coupling energy diagram.[70–73] The hybrid states are formed in a similar way as molecular states are generated by hybridizing two atomic states with similar energies (Figure 1.4b). These hybrid states result in unique photophysical properties to the plasmon-molecule coupled systems. Over the last few years, plasmon-molecule resonance coupling in hybrid nanostructures has been explored for various applications. Surface-enhanced Raman spectroscopy (SERS) is the first application of this type. Fleischmann observed Raman signal enhancement on the rough surface of Ag film in 1974, and this was also the first report on the interaction of surface plasmons with organic molecules.[74] Further, this finding leads to the growth of SERS. The highest Raman shift is observed when the plasmon resonance wavelengths of a metal

nanostructure are situated between the excitation and vibrationally shifted wavelengths. As light-absorbing dyes are commonly used in SERS studies, choosing the suitable nanostructures and excitation laser wavelengths are essential for obtaining the best SERS detection performance and gaining a better knowledge of the plasmon-molecule resonance coupling.

1.5.3. Fluorescence Enhancement.

In the third case, when both the absorption and emission of molecules overlap with those of plasmons, the emission intensity of the molecules increases significantly (Figure. 1.4c). When an organic molecule is placed near metal nanostructures, the fluorescence emission intensities change significantly because of plasmonic excitation, called plasmon-enhanced fluorescence (PEF). The fluorescence enhancement has usually been considered the result of two factors. One case is an increment in excitation rate caused by local electric field enhancements near metal nanostructure surfaces. The other effect is an increase in the rate of radiative emission caused by increasing local densities of photonic states surrounding metal nanostructures.[75,76]
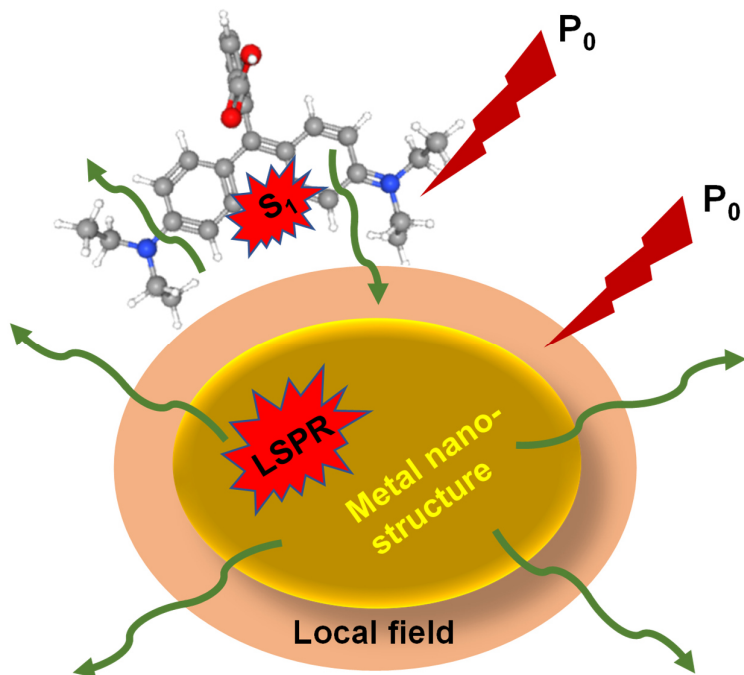
Figure 1.5. Cartoon diagram of plasmon-enhanced fluorescence.

A simplified cartoon diagram of PEF is shown in Figure 1.5. P_0 denotes the excitation power absorbed by a fluorophore conjugated with metal nanostructure. Metal nanostructures

can then generate an excited electronic state of the molecule as well as an LSPR within the nanostructure. The presence of the metal nanostructure is expected to have no significant effect on the non-radiative decay rate (k_{nr}) of the hybrid state. But the surface average of the local electric field intensity enhancement can be easily calculated by the equation: $|E| = \frac{|E_{loc}|}{|E_0|}$. Therefore, the new excitation power experienced by the local electric field will be determined by the formula[77] $<|E|^2>.P_0$. So, the quantum yield for the fluorophore is now calculated as Q_{loc} and the fluorophore enhanced emission is proportional to $F_{enhanced} \approx (<|E|^2>.P_0)\varepsilon Q_{loc}$. Additionally, the induced dipole in the nanostructures affects radiation power.[78] For a simple spherical nanoparticle with a radius of a, the dipole-induced applied field inside the sphere is proportional to E_0. $P = \varepsilon_0\varepsilon_m 4\pi a^3 \frac{\varepsilon - \varepsilon_m}{\varepsilon + 2\varepsilon_m} E_0$, where ε, ε_m, and ε_0 are the dielectric constant of the metal, medium and vacuum respectively. The resonant enhancement occurs at a minimum value of $|\varepsilon + 2\varepsilon_m|$.

For several materials, the increase in radiative emission rate was found to be exponential. This increase in emission rate results in very short fluorescence lifetimes, increased photostabilities, and more photons emitted per unit time. Therefore, the coupling between the emission frequency of the fluorophore and the resonance frequency of metal nanostructures can cause the metal to emit light (with enhanced intensity) at the same emission frequency (elastic scattering) of the fluorophore. This is also known as metal-enhanced fluorescence (MEF). MEF, like the SERS, also strongly relies on the plasmon wavelength of metal nanostructures. Furthermore, the distance between molecules and metal nanostructures is crucial in fluorescence enhancement or quenching.[79] Drexhage and co-workers[80] showed for the very first time in 1960 the distance-dependent decay rate of a fluorophore in front of a mirror; since then, the history of fluorescence on metal surfaces has proliferated. Various groups have shown throughout the PEF history that the signature of an electromagnetic component of a plasmonic system is dependent on the distance between molecules and metal nanostructures. Recent advancements in PEF or MEF emphasized the significance of PEF in stimulating novel approaches in analytical detection, single-molecule detection (SMD) and imaging, diagnostics, and nanostructure fabrication.

1.6.   Applications of Plasmon-Molecule Interactions.

The following section focuses on the various applications of these three types of plasmon-molecule interactions.

1.6.1. Applications of Plasmon-induced Refractive Index Sensing.

Low-cost, real-time, high-miniaturization and ultrasensitive sensors are in high demand for their use in environmental remediation and clinical diagnosis. Metal nanostructure-based refractive index plasmonic sensors are greatly attributed to this purpose. When the refractive index of the medium is increased, the plasmon peak shows a linear red shift. By simply monitoring the plasmon red shift, it is possible to detect the changes in the refractive index of the medium surrounding the metal nanostructures, which is very useful for optical sensing of chemical and biomolecular analytes.[81–85] Au-based plasmonic refractive sensors are reviewed in this chapter due to their high chemical stability, biological compatibility, and ease of conjugation with various chemical and biological molecules. However, there are two basic requirements for a plasmonic refractive index sensor: To detect the presence of a specific chemical or biological species, the surface of the nanostructures should be allowed to attach with recognition molecules particular to the target species. Surface capping should be designed in such a way so that the non-specific binding gets reduced. The changes in the refractive index after binding of the target molecules to the surface of nanostructures would be determined by various factors, such as the number of molecules bound per nanostructure, the molar mass of the molecules, their proximity to the nanostructures surface, and the refractive index of the medium. However, the refractive index shift caused by the binding of a few molecules is expected to be very low. To obtain excellent sensitivity in such conditions, the magnitude of the plasmon band shift caused by a slight change in refractive index in the local medium should be as high as possible.[84] Moreover, the small surface areas of metal nanostructures can significantly reduce non-specific interactions, allowing for more targeted binding interactions. Furthermore, because of the small size of metal nanostructures, small liquid sample volumes are required, which can overcome the mass-transport limit. Several experimental and theoretical studies have been reported over the last few decades for such refractive index sensors at both the ensemble and single-particle levels.[86–88] For example, Van Duyne and co-workers[89] first investigated plasmon resonance sensing for Alzheimer's disease using Ag nanotriangle monolayers fabricated using the lithography technique. The detection limit of down to ~1 pM concentration was obtained. Marco and co-workers[90] reported the detection of Stanozolol hormone with a detection limit of the pM level on glass substrates coated with Au nanoparticles. Chilkoti and co-workers[91] reported biotin-functionalized Au nanorods to detect streptavidin, with a detection limit of as low as 19 nM. Irudayaraj and co-workers[81] reported effectively detecting antiIgG targets using functionalized colloidal Au nanorods

containing IgG Fab segments. Due to the specific binding nature, anti-IgG targets in colloidal solution could thus bind to the functionalized gold nanorod probes, leading to the shift in longitudinal plasmon peak of Au nanorods. They also demonstrated shape-dependent plasmon resonance in multiplexed sensing. To sense three other IgG recognition units simultaneously, they used a mixture of three conjugated Au nanorods with different IgG recognition units with aspect ratios of 2.1, 4.5, and 6.3. Many previous studies have shown that the sensitivity of refractive index sensors increases as the localized plasmon wavelength increases for a particular metal nanostructure. For example, Au nanorings with a plasmon peak at 1300 nm had a refractive index sensitivity 12 times higher than Au nanospheres with a plasmon peak at 550 nm.[92–94] The metal nanoshell structure also significantly enhances sensitivity over simple spherical metal nanoparticles. Xia and co-workers[85] reported that hollow Au nanoshells exhibited six times higher plasmon sensitivity than a similar-sized solid Au nanosphere. El-Sayed and co-workers[95] performed electrodynamic simulations to explore plasmon sensing concerning the aspect ratio of colloidal gold nanorods (Figure 1.6).
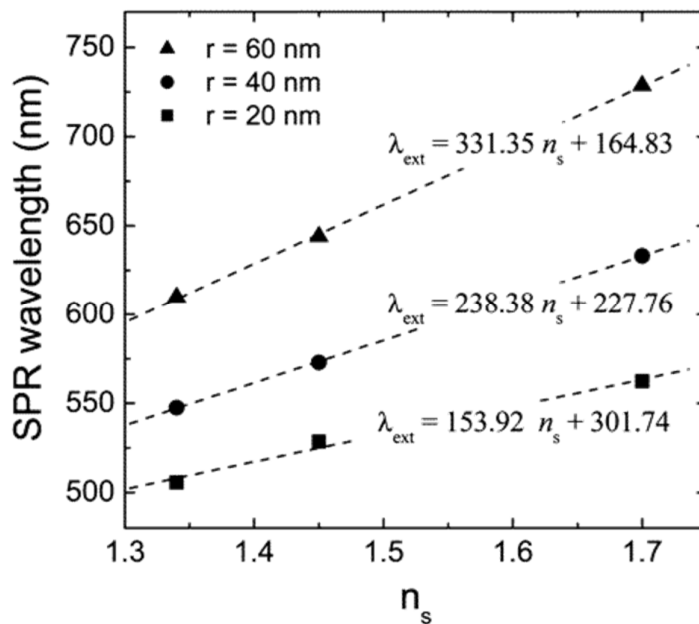
Figure 1.6. Shape tunability of the plasmonic sensitivity. By increasing the gold nanorod aspect ratio, the sensitivity of the longitudinal surface plasmon resonance to surrounding medium refractive index changes can be increased. Reproduced with permission from ref. [95].

Further, Wang and co-workers[96] studied the refractive index sensitivity of numerous Au nanostructures of different shapes and sizes (Figure 1.7). They varied the size and shape

of the Au nanostructures to produce plasmon wavelengths ranging from 525 nm to 1150 nm. They demonstrated that Au nanospheres with the shortest plasmon wavelength had the lowest refractive index sensitivity of 44 nm/RIU (Refractive index unit). In contrast, Au nanobranches with the longest wavelength possessed the maximum refractive index sensitivity of 703 nm/RIU. Furthermore, the refractive index sensitivities of Au nanorods and Au bipyramids increased as the plasmon wavelengths increased. Their findings revealed that the refractive index sensitivities were primarily determined by the shapes and sizes of the Au nanostructures. They also investigated how the refractive index varies with different shapes of Au nanostructures while keeping the longitudinal peak at the same wavelength.
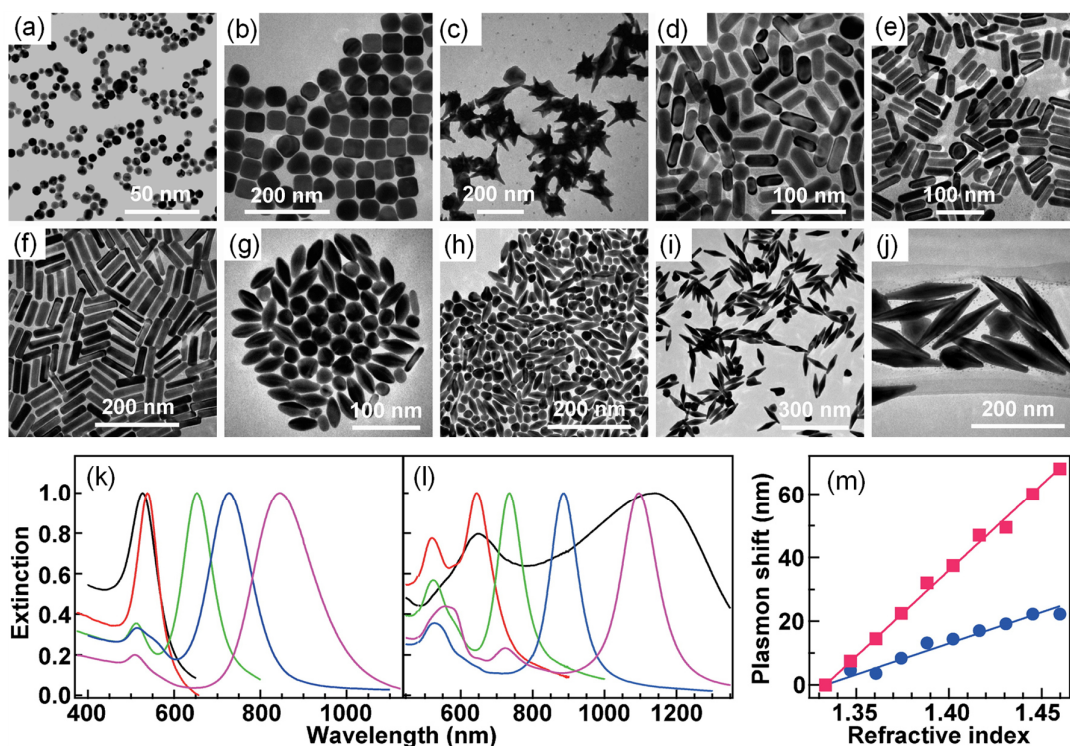
Figure 1.7. Au nanostructures with various shapes and sizes: (a) nanospheres, (b) nanocubes, (c) nanobranches, (d-f) nanorods, and (g-j) nanobipyramids with increasing aspect ratios; and normalized extinction spectra of (k) nanospheres (black), nanocubes (red), and three different nanorods (green, blue and purple) and (l) four different nanobipyramids (red, green, blue and purple) and nanobranches (black); and the dependency of the longitudinal plasmon shift on the refractive index (m) for the nanorods at 653 nm (blue circles) and nanobipyramids at 1096 nm (red squares), respectively. Reproduced with permission from ref. [96].

Furthermore, Wang and co-workers prepared seven Au nanostructures with a longitudinal plasmon peak at 730 nm, including large nanorods, nanobipyramids, oxidized nanobipyramids, dog-bone-like nanorods, peanut-like nanorods, and tiny nanorods. The refractive indices of these Au nanostructures was observed to be shape and curvature-dependent.[97] The large nanorods had the highest index sensitivity of 326 nm/RIU, while the tiny nanorods had the lowest of 156 nm/RIU. The refractive index sensitivities of such Au nanostructures were determined mainly by the ease with which the free-electron cloud in the nanostructure was shifted relative to the positive atomic lattice by an external electric field. When the displacement of the free-electron cloud in the nanostructures became easier, higher refractive index sensitivities were observed. In general, the removal of free electrons in nanostructures is determined by their polarizability and the local electric field around their surface, both of which are strongly anticipated by the shapes and sizes of the nanostructures.

1.6.2. Applications of Resonance Coupling.

When LSPR interact strongly with light-absorbing chromophores, a hybrid state is formed with distinct spectral properties that differ from individual constituents. Plasmon resonance frequency increases the local electric field near metal nanostructures. This strongly enhanced near-field has the potential to increase the spectroscopic signals of molecules in the proximity of metal nanostructures. The most common example of resonance coupling is SERS. Raman scattering spectroscopy can give comprehensive information about a molecular structure.

Figure 1.8. SERS is graphically represented as inelastic light scattering by molecules adsorbed onto the metallic surface.

The absorption frequency of an excited photon (ω_{ex}) coupled to the vibration frequency (ω_{vib}) of a molecule generates an emission at distinct frequencies $\omega_{em} = \omega_{ex} \pm \omega_{vib}$, where the sum or difference results in anti-Stokes or Stokes Raman scattering, respectively (Figure 1.8). As a result, three inelast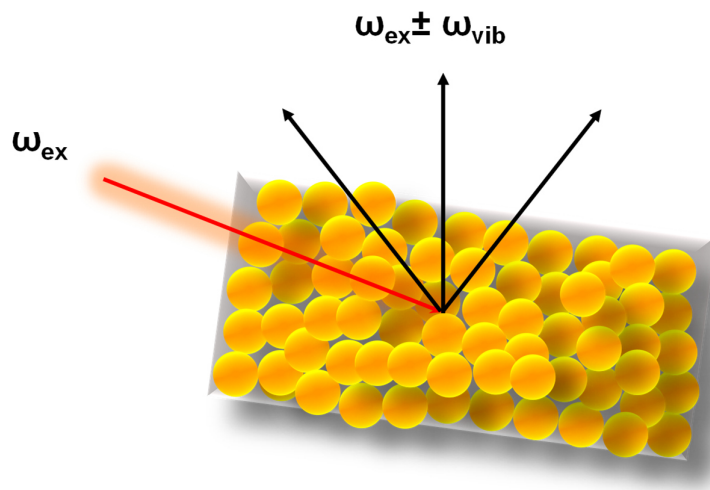ic transitions are engaged in this process: absorption, vibrational excitation, and emission. The environment affects vibrational excitation through chemical interaction, but the other two processes are governed by the availability of photonic states at various position of the molecules. One of the primary drawbacks of Raman scattering spectroscopy is that most molecules exhibit a weak Raman scattering signal. Only about one in 10 million scattered photons show Raman scattered effect. Therefore, the Raman scattering signal enhancement at the surface metal nanostructures (typically 10^5-10^6 times) is known as SERS. One of the primary reasons for this SERS enhancement is increasing the local electric field. Usually, computational electrodynamics is used to determine the increment of the electromagnetic field. When plasmons on a SERS substrate are excited at the frequency of ω_{ex}, the electric field amplitude $E(\omega_{ex})$ increases. The molecular positions are then used to evaluate $E(\omega_{ex})$. The SERS enhancement is thus defined as $|E(\omega_{ex})|^2|E(\omega')|^2/|E_0|^4$, where E_0 is the incident (laser) field amplitude and ω' is the Raman-shifted frequency.[98–100] As a result, the electromagnetic component of SERS enhancement is directly proportional to the square of the field strength experienced by any metal nanostructure. Changes in the chemical polarizability of the molecule as a consequence of the interaction with the metal surface are another source of SERS enhancement. According to Raman scattering theory, when molecules oscillate, the applied electric field can experience induced polarization (P_0) and emit scattered light at a Raman-shifted frequency of ω'. The strength of induced polarization (P_0) relies on the polarizability of the electrons in molecule (α^R_0) and the magnitude of the incident electromagnetic radiation E_0 (with incident frequency of ω_{ex}). Furthermore, the induced polarisation (P_0) can be determined by using the formula as follows: $P_0(\omega') = \alpha^R_0(\omega_{ex},\omega')E_0(\omega')$, where α^R_0 is changed in electron clouds during vibrations.[101] SERS has grown into a flourishing field of research and technology since its discovery. Many research articles have been published for this plasmonic enhancement of Raman scattering, both theoretically and in their diverse applications.

The Raman scattering enhancement is highly tuneable with respect to the shape, size, and composition of the metal nanostructure.[102] A schematic illustration of the SERS enhancement for various shapes of the Au nanostructures is shown in Figure 1.9. Since silver has more vital plasmonic fields than gold, silver nanostructures often provide more significant SERS enhancement than gold nanostructures.[103] The shape tunability of SERS

enhancement is commonly observed on gold nanorods.[104] Since nanorods have a sharper curvature than nanospheres, their plasmon fields are substantially more potent, resulting in an intense SERS at the longitudinal axis mode of resonance.[95] By varying the aspect ratio of the nanorod, it is possible to tune the resonance frequency of the Raman enhancement from visible to NIR.[105] Adjusting the SERS enhancement to the NIR region to study biomolecules offers vast benefits. Raman signals are generated by the excitation of a sample with a laser whose frequency is resonant with an electronic transition in the sample. But, the use of deep UV or visible lasers typically causes photochemical damage to such biomolecules. Furthermore, interference from fluorescence from specific residues often limits the usage of this technique for biomolecules. As a result, nanorod allows a NIR laser to produce a strong Raman signal without causing any photochemical damage or interference since biomolecules such as proteins and DNA do not absorb in the NIR region.[105] The potential to investigate fundamental science at the nanoscale using SERS to develop practical societal tools for personalized medicine and other challenges[7] puts SERS well for future advances in various fields such as electrochemistry, medicine, biology, and material sciences.

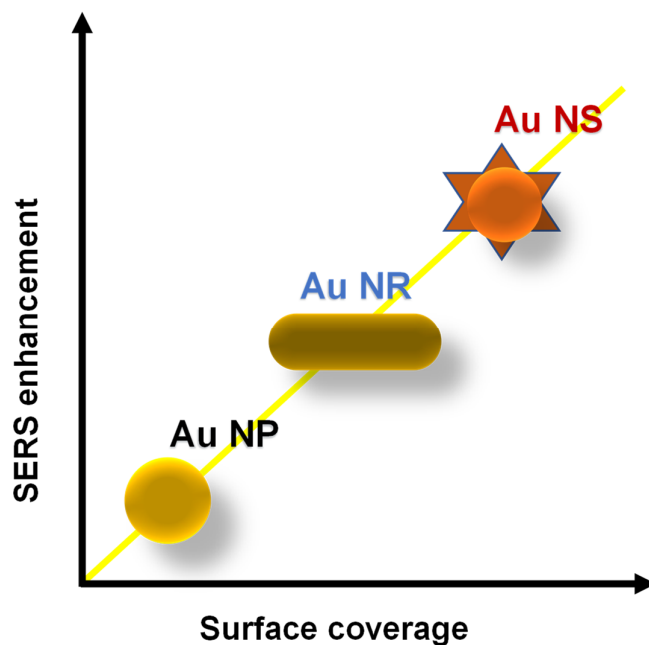**Figure 1.9**. Schematic illustration for the SERS enhancement as a factor of surface coverage for different gold nanostructures.

Besides SERS, the effect of numerous organic molecules with metal nanostructures was investigated to develop optoelectronic devices capable of energy transfer, switching and lasing. In the 1980s, Philpott and co-workers[106] and Olson and co-workers[107] studied the

coupling effect of Rhodamine B and the Nile red over Ag thin film both theoretically and experimentally. Further, Ebbesen and co-workers[108] used the same idea and developed a switchable photonic device by coating a poly(methylmethacrylate) film containing a photochromic dye on the outer surface of Ag hole arrays. UV and visible light were used to turn on and off the device. Similarly, Brongersma and co-workers[109] fabricated a non-volatile plasmonic switch on an aluminium film containing a photochromic dye with efficient switching power densities of ∼6.0 mW/cm^2 in a 1.5 μm × 8 μm device.

Scientists have studied the numerous photophysical properties resulting from the hybrid state to better understand the resonance coupling in terms of dye concentration and the plasmonic nature of metal nanostructures. Wiederrecht and co-workers[73] investigated a case study of coherent coupling between molecular J-aggregate excitons of 5,5'-dichloro-3,3'-disulfopropylthiacyanine sodium salt (TC) dye and noble metal nanostructures (Figure 1.10a). They showed that this resonance-coupling strongly depends on the position of the plasmon peak of metal nanoparticles. A constructive coherent coupling is observed for Ag nanoparticles, resulting in increased absorption of J-aggregate/metal nanoparticle heterostructures over bare nanoparticles whereas a destructive coherent coupling is observed for Au nanoparticles, resulting in decreased absorption. Halas and co-workers[70] further studied the wavelength-dependent coherent coupling nature of plasmon in hybrid nanostructures composed of Au nanoshells and a molecular J-aggregate of 2,2'-dimthyl-8-phenyl-5,6,5',6,-dibenzothiacarbocyanine chloride (Figure 1.10b). They showed that the plasmon energies of Au nanoshells could be adjusted systematically by varying the core size/shell thickness ratio. Furthermore, the asymmetric energy splitting and anti-crossing features of such hybrid nanostructures were clearly observed. Wang and co-workers[110] reported molecule-plasmon coupling in gold nanorods coated with the cyanine dye HITC (Figure 1.10c). Au nanorods of different longitudinal plasmon wavelengths were synthesized and covered with HITC by a layer-by-layer assembly method. It was observed that the optical properties of hybrid system were significantly different compared to its constituents and that the longitudinal plasmon peaks were split into two, thereby suggesting the molecule-plasmon coupling. Further, the coupling-induced plasmon shift depended on the dye concentration and the space between the dye and the nanorod. They also investigated the effect of different dyes on the resonance coupling of different Au nanostructures. Au nanostructures were chosen for each dye to match the longitudinal plasmon resonance peak with the dye absorption peak as closely as possible to increase the resonance coupling strength. Red-shifted plasmon peaks were observed, which differed significantly between dyes. The increase in plasmon shifting

was observed when the molecular volume-normalized absorptivity was increased. Furthermore, the pH-sensitive resonance coupling between Au nanorods and HITC dye was observed. They also looked into resonance coupling on single Au nanorods. The scattering peak position and intensity caused by resonance coupling shifted systematically with respect to the initial longitudinal plasmon wavelength. Further, they showed the switchable nature of resonance coupling using photo decomposing of HITC molecules. When the dye was decomposed by laser illumination, the resonance coupling was switched off. Thomas and co-workers[111] studied the role of oscillator strengths and spectral widths on the coupling between plasmons and excitons (Figure 1.10d). Two systems were designed for studying plexitonic interactions wherein chromophores were attached covalently and non-covalently to plasmonic structures. The chromophores were selected in such a way as to have absorbance in the entire UV-vis region. The experimental data supported the importance of spectral widths and effective oscillator strengths in governing plexcitonic coupling. These studies laid the foundation for developing various ultrasensitive sensing and photonic devices based on resonance coupling.
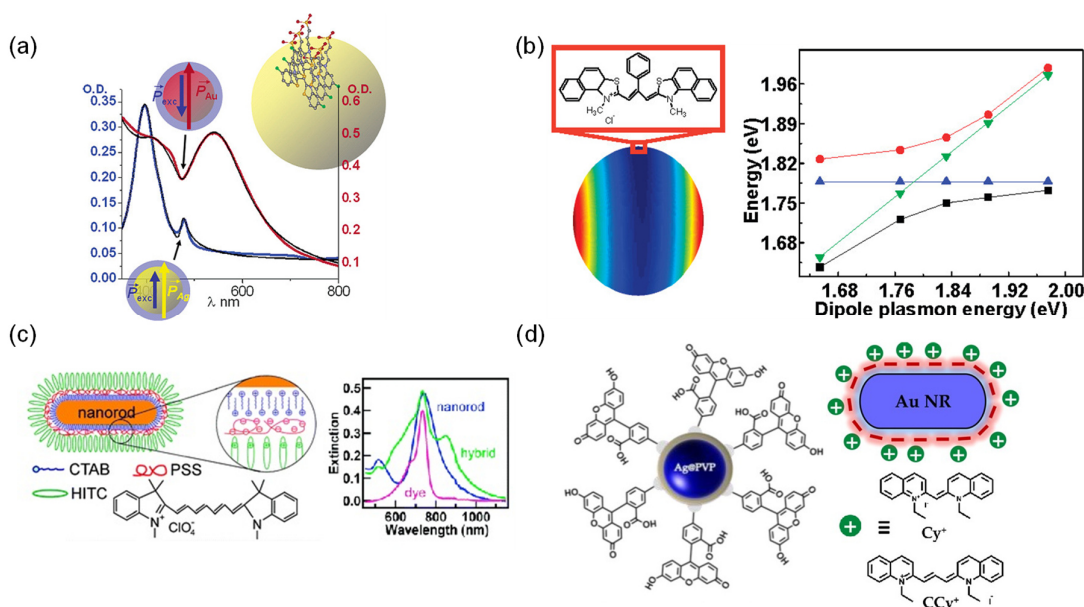
Figure 1.10. Schematic representation of (a) ground-state spectra of dibenzothiacarbocyanine dye coated Ag and Au nanoparticles, (b) hybrid nanostructure of Au nanoshell and thiacarbocyanine dye, (c) HITC-Au nanorod hybrid nanostructure (left), and (right) their absorption spectra, and (d) Ag nanoparticles functionalized with fluorescein isothiocyanate (left) and (right) Au nanorods functionalized with 1,1'-diethyl-2,2'-cyanine iodide or 1,1'-diethyl-2,2'-carbocyanine iodide. Reproduced with permission from ref. [73, 70, 110 and 111].

1.6.3. Applications of Plasmon- or Metal-enhanced Fluorescence.

In general, two factors affect the fluorescence properties of a fluorophore: (i) excitation of an electron from the ground state to an excited state and (ii) radiative transition from the excited state to the ground state. The plasmon resonance peak of a metal nanostructure can interfere strongly with both these processes. Separation of the fluorophore from the metal surface has been found to be important in both of these processes. Werts and co-workers[112] showed that fluorescence quenching occurred when the distance between fluorophores and the metal surface was less than 5 nm. After a certain distance, metal nanostructures showed significant enhancements in an electric field, excitation and radiative decay rates than the non-radiative decay rate, resulting in increased fluorescence intensities and reduced emission lifetimes.[113–115] Bagchi and co-workers[116] investigated theoretically the distance dependence MEF, precisely the energy transfer rate from a dye to a nanoparticle as part of the more significant issue of excitation energy transfer. Geddes and co-workers[79] used a DNA scaffold to determine the distance-dependent MEF quantitatively, well-matched with theoretical calculations. Furthermore, the coupling with the surface plasmon could alter emission direction and spectral shape of fluorophores. Several studies on MEF-based devices have been reported over the years, including fluorescence microscopy[117], fluorescence microarray scanners[118], microplate readers[119], and new devices developed for fluorescence signal amplification. Furthermore, several MEF-based sensors[120,121] have been documented in the literature to detect various analytes, such as biomarkers, pathogens, and toxins, to aid in the early diagnosis of diseases.

The fluorescence enhancement factor is critical in plasmon or metal-enhanced fluorescence experiments. Consequently, many systematic studies are being conducted to understand the factors influencing the enhancement factor and find the upper limit. Moreover, this fluorescence enhancement has been addressed at the single-particle level, avoiding the influence of inhomogeneous broadening and the system's non-uniformity of excitation and emission. For instance, Moerner and co-workers[11] developed Au bowtie nanoantennas embedded in a polymer matrix with a NIR light-absorbing dye (Figure 1.11a). The fluorescence enhancement factor is found to be up to 1340, the highest ever observed. Wang and co-workers[122] investigated fluorescence imaging and spectroscopic measurements on a single-particle level of Au nanorods core-shell/oxazine 725 heterostructures (Figure 1.11b). Orrit and co-workers[123] showed plasmon-enhanced single-molecule fluorescence enhancement of a dye conjugated with Au nanorods coated on glass by a factor of 1100 (Figure 1.11c). Chen and co-workers[124] used super-resolution fluorescence microscopy to

monitor a single catalytic reaction on an Au nanorod surface with a spatial resolution of ~40 nm (Figure 1.11d).
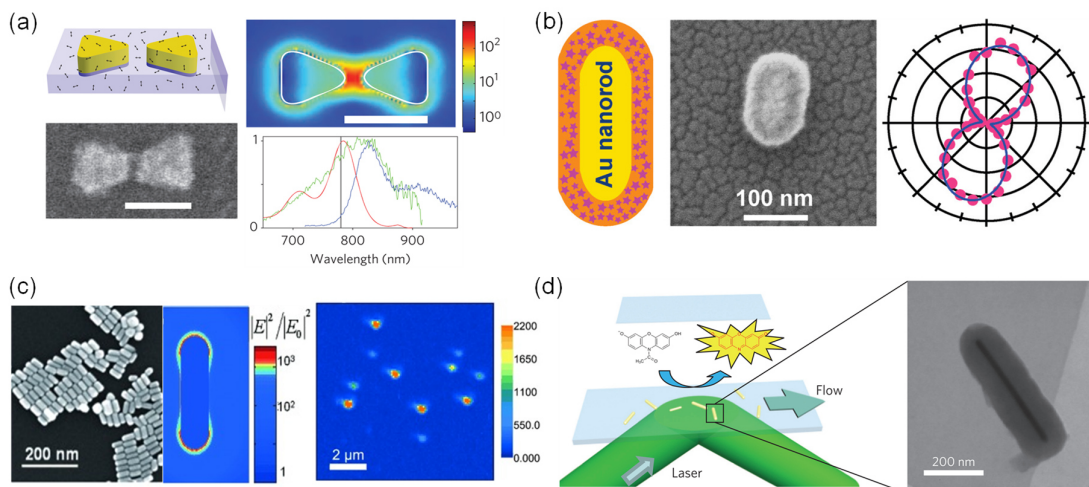
Figure 1.11. Schematic representation of (a) MEF of NIR dye loaded Au bowtie nanoantennas, (b) polar plot of the fluorescence intensity of Au nanorod-oxazine 725 hybrid nanostructure, (c) fluorescence imaging of SMD enhanced by Au nanorod and (d) catalysis by the silica-coated Au nanorod Reproduced with permission from ref. [11, 122, 123 and 124].

DNA origami has been used to fabricate MEF nano-architectures due to its molecular self-assembly nature. Tinnefeld and co-workers[125] used DNA origami to arrange Au NP dimers to generate variable inter-particle distance and then modulated the plasmonic hotspot to enhance the plasmon-enhanced fluorescence. Maximum fluorescence enhancement of 117-fold was observed when a dye molecule was placed in the 23-nanometer gap between 100-nanometer Au nanoparticles. Knoll and co-workers[126] employed MEF techniques to investigate the kinetic parameters of mismatched DNA interactions in DNA hybridization. Liang and co-workers[119] designed a novel Au nanorod array biochip to detect molecular beacons at up to 10 pM. Many studies showed that these plasmonic nanoantennas are used for various applications, including DNA binding assays[125], genetic disorder diagnosis[127], forensic testing[10], and ultra-sensing sample matrix under physiological conditions[121].

1.7.   Applications of Plasmon-Molecule Interaction in Photodynamic Therapy.

Photodynamic therapy (PDT) is a therapeutic approach that is particularly effective for treating malignant and premalignant tumours. In the early 1900s, using PDT as a novel therapeutic approach was proposed. H. Tappeiner and A. Jodlbauer coined the term

"photodynamic action" upon finding the demand for oxygen in photosensitization reactions.[128] The first big breakthrough in PDT happened in 1975 at the Roswell Park Cancer Institute in Buffalo. Dougherty and co-workers[129] reported first-time successful treatment of tumours using PDT in animal specimens, beginning a new era for this therapy. The first PDT clinical trials were conducted in the late 1970s. The effects of light and hematoporphyrin derivatives (HpD) on five patients with bladder cancer were investigated in this study.[130]

PDT comprises three major components: a photosensitizer (PS), light, and molecular oxygen. PDT mainly involves the activation of a photosensitizer by light, which results in the generation of cytotoxic reactive oxygen species (e.g., singlet oxygen) within cells, causing irreversible cellular damage and cell death. PDTs are categorized into two types, denoted as type I and type II, based on the photochemical reaction process used to generate reactive oxygen species (ROS). Upon photoactivation, PS goes to the excited singlet state from the ground singlet state and then to the excited triplet state via intersystem crossing (ISC). For type I PDT, the PS in the triplet excited state participates in an electron transfer process to react directly with triplet oxygen ($^3O_2$) or cellular substrate to produce superoxide anions ($O_2 \cdot^-$) and hydroxyl radicals (OH·), respectively.[131] However, cytotoxic singlet oxygen ($^1O_2$) is produced in type II PDT due to an energy transfer between the PS in the triplet excited state and the surrounding $^3O_2$[132] (Figure 1.12).
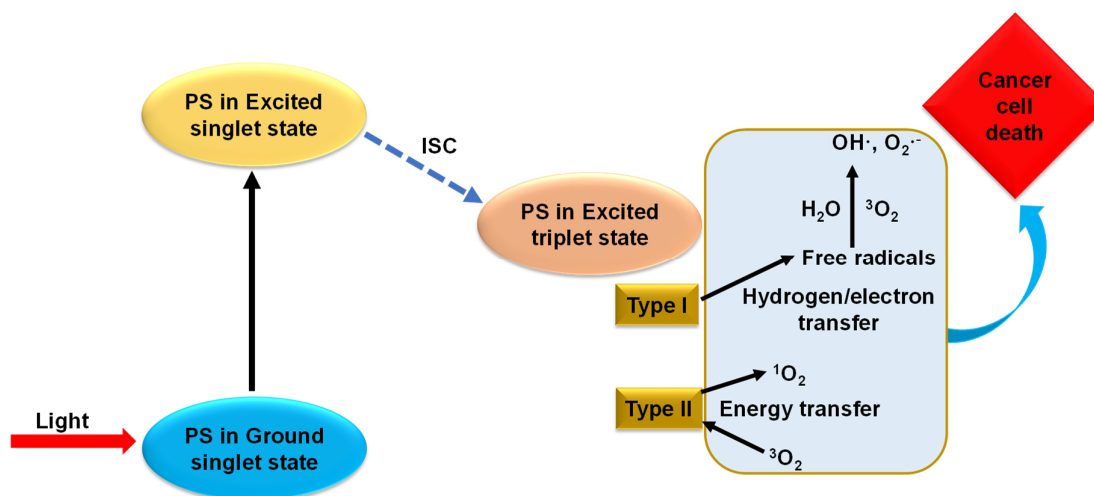
Figure 1.12. Schematic illustration of the PDT mechanisms.

An ideal PS should have qualities like a high capacity for singlet oxygen generation, absorption bands within the therapeutic window, and the capabilities to colocalize in cancer tissue. The advancement of PDT primarily depends on developing new luminescent PS with

excellent photostability and the potential to generate singlet oxygen in the NIR absorption region due to more tissue penetration.[133] Scientists have worked hard to develop new PS, ranging from the first generation, such as porphyrins and their derivatives[134], to the second generation, such as chlorins and phthalocyanines[135,136], to the third generation, including their conjugation with antibodies or encapsulation with carriers[137,138], to provide more targeted therapy (Figure 1.13). Further, 4,4-difluoro-4-bora-3a,4a-diaza-s-indacene (BODIPY)[139] has gained much importance in scientific research as an efficient photosensitizer used as a PDT agent of cancers as an alternative class to nonporphyrin-based photosensitizers (Figure 1.13). The inclusion of a heavy atom in the BODIPY core, such as Br or I, enhances the excited state intersystem crossing, facilitating singlet oxygen production.[140,141] However, most PSs have limited use in cellular conditions due to poor solubility and fluorescence quenching in the cellular medium. As a result, two aspects of photosensitizers should be considered: first, their photophysics, which is crucial for the generation of reactive oxygen species efficiently, and second, their distribution in cellular environments, specifically their ability to localize in cell membranes, which is the site of action in PDT. Several reports have been published over the last few decades on designing small-molecule PSs[142], activatable PSs[143,144], and nanosystem-based approaches[145–148] for improving PDT.

Figure 1.13. Selected examples of photosensitisers (PSs).

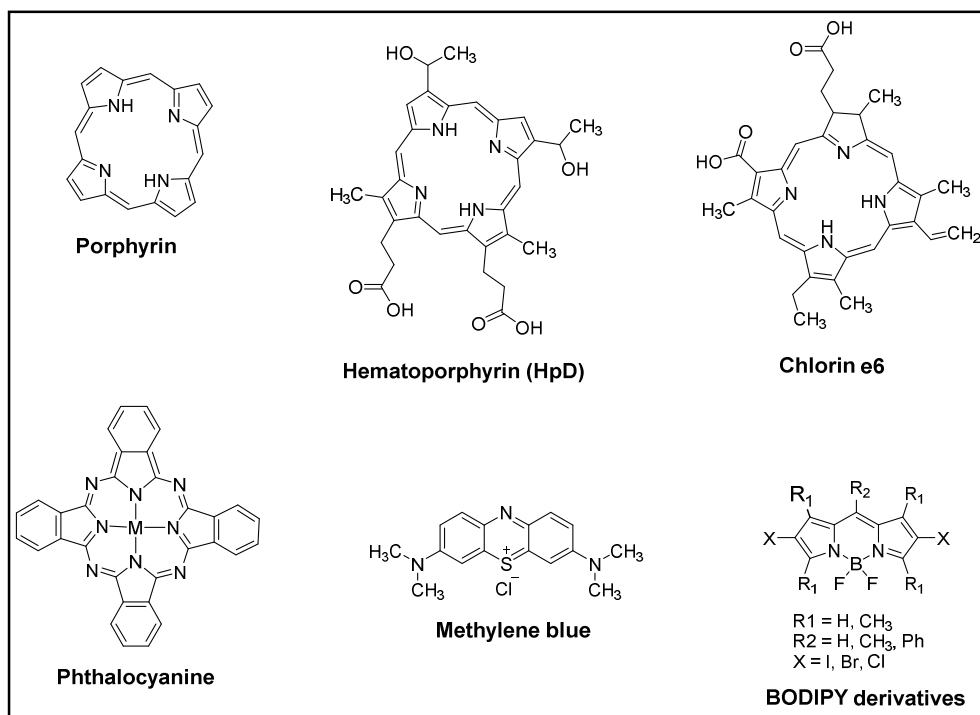Plasmon-molecule interactions have incredible potential in materials science and biology as discussed earlier. Several literature reports exemplify their utility as ultrafast switches, bistable devices, modulators, sensors, photocatalysts and biological imaging agents.[149–151,57,152,153] A few examples are also known wherein molecule-plasmon interactions have been utilized in PDT. For instance, Geddes and co-workers[154] reported that this principle could be employed for enhancing singlet oxygen generation of organic photosensitizers. It was shown that the singlet oxygen yield of Rose Bengal was dependent on the theoretical electric field enhancement or enhanced absorption of the photosensitizer in the presence of metallic nanoparticles in close proximity. Although the mechanism of singlet oxygen generation was speculated to be improved triplet yields, no experimental evidence was provided to substantiate the same.[155] It was also suggested that such systems are potentially valuable for PDT. Chen and co-workers[156] showed that strong plasmon resonance coupling enhanced singlet oxygen generation in an electrostatically bound AuNRs-chlorin e6 system. Further, they utilized it to kill the cancer cells. In another study, Wu and co-workers[157] reported that plasmon resonance energy transfer (PRET) from plasmonic nanoparticles to PSs caused plasmon quenching dips, an effective technique to enhance $^1O_2$ generation. They used the photosensitizer chlorin e6 with AuNR as a model system for this study. When the LSPR band of Au NR overlaps with the Q band of Ce6, and the distance between Ce6 and the Au NR is within the acting distance of PRET, a significant quenching dip in the LSPR band was observed. Plasmon-molecule interactions are also employed for antibacterial activity via the PDT method. For instance, Zhang and co-workers[158] reported that the resonance coupling between the surface plasmon of silver nanoparticles and photosensitizers enhanced singlet oxygen generation by up to three-fold. They evaluated the PDI activity of the hybrid photosensitizer on a model gram-positive bacterium, *Staphylococcus epidermidis*, as well as gram-negative bacteria, *Escherichia coli*, and drug-resistant *Acinetobacter baumannii*. They showed that their nanohybrid systems killed both gram-positive and gram-negative bacteria efficiently compared to the individual component. Heyne and co-workers[159] showed metal-enhanced $^1O_2$ generation in silica-coated silver nanocubes coupled with Rose Bengal dye. They also used it for the photodynamic killing of Gram-positive bacteria, *Staphylococcus aureus,* and Gram-negative bacteria, *Escherichia coli*.

1.8.   Scope and Objectives of the Present Investigation.

As previously discussed, plasmon-molecule interactions have sparked considerable interest for their numerous applications in material science and biology. The above sections summarized various aspects of surface plasmons, excitons, and their interaction. Furthermore, the various categories of plasmon-molecule interactions and their applications were discussed. Recent advances in plasmon-molecule interaction for applications in PDT were also reviewed. Although the results of such investigations were promising, the mechanistic details of are generally overlooked and theoretical calculations have been mainly used to support their observations.

Our group recently reported a three-component heavy atom-free supramolecular nanocomposite containing tryptophan, a BODIPY molecule, and gold nanoparticles.[160] The BODIPY molecule was observed to be non-covalently attached to the surface of gold nanoparticles through various supramolecular interactions. The nanocomposite formation resulted in significant changes in the photophysical properties of their components. The nanocomposites were also observed to generate singlet oxygen more efficiently than their components. It was also proposed that the observed differences in photophysical properties were caused by the emergence of a hybrid state. Motivated by these facts, this dissertation aims to study the photophysical properties of a series of nanocomposites to reveal the underlying mechanism of plasmon-molecule interactions. One of the challenges in this area is the inability to control the size of molecular aggregates interacting with metal nanoparticles. To address this issue, we attempted to simplify the synthetic methodology by carefully designing the dye molecules and their self-assembly around nanoparticles. In this scenario, this dissertation is devoted to tuning the photophysical properties of dye-loaded gold nanoparticles through plasmon-molecule coupling.

Chapter 2 describes the synthesis and characterization of dye molecules and their nanocomposites. NMR spectroscopy revealed that various supramolecular interactions between the individual components play a vital role in forming stable nanocomposites. We studied the effect of structural variations in the dye molecules on nanocomposite formation and it was observed that sterically bulky molecule destabilizes the nanocomposites. Further, a naphthalidenimine-boron complex containing a stimuli-responsive group was employed to study the immediate effect of environment on the photophysical properties. We also synthesized a multi-chromophoric nanocomposite containing two dye molecules to study the impact of interaction between the two molecules on the photophysics of the nanocomposites.

Chapter 3 discusses the photophysical properties of all the nanocomposites. The nanocomposite formation resulted in significant changes in the photophysical properties of their components: bathochromic shifts were observed in the absorption maxima of the dye molecules and gold nanoparticles, whereas the fluorescence of the dye molecules was completely quenched. On the other hand, in the multi-chromophoric nanocomposite, Förster resonance energy transfer (FRET) was observed to occur between the two dye molecules on the surface of gold nanoparticles. This opened up radiative pathways and made this nanocomposite moderately fluorescent. In the case of the stimuli-responsive naphthalidenimine-boron complex, wherein the absorption overlap was minimal with gold nanoparticles but a significant overlap was observed between the fluorescence of the dye and the absorption of gold nanoparticles, plasmon-enhanced luminescence was observed. Thus, our findings highlight the importance of spectral overlap between the dye molecule and gold nanoparticles on plasmon-molecule coupling. Further, the chemical structure of dye molecules significantly affected the photostability and photosensitization properties of the nanocomposites.

Chapter 4 focuses on the potential application of the synthesized nanocomposites as photosensitizers for PDT. Ultrafast spectroscopy was used to map the excited state processes in the nanocomposites and our investigations revealed hot electron migration from the BODIPY dyes to gold nanoparticles. Further, the nanocomposites exhibited enhanced plasmonic lifetimes, increasing singlet oxygen generation upon plasmonic photoexcitation. However, we observed a reversal in the direction of hot electron migration from gold nanoparticles to the naphthalidenimine-boron complex which resulted in enhanced luminescence. Further, the nanocomposites were found to be photostable and biocompatible and thus were utilized as photocytotoxic agents against cancer cells and luminescence imaging agents.

1.9.   References.

[1]   N. J. Halas, *Nano Lett.* **2010**, *10*, 3816–3822.

[2]   J. A. Schuller, E. S. Barnard, W. Cai, Y. C. Jun, J. S. White, M. L. Brongersma, *Nat. Mater.* **2010**, *9*, 193–204.

[3]   J. Zhao, L. J. Sherry, G. C. Schatz, R. P. Van Duyne, *IEEE J. Sel. Top. Quantum Electron.* **2008**, *14*, 1418–1429.

[4]   E. Ozbay, *Science* **2006**, *311*, 189–193.

[5] A. Csaki, T. Schneider, J. Wirth, N. Jahr, A. Steinbrück, O. Stranik, F. Garwe, R. Müller, W. Fritzsche, *Philos. T. Roy. Soc. A* **2011**, *369*, 3483–3496.

[6] H. Chen, T. Ming, L. Zhao, F. Wang, L.-D. Sun, J. Wang, C.-H. Yan, *Nano Today* **2010**, *5*, 494–505.

[7] J. Langer, D. Jimenez de Aberasturi, J. Aizpurua, R. A. Alvarez-Puebla, B. Auguié, J. J. Baumberg, G. C. Bazan, S. E. J. Bell, A. Boisen, A. G. Brolo, J. Choo, D. Cialla-May, V. Deckert, L. Fabris, K. Faulds, F. J. García de Abajo, R. Goodacre, D. Graham, A. J. Haes, C. L. Haynes, C. Huck, T. Itoh, M. Käll, J. Kneipp, N. A. Kotov, H. Kuang, E. C. Le Ru, H. K. Lee, J.-F. Li, X. Y. Ling, S. A. Maier, T. Mayerhöfer, M. Moskovits, K. Murakoshi, J.-M. Nam, S. Nie, Y. Ozaki, I. Pastoriza-Santos, J. Perez-Juste, J. Popp, A. Pucci, S. Reich, B. Ren, G. C. Schatz, T. Shegai, S. Schlücker, L.-L. Tay, K. G. Thomas, Z.-Q. Tian, R. P. Van Duyne, T. Vo-Dinh, Y. Wang, K. A. Willets, C. Xu, H. Xu, Y. Xu, Y. S. Yamamoto, B. Zhao, L. M. Liz-Marzán, *ACS Nano* **2020**, *14*, 28–117.

[8] D.-K. Lim, K.-S. Jeon, H. M. Kim, J.-M. Nam, Y. D. Suh, *Nat. Mater.* **2010**, *9*, 60–67.

[9] Y. Fang, N.-H. Seong, D. D. Dlott, *Science* **2008**, *321*, 388–392.

[10] J.-F. Li, C.-Y. Li, R. F. Aroca, *Chem. Soc. Rev.* **2017**, *46*, 3962–3979.

[11] A. Kinkhabwala, Z. Yu, S. Fan, Y. Avlasevich, K. Müllen, W. E. Moerner, *Nature Photon.* **2009**, *3*, 654–657.

[12] T. Hirakawa, P. V. Kamat, *J. Am. Chem. Soc.* **2005**, *127*, 3928–3934.

[13] Y. Tian, T. Tatsuma, *J. Am. Chem. Soc.* **2005**, *127*, 7632–7637.

[14] K. Awazu, M. Fujimaki, C. Rockstuhl, J. Tominaga, H. Murakami, Y. Ohki, N. Yoshida, T. Watanabe, *J. Am. Chem. Soc.* **2008**, *130*, 1676–1680.

[15] S. D. Standridge, G. C. Schatz, J. T. Hupp, *J. Am. Chem. Soc.* **2009**, *131*, 8407–8409.

[16] A. V. Kabashin, P. Evans, S. Pastkovsky, W. Hendren, G. A. Wurtz, R. Atkinson, R. Pollard, V. A. Podolskiy, A. V. Zayats, *Nat. Mater.* **2009**, *8*, 867–871.

[17] B. Sepúlveda, P. C. Angelomé, L. M. Lechuga, L. M. Liz-Marzán, *Nano Today* **2009**, *4*, 244–251.

[18] J. N. Anker, W. P. Hall, O. Lyandres, N. C. Shah, J. Zhao, R. P. Van Duyne, *Nat. Mater.* **2008**, *7*, 442–453.

[19] G. L. Liu, Y. Yin, S. Kunchakarra, B. Mukherjee, D. Gerion, S. D. Jett, D. G. Bear, J. W. Gray, A. P. Alivisatos, L. P. Lee, F. F. Chen, *Nat. Nanotechnol.* **2006**, *1*, 47–52.

[20] R. H. Ritchie, *Phys. Rev.* **1957**, *106*, 874–881.

[21] H. A. Atwater, *Sci. Am.* **2007**, *296*, 56–63.

[22] Z. Zhang, Y. Fang, W. Wang, L. Chen, M. Sun, *Adv. Sci.* **2016**, *3*, 1500215.

[23] W. Zhao, S. Wang, B. Liu, I. Verzhbitskiy, S. Li, F. Giustiniano, D. Kozawa, K. P. Loh, K. Matsuda, K. Okamoto, R. F. Oulton, G. Eda, *Adv. Mater.* **2016**, *28*, 2709–2715.

[24] A. W. Wark, H. J. Lee, R. M. Corn, *Anal. Chem.* **2005**, *77*, 3904–3907.

[25] M. Wang, M. Ye, J. Iocozzia, C. Lin, Z. Lin, *Adv. Sci.* **2016**, *3*, 1600024.

[26] G. C. Papavassiliou, *Prog. Solid State Chem.* **1979**, *12*, 185–271.

[27] S. Link, M. A. El-Sayed, *Int. Rev. Phys. Chem.* **2000**, *19*, 409–453.

[28] K. L. Kelly, E. Coronado, L. L. Zhao, G. C. Schatz, *J. Phys. Chem. B* **2003**, *107*, 668–677.

[29] S. Link, M. A. El-Sayed, *Annu. Rev. Phys. Chem.* **2003**, *54*, 331–366.

[30] T. Sannomiya, J. Vörös, *Trends Biotechnol.* **2011**, *29*, 343–351.

[31] S. I. Azzam, A. V. Kildishev, R.-M. Ma, C.-Z. Ning, R. Oulton, V. M. Shalaev, M. I. Stockman, J.-L. Xu, X. Zhang, *Light Sci. Appl.* **2020**, *9*, 1–21.

[32] B. Munkhbat, H. Pöhl, P. Denk, T. A. Klar, M. C. Scharber, C. Hrelescu, *Adv. Opt. Mater.* **2016**, *4*, 772–781.

[33] M.-K. Kwon, J.-Y. Kim, B.-H. Kim, I.-K. Park, C.-Y. Cho, C. C. Byeon, S.-J. Park, *Adv. Mater.* **2008**, *20*, 1253–1257.

[34] E. S. Arinze, B. Qiu, G. Nyirjesy, S. M. Thon, *ACS Photonics* **2016**, *3*, 158–173.

[35] A. Hörl, G. Haberfehlner, A. Trügler, F.-P. Schmidt, U. Hohenester, G. Kothleitner, *Nat. Commun.* **2017**, *8*, 37.

[36] F. Monticone, A. Alù, *Rep. Prog. Phys.* **2017**, *80*, 036401.

[37] F. Benz, C. Tserkezis, L. O. Herrmann, B. de Nijs, A. Sanders, D. O. Sigle, L. Pukenas, S. D. Evans, J. Aizpurua, J. J. Baumberg, *Nano Lett.* **2015**, *15*, 669–674.

[38] S. Lal, S. Link, N. J. Halas, in *Nanoscience and Technology*, Co-Published With Macmillan Publishers Ltd, UK, **2009**, pp. 213–220.

[39] Z. Zhang, P. Xu, X. Yang, W. Liang, M. Sun, *J. Photochem. Photobiol., C* **2016**, *27*, 100–112.

[40] W. Y. Liang, *Phys. Educ.* **1970**, *5*, 226–228.

[41] J. Frenkel, *Phys. Rev.* **1931**, *37*, 17–44.

[42] V. Agranovich, H. Benisty, C. Weisbuch, *Solid State Commun.* **1997**, *102*, 631–636.

[43] T. Cramer, A. Wanner, P. Gumbsch, *Phys. Status Solidi A* **1997**, *164*, R5–R6.

[44] M. S. Dresselhaus, G. Dresselhaus, S. Cronin, A. Gomes Souza Filho, *Solid State Properties: From Bulk to Nano*, Springer US, MIT, MA, **2018**.

[45] S. M. Menke, R. J. Holmes, *Energy Environ. Sci.* **2014**, *7*, 499–512.

[46] A. M. Askar, K. Shankar, *J. Nanosci. Nanotechnol.* **2016**, *16*, 5890–5901.

[47] J. F. Muth, J. H. Lee, I. K. Shmagin, R. M. Kolbas, H. C. Casey, B. P. Keller, U. K. Mishra, S. P. DenBaars, *Appl. Phys. Lett.* **1997**, *71*, 2572–2574.

[48] R. Kisslinger, W. Hua, K. Shankar, *Polymers* **2017**, *9*, 35.

[49] J. R. Schaibley, H. Yu, G. Clark, P. Rivera, J. S. Ross, K. L. Seyler, W. Yao, X. Xu, *Nat. Rev. Mater.* **2016**, *1*, 1–15.

[50] C. J. Bardeen, *Annu. Rev. Phys. Chem.* **2014**, *65*, 127–148.

[51] A. S. Davydov, *Sov. Phys. Usp.* **1964**, *7*, 145.

[52] J. Yuen-Zhou, S. K. Saikin, T. Zhu, M. C. Onbasli, C. A. Ross, V. Bulovic, M. A. Baldo, *Nat. Commun.* **2016**, *7*, 11783.

[53] N. T. Fofang, N. K. Grady, Z. Fan, A. O. Govorov, N. J. Halas, *Nano Lett.* **2011**, *11*, 1556–1560.

[54] P. Törmä, W. L. Barnes, *Rep. Prog. Phys.* **2014**, *78*, 013901.

[55] A. O. Govorov, G. W. Bryant, W. Zhang, T. Skeini, J. Lee, N. A. Kotov, J. M. Slocik, R. R. Naik, *Nano Lett.* **2006**, *6*, 984–994.

[56] X. Liu, T. Galfsky, Z. Sun, F. Xia, E. Lin, Y.-H. Lee, S. Kéna-Cohen, V. M. Menon, *Nature Photon.* **2015**, *9*, 30–34.

[57] F. Nan, S.-J. Ding, L. Ma, Z.-Q. Cheng, Y.-T. Zhong, Y.-F. Zhang, Y.-H. Qiu, X. Li, L. Zhou, Q.-Q. Wang, *Nanoscale* **2016**, *8*, 15071–15078.

[58] T. K. Hakala, J. J. Toppari, A. Kuzyk, M. Pettersson, H. Tikkanen, H. Kunttu, P. Törmä, *Phys. Rev. Lett.* **2009**, *103*, 053602.

[59] K. Hennessy, A. Badolato, M. Winger, D. Gerace, M. Atatüre, S. Gulde, S. Fält, E. L. Hu, A. Imamoğlu, *Nature* **2007**, *445*, 896–899.

[60] J. Galego, F. J. Garcia-Vidal, J. Feist, *Phys. Rev. X* **2015**, *5*, 041022.

[61] A. Fontcuberta i Morral, F. Stellacci, *Nat. Mater.* **2012**, *11*, 272–273.

[62] J. McKeever, A. Boca, A. D. Boozer, J. R. Buck, H. J. Kimble, *Nature* **2003**, *425*, 268–271.

[63] D. E. Chang, A. S. Sørensen, E. A. Demler, M. D. Lukin, *Nat. Phys.* **2007**, *3*, 807–812.

[64] B. Kolaric, B. Maes, K. Clays, T. Durt, Y. Caudano, *Adv. Quantum Technol.* **2018**, *1*, 1800001.

[65] E. Cao, W. Lin, M. Sun, W. Liang, Y. Song, *J. Nanophotonics.* **2018**, *7*, 145–167.

[66] S. Dufferwiel, S. Schwarz, F. Withers, A. a. P. Trichet, F. Li, M. Sich, O. Del Pozo-Zamudio, C. Clark, A. Nalitov, D. D. Solnyshkov, G. Malpuech, K. S. Novoselov, J. M. Smith, M. S. Skolnick, D. N. Krizhanovskii, A. I. Tartakovskii, *Nat. Commun.* **2015**, *6*, 8579.

[67] M. Pelton, Y. Yamamoto, *Phys. Rev. A* **1999**, *59*, 2418–2421.

[68] A. P. Manuel, A. Kirkey, N. Mahdi, K. Shankar, *J. Mater. Chem. C* **2019**, *7*, 1821–1853.

[69] M. S. Tame, K. R. McEnery, Ş. K. Özdemir, J. Lee, S. A. Maier, M. S. Kim, *Nat. Phys.* **2013**, *9*, 329–340.

[70] N. T. Fofang, T.-H. Park, O. Neumann, N. A. Mirin, P. Nordlander, N. J. Halas, *Nano Lett.* **2008**, *8*, 3481–3487.

[71] G. A. Wurtz, P. R. Evans, W. Hendren, R. Atkinson, W. Dickson, R. J. Pollard, A. V. Zayats, W. Harrison, C. Bower, *Nano Lett.* **2007**, *7*, 1297–1303.

[72] T. Ambjörnsson, G. Mukhopadhyay, S. P. Apell, M. Käll, *Phys. Rev. B* **2006**, *73*, 085412.

[73] G. P. Wiederrecht, G. A. Wurtz, J. Hranisavljevic, *Nano Lett.* **2004**, *4*, 2121–2125.

[74] M. Fleischmann, P. J. Hendra, A. J. McQuillan, *Chem. Phys. Lett.* **1974**, *26*, 163–166.

[75] T. H. Taminiau, F. D. Stefani, N. F. van Hulst, *New J. Phys.* **2008**, *10*, 105005.

[76] P. Anger, P. Bharadwaj, L. Novotny, *Phys. Rev. Lett.* **2006**, *96*, 113002.

[77] P. Albella, F. Moreno, J. M. Saiz, F. González, *Opt. Express* **2008**, *16*, 12872–12879.

[78] E. Fort, S. Grésillon, *J. Phys. D: Appl. Phys.* **2007**, *41*, 013001.

[79] A. I. Dragan, E. S. Bishop, J. R. Casas-Finet, R. J. Strouse, J. McGivney, M. A. Schenerman, C. D. Geddes, *Plasmonics* **2012**, *7*, 739–744.

[80] K. H. Drexhage, H. Kuhn, F. P. Schäfer, *Ber. Bunsenges. Phys. Chem.* **1968**, *72*, 329–329.

[81] C. Yu, J. Irudayaraj, *Anal. Chem.* **2007**, *79*, 572–579.

[82] A. J. Haes, W. P. Hall, L. Chang, W. L. Klein, R. P. Van Duyne, *Nano Lett.* **2004**, *4*, 1029–1034.

[83] A. D. McFarland, R. P. Van Duyne, *Nano Lett.* **2003**, *3*, 1057–1062.

[84] A. J. Haes, R. P. Van Duyne, *J. Am. Chem. Soc.* **2002**, *124*, 10596–10604.

[85] Y. Sun, Y. Xia, *Anal. Chem.* **2002**, *74*, 5297–5305.

[86] J. Yang, J.-C. Wu, Y.-C. Wu, J.-K. Wang, C.-C. Chen, *Chem. Phys. Lett.* **2005**, *416*, 215–219.

[87] G. Raschke, S. Brogl, A. S. Susha, A. L. Rogach, T. A. Klar, J. Feldmann, B. Fieres, N. Petkov, T. Bein, A. Nichtl, K. Kürzinger, *Nano Lett.* **2004**, *4*, 1853–1857.

[88] J. J. Mock, D. R. Smith, S. Schultz, *Nano Lett.* **2003**, *3*, 485–491.

[89] A. J. Haes, L. Chang, W. L. Klein, R. P. Van Duyne, *J. Am. Chem. Soc.* **2005**, *127*, 2264–2271.

[90] M. P. Kreuzer, R. Quidant, G. Badenes, M.-P. Marco, *Biosens. Bioelectron.* **2006**, *21*, 1345–1349.

[91] S. M. Marinakos, S. Chen, A. Chilkoti, *Anal. Chem.* **2007**, *79*, 5278–5283.

[92] R. Bukasov, J. S. Shumaker-Parry, *Nano Lett.* **2007**, *7*, 1113–1118.

[93] E. M. Larsson, J. Alegret, M. Käll, D. S. Sutherland, *Nano Lett.* **2007**, *7*, 1256–1263.

[94] N. Nath, A. Chilkoti, *Anal. Chem.* **2002**, *74*, 504–509.

[95] K.-S. Lee, M. A. El-Sayed, *J. Phys. Chem. B* **2006**, *110*, 19220–19225.

[96] H. Chen, X. Kou, Z. Yang, W. Ni, J. Wang, *Langmuir* **2008**, *24*, 5233–5237.

[97] H. Chen, L. Shao, K. C. Woo, T. Ming, H.-Q. Lin, J. Wang, *J. Phys. Chem. C* **2009**, *113*, 17691–17697.

[98] S. L. Kleinman, B. Sharma, M. G. Blaber, A.-I. Henry, N. Valley, R. G. Freeman, M. J. Natan, G. C. Schatz, R. P. Van Duyne, *J. Am. Chem. Soc.* **2013**, *135*, 301–308.

[99] K. L. Wustholz, A.-I. Henry, J. M. McMahon, R. G. Freeman, N. Valley, M. E. Piotti, M. J. Natan, G. C. Schatz, R. P. Van Duyne, *J. Am. Chem. Soc.* **2010**, *132*, 10903–10910.

[100] L. K. Ausman, G. C. Schatz, *J. Chem. Phys.* **2009**, *131*, 084708.

[101] E. C. Le Ru, P. G. Etchegoin, *MRS Bull.* **2013**, *38*, 631–640.

[102] D. M. Solís, J. M. Taboada, F. Obelleiro, L. M. Liz-Marzán, F. J. García de Abajo, *ACS Photonics* **2017**, *4*, 329–337.

[103] J. Qiu, X. Jiang, C. Zhu, M. Shirai, J. Si, N. Jiang, K. Hirao, *Angew. Chem. Int. Ed.* **2004**, *116*, 2280–2284.

[104] C. J. Orendorff, L. Gearheart, N. R. Jana, C. J. Murphy, *Phys. Chem. Chem. Phys.* **2006**, *8*, 165–170.

[105] X. Huang, I. H. El-Sayed, W. Qian, M. A. El-Sayed, *Nano Lett.* **2007**, *7*, 1591–1597.

[106] I. Pockrand, J. D. Swalen, J. G. Gordon, M. R. Philpott, *J. Chem. Phys.* **1979**, *70*, 3401–3408.

[107] A. M. Glass, P. F. Liao, J. G. Bergman, D. H. Olson, *Opt. Lett., OL* **1980**, *5*, 368–370.

[108] J. Dintinger, S. Klein, T. W. Ebbesen, *Adv. Mater.* **2006**, *18*, 1267–1270.

[109] R. A. Pala, K. T. Shimizu, N. A. Melosh, M. L. Brongersma, *Nano Lett.* **2008**, *8*, 1506–1510.

[110] W. Ni, Z. Yang, H. Chen, L. Li, J. Wang, *J. Am. Chem. Soc.* **2008**, *130*, 6692–6693.

[111] R. Thomas, A. Thomas, S. Pullanchery, L. Joseph, S. M. Somasundaran, R. S. Swathi, S. K. Gray, K. G. Thomas, *ACS Nano* **2018**, *12*, 402–415.

[112]   G. Schneider, G. Decher, N. Nerambourg, R. Praho, M. H. V. Werts, M. Blanchard-Desce, *Nano Lett.* **2006**, *6*, 530–536.

[113]   G. Zoriniants, W. L. Barnes, *New J. Phys.* **2008**, *10*, 105002.

[114]   J. Zhang, Y. Fu, M. H. Chowdhury, J. R. Lakowicz, *Nano Lett.* **2007**, *7*, 2101–2107.

[115]   S. Kühn, U. Håkanson, L. Rogobete, V. Sandoghdar, *Phys. Rev. Lett.* **2006**, *97*, 017402.

[116]   S. Saini, G. Srinivas, B. Bagchi, *J. Phys. Chem. B* **2009**, *113*, 1817–1832.

[117]   Q. Wei, G. Acuna, S. Kim, C. Vietz, D. Tseng, J. Chae, D. Shir, W. Luo, P. Tinnefeld, A. Ozcan, *Sci. Rep.* **2017**, *7*, 2124.

[118]   Y. Ding, J. Ling, Y. Qiao, Z. Li, Z. Sun, J. Cai, Y. Guo, H. Wang, *Sci. Rep.* **2016**, *6*, 38602.

[119]   Z. Mei, L. Tang, *Anal. Chem.* **2017**, *89*, 633–639.

[120]   M. Wang, M. Wang, G. Zheng, Z. Dai, Y. Ma, *Nanoscale Adv.* **2021**, *3*, 2448–2465.

[121]   Y. Jeong, Y.-M. Kook, K. Lee, W.-G. Koh, *Biosens. Bioelectron.* **2018**, *111*, 102–116.

[122]   T. Ming, L. Zhao, Z. Yang, H. Chen, L. Sun, J. Wang, C. Yan, *Nano Lett.* **2009**, *9*, 3896–3903.

[123]   H. Yuan, S. Khatua, P. Zijlstra, M. Yorulmaz, M. Orrit, *Angew. Chem. Int. Ed.* **2013**, *125*, 1255–1259.

[124]   X. Zhou, N. M. Andoy, G. Liu, E. Choudhary, K.-S. Han, H. Shen, P. Chen, *Nat. Nanotechnol* **2012**, *7*, 237–241.

[125]   G. P. Acuna, F. M. Möller, P. Holzmeister, S. Beater, B. Lalkens, P. Tinnefeld, *Science* **2012**, *338*, 506–510.

[126]   T. Liebermann, W. Knoll, P. Sluka, R. Herrmann, *Colloids Surf. A Physicochem. Eng. Asp.* **2000**, *169*, 337–350.

[127]   K. Aslan, I. Gryczynski, J. Malicka, E. Matveeva, J. R. Lakowicz, C. D. Geddes, *Curr. Opin. Biotechnol.* **2005**, *16*, 55–62.

[128]   V. T. H, *Munch. Med. Wochenschr.* **1903**, *1*, 2042–2044.

[129]   T. J. Dougherty, G. B. Grindey, R. Fiel, K. R. Weishaupt, D. G. Boyle, *J. Natl. Cancer Inst.* **1975**, *55*, 115–121.

[130]   T. J. Dougherty, J. E. Kaufman, A. Goldfarb, K. R. Weishaupt, D. Boyle, A. Mittleman, *Cancer Res.* **1978**, *38*, 2628–2635.

[131]   J. Dang, H. He, D. Chen, L. Yin, *Biomater. Sci.* **2017**, *5*, 1500–1511.

[132]   M. Dichiara, O. Prezzavento, A. Marrazzo, V. Pittalà, L. Salerno, A. Rescifina, E. Amata, *Eur. J. Med. Chem.* **2017**, *142*, 459–485.

[133]   P. Chinna Ayya Swamy, G. Sivaraman, R. N. Priyanka, S. O. Raja, K. Ponnuvel, J. Shanmugpriya, A. Gulyani, *Coord. Chem. Rev.* **2020**, *411*, 213233.

[134]   J. Kou, D. Dou, L. Yang, *Oncotarget* **2017**, *8*, 81591–81603.

[135]   U. Bazylińska, J. Pietkiewicz, J. Saczko, M. Nattich-Rak, J. Rossowska, A. Garbiec, K. A. Wilk, *Eur. J. Pharm. Sci.* **2012**, *47*, 406–420.

[136]   R. R. Allison, G. H. Downie, R. Cuenca, X.-H. Hu, C. J. Childs, C. H. Sibata, *Photodiagnosis Photodyn. Ther.* **2004**, *1*, 27–42.

[137]   I. S. Mfouo-Tynga, L. D. Dias, N. M. Inada, C. Kurachi, *Photodiagnosis Photodyn. Ther.* **2021**, *34*, 102091.

[138]   L. B. Josefsen, R. W. Boyle, *Br. J. Pharmacol.* **2008**, *154*, 1–3.

[139]   S. G. Awuah, Y. You, *RSC Adv.* **2012**, *2*, 11169–11183.

[140]   A. J. Sánchez-Arroyo, E. Palao, A. R. Agarrabeitia, M. J. Ortiz, D. García-Fresnadillo, *Phys. Chem. Chem. Phys.* **2017**, *19*, 69–72.

[141]   T. Yogo, Y. Urano, Y. Ishitsuka, F. Maniwa, T. Nagano, *J. Am. Chem. Soc.* **2005**, *127*, 12162–12163.

[142]   X. Zhao, J. Liu, J. Fan, H. Chao, X. Peng, *Chem. Soc. Rev.* **2021**, *50*, 4185–4219.

[143]   X. Li, S. Kolemen, J. Yoon, E. U. Akkaya, *Adv. Funct. Mater.* **2017**, *27*, 1604053.

[144]   W. Wu, X. Shao, J. Zhao, M. Wu, *Adv. Sci.* **2017**, *4*, 1700113.

[145]   J. Li, K. Pu, *Acc. Chem. Res.* **2020**, *53*, 752–762.

[146]   Y. Zhang, C. Xu, X. Yang, K. Pu, *Adv. Mater.* **2020**, *32*, 2002661.

[147]   J. Li, K. Pu, *Chem. Soc. Rev.* **2019**, *48*, 38–71.

[148]   Y. Shen, A. J. Shuhendler, D. Ye, J.-J. Xu, H.-Y. Chen, *Chem. Soc. Rev.* **2016**, *45*, 6725–6741.

[149]   D. Liu, C. Xue, *Adv. Mater.* **2021**, 2005738.

[150]   S. Swaminathan, V. G. Rao, J. K. Bera, M. Chandra, *Angew. Chem., Int. Ed.* **2021**, *60*, 12532–12538.

[151]   L. Zhou, M. Lou, J. L. Bao, C. Zhang, J. G. Liu, J. M. P. Martirez, S. Tian, L. Yuan, D. F. Swearer, H. Robatjazi, E. A. Carter, P. Nordlander, N. J. Halas, *Proc. Natl. Acad. Sci. U.S.A.* **2021**, *118*, e2022109118.

[152]   T. Vo-Dinh, A. M. Fales, G. D. Griffin, C. G. Khoury, Y. Liu, H. Ngo, S. J. Norton, J. K. Register, H.-N. Wang, H. Yuan, *Nanoscale* **2013**, *5*, 10127–10140.

[153]   H. Choi, S.-J. Ko, Y. Choi, P. Joo, T. Kim, B. R. Lee, J.-W. Jung, H. J. Choi, M. Cha, J.-R. Jeong, I.-W. Hwang, M. H. Song, B.-S. Kim, J. Y. Kim, *Nature Photon.* **2013**, *7*, 732–738.

[154]   Y. Zhang, K. Aslan, M. J. R. Previte, C. D. Geddes, *Proc. Natl. Acad. Sci. U.S.A.* **2008**, *105*, 1798–1802.

[155]   Y. Zhang, K. Aslan, M. J. R. Previte, C. D. Geddes, *J. Fluoresc.* **2007**, *17*, 345–349.

[156]   X. Huang, X.-J. Tian, W. Yang, B. Ehrenberg, J.-Y. Chen, *Phys. Chem. Chem. Phys.* **2013**, *15*, 15727–15733.

[157]   H. Zhang, H. Li, H. Fan, J. Yan, D. Meng, S. Hou, Y. Ji, X. Wu, *Nano Res.* **2018**, *11*, 1456–1469.

[158]   B. Hu, X. Cao, K. Nahan, J. Caruso, H. Tang, P. Zhang, *J. Mater. Chem. B* **2014**, *2*, 7073–7081.

[159]   N. Macia, R. Bresoli-Obach, S. Nonell, B. Heyne, *J. Am. Chem. Soc.* **2019**, *141*, 684–692.

[160]   P. P. P. Kumar, P. Yadav, A. Shanavas, S. Thurakkal, J. Joseph, P. P. Neelakandan, *Chem. Commun.* **2019**, *55*, 5623–5626.

Chapter 2

Synthesis and Characterization
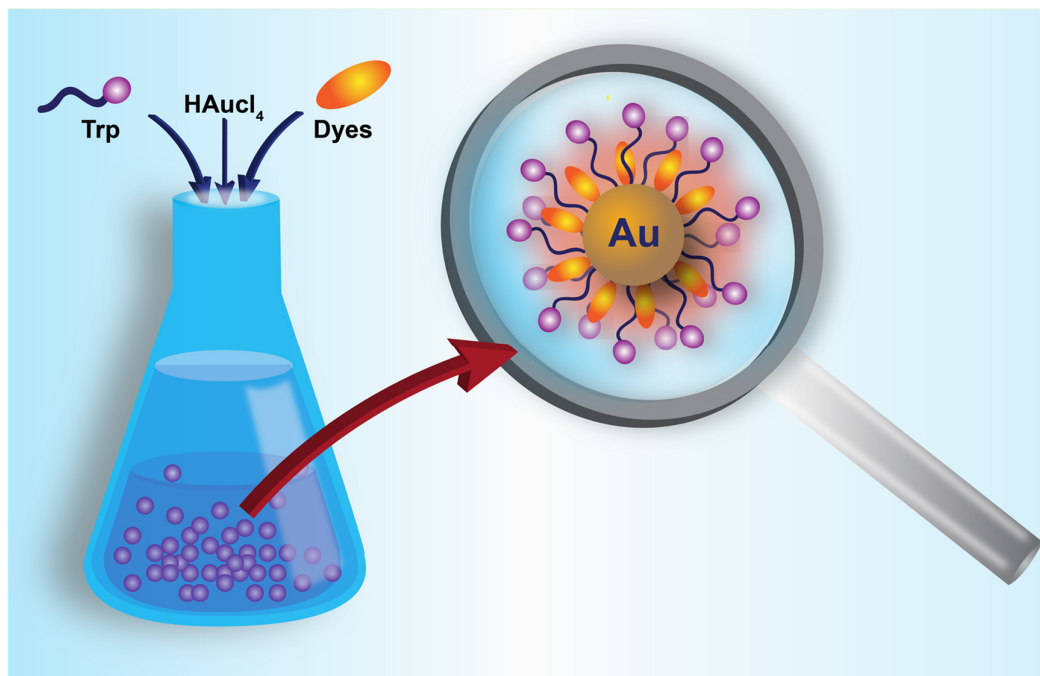
2.1.   Introduction.

Metal nanoparticles (MNPs) combined with molecular adsorbates (dyes) provide a platform to construct heterostructures or 'hybrid' materials whose photophysical properties may be tuned at the nanoscale.[1–6] Molecules that absorb light near the surface plasmon resonance (SPR) absorption peak of MNPs can induce changes in the photophysical and electronic properties of the hybrid system as compared to their individual constituents due to plasmon-molecule interactions.[7–18] Plasmon-molecule interaction is typically governed by the spectral overlap between the molecular and plasmonic resonances, the concentration of the dyes, and the distance between nanoparticles and the dyes.[19–23] In the recent past, plasmon-molecule coupled systems have been extensively studied because of their potential applications in the fields of materials science and biology. The development of plasmon-molecule coupled systems has sparked an enormous interest because of its fascinating properties. They have been used in various applications including optoelectronics[24–27], sensors[28–35], photocatalysis[36–44], and bioimaging[45–49].

The plasmon-molecule interactions in several MNP-dye combinations were studied in the recent past. In several reports, scientists primarily discussed the design and application of plasmon-molecule coupled systems. However, no systematic studies have been conducted to investigate the effect of the chemical structure and functional groups of dye molecules on plasmon-molecule interactions. We chose gold nanoparticles as MNPs for our studies due to their low toxicity, light absorption at specific wavelengths, and size and shape-dependent absorption profiles.[50,51] Further, we chose boron-containing organic dyes for our study due to their impressive luminescence properties in the visible range.[52,53] To investigate the effect of chemical composition on the stability and photophysical properties of dye-loaded gold nanoparticles, we used a series of 4,4'-difluoro-4-bora-3a,4a-diaza-s-indacene (BODIPY) molecules **B1-B5** with varying structural bulkiness.

BODIPY was discovered in 1968 by Treibs and Kreuzer while attempting to synthesize acylated pyrrole from dimethyl pyrrole and acetic anhydride using $BF_3.OEt_2$ as a Lewis acid.[54] BODIPYs consist of two pyrrole heterocycles linked by a methene bridge and a boron atom. BODIPYs exhibit excellent photostability, sharp absorption, and emission profiles with high fluorescent quantum yield.[53] Moreover, the optical properties of BODIPYs can be tuned through simple derivatizations of the BODIPY core at the α-, β-, meso-, and B(III) positions by incorporating different substituents with varying electron densities (Figure 2.1). Furthermore, BODIPY could be functionalized with heavy atoms and transition metal complexes to increase the population of excited triplet states.[55–57] Because of their remarkable photophysical and electrochemical properties, BODIPYs have been used for a variety of applications in various fields such as bioimaging, lasers, organic light-emitting diodes (OLEDs), dye-sensitized solar cells (DSSCs), nonlinear optics (NLOs), sensing, photodynamic therapy, and so on.[58–64] However, biological applications of BODIPYs are limited due to time-consuming synthesis with low overall yields and poor water solubility and fluorescence quenching in aqueous medium. Several strategies have been used to improve the utility of BODIPYs in aqueous medium. Supramolecular self-assembled nanostructures with various supporting matrices such as surfactants and polymers were the most commonly used technique.[65,66] We used gold nanoparticles as a matrix in this study, which not only aids in self-assembly but also modulates the photophysical properties of the system.[67–69] Furthermore, the naphthalidenimine-boron complex (**B6**) containing a stimuli-responsive group was used where the absorption overlap was minimal, but a significant overlap was observed between the fluorescence of **B6** and the absorption of gold

nanoparticles to study the effect of the immediate environment and absorption overlap on the photophysical properties of nanocomposites.
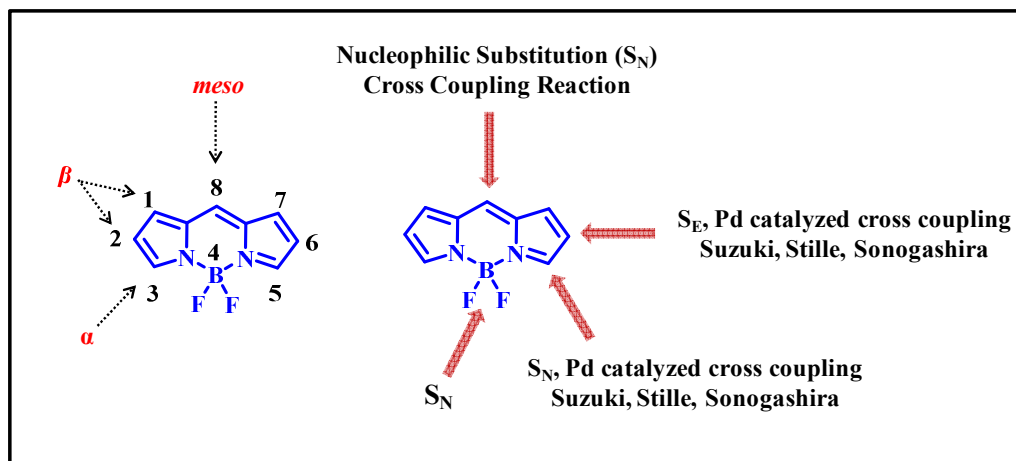

Figure 2.1. Nomenclature of BODIPYs and the commonly employed reactions for its functionalization.
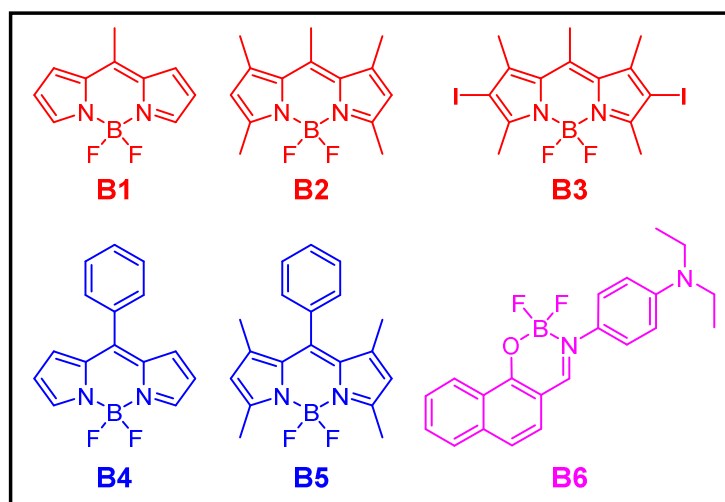

Chart 2.1. Chemical structures of dyes **B1-B6** used in this study.

2.2.   Results.

2.2.1.   Syntheses of Dye Molecules.

BODIPY molecules **B1-B5** and the naphthalidenimine-boron complex **B6** used in this study were synthesized as per literature procedures (Chart 2.1).[70–75] BODIPYs **B1**, **B2**, **B4**, and **B5** were synthesized by reaction of pyrrole or 2,4-dimethyl pyrrole with acetyl chloride or benzoyl chloride, followed by the reaction with $BF_3.OEt_2$ as shown in Scheme 2.1. The percent yields for **B1**, **B2**, **B4,** and **B5** were found to be 30%, 24%, 15%, and 18%, respectively. BODIPY molecule **B2** was subsequently reacted with N-iodosuccinimide to

give BODIPY **B3**, as shown in Scheme 2.2 with a yield of 82%. The naphthalidenimine-boron complex **B6** was synthesized by the condensation reaction of N,N-diethyl-*p*-phenylenediamine with 2-hydroxy-1-naphthaldehyde in methanol followed by boron complexation with BF$_3$.OEt$_2$ as shown in Scheme 2.3. The percent yield for **B6** was found to be 78%.
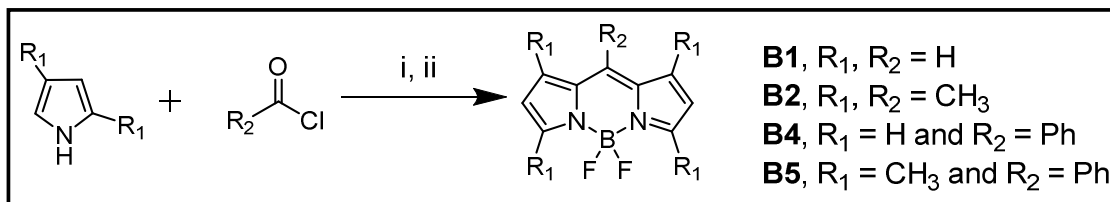
Scheme 2.1. Synthesis of BODIPYs **B1**, **B2**, **B4**, and **B5**. Reaction conditions (i) dry CH$_2$Cl$_2$, rt, 10-12 hrs, (ii) Et$_3$N, BF$_3$.OEt$_2$, 0 °C, 4-6 hrs.
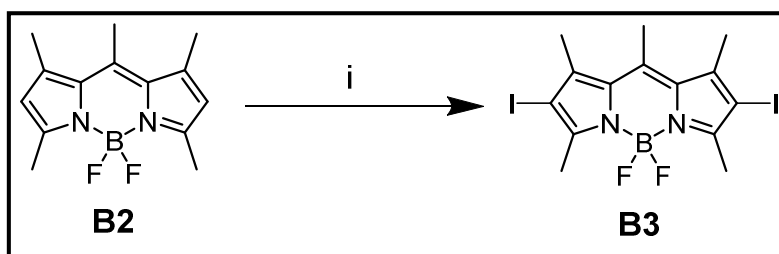
Scheme 2.2. Synthesis of BODIPY **B3**. Reaction conditions (i) N-iodosuccinimide, dry CH$_2$Cl$_2$, rt, 4 hrs.
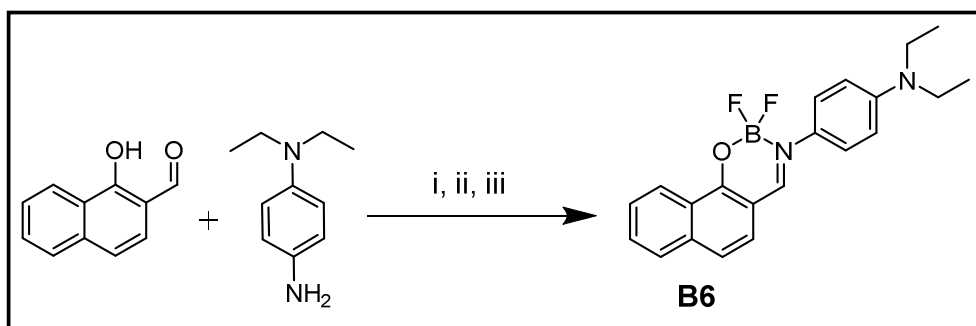
Scheme 2.3. Synthesis of molecule **B6**. Reaction conditions (i) MeOH, reflux, 4 hrs, (ii) dry CH$_2$Cl$_2$, N$_2$, 0 °C, 30 minutes, (iii) Et$_3$N, BF$_3$.OEt$_2$, rt, 4 hrs.

2.2.2. Characterization of Dye Molecules.

The dye molecules (**B1-B6**) were characterized by ^{1}H NMR and mass spectrometry. In the ^{1}H NMR spectrum of **B1**, we observed peaks corresponding to six aromatic and three aliphatic protons. Fifteen aliphatic and two aromatic proton signals were observed in ^{1}H spectrum of **B2** thereby confirming its synthesis. Furthermore, the disappearance of the two aromatic protons upon iodination confirmed the conversion of **B2** to **B3**. Next, eleven

aromatic proton signals in ^{1}H spectrum confirmed the synthesis of **B4**. Similarly, the synthesis of **B5** was determined by observing the seven aromatic and twelve aliphatic proton signals. Moreover, we observed eleven aromatic proton signal, four aliphatic proton signal having quartet at 3.43 ppm and six more aliphatic proton signal having triplet at 1.22 ppm, which confirmed the formation of **B6** (Figure 2.2).

2.2.3. Syntheses of Dye-loaded Gold Nanoparticles.

The dye-loaded gold nanoparticles were prepared by the reaction of tryptophan, HAuCl$_4$, and the dye molecules. In a typical synthesis, a concentrated solution of a dye (**B1-B6**) in acetone was mixed with a solution of HAuCl$_4$ and tryptophan in water and stirred at 25 °C for 16 hours to yield the nanocomposites (**NC1-NC6**), as shown in Scheme 2.4a. We also synthesized tryptophan capped gold nanoparticles (**Au NP**) as a control system, as shown in Scheme 2.4a. Furthermore, we prepared the organic nanoparticles (**ONP1-ONP6**) of the individual dyes using the reprecipitation method followed by stirring for 16 hours as shown in Scheme 2.4c.

Further, the multi-chromophoric nanocomposites (**NC7**) was synthesized by the mixing of **B2** and **B3** in acetone with a solution of HAuCl$_4$ and tryptophan in water and stirring at 25 °C for 16 hours. The mixed organic nanoparticles of **B2** and **B3** was also prepared using the same method as shown in Scheme 2.4b. After the synthesis, the precipitated gold nanoparticles (**Au NP**), organic nanoparticles (**ONP1-ONP7**) and nanocomposites (**NC1-NC7**) were collected by centrifugation and further purified by washing with deionized (DI) water thrice. They were further redispersed in DI water and characterized by various microscopic and spectroscopic techniques. The characterization data for all systems will be discussed in subsequent sections.
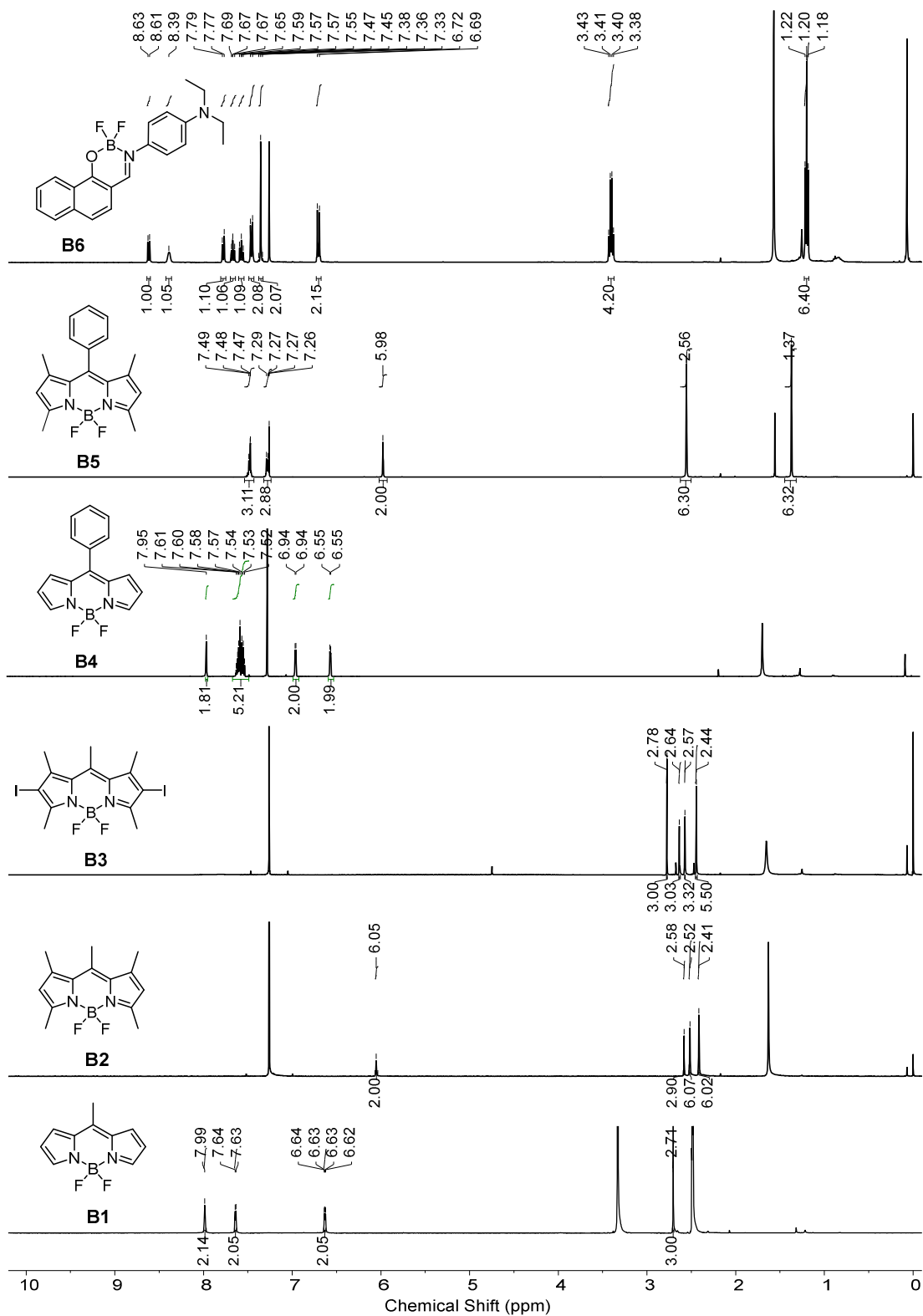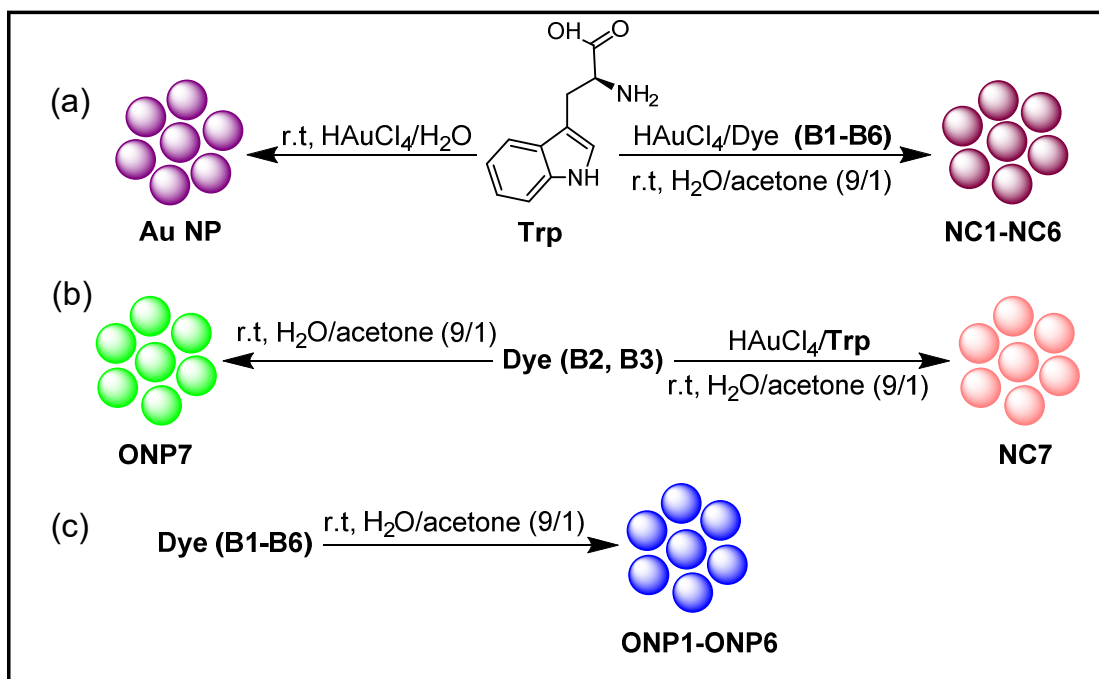
Figure 2.2. ^{1}H NMR spectrum of **B1** in DMSO-d_6 and **B2-B6** in CDCl$_3$ at 298 K.

Scheme 2.4. General scheme for the synthesis of (a) L-tryptophan capped gold nanoparticles (**Au NP**), the nanocomposites **NC1-NC6**, (b) multi-chromophoric nanocomposites **NC7**, its organic nanoparticles **ONP7** and (c) organic nanoparticles **ONP1-ONP6** of individual dyes **B1-B6**.

2.2.4. Characterization of Dye-loaded Gold Nanoparticles.

The shape and size of nanocomposites were ascertained by high-resolution transmission electron microscopy (HR-TEM), which showed spherical particles with an average diameter of 97 ± 3, 66 ± 3, 70 ± 2, 60 ± 3, 57 ± 3, 65 ± 2 and 54 ± 1 nm, respectively for **NC1-NC7** (Table 2.1 and Figure 2.3). Dynamic light scattering (DLS) measurements of the nanocomposites also corroborated with the HR-TEM measurements, wherein we observed particle sizes of 98 ± 3, 70 ± 1, 73 ± 1, 62 ± 3, 58 ± 3, 69 ± 1, and 56 ± 1 nm, respectively for **NC1-NC7** (Figure 2.4). Our control system, gold nanoparticles (**Au NP**) also exhibited spherical shapes with an average diameter of 35 ± 3 nm in HR-TEM whereas DLS revealed a size of 32 ± 3 nm for the same (Table 2.1 and Figures 2.3a and 2.4a). The organic nanoparticles **ONP1-ONP6** were characterized by DLS and exhibited particle sizes with an average diameter of 92 ± 3, 147 ± 4, 190 ± 3, 158 ± 3, 187 ± 4, and 139 ± 1 nm (Table 2.1 and Figure 2.5). Furthermore, the synthesis of multi-chromophoric organic nanoparticles (**ONP7**) containing both **B2** and **B3** was attempted under similar conditions; however, the synthesis was not reproducible, and particles with different size distributions were obtained

for different batches (Figure 2.6). The formation of nanocomposites was further confirmed by elemental maps and EDX analyses using various microscopic techniques. The presence of gold, carbon, nitrogen, oxygen, boron, fluorine, and iodine in **NC7** was confirmed by elemental mapping and EDX analysis using HR-TEM and field emission scanning electron microscopy (FESEM) (Figures 2.7 and 2.8). Further, we used FESEM to confirm the formation of **NC6**. We observed a spherical particle size of 70 ± 1 nm for **NC6** and the elemental maps and EDX analysis revealed the presence of gold, carbon, nitrogen, oxygen, boron, and fluorine in **NC6** (Figure 2.9).
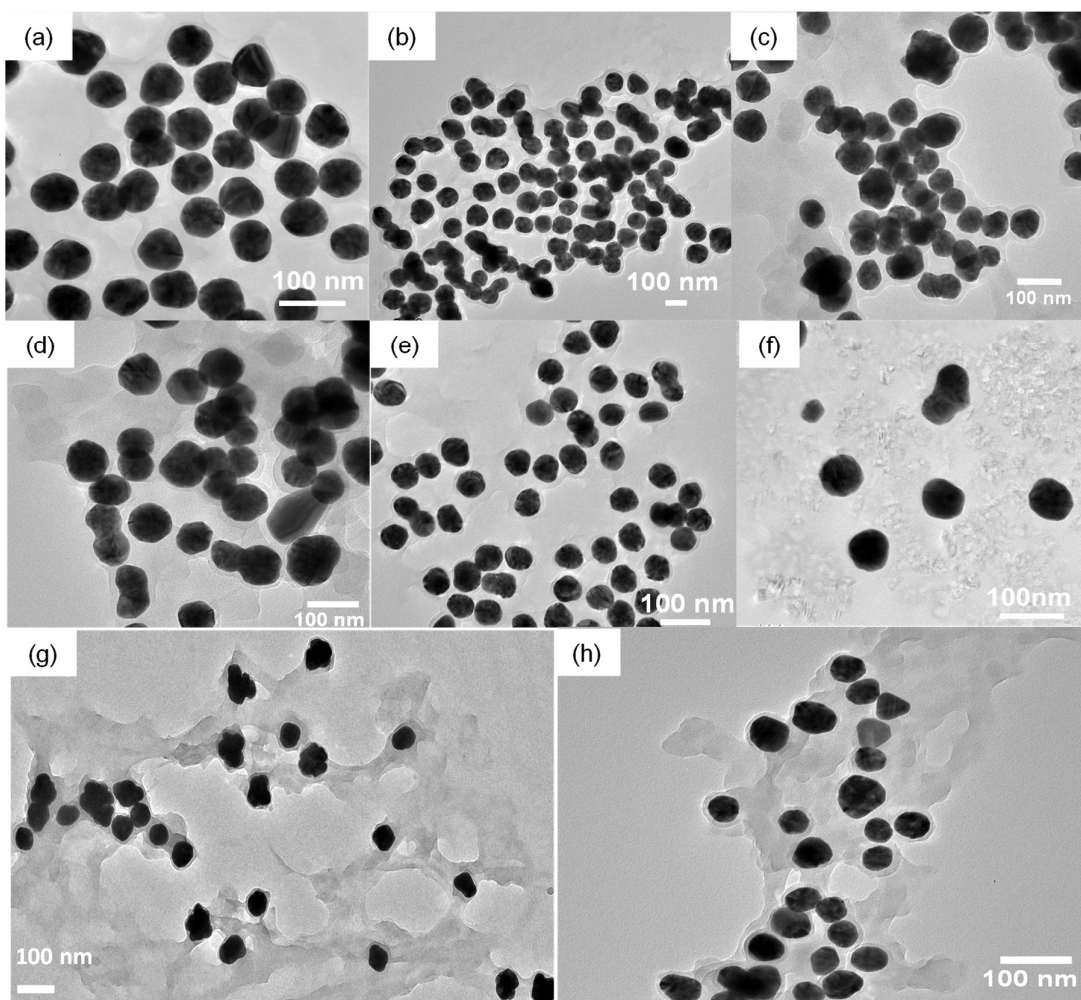

Figure 2.3. High-resolution transmission electron microscopy (HR-TEM) images of (a) **Au NP** and (b-h) **NC1-NC7** were obtained by drop-casting aqueous solutions of the nanocomposites. The observed average particle sizes were 35 ± 3 nm for **Au NP** and 97 ± 3, 66 ± 3, 70 ± 2, 60 ± 3, 57 ± 3, 65 ± 2, and 54 ± 1 nm for **NC1-NC7**, respectively.
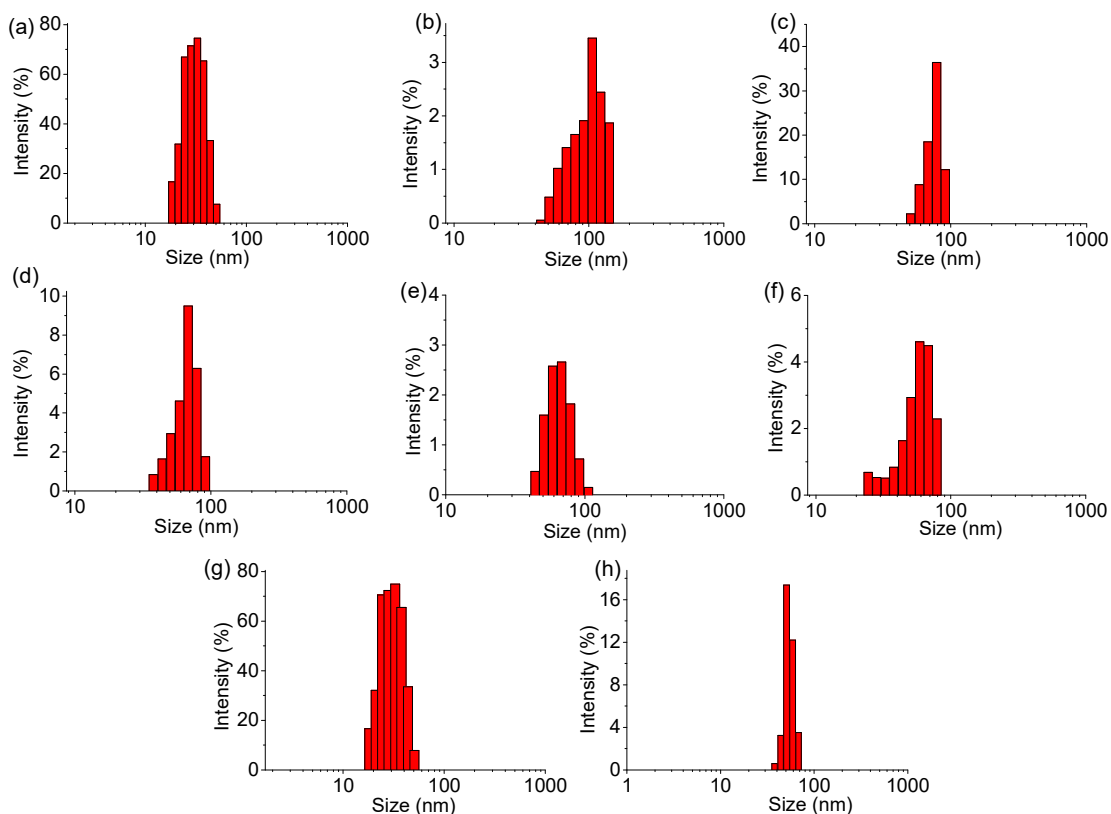
Figure 2.4. Particle size analysis of **Au NP** and **NC1-NC7** by dynamic light scattering in water. The observed average particle sizes were 32 ± 3 nm for **Au NP** and 98 ± 3, 70 ± 1, 73 ± 1, 62 ± 3, 58 ± 3, 69 ± 1, and 56 ± 1 nm for **NC1-NC7**, respectively.
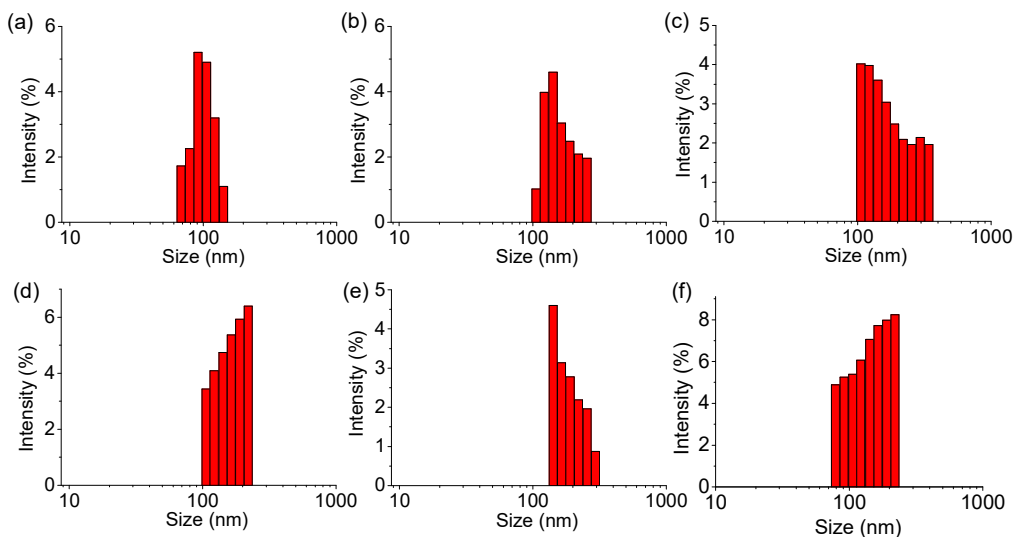

Figure 2.5. Particle size analysis of **ONP1-ONP6** by dynamic light scattering in water. The observed average particle sizes were 92 ± 3, 147 ± 4, 190 ± 3, 158 ± 3, 187 ± 4, and 139 ± 1 nm for **ONP1-ONP6**, respectively.
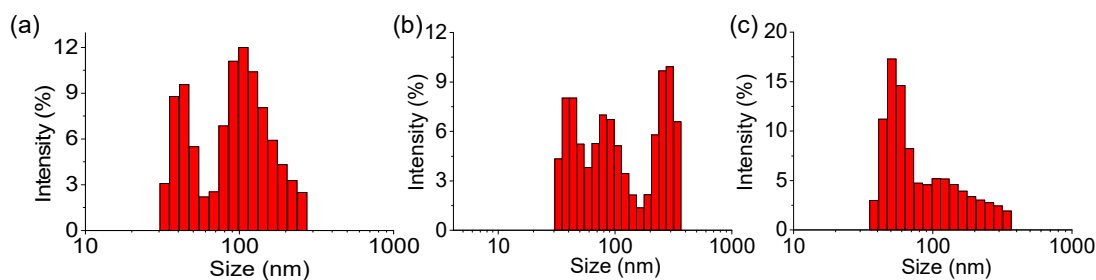
Figure 2.6. Particle size analysis by dynamic light scattering of three different batches of **ONP7** in water. The observed average particle sizes were 200 ± 1, 290 ± 1, and 324 ± 1 nm for (a-c), respectively.

Table 2.1. Particle sizes of gold nanoparticles **Au NP**, the nanocomposites **NC1-NC7** and the organic nanoparticles **ONP1-ONP6** in water.

System	Average Diameter (nm)
Au NP	35 ± 3
NC1	97 ± 3
NC2	66 ± 3
NC3	70 ± 2
NC4	60 ± 3
NC5	57 ± 3
NC6	65 ± 2
NC7	54 ± 1
ONP1	92 ± 3
ONP2	147 ± 4
ONP3	190 ± 3
ONP4	158 ± 3
ONP5	187 ± 4
ONP6	139 ± 1

Note: Particle size for **Au NP**, **NC1-NC7** was measured by using HR-TEM and DLS whereas particle size for **ONP1-ONP6** was measured by DLS.
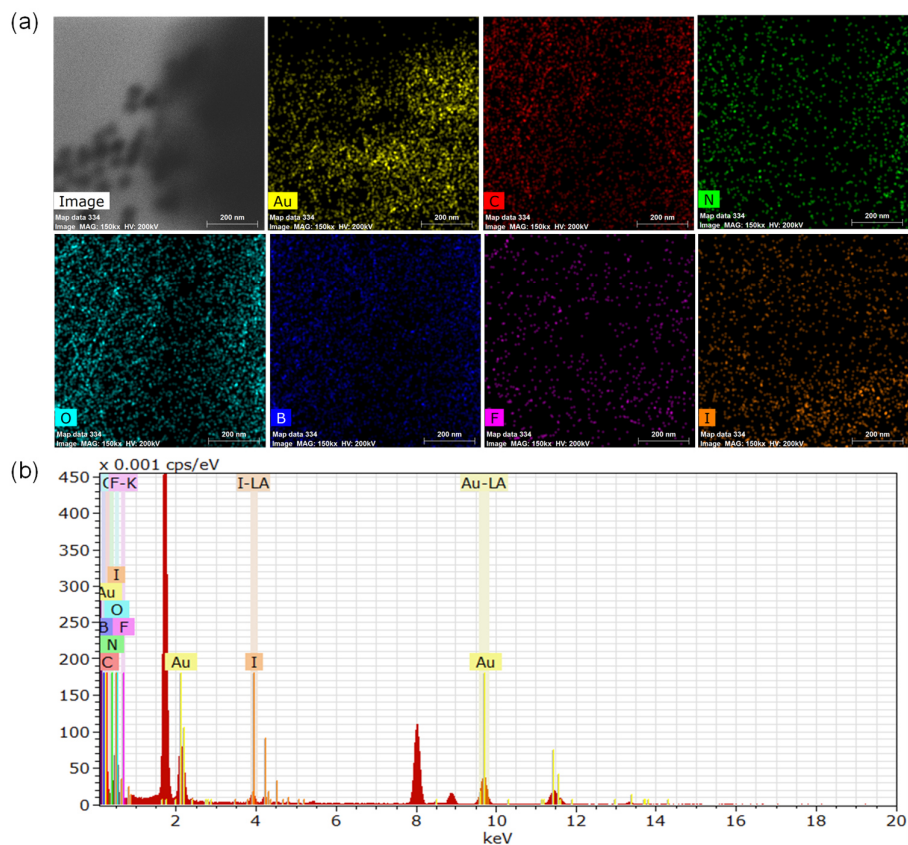
Figure 2.7. (a) HR-TEM micrographs with elemental maps and (b) EDX analysis of **NC7** in water.

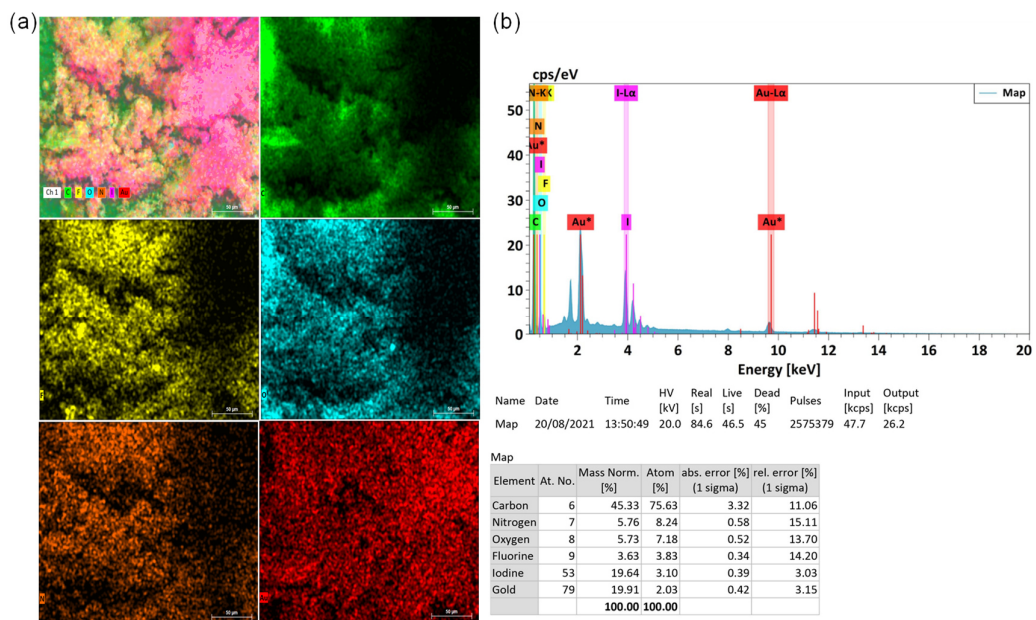| Element	At. No.	Mass Norm. [%]	Atom [%]	abs. error [%] (1 sigma)	rel. error [%] (1 sigma)
Carbon	6	45.33	75.63	3.32	11.06
Nitrogen	7	5.76	8.24	0.58	15.11
Oxygen	8	5.73	7.18	0.52	13.70
Fluorine	9	3.63	3.83	0.34	14.20
Iodine	53	19.64	3.10	0.39	3.03
Gold	79	19.91	2.03	0.42	3.15
		100.00	100.00		

Figure 2.8. Elemental maps obtained from field emission scanning electron microscopy (FESEM) and (b) EDX analysis with atom percentage of element for **NC7** in water.
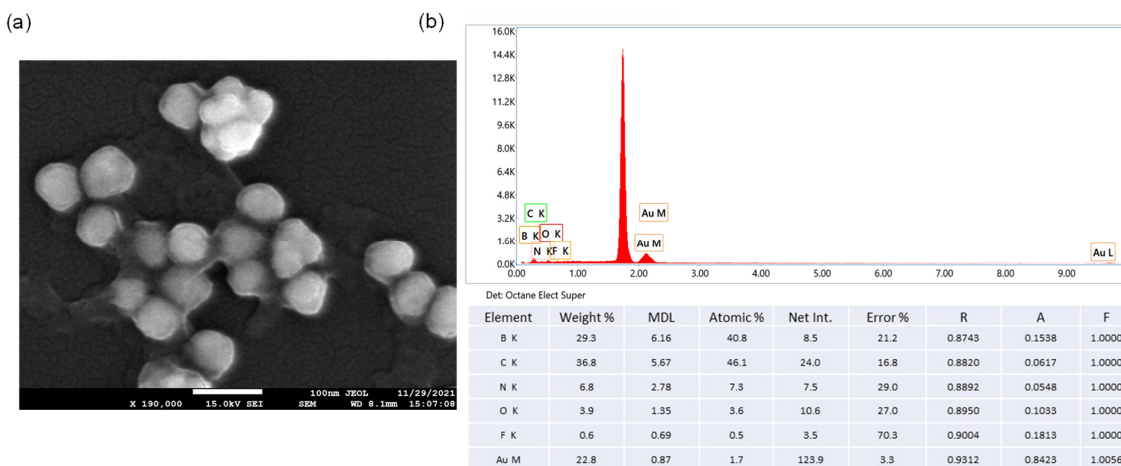
Figure 2.9. (a) Field emission scanning electron microscopy (FESEM) image of **NC6**. The observed average particle size was 70 ± 1 nm. (b) EDX analysis with atom percentage of all elements in **NC6** in water.

The formation of nanocomposites **NC1-NC7** was further substantiated by UV-Vis absorption spectroscopy. The dye molecules **B1-B6** exhibited absorption peaks at 495, 490, 520, 496, 497 and 450 nm, respectively (Figure 2.10a). The gold nanoparticles **Au NP** showed an absorption maximum of 530 nm. On the other hand, the nanocomposites **NC1-NC4** exhibited two absorption peaks at 497 and 550, 520 and 566, 450-800, 498 and 557 nm, respectively, which could be assigned to the electronic transitions in the dye molecules and SPR in gold nanoparticles (Figure 2.10b). As a result of the formation of nanocomposites, the molecular peak and surface plasmon resonance (SPR) peak of **Au NP** underwent a bathochromic shift. However, **NC6** exhibited absorption maxima at 443 and 523 nm having a blue shift in the molecular and plasmon peak. Similarly, **NC7** showed a unique broad absorption spectrum from 410-800 nm, indicating a strong interaction between the individual components (Figure 2.10b). It is to be noted that the nanocomposite **NC5** synthesized from **B5** – the bulkiest of all the BODIPYs used herein – behaved strangely: there were inconsistencies in the size of the nanocomposites obtained from different batches, and their absorption spectra could not be reproduced (Figure 2.11). The peculiar behaviour of **NC5** indicates the role of structural features in the nanocomposite formation. It is assumed that the steric hindrance imposed by the bulky methyl and phenyl groups, **B5** does not interact efficiently with gold, resulting in unstable nanocomposites. Because of the ambiguity in the structure of **NC5**, it was not used for further studies.
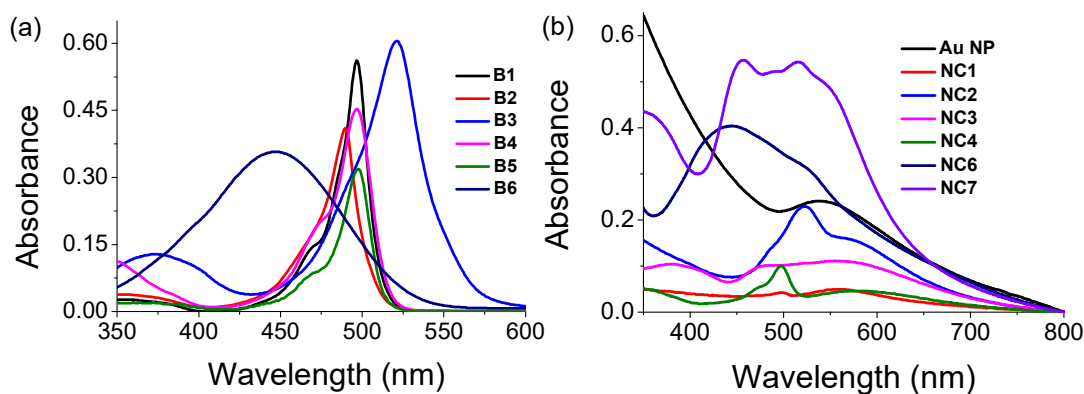
Figure 2.10. UV-Vis absorption spectra of (a) dye molecules **B1-B6** (11, 17, 12, 18, 12 and 12 µM, respectively) in acetonitrile and (b) **Au NP** and nanocomposites **NC1-NC4** and **NC6-NC7** in water. [**NC1-NC4**], 16 µg/mL; [**NC7** and **Au NP**], 12 µg/mL and [**NC6**], 16.6 µg/mL.
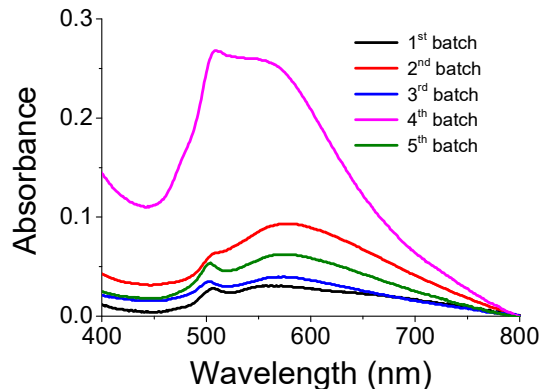

Figure 2.11. UV-Vis absorption spectra of **NC5** in water were obtained from different batches. [**NC5**], 20 µg/mL for the 1st, 2nd, 3rd and 5th batch and 50 µg/mL for the 4th batch.

2.2.5. Binding of Individual Components in the Nanocomposites.

After synthesis and characterization, we are interested in studying the binding strength between the individual components in nanocomposites using NMR spectroscopy. First, we investigated how the chemical structure of BODIPY dyes **B1-B3** affects the stability of nanocomposites **NC1-NC3**. In this direction, we recorded the ^{1}H NMR spectra of tryptophan (**Trp**), **Au NP** and the nanocomposites **NC1-NC3** in D$_2$O. It was observed that the aliphatic protons H$_c$ and H$_d$ of **Trp** showed downfield shifts of Δδ 0.30 and 0.10 ppm, respectively, after being accommodated in **Au NP** whereas the aromatic protons H$_{e-j}$ showed negligible shifts under the same conditions (Figure 2.12a, b). On the other hand, the aliphatic proton H$_c$ of tryptophan appeared upfield in **NC1** as compared to **Au NP**, whereas the aromatic protons H$_{e-j}$ appeared downfield (Figure 2.12b, c). In **NC2** and **NC3**, the chemical shift position of the

aliphatic proton H_c was intermediate to **Au NP** and **NC1**, whereas the aromatic protons H_{e-j} were significantly downfield shifted (Figure 2.12d, e). The observation of downfield shift for H_c in **Au NP** as compared to **Trp** suggests that the side chain of the tryptophan moiety is bound strongly to gold in **Au NP**, whereas the aromatic rings interacted minimally. In **NC1**, the position of H_c is similar to that in **Trp**, indicating that the tryptophan moieties are displaced by **B1**, thereby implying strong interaction of **B1** with gold. The intermediate position of H_c in **NC2** and **NC3** as compared to **Au NP** and **NC1** suggests that the interaction between **B2** and **B3** with gold is weak because of their steric bulkiness imparted by the methyl groups on the BODIPY core. On the other hand, the downfield shift of the aromatic protons of **NC2** and **NC3** indicates a strong interaction between the methyl groups of the BODIPY **B2** and **B3** with the aromatic ring of tryptophan.
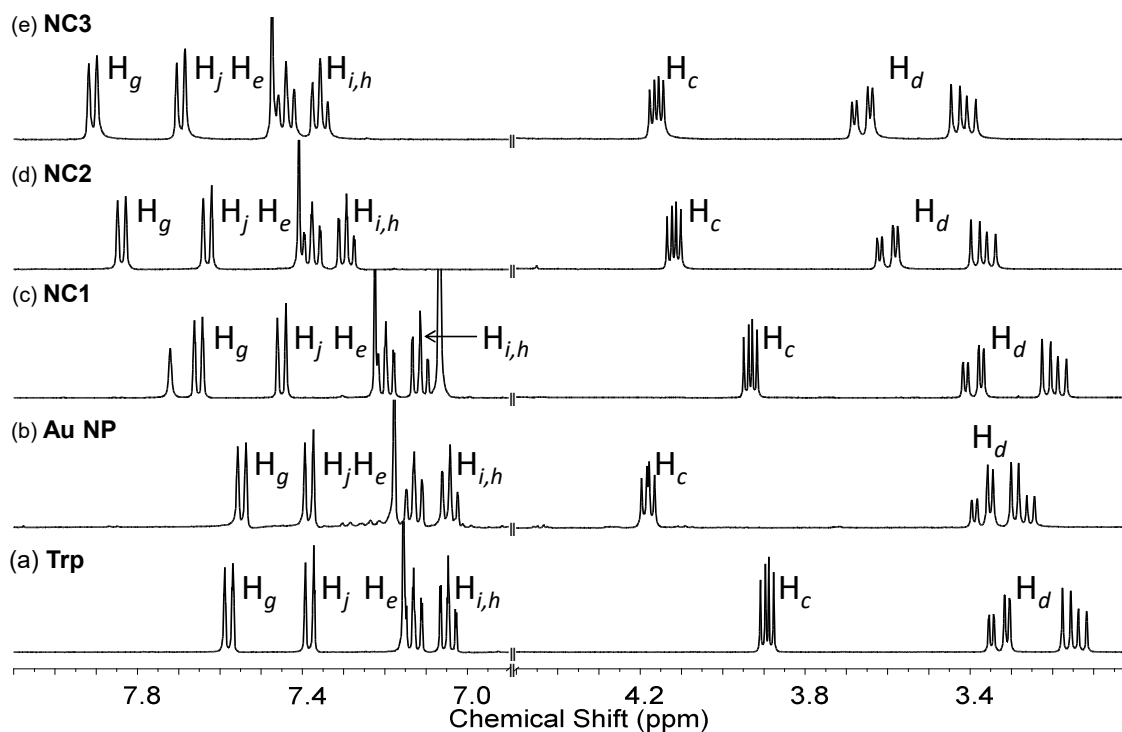

Figure 2.12. ^{1}H NMR spectra of (a) tryptophan (**Trp**), (b) **Au NP**, and (c-e) the nanocomposites **NC1-NC3** in D_2O.

Furthermore, we observed a broad peak in the ^{19}F NMR spectrum of **ONP1** in D_2O whereas three broad peaks were observed for **NC1** (Figure 2.13b, c). A comparison of ^{1}H-^{1}H COSY measurements and integral peak values for **NC1** and **ONP1** and **Au NP** indicated a strong interaction between the protons of **B1** and tryptophan (Figures 2.14, 2.15, and 2.16). The significant changes in the ^{19}F NMR spectrum of **NC1** as compared to **B1** substantiate the

strong interaction of **B1** with gold. Further, it is proposed that hydrogen bonds are formed between the aromatic –NH of the tryptophan and a fluorine atom of the –BF$_2$ unit of **B1**. Further, the comparison of ^{1}H-^{1}H COSY measurements and integral peak values for **NC1**, **ONP1**, and **Au NP** were also supportive of the strong interaction between the protons of **B1** and tryptophan. The incorporation of both tryptophan and BODIPY **B1** moieties and their strong association in **NC1** was also demonstrated by the ^{1}H-^{1}H DOSY spectrum (Figure 2.17).
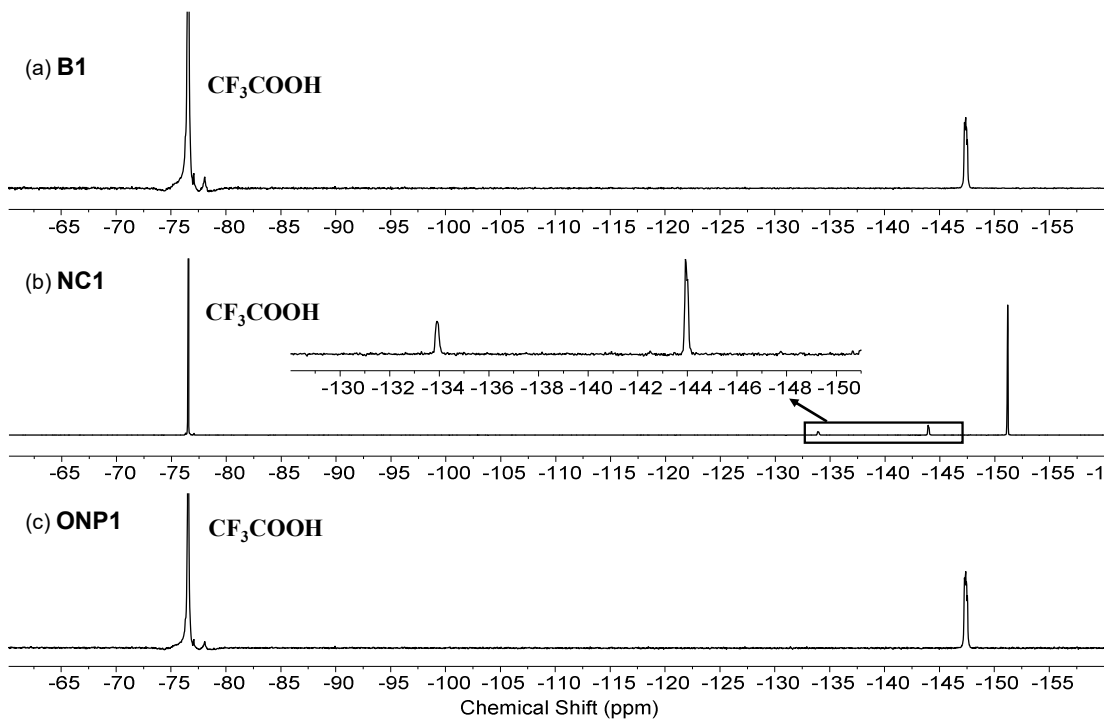

Figure 2.13[76]. ^{19}F NMR spectra of (a) **B1** in CDCl$_3$, (b) the nanocomposite **NC1**, and (c) the organic nanoparticles **ONP1** in D$_2$O.
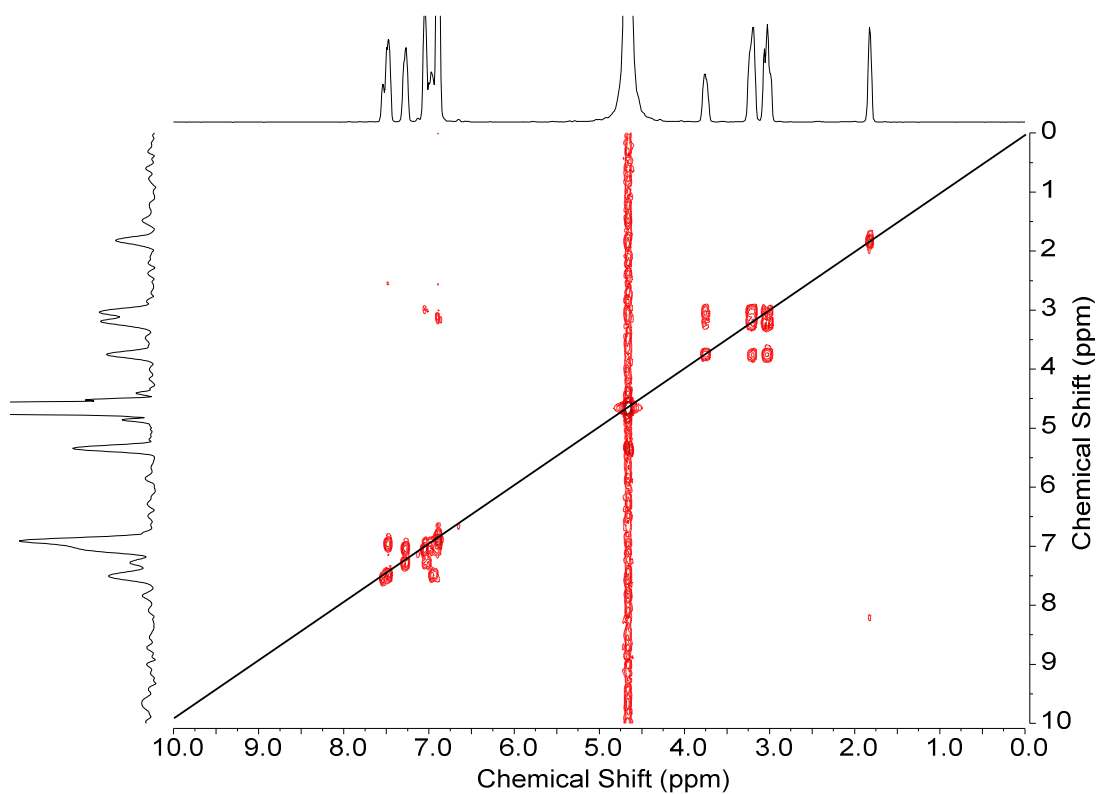
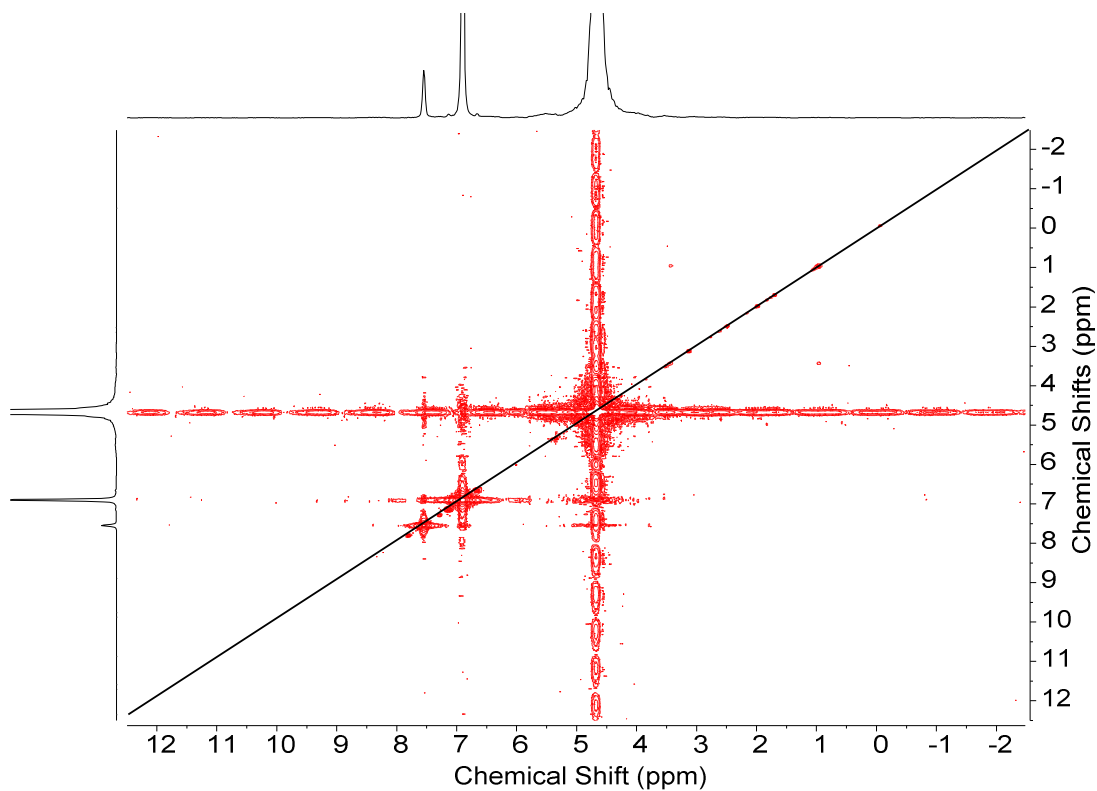**Figure 2.14**[76]**.** ^{1}H-^{1}H COSY spectrum of the nanocomposite **NC1** in D$_2$O.

Figure 2.15[76]**.** ^{1}H-^{1}H COSY spectrum of the organic nanoparticle **ONP1** in D$_2$O.
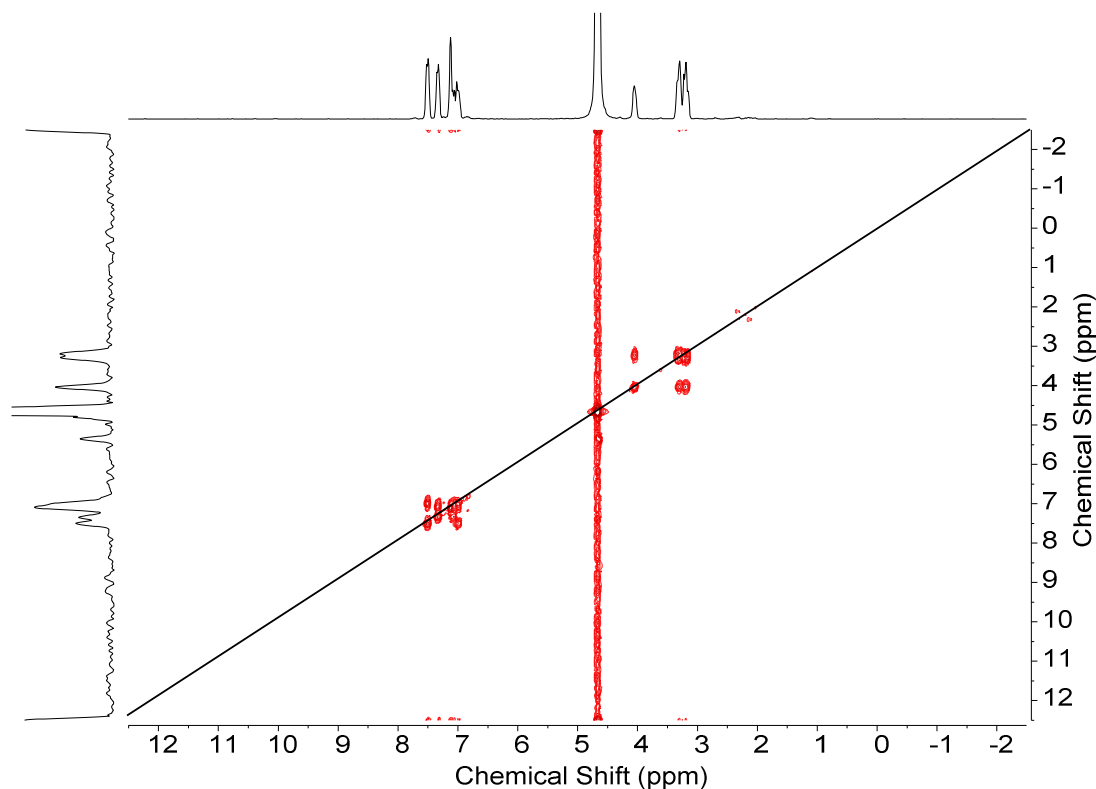
Figure 2.16[76]**.** ^{1}H-^{1}H COSY spectrum of gold nanoparticles **Au NP** in D$_2$O.
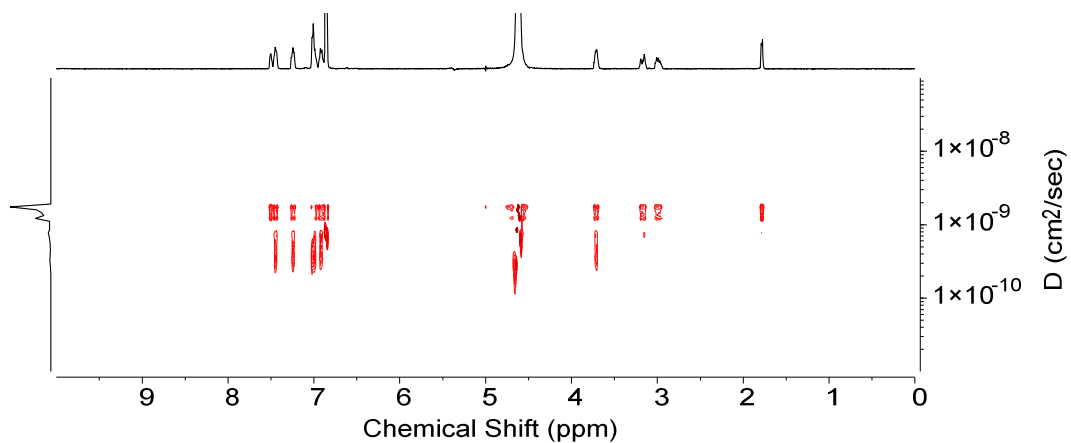
Figure 2.17[76]**.** ^{1}H-^{1}H DOSY spectrum of the nanocomposite **NC1** in D$_2$O.

Based on the NMR data, we propose a model for the nanocomposites as shown in Figure 2.18. It is inferred that the composition of the nanocomposites is complex, and the synergism of multiple non-covalent interactions stabilizes the nanocomposites. The observed downfield shifts in the aromatic region could thus be the result of a combination of hydrogen bonding, π-π stacking, and CH-π interactions between the BODIPY core and the indole ring of tryptophan. The varying steric bulkiness and the hydrophobicity of the BODIPY molecules

thus define the binding strength of the BOIDPYs to gold through supramolecular interactions, eventually resulting in nanocomposites with differing stabilities.

Figure 2.18. Schematic representation showing the (a) chemical composition and (b) the various non-covalent interactions in the nanocomposite **NC1**.

Similarly, we also studied the binding interaction between the various constituents in the nanocomposite **NC6** using NMR s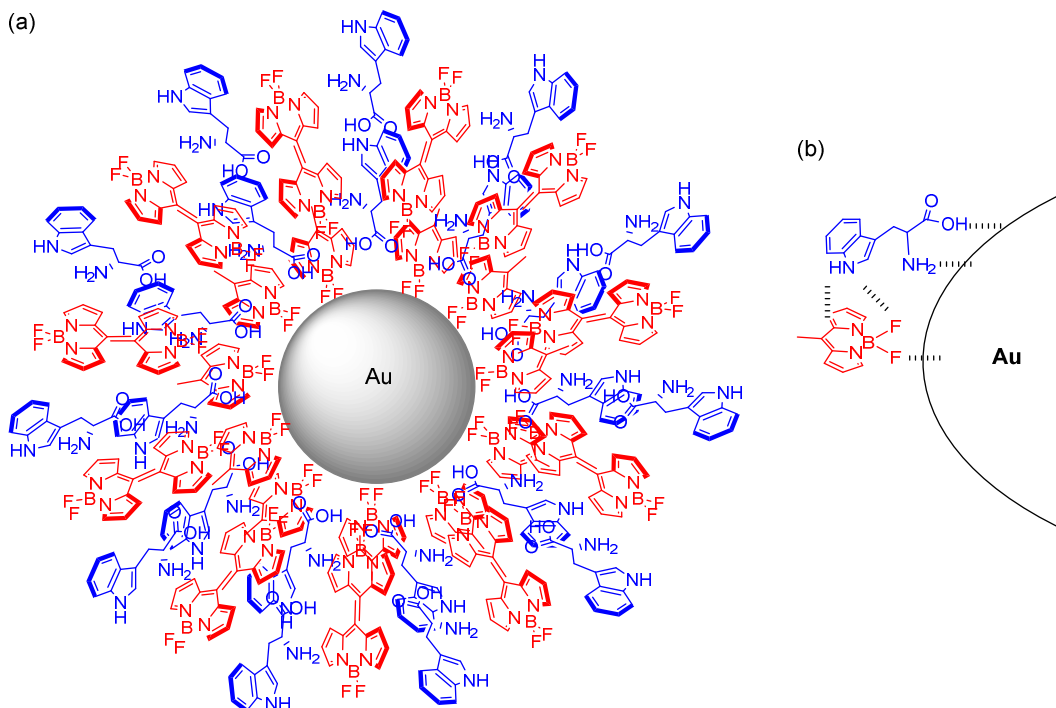pectroscopy. The H_c proton of the tryptophan moiety exhibited an upfield shift in **NC6** as compared to **Au NP**, whereas the aromatic protons H_e-H_j showed a downfield shift. The position of the H_c proton (δ, 4.06 ppm) was intermediate in **NC6** as compared to **Trp** (δ, 3.90 ppm) and **Au NP** (δ, 4.20 ppm) which suggested that the interaction of **B6** with gold is moderate (Figure 2.19). This observation also indicates that a few of the tryptophan moieties on the surface of gold nanoparticles are replaced by **B6** upon nanocomposite formation. Further, the incorporation of **B6** and **Trp** in **NC6** was also evidenced by ^{19}F NMR spectroscopy. The $–BF_2$ moiety exhibited a broad quartet in the ^{19}F NMR spectrum of **ONP6** from δ −135.01 to −135.13 ppm in D_2O, which was observed to shift downfield significantly to δ −77.37 ppm in **NC6** in D_2O (Figure 2.20). This downfield shift in NMR spectra suggested that various supramolecular interactions were responsible for holding **B6** on the surface of gold nanoparticles in **NC6**.
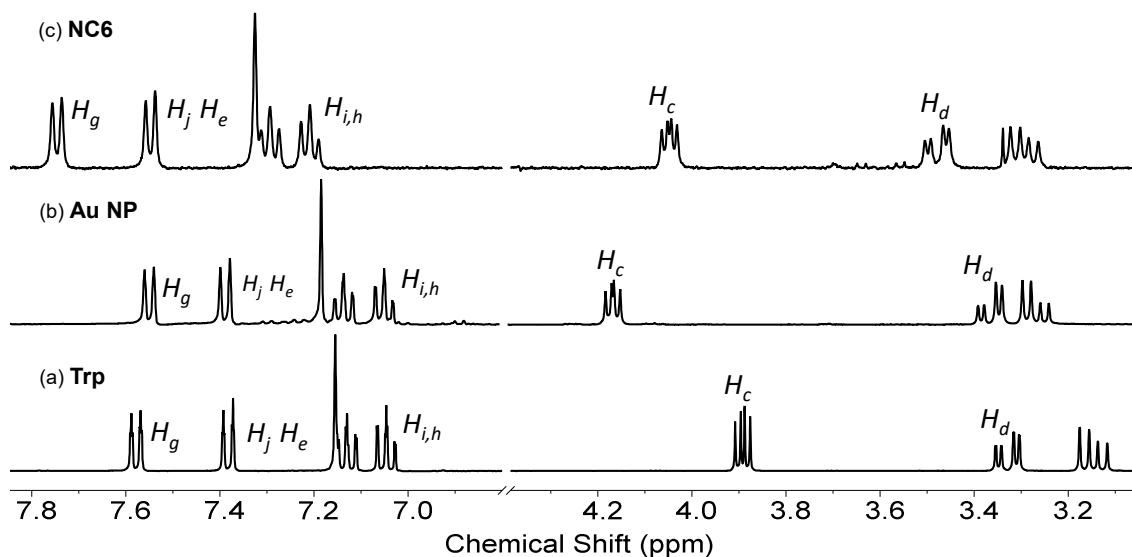
Figure 2.19. ^{1}H NMR spectra of (a) **Trp**, (b) **Au NP**, and (c) the nanocomposite **NC6** in D$_2$O.
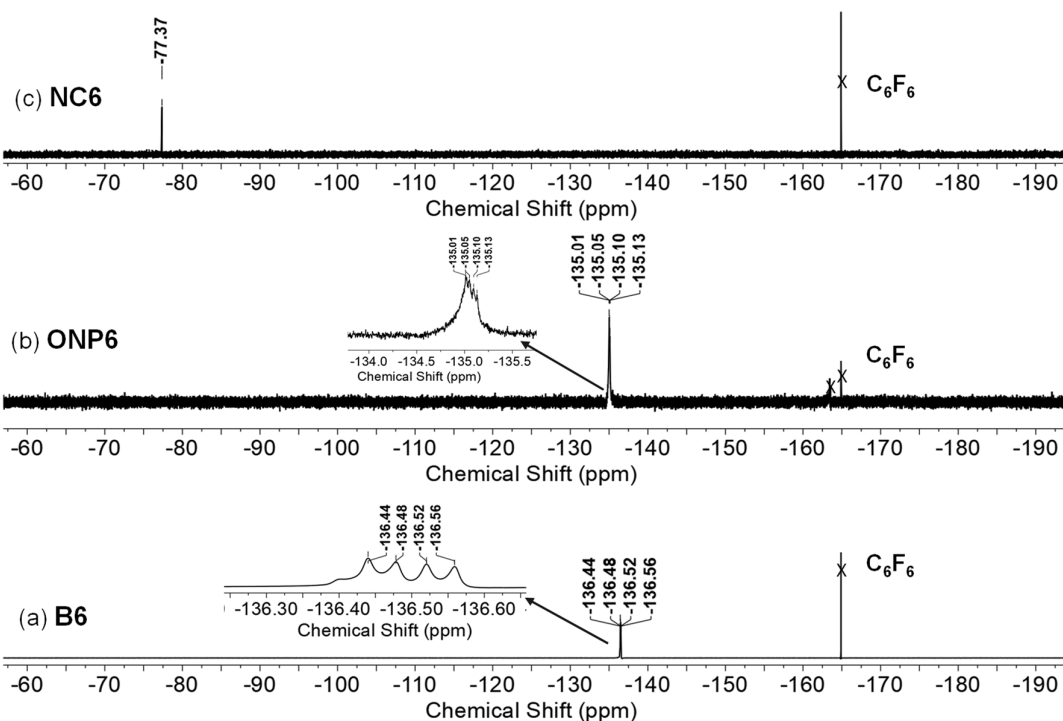
Figure 2.20. ^{19}F NMR spectra of (a) molecule **B6** in CDCl$_3$ and (b) **ONP6** and (c) the nanocomposite **NC6** in D$_2$O.

2.3. Quantification of Dye-loading in Nanocomposites.

After synthesis and characterization, we wanted to estimate the amount of dye molecules incorporated into the nanocomposites using the solvent extraction method. The dyes incorporated in the nanocomposites was extracted using dichloromethane (the extraction

protocol is described in the experimental section), and the extracted dyes were quantified using UV-Vis absorption spectroscopy (Figure 2.21). As the interaction between **B1** and gold was strong, simple solvent extraction failed to remove the incorporated dye, so, we used cysteine as a competing ligand to evict **B1** from **NC1**. However, because of the comparatively weaker interaction between other BODIPYs and gold, we could extract those dyes from the nanocomposites **NC2**, **NC3**, **NC4**, **NC6** and **NC7**. UV-Vis absorption spectral analysis of the extracted DCM part revealed the w/w loading content of dyes **B1-B4** and **B6** incorporated in nanocomposites **NC1-NC4** and **NC6** as 19, 13, 57, 8 and 10%, respectively (Table 2.2). We used ^{1}H NMR spectroscopy to estimate the loading content in **NC6** utilizing a mixture of extracted **B6** from **NC6** and a known concentrated solution of **B6** in CDCl$_3$, which also matched with the UV-vis absorption estimated values (Figures 2.22 and 2.23). Furthermore, the w/w loading content of **B2** and **B3** in multi-chromophoric nanocomposite **NC7** was found to be 9 and 20%, respectively (Table 2.2). It is clear that co-encapsulation reduced their loading content within **NC7** because we used nearly half the concentration of **B2** and **B3** during synthesis. After DCM extraction, the aqueous part of each nanocomposite showed only the surface plasmon peak of **Au NP** in UV-Vis spectroscopy. Considering the fact that a simple solvent extraction protocol could extract the dyes, covalent modification may be ruled out, and it is apparent that the dyes were incorporated into the nanocomposites through reversible supramolecular interactions.

Table 2.2. Dye-loading contents of **B1**-**B6** in various nanocomposites.

Sample	Loading Content (w/w %)
NC1	19%
NC2	13%
NC3	57%
NC4	8%
NC6	10%
NC7	**B2** (9%) and **B3** (20%)
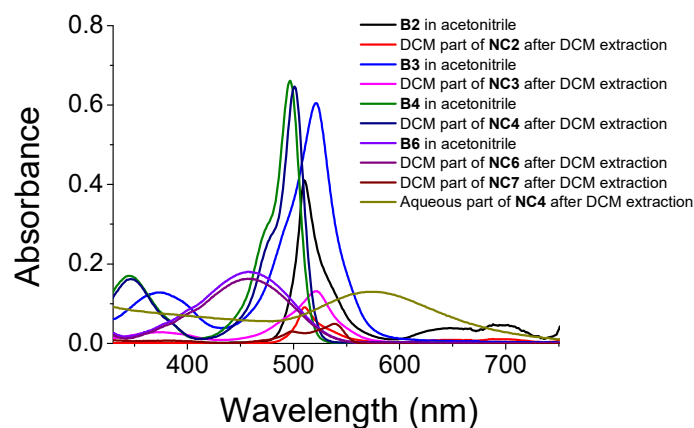
Figure 2.21. Comparison of the UV-Vis absorption spectra of **B2**, **B3**, **B4** and **B6** in acetonitrile with the dichloromethane extract of **NC2**, **NC3**, **NC4**, **NC6** and **NC7**, and the aqueous part of **NC4** after DCM extraction.
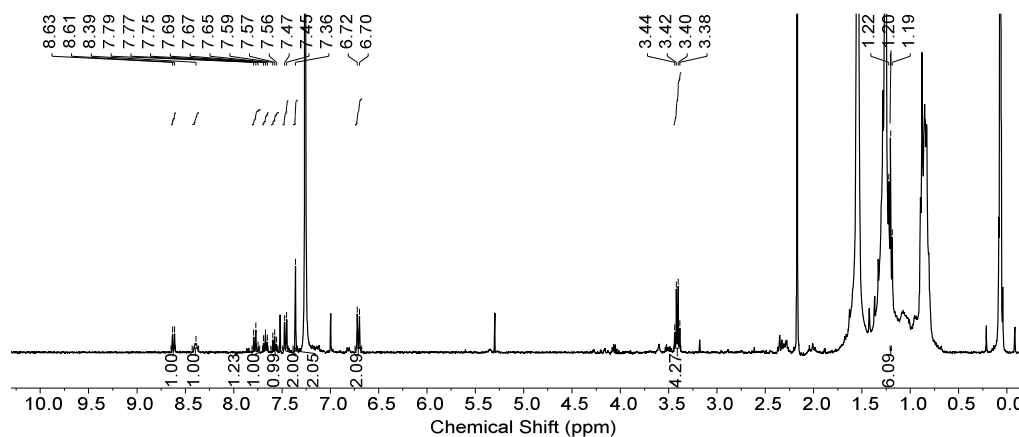

Figure 2.22. ^{1}H NMR spectrum of extracted **B6** from **NC6** in CDCl$_3$.
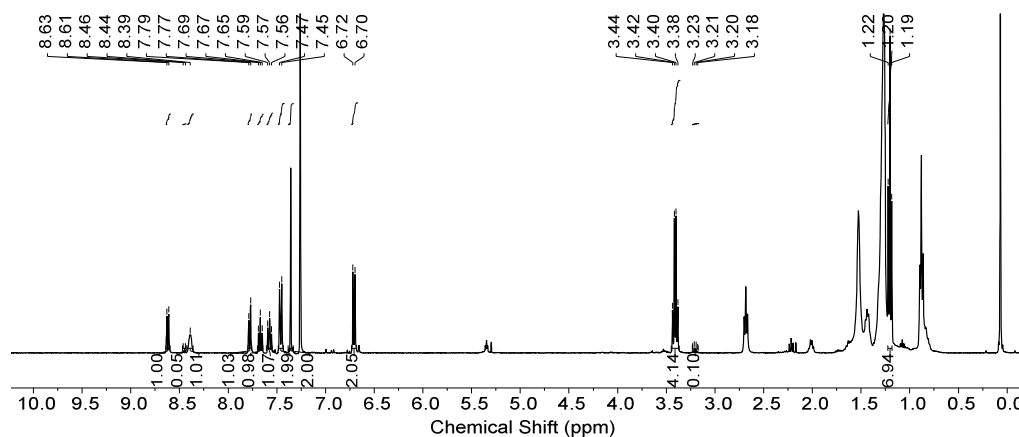

Figure 2.23. ^{1}H NMR spectrum of the mixture of **B6** (7.2 mM) and extracted **B6** from **NC6** in CDCl$_3$.

2.4.   Conclusions.

In summary, we have synthesized a series of water-soluble supramolecular nanocomposites **NC1-NC6** containing BODIPY derivatives **B1-B5** or the naphthalidenimine-boron complex **B6** and gold nanoparticles via a simple synthetic procedure. Additionally, we also synthesized a multi-chromophoric nanocomposite **NC7** by incorporating two electronically distinct BODIPY chromophores, **B2** and **B3**. The stability and strength of the nanocomposites were studied by NMR spectroscopy. It was observed that an increase in the steric bulkiness of the BODIPY molecules destabilized the nanocomposites. Further, we proposed that the downfield shift of the aromatic protons tryptophan moieties in nanocomposites was caused by a combination of hydrogen bonding, π-π stacking, and CH-π interactions between the indole ring of tryptophan and dye molecules, which determined the stability of nanocomposites. Furthermore, the interaction of SPR on gold nanoparticles and dye molecules significantly changed their SPR and molecular peak, confirming the formation of stable nanocomposites. The dye loading experiment also revealed that the dyes were incorporated into the nanocomposites through reversible supramolecular interactions.

2.5.   Experimental Section.

2.5.1. General Techniques.

All experiments were carried out at room temperature (25 ± 1 ºC) unless otherwise mentioned. NMR spectra were measured on a 400 MHz Bruker Avance II 400. Chemical shifts are reported in parts per million (δ) calibrated using tetramethyl silane as an internal standard for samples in $CDCl_3$ and DMSO-d_6 and to the residual solvent signals at δ 4.79 ppm for samples in D_2O. ^{19}F NMR spectra were referenced by inserting a sealed capillary containing 5% trifluoroacetic acid (s, δ –76.55 ppm) in D_2O into the NMR tube. Hexafluorobenzene was also used in a sealed capillary tube as the internal standard for ^{19}F NMR spectra, and the reference peak position for ^{19}F was taken as δ –164.9 ppm. Mass spectra were measured on a Shimadzu GC coupled with a GCMS-QP 2010 plus mass detector or a single-quadrupole mass spectrometer Quantum (Shimadzu) with 100% dimethyl polysiloxane (Restek Rxi-1 ms; 30 mm × 0.25 mm, 0.25 μm film thickness) column. HR-TEM images were acquired on a Jeol 2100 HR operating at 120 kV. Samples were prepared by depositing a drop of diluted nanoparticle suspension on a 300 mesh TEM grid and dried under vacuum for 2 hours. Field emission scanning electron microscope (FESEM) images were captured using Bruker Nano GmbH Gemini SEM 500 FESEM and Jeol JSM-7610FPlus FESEM. A dynamic light scattering experiment was performed using Malvern Zetasizer 2000

DLS spectrometer with a 633 nm CW laser. The particles were dispersed in Milli Q water before analysis. Absorption spectra were recorded on a Shimadzu UV-Vis spectrophotometer in 3 mL quartz cuvettes having a path length of 1 cm.

2.5.2. Materials.

Pyrrole, 2,4-dimethyl pyrrole, and boron trifluoride diethyl etherate were purchased from Alfa Aesar. 1-Hydroxynapthaldehyde and N,N-diethyl-p-phenylenediamine were purchased from TCI Chemicals. $HAuCl_4$, benzoyl chloride, N-iodosuccinimide, glycine, and 1,3-diphenylisobenzofuran (DPBF) were purchased from Sigma-Aldrich. Acetyl chloride, L-tryptophan, silica gel (60-120 mesh), sodium sulphate, acetone, dichloromethane, hexane, methanol, and triethylamine were purchased locally. Solvents were distilled before use. Distilled water was used for all experiments.

2.6. Syntheses.

2.6.1. Synthesis of BODIPY B1 and B2.[71,73]

Freshly distilled pyrrole (0.48 mL, 7 mmol) or 2,4-dimethyl pyrrole (0.72 mL, 7 mmol) was dissolved in 100 mL dry dichloromethane, and acetyl chloride (0.24 mL, 3.5 mmol) was added drop-wise under an atmosphere of nitrogen at 25 ºC. The reaction mixture was then stirred for 12 hours at 25 ºC. After cooling to 0 ºC in an ice bath, triethylamine (2.5 mL, 17.5 mmol) was added and stirred for 30 minutes. $BF_3.OEt_2$ (1.29 mL, 10.5 mmol) was then added and stirred for another 12 hours at 25 ºC. The reaction mixture was washed with water (3 × 25 mL) and brine solution (20 mL), and the organic layers were collected, dried over Na_2SO_4, filtered, and evaporated to get a dark residue. The crude product was purified by column chromatography over silica gel using a mixture of dichloromethane and hexane to afford compound **B1** or **B2**.

B1 (30% yield): ^1H NMR DMSO-d_6, 298 K, 400 MHz) δ (ppm) 2.71 (s, 3H), 6.62-6.64 (m, 2H), 7.63-7.64 (d, 2H, J = 4 Hz), 7.99 (s, 2H); GC-MS m/z calculated for $C_{10}H_{10}BF_2N_2$ $(M+H)^+$: 207.09, found: 207.10.

B2 (24% yield): ^1H NMR (CDCl$_3$, 298 K, 400 MHz) δ (ppm) 2.41 (s, 6H), 2.52 (s, 6H), 2.58 (s, 3H), 6.05 (s, 2H), GC-MS m/z calculated for $C_{14}H_{17}BF_2N_2$ $[M]^+$: 262.15, found: 262.10.

2.6.2. Synthesis of BODIPY B3.[71]

To a solution of **B2** (50 mg, 0.19 mmol) in dry CH_2Cl_2 (10 mL), N-iodosuccinimide (257 mg, 1.14 mmol) was added, and the reaction was stirred under an atmosphere of nitrogen at 25 ºC for 3 hours. The reaction mixture was then washed with water (3 × 25 mL) and brine solution (20 mL); the organic layers were collected, dried over Na_2SO_4, filtered, and evaporated to get a pink residue. The crude product was purified by column chromatography over silica gel using a mixture of dichloromethane and hexane to afford compound **B3** in an 82% yield. ^1H NMR ($CDCl_3$, 298 K, 400 MHz) δ (ppm) 2.44 (s, 6H), 2.57 (s, 3H), 2.64 (s, 3H), 2.78 (s, 3H); GC-MS m/z calculated for $C_{14}H_{15}BF_2N_2I_2$ $[M]^+$: 513.90, found: 513.83.

2.6.3. Synthesis of BODIPY B4 and B5.[72,73]

Freshly distilled pyrrole (0.5 g, 7.45 mmol) or 2,4-dimethyl pyrrole (0.5 g, 5.25 mmol) and benzoyl chloride (0.37 g, 2.63 mmol) were dissolved in 150 mL dry DCM, and the reaction mixture was stirred for 16 hours at room temperature. After cooling the reaction mixture to 0 ºC, triethylamine (3 mL) was added and stirred for 5 minutes, followed by $BF_3 \cdot OEt_2$ (2 mL). The reaction mixture was allowed to warm up to room temperature, and stirring was continued for 4 hours. The reaction mixture was then washed with water thrice (15 mL each), and the organic layer was collected and dried over sodium sulphate. The solvent was evaporated off using a rotary evaporator. The product was purified by column chromatography on silica gel (60-120 mesh) using a 1:1 mixture of hexane and DCM to afford the product.

B4 (15 % yield): ^1H NMR ($CDCl_3$, 400 MHz, 298 K) δ (ppm) 6.55 (2H, d, J = 4 Hz), 6.94 (2H, d, J = 4 Hz), 7.52-7.61 (5H, m), 7.95 (2H, s); GC-MS m/z calculated for $C_{15}H_{11}BF_2N_2$ $(M)^+$: 268.09, found: 268.16.

B5 (18% yield): ^1H NMR ($CDCl_3$, 400 MHz, 298 K) δ (ppm) 1.37 (6H, s), 2.56 (6H, s), 5.98 (2H, s), 7.26-7.29 (2H, m), 7.47-7.49 (3H, m); GC-MS m/z calculated for $C_{19}H_{19}BF_2N_2$ $(M)^+$: 324.16, found: 324.10.

2.6.4. Synthesis of naphthalidenimine-boron complex, B6.[70]

1-Hydroxy-2-naphthaldehyde (250 mg, 1.45 mmol) and N,N-diethyl-p-phenylenediamine (0.28mL, 1.45 mmol) were refluxed in methanol (30 mL) for 4 hours. The

solvent was evaporated in a rotary evaporator, and the dark orange residue was dissolved in 50 mL anhydrous dichloromethane (DCM) and cooled to 0 ºC in an ice bath. After adding triethylamine (0.5 mL, 2.978 mM), the reaction mixture was stirred for 15 minutes, followed by $BF_3.OEt_2$ (1 mL, 7.446 mM) and stirred for 4 hours at room temperature. The solvents were then evaporated in a rotary evaporator. The crude product was purified by column chromatography on silica gel using a mixture of DCM and hexane (50:50) as the eluent to yield **B6** in 78 % as a red powder. M.p.: 261-262 ºC; ^{1}H NMR (CDCl$_3$, 400 MHz, 298 K) δ (ppm) 1.22-1.18 (t, 6H), 3.43-3.38 (m, 4H), 6.72-6.69 (d, J = 12 Hz, 2H), 7.38-7.33 (m, 2H), 7.47-7.45 (d, J = 8 Hz, 2H), 7.59-7.55 (m, 1H), 7.69-7.65 (m, 1H), 7.79-7.77 (d, J = 8 Hz, 1H), 8.39 (s, 1H), 8.63-8.61 (d, J = 8 Hz, 1H); HRMS (ESI-MS) m/z calculated for $C_{21}H_{21}BF_2N_2O$ [M+H]$^+$: 367.1715; found: 367.1784.

2.6.5. Synthesis of nanocomposites NC1-NC6.

A solution of L-tryptophan (25 mM) in 8 mL Milli Q water was kept under constant stirring. An aqueous solution of $HAuCl_4$ was added (1 mL from a 5 mM stock solution), followed by a solution of individual dye molecule (**B1-B6**) in acetone (1 mL from a 5 mM stock solution). The solution, which turned brown upon mixing, was stirred for 16 hours at 25 ºC. The precipitated residue was collected after centrifugation, washed with Milli Q water (3 × 1 mL), dried, and redispersed in Milli Q water. The formation of nanocomposites was monitored through UV-Vis absorption spectroscopy and was characterized by DLS and TEM.

2.6.6. Synthesis of multi-chromophoric nanocomposite NC7.

For the synthesis of multi-chromophoric nanocomposites **NC7**, an aqueous solution of L-tryptophan (25 mM) in 7 mL and $HAuCl_4$ (2.5 mM) in 1 mL was mixed with the solution of **B2** and **B3** in acetone (1 mL each from 2.5 mM stock solutions). The solution, which turned brown-orange upon mixing, was stirred for 16 hours at 25 ºC. The precipitated nanocomposites was purified by centrifugation and characterized by various spectroscopic and microscopic techniques.

2.6.7. Synthesis of tryptophan capped gold nanoparticles (Au NP).

A stirred solution of L-tryptophan (25 mM) in 9 mL water was added to an aqueous solution of $HAuCl_4$ (1 mL from a 5 mM stock solution). The solution was observed to turn pale pink upon mixing. The reaction mixture was stirred for 10 minutes, centrifuged, and the residue was collected, washed with water (3 × 1 mL), dried, and dispersed in water. The

formation of nanocomposites was monitored through UV-Vis absorption spectroscopy and was characterized by DLS and TEM.

2.6.8. Synthesis of organic nanoparticles ONP1-ONP7.

Organic nanoparticles were synthesized by a simple reprecipitation method. To 9 mL of Milli Q water, 1 mL from a 5 mM stock solution of individual dye molecule (**B1-B6**) in acetone was added, and the resulting suspension was stirred for 12 hours. The reaction mixture was then centrifuged, the residue was collected, washed with water (3 × 1 mL), dried, and redispersed in Milli Q water. The formation of nanoparticles was monitored through UV-Vis absorption spectroscopy and DLS.

Further, the synthesis of multi-chromophoric organic nanoparticles **ONP7** containing both **B2** and **B3** was attempted under similar conditions. To 8 mL of Milli Q water, 1 mL of each molecule **B2** (2.5 mM) and **B3** (2.5 mM) in acetone was added, and the resulting suspension was stirred for 12 hours. The reaction mixture was then centrifuged, the residue was collected, washed with water (3 × 1 mL), dried, and redispersed in Milli Q water. The formation of nanoparticles was monitored through UV-Vis absorption spectroscopy and DLS.

2.7. Quantification of dye loading.

1 mL of a solution of the nanocomposites (**NC1-NC4** and **NC6-NC7**) was stirred with 1 mL of DCM in a glass vial for 3 hours. The DCM part was extracted three times and dried on anhydrous Na_2SO_4. Further, the DCM part was adjusted to 1 mL using DCM and analysed by UV-vis spectroscopy. The incorporated dye content in nanocomposites was calculated by comparing it with the absorbance of a standard stock solution of dye molecules (**B1-B6**) in DCM. The loading content of **B6** was calculated by ^{1}H NMR spectroscopy using a mixture of extracted **B6** from **NC6** and a known concentrated solution of **B6** in $CDCl_3$.[77] The signals of the known concentration of **B6** were integrated and normalized to which the unknown extracted **B6** was added, and the increase in the integral was measured. The concentration of the extracted **B6** was then calculated by using the formula equation 2.1,

$$C_X = \frac{I_X}{I_{cal}} \times \frac{N_{Cal}}{N_X} \times C_{cal} \qquad (2.1)$$

where I, N, and C are the integral area, the number of nuclei, and the concentration of the concentrated **B6** (cal) and extracted **B6** (x).

2.8. References.

[1] R. Thomas, A. Thomas, S. Pullanchery, L. Joseph, S. M. Somasundaran, R. S. Swathi, S. K. Gray, K. G. Thomas, *ACS Nano* **2018**, *12*, 402–415.

[2] N. T. Fofang, N. K. Grady, Z. Fan, A. O. Govorov, N. J. Halas, *Nano Lett.* **2011**, *11*, 1556–1560.

[3] T. K. Hakala, J. J. Toppari, A. Kuzyk, M. Pettersson, H. Tikkanen, H. Kunttu, P. Törmä, *Phys. Rev. Lett.* **2009**, *103*, 053602.

[4] N. T. Fofang, T.-H. Park, O. Neumann, N. A. Mirin, P. Nordlander, N. J. Halas, *Nano Lett.* **2008**, *8*, 3481–3487.

[5] W. Ni, Z. Yang, H. Chen, L. Li, J. Wang, *J. Am. Chem. Soc.* **2008**, *130*, 6692–6693.

[6] G. P. Wiederrecht, G. A. Wurtz, J. Hranisavljevic, *Nano Lett.* **2004**, *4*, 2121–2125.

[7] J. Langer, D. Jimenez de Aberasturi, J. Aizpurua, R. A. Alvarez-Puebla, B. Auguié, J. J. Baumberg, G. C. Bazan, S. E. J. Bell, A. Boisen, A. G. Brolo, J. Choo, D. Cialla-May, V. Deckert, L. Fabris, K. Faulds, F. J. García de Abajo, R. Goodacre, D. Graham, A. J. Haes, C. L. Haynes, C. Huck, T. Itoh, M. Käll, J. Kneipp, N. A. Kotov, H. Kuang, E. C. Le Ru, H. K. Lee, J.-F. Li, X. Y. Ling, S. A. Maier, T. Mayerhöfer, M. Moskovits, K. Murakoshi, J.-M. Nam, S. Nie, Y. Ozaki, I. Pastoriza-Santos, J. Perez-Juste, J. Popp, A. Pucci, S. Reich, B. Ren, G. C. Schatz, T. Shegai, S. Schlücker, L.-L. Tay, K. G. Thomas, Z.-Q. Tian, R. P. Van Duyne, T. Vo-Dinh, Y. Wang, K. A. Willets, C. Xu, H. Xu, Y. Xu, Y. S. Yamamoto, B. Zhao, L. M. Liz-Marzán, *ACS Nano* **2020**, *14*, 28–117.

[8] X. Wang, S.-C. Huang, S. Hu, S. Yan, B. Ren, *Nat. Rev. Phys.* **2020**, *2*, 253–271.

[9] A. B. Taylor, P. Zijlstra, *ACS Sens.* **2017**, *2*, 1103–1122.

[10] J.-F. Li, C.-Y. Li, R. F. Aroca, *Chem. Soc. Rev.* **2017**, *46*, 3962–3979.

[11] H. Chen, T. Ming, L. Zhao, F. Wang, L.-D. Sun, J. Wang, C.-H. Yan, *Nano Today* **2010**, *5*, 494–505.

[12] D.-K. Lim, K.-S. Jeon, H. M. Kim, J.-M. Nam, Y. D. Suh, *Nat. Mater.* **2010**, *9*, 60–67.

[13] A. Kinkhabwala, Z. Yu, S. Fan, Y. Avlasevich, K. Müllen, W. E. Moerner, *Nature Photon.* **2009**, *3*, 654–657.

[14] M. A. Noginov, G. Zhu, A. M. Belgrave, R. Bakker, V. M. Shalaev, E. E. Narimanov, S. Stout, E. Herz, T. Suteewong, U. Wiesner, *Nature* **2009**, *460*, 1110–1112.

[15] B. Sepúlveda, P. C. Angelomé, L. M. Lechuga, L. M. Liz-Marzán, *Nano Today* **2009**, *4*, 244–251.

[16] M.-K. Kwon, J.-Y. Kim, B.-H. Kim, I.-K. Park, C.-Y. Cho, C. C. Byeon, S.-J. Park, *Adv. Mater.* **2008**, *20*, 1253–1257.

[17] P. Anger, P. Bharadwaj, L. Novotny, *Phys. Rev. Lett.* **2006**, *96*, 113002.

[18] F. Stellacci, C. A. Bauer, T. Meyer-Friedrichsen, W. Wenseleers, S. R. Marder, J. W. Perry, *J. Am. Chem. Soc.* **2003**, *125*, 328–329.

[19] J. Jana, M. Ganguly, T. Pal, *RSC Adv.* **2016**, *6*, 86174–86211.

[20] H. Chen, L. Shao, K. C. Woo, J. Wang, H.-Q. Lin, *J. Phys. Chem. C* **2012**, *116*, 14088–14095.

[21] J. Zhao, L. Jensen, J. Sung, S. Zou, G. C. Schatz, R. P. Van Duyne, *J. Am. Chem. Soc.* **2007**, *129*, 7647–7656.

[22] K. L. Kelly, E. Coronado, L. L. Zhao, G. C. Schatz, *J. Phys. Chem. B* **2003**, *107*, 668–677.

[23] S. Link, M. A. El-Sayed, *Int. Rev. Phys. Chem.* **2000**, *19*, 409–453.

[24] F. Monticone, A. Alù, *Rep. Prog. Phys.* **2017**, *80*, 036401.

[25] F. Benz, C. Tserkezis, L. O. Herrmann, B. de Nijs, A. Sanders, D. O. Sigle, L. Pukenas, S. D. Evans, J. Aizpurua, J. J. Baumberg, *Nano Lett.* **2015**, *15*, 669–674.

[26] R. D. Artuso, G. W. Bryant, *Nano Lett.* **2008**, *8*, 2106–2111.

[27] R. A. Pala, K. T. Shimizu, N. A. Melosh, M. L. Brongersma, *Nano Lett.* **2008**, *8*, 1506–1510.

[28] Y. Jeong, Y.-M. Kook, K. Lee, W.-G. Koh, *Biosens. Bioelectron.* **2018**, *111*, 102–116.

[29] A. V. Kabashin, P. Evans, S. Pastkovsky, W. Hendren, G. A. Wurtz, R. Atkinson, R. Pollard, V. A. Podolskiy, A. V. Zayats, *Nat. Mater.* **2009**, *8*, 867–871.

[30] J. N. Anker, W. P. Hall, O. Lyandres, N. C. Shah, J. Zhao, R. P. Van Duyne, *Nat. Mater.* **2008**, *7*, 442–453.

[31] A. W. Wark, H. J. Lee, R. M. Corn, *Anal. Chem.* **2005**, *77*, 3904–3907.

[32] M. P. Kreuzer, R. Quidant, G. Badenes, M.-P. Marco, *Biosens. Bioelectron.* **2006**, *21*, 1345–1349.

[33] A. J. Haes, W. P. Hall, L. Chang, W. L. Klein, R. P. Van Duyne, *Nano Lett.* **2004**, *4*, 1029–1034.

[34] A. J. Haes, R. P. Van Duyne, *J. Am. Chem. Soc.* **2002**, *124*, 10596–10604.

[35] N. Nath, A. Chilkoti, *Anal. Chem.* **2002**, *74*, 504–509.

[36] M. Ahlawat, A. Roy, V. Govind Rao, *ChemNanoMat* **2022**, *8*, e202100416.

[37] S. Swaminathan, V. G. Rao, J. K. Bera, M. Chandra, *Angew. Chem., Int. Ed.* **2021**, *60*, 12532–12538.

[38] L. Zhou, M. Lou, J. L. Bao, C. Zhang, J. G. Liu, J. M. P. Martirez, S. Tian, L. Yuan, D. F. Swearer, H. Robatjazi, E. A. Carter, P. Nordlander, N. J. Halas, *Proc. Natl. Acad. Sci. U.S.A.* **2021**, *118*, e2022109118.

[39] A. Gellé, T. Jin, L. de la Garza, G. D. Price, L. V. Besteiro, A. Moores, *Chem. Rev.* **2020**, *120*, 986–1041.

[40] J. Guo, Y. Zhang, L. Shi, Y. Zhu, M. F. Mideksa, K. Hou, W. Zhao, D. Wang, M. Zhao, X. Zhang, J. Lv, J. Zhang, X. Wang, Z. Tang, *J. Am. Chem. Soc.* **2017**, *139*, 17964–17972.

[41] L. Yang, Q. Zhan, Z. Wang, Q. Chen, J. Tong, D. Fang, L. Xia, M. Jin, *J. Mater. Chem. A* **2017**, *5*, 10150–10153.

[42] M. Wen, S. Takakura, K. Fuku, K. Mori, H. Yamashita, *Catalysis Today* **2015**, *242*, 381–385.

[43] Q. Xiao, S. Sarina, A. Bo, J. Jia, H. Liu, D. P. Arnold, Y. Huang, H. Wu, H. Zhu, *ACS Catal.* **2014**, *4*, 1725–1734.

[44] F. Wang, C. Li, H. Chen, R. Jiang, L.-D. Sun, Q. Li, J. Wang, J. C. Yu, C.-H. Yan, *J. Am. Chem. Soc.* **2013**, *135*, 5588–5601.

[45] J. C. S. Simões, S. Sarpaki, P. Papadimitroulas, B. Therrien, G. Loudos, *J. Med. Chem.* **2020**, *63*, 14119–14150.

[46] U. N. Pan, P. Sanpui, A. Paul, A. Chattopadhyay, *ACS Appl. Bio Mater.* **2019**, *2*, 3144–3152.

[47] T. Vo-Dinh, H.-N. Wang, J. Scaffidi, *J. Biophoton.* **2010**, *3*, 89–102.

[48] J. Ma, X. Wang, J. Feng, C. Huang, Z. Fan, *Small* **2021**, *17*, 2004287.

[49] H. Chen, Z. Cheng, X. Zhou, R. Wang, F. Yu, *Anal. Chem.* **2022**, *94*, 143–164.

[50] E. C. Dreaden, A. M. Alkilany, X. Huang, C. J. Murphy, M. A. El-Sayed, *Chem. Soc. Rev.* **2012**, *41*, 2740–2779.

[51] R. Bukasov, J. S. Shumaker-Parry, *Nano Lett.* **2007**, *7*, 1113–1118.

[52] R. Chan-Navarro, V. M. Jiménez-Pérez, B. M. Muñoz-Flores, H. V. R. Dias, I. Moggio, E. Arias, G. Ramos-Ortíz, R. Santillan, C. García, M. E. Ochoa, M. Yousufuddin, N. Waksman, *Dyes Pigm.* **2013**, *99*, 1036–1043.

[53] A. Loudet, K. Burgess, *Chem. Rev.* **2007**, *107*, 4891–4932.

[54] A. Treibs, F.-H. Kreuzer, *Liebigs Ann.* **1968**, *718*, 208–223.

[55] R. Prieto-Montero, A. Prieto-Castañeda, R. Sola-Llano, A. R. Agarrabeitia, D. García-Fresnadillo, I. López-Arbeloa, A. Villanueva, M. J. Ortiz, S. de la Moya, V. Martínez-Martínez, *Photochem. Photobiol* **2020**, *96*, 458–477.

[56] A. Turksoy, D. Yildiz, E. U. Akkaya, *Coord. Chem. Rev.* **2019**, *379*, 47–64.

[57] J. Zhao, K. Xu, W. Yang, Z. Wang, F. Zhong, *Chem. Soc. Rev.* **2015**, *44*, 8904–8939.

[58] M. Poddar, R. Misra, *Coord. Chem. Rev.* **2020**, *421*, 213462.

[59] S. Kolemen, E. U. Akkaya, *Coord. Chem. Rev.* **2018**, *354*, 121–134.

[60] D. Ho, R. Ozdemir, H. Kim, T. Earmme, H. Usta, C. Kim, *ChemPlusChem* **2019**, *84*, 18–37.

[61] D. K. Kölmel, A. Hörner, J. A. Castañeda, J. A. P. Ferencz, A. Bihlmeier, M. Nieger, S. Bräse, L. A. Padilha, *J. Phys. Chem. C* **2016**, *120*, 4538–4545.

[62] Q. P. B. Nguyen, H. M. Hwang, M.-S. Song, H. J. Song, G. H. Kim, J. H. Kwon, N. Y. Shim, K. Y. Chai, *Bull. Korean Chem. Soc.* **2014**, *35*, 1247–1250.

[63] S. G. Awuah, Y. You, *RSC Adv.* **2012**, *2*, 11169–11183.

[64] A. Costela, I. García-Moreno, R. Sastre, *Phys. Chem. Chem. Phys.* **2003**, *5*, 4745–4763.

[65] C. Stoffelen, J. Huskens, *Small* **2016**, *12*, 96–119.

[66] X. J. Loh, *Mater. Horiz.* **2014**, *1*, 185–195.

[67] A. Rahman, P. P. Praveen Kumar, P. Yadav, T. Goswami, A. Shanavas, H. N. Ghosh, P. P. Neelakandan, *ACS Appl. Nano Mater.* **2022**, *5*, 6532–6542.

[68] A. Rahman, T. Goswami, N. Tyagi, H. N. Ghosh, P. P. Neelakandan, *J. Photochem. Photobiol., A* **2022**, *432*, 114067.

[69] P. P. P. Kumar, A. Rahman, T. Goswami, H. N. Ghosh, P. P. Neelakandan, *ChemPlusChem* **2021**, *86*, 87–94.

[70] K. Naim, S. C. Sahoo, P. P. Neelakandan, *ACS Appl. Mater. Interfaces* **2022**, *14*, 22650–22657.

[71] A. Maity, A. Sarkar, A. Sil, S. B. B. N, S. K. Patra, *New J. Chem.* **2017**, *41*, 2296–2308.

[72] X.-Z. Wang, Q.-Y. Meng, J.-J. Zhong, X.-W. Gao, T. Lei, L.-M. Zhao, Z.-J. Li, B. Chen, C.-H. Tung, L.-Z. Wu, *Chem. Commun.* **2015**, *51*, 11256–11259.

[73] M. Zhang, E. Hao, Y. Xu, S. Zhang, H. Zhu, Q. Wang, C. Yu, L. Jiao, *RSC Adv.* **2012**, *2*, 11215–11218.

[74] W. Li, L. Li, H. Xiao, R. Qi, Y. Huang, Z. Xie, X. Jing, H. Zhang, *RSC Adv.* **2013**, *3*, 13417–13421.

[75] R. W. Wagner, J. S. Lindsey, *Pure Appl. Chem.* **1996**, *68*, 1373–1380.

[76] P. P. P. Kumar, P. Yadav, A. Shanavas, S. Thurakkal, J. Joseph, P. P. Neelakandan, *Chem. Commun.* **2019**, *55*, 5623–5626.

[77] S. K. Bharti, R. Roy, *TrAC, Trends Anal. Chem.* **2012**, *35*, 5–26.

Chapter 3

Photophysical Properties
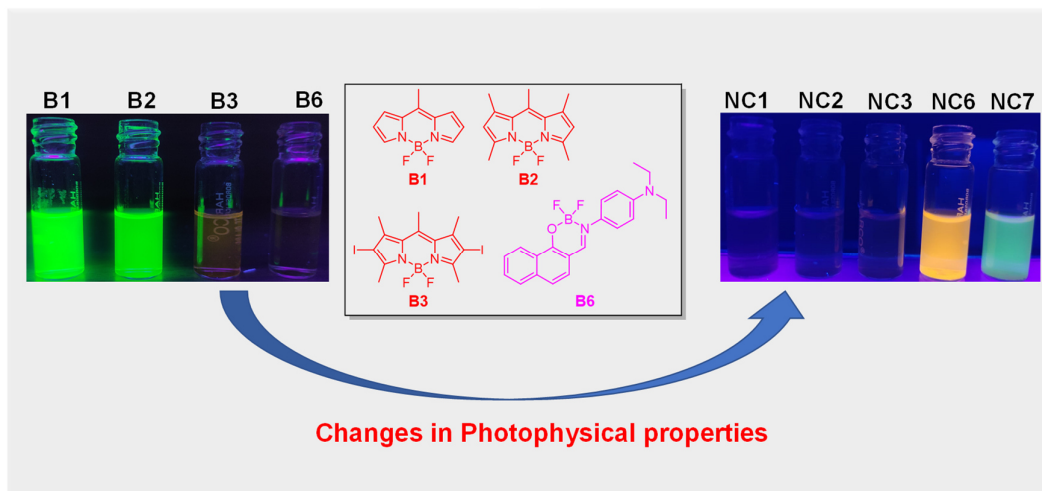
3.1. Introduction.

Plasmon-molecule coupling causes a variety of fascinating phenomena such as surface-enhanced Raman scattering, plasmon-enhanced fluorescence, refractive index-induced plasmon shifting, plasmon-enhanced nonlinear optical properties, etc.[1–13] The photophysical and electronic properties of plasmon-molecule coupled systems differ substantially from their individual constituents.[14–17] Importantly, the photophysical properties of these systems are determined by the strength of the plasmon-molecule coupling.[18] Recent advancements in plasmon-molecule coupling show that the coupling strength is dependent on various parameters such as the concentration of the dye molecules, spectral overlap between the dye molecules and plasmons, and distance between the dye molecules and the plasmonic surfaces.[19–25] On the other hand, photophysical properties of organic dyes is compromised under physiological conditions because of aggregation and other intermolecular interactions.[26,27] Various self-assembled structures containing organic photosensitizers, such as micelles, vesicles, or nanoparticles, are prepared using polymers or surfactants as a supporting matrix to prevent aggregation and improve water solubility.[28–30] However, these support matrices rarely interact electronically with organic molecules, whereas the usage of metal nanoparticles aids not only in the self-assembly process but also in modulating the photosensitization properties.[31–35] The impact of chemical structure and functional groups of dye molecules on plasmon-molecule coupling, which eventually can

result in significant changes in photophysical and photosensitization properties, are not yet explored systematically.

      This chapter discusses the effect of the chemical structure and functional groups of dye molecules on the photophysical and photosensitization properties of plasmon-molecule coupled systems. Our findings show that the chemical structure of the dye molecules **B1-B6** has a significant impact on the photophysical properties of dye-loaded gold nanoparticles **NC1-NC7** (Chart 3.1). We investigated the photostability and photosensitization properties of nanocomposites, and found that the chemical structure had a significant impact on them. Furthermore, we presume that molecules aggregate on the surface of gold nanoparticles. To evaluate the changes in the photophysical properties of dyes upon aggregation, we carried out systematic aggregation studies of dye molecules in water-acetonitrile mixtures. Our findings show that the chemical structure of the dye molecules influences their aggregation behaviour. In the case of mixed aggregates of BODIPY **B2** and **B3**, on the other hand, we observed Förster resonance energy transfer (FRET) between aggregates of **B2** and **B3**. Furthermore, the effect of the immediate environment on the photophysical properties of nanocomposites **NC6** containing the stimuli-responsive group naphthalidenimine-boron complex **B6** was investigated in glycine buffer at different pH. We also investigated the photophysical properties of a multi-chromophoric nanocomposite **NC7** containing two BODIPY molecules **B2** and **B3**, where we observed simultaneous FRET and hot electron transfer. Despite numerous reports of energy transfer between gold and organic motifs, there is no precedence for gold nanoparticles acting as a matrix to facilitate FRET between two organic chromophores.
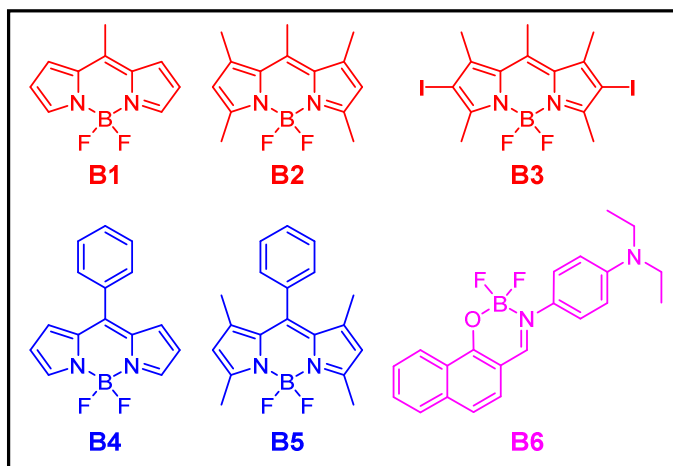

Chart 3.1. Chemical structures of the dyes **B1-B6** used in this study.

3.2. Results.

The photophysical properties of various systems are presented in the following order: dye molecules **B1**-**B6** in acetonitrile, their aggregation behaviour in water-acetonitrile mixture, organic nanoparticles **ONP1-ONP6** and the nanocomposites **NC1-NC7**.

3.2.1. Photophysical Properties of Dye Molecules.

BODIPY dyes generally demonstrate high fluorescence quantum yields, narrow emission bandwidths with high peak intensities, and relatively high absorption coefficients in solution.[36–38] Furthermore, they have excitation/emission wavelengths in the visible range. Similar to this general perspective, we also observed sharp absorption and emission peaks with high fluorescence quantum yields for the BODIPY dyes **B1-B5** which in acetonitrile exhibited absorption peaks at 495, 490, 520, 496, and 497 nm, and the emission peaks at 520, 509, 560, 517, and 508 nm, respectively (Figure 3.1). As represented in Table 3.1, high fluorescence quantum yields were observed for the molecules **B1**, **B2** and **B5** whereas the fluorescence quantum yield of **B3** was found to be low due to the heavy atom effect, which facilitates intersystem crossing. However, the rotation of the *meso*-phenyl group about the C-C single bond causes non-radiative decays thereby resulting in low fluorescence quantum yield for **B4**.[39] Further, the excited state lifetime was measured by time-correlated single-photon counting (TCSPC) experiments and the molecules **B1-B3** and **B5** exhibited mono-exponential fluorescence decay profiles with lifetime values of 8.41 ± 0.05, 5.85 ± 0.02, 1.63 ± 0.01 and 3.95 ± 0.04 ns, respectively (Table 3.1 and Figure 3.2).
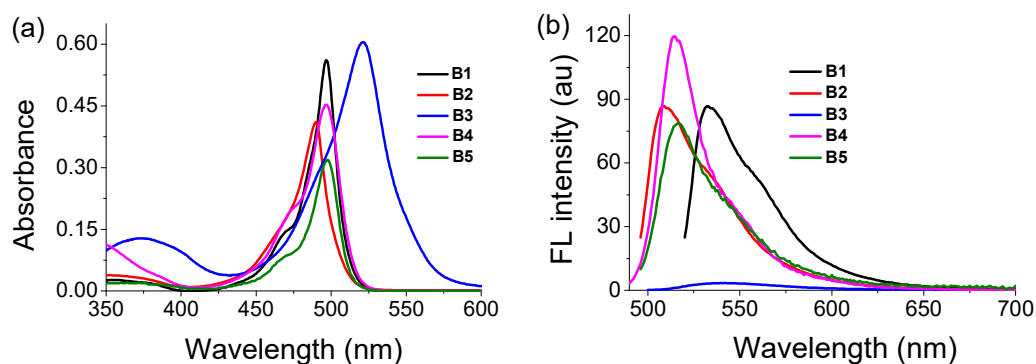

Figure 3.1. (a) UV-Vis absorption and (b) fluorescence spectra of **B1-B5** (11, 17, 12, 18 and 12 µM, respectively) in acetonitrile. Excitation wavelength, 490 nm for **B1**, **B2**, **B4** and **B5** and 520 nm for **B3**.
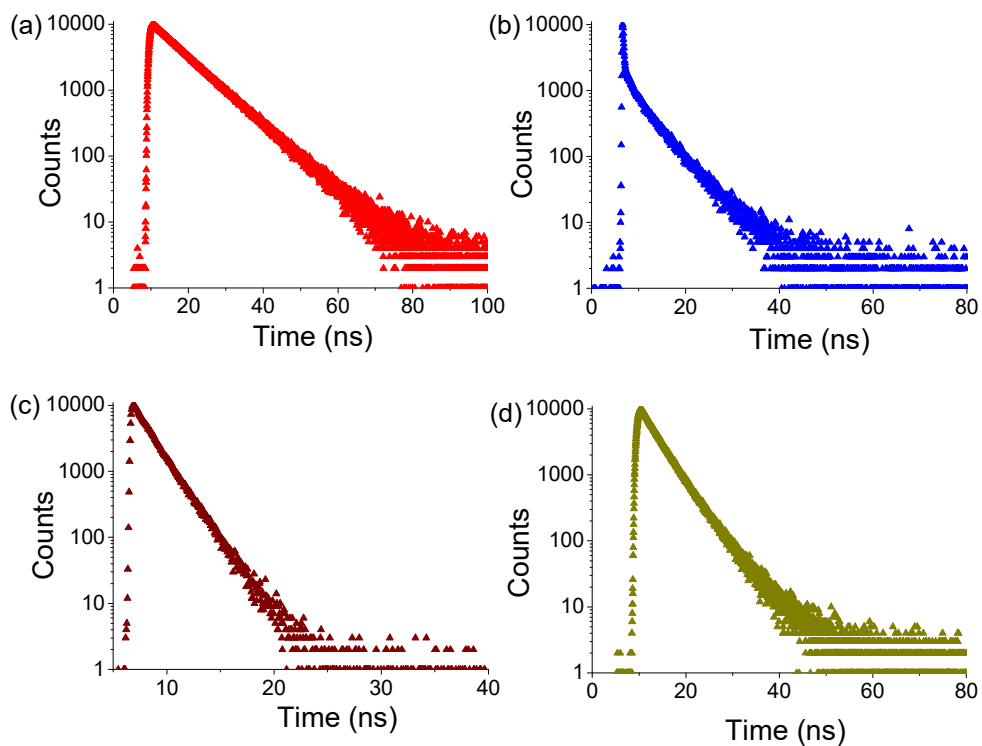
Figure 3.2. Fluorescence lifetime decay profiles of (a) **B1** (11 µM), (b) **B2** (17 µM), (c) **B3** (12 µM) and (d) **B5** (12 µM) in acetonitrile. Excitation wavelength, 440 nm.

Table 3.1. Photophysical properties of the dye molecules **B1-B6** in acetonitrile under various experimental conditions.

System	λ_{abs} (nm)	λ_{em} (nm)	Φ_f	τ (ns)
B1	495	520	0.87	8.41 ± 0.05
B2	490	509	0.95	5.85 ± 0.02
B3	520	560	0.01	1.63 ± 0.01
B4	496	517	0.03	*n.d.*
B5	497	508	0.65	3.95 ± 0.04
B6	450	630	*n.d.*	*n.d.*
B6 + HCl	425	502	0.63	9.37 ± 0.01

n.d., Not determined due to low or quenched emission nature of materials.

On the other hand, the naphthalidenimine-boron complex **B6** showed a broad absorption and emission spectrum in acetonitrile with maxima at 450 and 630 nm, respectively (Figure 3.3). Very low fluorescence intensity was observed for **B6** in acetonitrile (Table 3.1). It is anticipated that because of the charge transfer from (diethyl)amino (donor)

to boryl group (acceptor), **B6** showed a low fluorescence quantum yield in polar solvents like acetonitrile. To confirm the charge transfer phenomenon, we recorded the emission spectrum of **B6** after adding a drop of hydrochloric acid to the solution of **B6** in acetonitrile. It was observed that absorption and emission maxima exhibited substantial blue shifts to 425 and 502 nm, respectively after the addition of hydrochloric acid (Figure 3.3). Further, significant increase was observed in the fluorescence intensity with a fluorescence quantum yield of 0.63 (Table 3.1). The enhancement in the fluorescence was also observed visually wherein **B6** in acetonitrile was colourless while the addition of hydrochloric acid resulted in bright green emission under UV light (inset of Figure 3.3a). The addition of hydrochloric acid facilitates protonation of the (diethyl)amino group, which inhibits the charge transfer process and causes emission from the locally excited state of **B6**, which exhibited enhanced intensity and blue-shifted emission maximum. Furthermore, we observed a mono-exponential fluorescence decay profile with a lifetime of 9.37 ± 0.01 ns after the addition of hydrochloric acid (inset of Figure 3.3b). In contrast, the lifetime of **B6** in acetonitrile was unreliable due to very low emission. This dye **B6** thus serves as an ideal choice for studying the effect of immediate environment on nanocomposite formation.
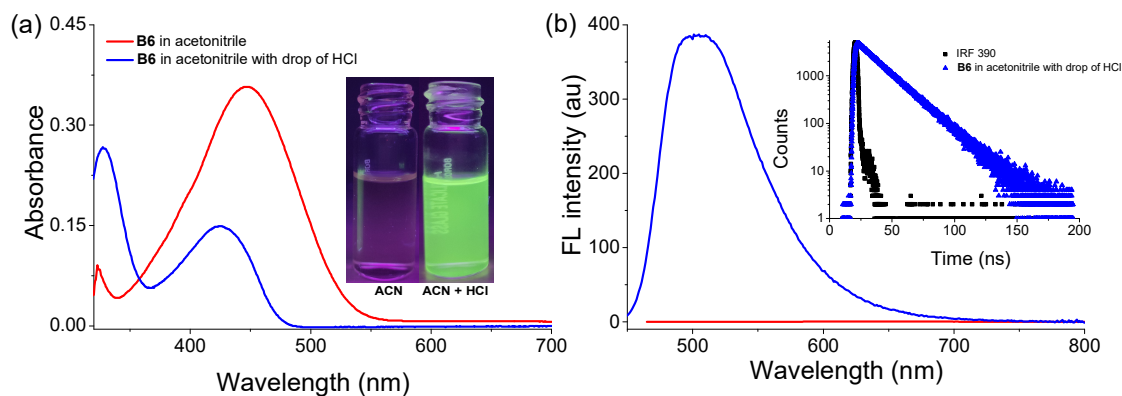

Figure 3.3. (a) UV-Vis absorption and (b) fluorescence spectra of **B6** (12 µM) in acetonitrile and after the addition of a drop of hydrochloric acid. Inset of (a) shows photographs of **B6** in acetonitrile and after the addition of a drop of hydrochloric acid under UV light and inset of (b) shows the fluorescence lifetime decay profiles of **B6** after the addition of a drop of HCl.

3.2.2. Aggregation of BODIPY Molecules.

As described in section 2.2.4 of Chapter 2, it is assumed that chromophores aggregate on the surface of gold nanoparticles during nanocomposite formation. So, we were curious to investigate the aggregation properties of BODIPY molecules **B1-B3** systematically which formed stable nanocomposites. It is widely acknowledged that the optical properties of

aggregates differ significantly from those of their monomeric forms. The aggregation behaviour of molecules **B1-B3** were investigated by varying the water content from 0 to 90% in acetonitrile. BODIPY molecules **B1-B3** exhibited sharp absorption peaks at 495, 490, and 520 nm and emission peaks at 520, 509, and 560 nm in acetonitrile (Figure 3.1a). When the solvent system was gradually changed from 0 to 90% water in acetonitrile, only minor changes were observed in the absorption and emission maxima of molecules **B1** and **B2** (Figure 3.4).
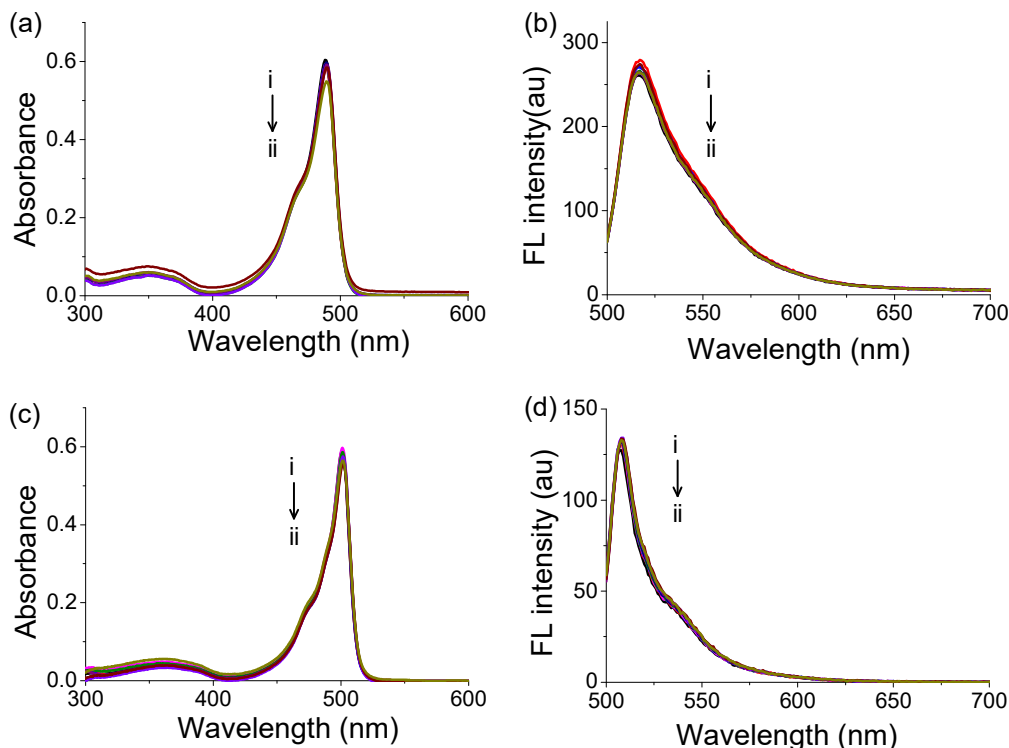
Figure 3.4. (a, c) UV-Vis absorption and (b, d) fluorescence spectra of **B1** (13 μM) and **B2** (21 μM) in water-acetonitrile mixtures. (i) 100% acetonitrile and (ii) 90% water- acetonitrile mixture. Excitation wavelength, 490 nm.

Under similar experimental conditions, significant changes were observed in the photophysical properties of the molecule **B3**. When the amount of water was increased from 0 to 60%, we noticed a gradual hypochromic shift in the absorption maximum at 520 nm. A further increase in the water content to 90% resulted in significant hypsochromic shifts and the appearance of a new absorption maximum at 463 nm (Figure 3.5a). Following the changes in the absorption spectrum, the emission intensity of **B3** gradually decreased as the water content increased from 0 to 60%, and an increase in the water content to 90% resulted in a sudden decrease in the emission intensity (inset of Figure 3.5b). It was also observed that

when the water content was more than 80%, a new peak appeared at 502 nm (inset of Figure 3.5b).
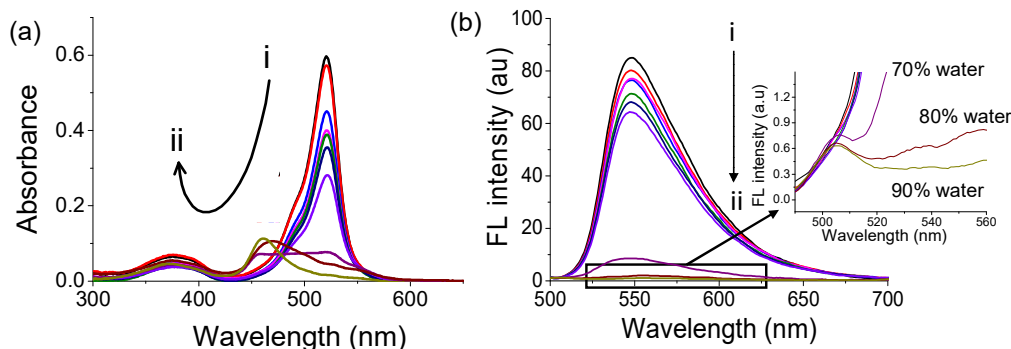

Figure 3.5. (a) UV-Vis absorption and (b) fluorescence spectra of **B3** (14 μM) in water-acetonitrile mixtures. (i) 100% acetonitrile, (ii) 90% water-acetonitrile mixture. Inset shows the emergence of a peak at 502 nm. Excitation wavelength, 490 nm.

Next, we investigated the aggregation behaviour of the sterically bulky BODIPY **B5**, which failed to form a stable nanocomposite (Section 2.2.4, Chapter 2). A minor change was observed in the absorption maximum of **B5** when the amount of water was increased from 0 to 80%. Further, we observed a hypochromic shift in the absorption maximum at 497 nm and broadening around 520 nm at 90% water content (Figure 3.6a). A gradual decrease in the emission maximum at 508 nm was observed when the water content was increased from 0 to 80%. Further, a significant hypsochromic shift in the emission maximum of **B5** was observed in 90% water-acetonitrile (Figure 3.6b). A subtle change in the *meso*-position of a phenyl group in **B5** BODIPY caused a significant decrease in fluorescence intensity, indicating that a fast aggregation is plausible for **B5** due to the more hydrophobic phenyl group.
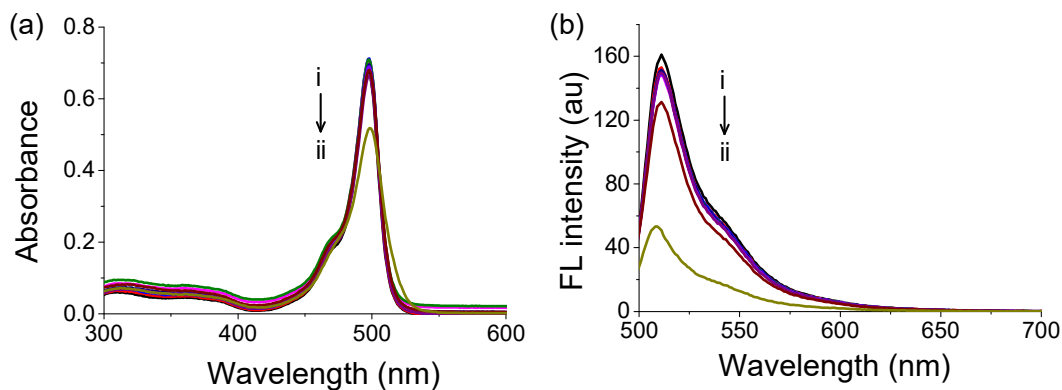

Figure 3.6. (a) UV-Vis absorption and (b) fluorescence spectra of **B5** (21 μM) in water-acetonitrile mixtures. (i) 100% acetonitrile and (ii) 90% water-acetonitrile mixture. Excitation wavelength, 490 nm.

We were curious to study the aggregation of a physical mixture of molecules **B2** and **B3** under similar conditions since we used **B2** and **B3** to synthesize the multi-chromophoric nanocomposite **NC7**. We observed two absorption peaks at 490 and 520 nm in an equimolar mixture of **B2** and **B3** in acetonitrile, whereas emission maxima were observed at 509 and 538 nm. These peaks are assigned to individual molecules. The observation of identical peaks for the physical mixture as compared to the individual constituents indicated that the interaction between **B2** and **B3** in acetonitrile was negligible. We observed a decrease in the absorbance peak at 490 nm as the water content was increased, whereas the peak at 520 nm disappeared. Furthermore, a new shoulder emerged at 471 nm, indicating that the molecules were aggregated in 90% water-acetonitrile mixture (Figure 3.7a). Surprisingly, the fluorescence changes exhibited by the mixture of **B2** and **B3** upon increasing the water content were markedly different as compared to the individual molecules. While minor changes and a decrease in intensity were observed for **B2** and **B3**, respectively, we observed an enhancement in the emission intensity at 507 nm in the case of the mixture of **B2** and **B3** when the water content was increased to 90% (Figure 3.7b). To ascertain the origin of the fluorescence enhancement, we measured the fluorescence lifetimes of the mixture of **B2** and **B3** in 90% water-acetonitrile. It was observed that the mixture of **B2** and **B3** exhibited a mono-exponential decay with a lifetime of 6.37 ± 0.01 ns (Figure 3.8).
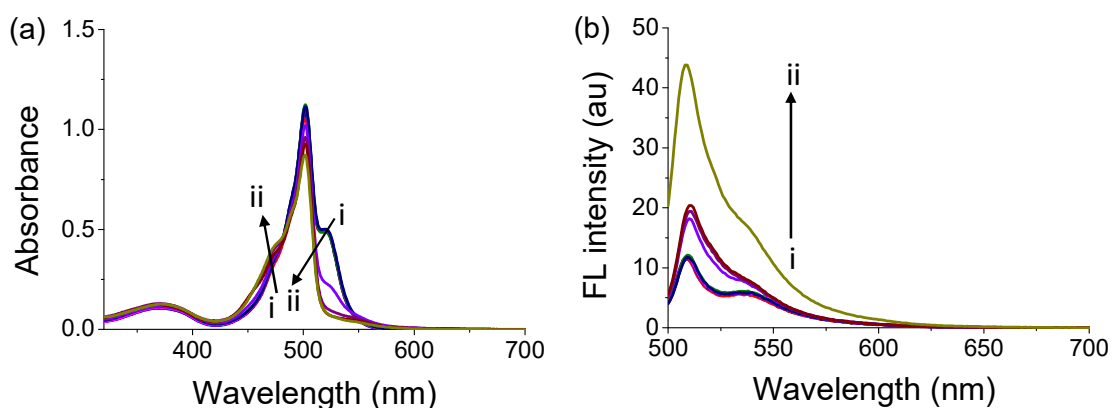

Figure 3.7. (a) UV-Vis absorption and (b) fluorescence spectra of a mixture of **B2** (21 μM) and **B3** (14 μM) in water-acetonitrile mixtures. (i) 100% acetonitrile and (ii) 90% water-acetonitrile mixture. Excitation wavelength, 490 nm.
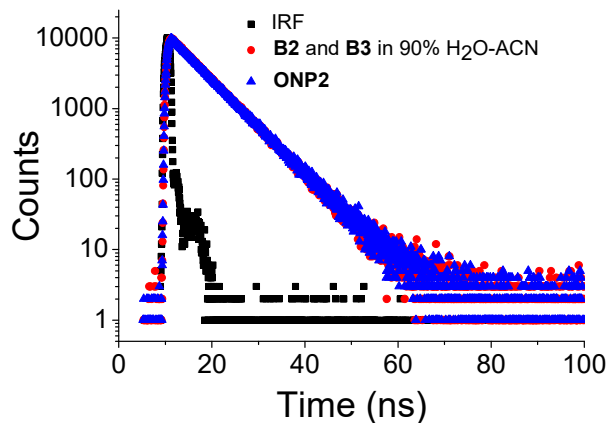
Figure 3.8. Fluorescence lifetime decay profiles of the aggregates of **B2** and **B3** in 90% water-acetonitrile mixture and **ONP2** (8.6 μg/mL) in water. Excitation wavelength, 440 nm.

The changes in the spectroscopic properties of **B1**, **B2**, and **B3** in acetonitrile-water mixtures indicated molecular aggregation. While the minor differences in the absorbance and fluorescence of **B1** and **B2** showed the formation of random aggregates, the blue-shift in absorption and quenching of fluorescence of **B3** indicated *H*-type aggregation. Furthermore, the significant decrease in the absorbance and the quenching of the fluorescence of **B5** showed that the hydrophobic phenyl group caused π-π stacking between the aromatic cores and led to fast molecular aggregation in **B5**. On the other hand, blue-shift in the absorption and fluorescence enhancement of a mixture of **B2** and **B3** indicated a different type of aggregation.

3.2.3. Förster Resonance Energy Transfer (FRET) between the Aggregates of B2 and B3.

It is proposed that the enhanced fluorescence in the case of the mixed aggregates of **B2** and **B3** arises because of a Förster resonance energy transfer (FRET) process from the aggregates of **B3** to the aggregates of **B2**. A substantial overlap between the emission spectrum of the aggregates of **B3** with the absorption spectrum of the aggregates of **B2** further confirms the feasibility of FRET (Figure 3.9). Furthermore, the fluorescence lifetime value for the mixture of **B2** and **B3** aggregates (6.37 ± 0.01 ns) is quite comparable with the lifetime value of **B2** (5.85 ± 0.02 ns) and **ONP2** (6.42 ± 0.01 ns), substantiating FRET between the aggregates of **B3** and **B2** (Table 3.1).
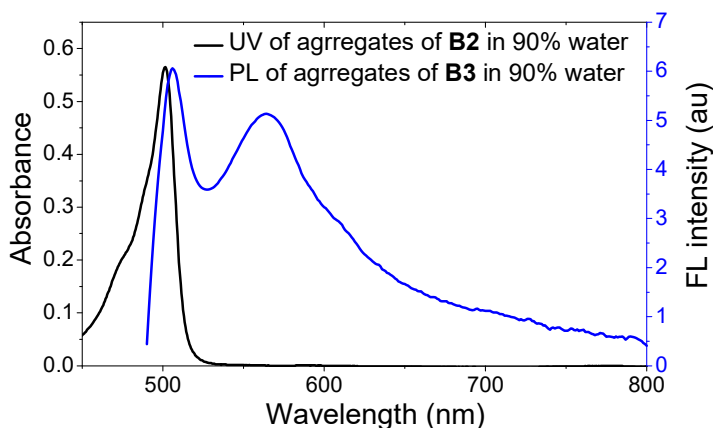
Figure 3.9. Overlap between the normalized absorption spectrum of the aggregates of **B2** and the normalized emission spectrum of the aggregates of **B3** in 90% water-acetonitrile mixture.

Next, we employed femtosecond transient absorption spectroscopy (TA) to understand the FRET phenomena.[40,41] In acetonitrile, molecules **B2** and **B3** showed TA signals at 500 and 520 nm, respectively. In the case of the aggregates of the mixture of **B2** and **B3**, the signature of the molecule **B3** disappeared. In 90% water-acetonitrile mixture, the TA signal for the mixture of **B2** and **B3** consisted of the features of the molecule **B2** at 500 nm and an aggregation-based bleach at 463 nm (Figure 3.10). We also compared the dynamics of the molecular bleach signal of **B2** with the similar bleach feature of a mixture of **B2** and **B3** in a 90% water-acetonitrile mixture. The mixture of **B2** and **B3** exhibited much slower dynamics than the pure **B2** in acetonitrile (Figure 3.11). These findings are consistent with our steady-state fluorescence measurements and support FRET between aggregates of **B2** and **B3**. It is worth noting that FRET is only feasible in the aggregated state due to the complementarity between the emission and absorption spectra of the aggregates. It may also be noted that only minor changes were observed in the steady-state and TA peak positions of a mixture of **B2** and **B3** in acetonitrile compared to the individual molecules, thereby indicating negligible interaction between **B2** and **B3** in acetonitrile.
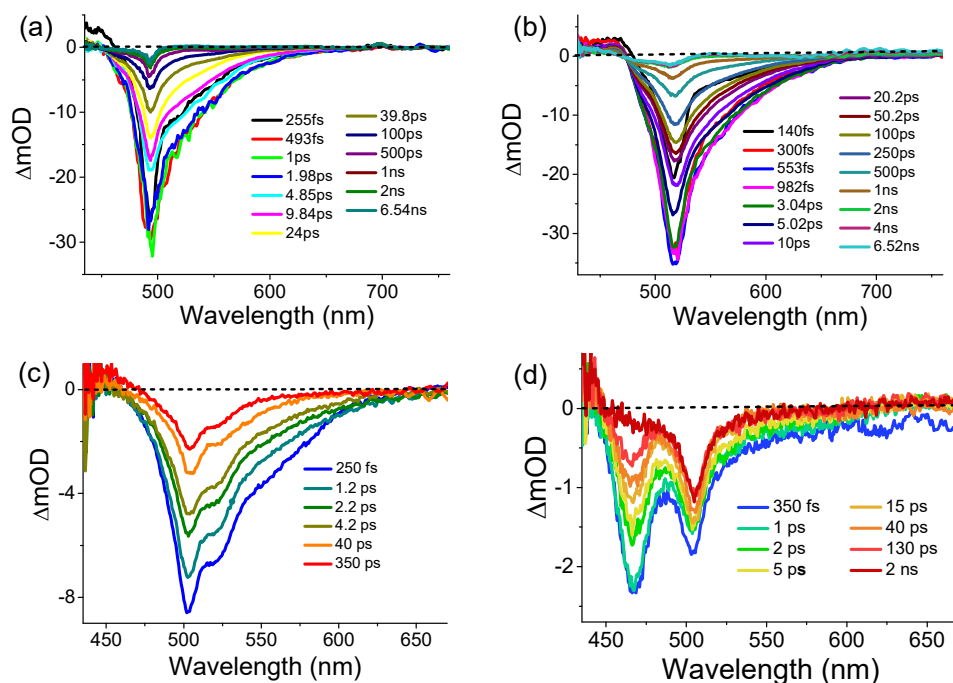
Figure 3.10. Transient absorption spectra of (a) **B2** (49 μM) and (b) **B3** (31 μM) in acetonitrile and a mixture of **B2** (21 μM) and **B3** (14 μM) in (c) acetonitrile and (d) 90% water-acetonitrile, respectively. Excitation wavelength, 450 nm.
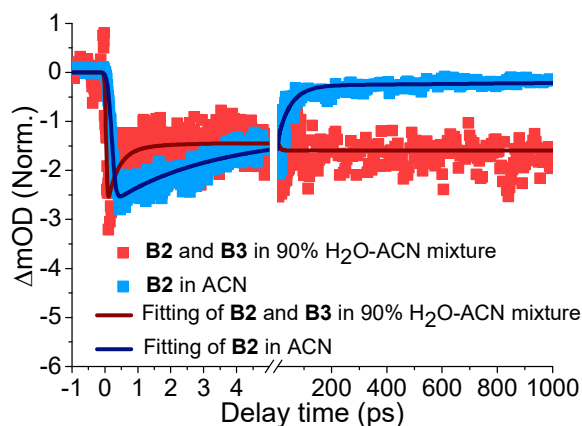

Figure 3.11. Comparison of the dynamics of the characteristic bleach feature of molecule **B2** in acetonitrile and a mixture of **B2** and **B3** in 90% water-acetonitrile.

3.2.4. Aggregation of B6.

The aggregation properties of the naphthalidenimine-boron complex **B6** was studied by varying the water content from 0 to 90% in an acetonitrile-water mixture system. **B6** exhibited an absorption maximum at 450 nm in acetonitrile and when the solvent system was progressively changed from 0 to 40% water in acetonitrile, a minor change was observed in the absorption intensity. However, in 50% water-acetonitrile, we noticed a hypochromic shift

in absorption maxima at 450 nm. When the water content was further increased from 60 to 90%, a broadening along with a bathochromic shift and a hypochromic shift from 450 nm to 540 nm were evidenced (Figure 3.12a). **B6** showed an emission maximum at 630 nm in acetonitrile and when the water content was increased from 0 to 50%, a minor change was observed in the fluorescence intensity (inset of Figure 3.12b). This could be due to the retention of the monomeric state of molecule **B6** in the presence of lower water content. Surprisingly, an enhancement in fluorescence intensity and a hypsochromic shift in peak maxima at 590 nm were noticed while increasing the water content from 60 to 80%. Furthermore, we observed a reduction in emission intensity at 90% water content which was accompanied by red-shifted emission maxima at 600 nm (Figure 3.12b). It is inferred that fast aggregation of **B6** at higher water content (≥90%) resulted in the formation of less-emissive amorphous species whereas in lower water content (≤90%), it favoured the formation of highly emissive crystalline aggregates.[42] When **B6** was observed under a UV lamp, significant orange fluorescence was observed with the naked eye above 60% water content whereas the solution was colourless below 60% (Figure 3.13). These observations suggest aggregation-induced emission (AIE) for **B6**.
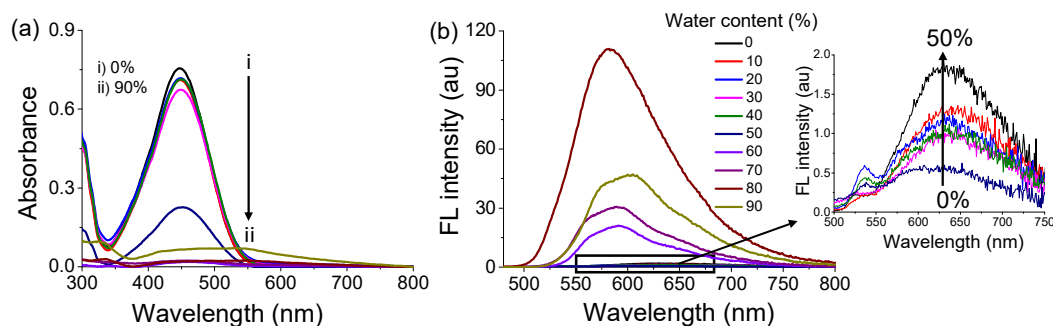

Figure 3.12. (a) UV-Vis absorption and (b) fluorescence spectra of **B6** (18 μM) in acetonitrile-water mixtures. Inset of (b) shows the spectral changes up to 50% water content.

To gain insights into the aggregation behaviour, we measured the fluorescence lifetime for the aggregates of molecule **B6** from 60 to 90% water content. The data below 60% water content was unreliable due to the low emission. When water content was increased from 60 to 90%, the contribution of the short-lived component gradually increased, whereas the contribution of long-lived component decreased significantly (Table 3.2 and Figure 3.14). This change presumably indicates the transition from the charge transfer state to the locally excited state, which accounts for the shortened lifetime.
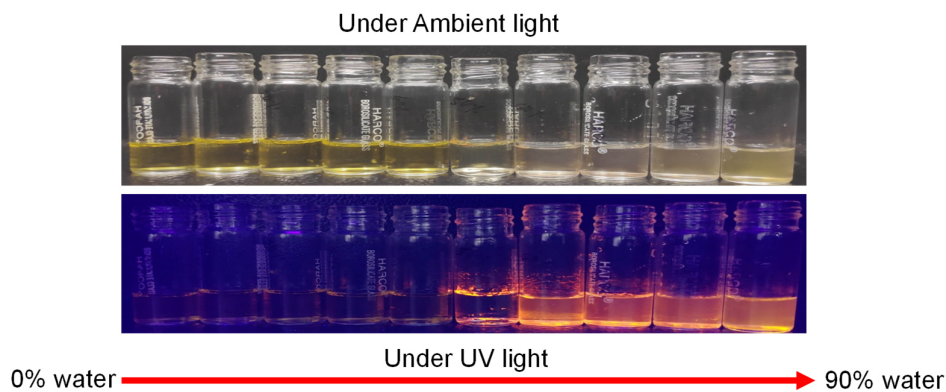
Under Ambient light

Under UV light

0% water ➔ 90% water

Figure 3.13. Photograph of **B6** (18 μM) in acetonitrile-water mixtures (from 0 to 90%) under ambient and UV light.
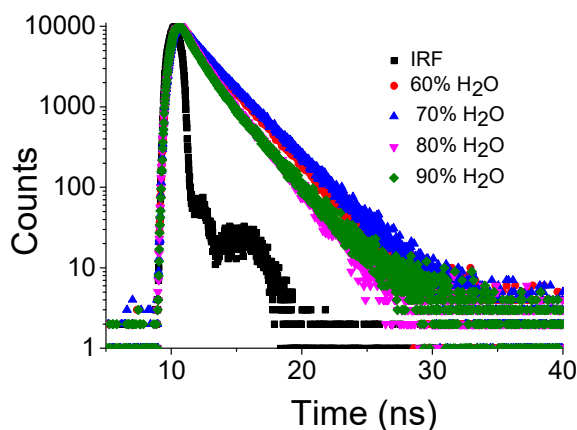

Figure 3.14. Fluorescence lifetime decay profiles of **B6** (18 μM) in different water-acetonitrile mixtures. Excitation wavelength, 440 nm.

Table 3.2. Fluorescence lifetimes of **B6** in water-acetonitrile mixtures.

Solvent	τ_1 (ns)	τ_2 (ns)
60% water-acetonitrile	0.97±0.03 (16.31%)	2.58±0.005 (83.69%)
70% water-acetonitrile	1.00±0.04 (12.63%)	2.68±0.005 ns (87.37%)
80% water-acetonitrile	0.88±0.02 (29.82%)	2.25±0.005 ns (70.18%)
90% water-acetonitrile	0.92±0.01 (39.08%)	2.44±0.006 ns (60.92%)

3.2.5. Photophysical Properties of Organic Nanoparticles ONP1-ONP6.

BODIPY molecules are prone to show aggregation caused quenching (ACQ) or weak emission due to the self-absorption and strong π-π interaction caused by planar π-conjugated structures.[37,43] We investigated the photophysical properties of organic nanoparticles (**ONPs**) of BODIPYs in water. The absorption and emission spectra of **ONPs** in aqueous

media significantly differed from those of the corresponding molecules and the aggregates in acetonitrile-water mixture. The formation of organic nanoparticles primarily broadened the absorption and emission spectra. The absorption and emission maxima of the organic nanoparticles **ONP1-ONP5** were observed at 495, 455 and 488, 530 (br), 490 and 487 (br), and at 526, 515, 550, 499, and 506 nm, respectively. Furthermore, the emission intensities of **ONP1-ONP5** significantly reduced and had lower fluorescence quantum yields (Table 3.3 and Figure 3.15b). This finding indicates that BODIPY molecules **B1-B5** exhibited prominent ACQ behaviour in aqueous media during organic nanoparticle formation. The naphthalidenimine-boron complex **B6**, on the other hand, behaved differently during nanoparticle formation. We observed a broad absorption spectrum with an absorption maximum at 540 nm for **ONP6** whereas the emission maximum showed a blue-shift to 590 nm (Figures 3.15a and 3.16a). It is noteworthy to see a significant increase in the fluorescent intensity of **ONP6** with a moderately good fluorescence quantum yield of 0.16. (Table 3.3). The enhancement in fluorescence intensity in **ONP6** was confirmed by the fluorescence lifetime decay measurement. We observed a bi-exponential lifetime decay with a lifetime value of 0.69 ± 0.008 ns (69.45%) and 1.89 ± 0.01 ns (30.55%), whereas the lifetime data for **B6** in acetonitrile was not reliable due to significantly low emission (Figure 3.16b). These spectral characteristics indicated different types of aggregation of dye molecules during the organic nanoparticle formation which is dependent on their chemical structure.

Table 3.3. Photophysical properties of the organic nanoparticles **ONP1-ONP6** in water.

System	λ_{abs} (nm)	λ_{em} (nm)	Φ_f
ONP1	495	526	0.10
ONP2	455 and 488	515	0.05
ONP3	530 (br)	550	*n.d.*
ONP4	490	499	*n.d.*
ONP5	487 (br)	506	*n.d.*
ONP6	540 (br)	590	0.16

n.d., Not determined due to low or quenched emission nature of materials.

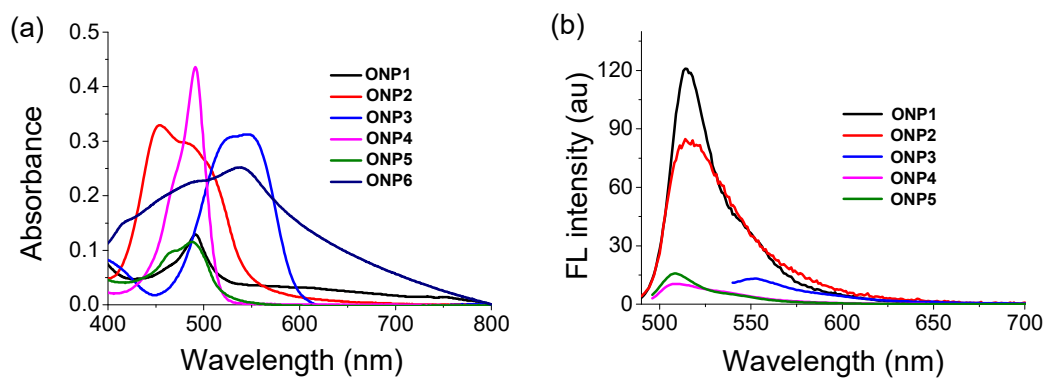**Figure 3.15.** (a) UV-Vis absorption and (b) fluorescence spectra of **ONP1-ONP6** (9.3, 8.6, 9.2, 19, 12, and 12.2 µg/mL, respectively) in water.
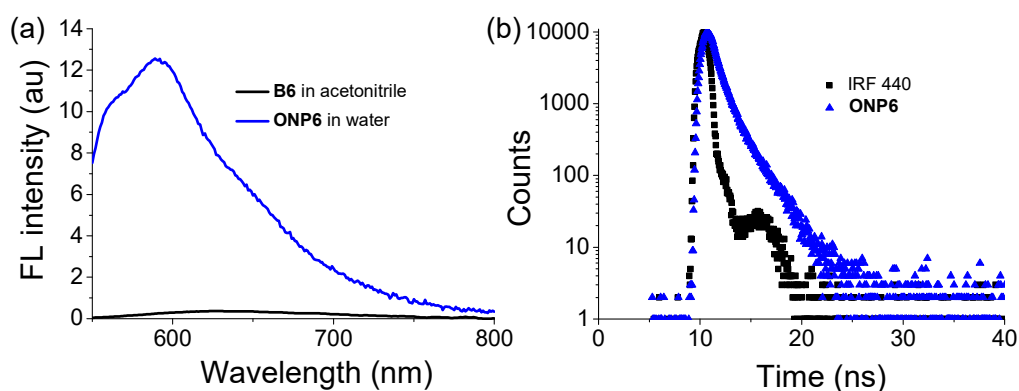

Figure 3.16. (a) A comparison of fluorescence spectra of **B6** in acetonitrile and **ONP6** in water and (b) fluorescence lifetime decay profiles of **ONP6** in water. [**B6**], 16 µM and [**ONP6**], 12.2 µg/mL.

3.2.6. Absorption and Fluorescence Properties of Nanocomposites.

The absorption maximum of nanocomposites revealed distinct peaks attributed to their constituents, namely dye the molecules and the gold nanoparticles. However, it is important to note that the absorption spectra of the nanocomposites were not additive of the individual components and moreover differed significantly from those of their constituents. For example, nanocomposite **NC1** containing BODIPY **B1**, nanocomposite **NC2** containing BODIPY **B2**, and nanocomposite **NC4** containing BODIPY **B4** showed two absorption peaks at 497 and 550 nm, 520 and 560 nm, and 498 and 557 nm, respectively (Table 3.4 and Figure 3.17a). Gold nanoparticles **Au NP**, on the other hand, exhibited absorption maxima at 530 nm due to surface plasmon resonance (SPR) (Table 3.4 and Figure 3.17a). This suggested that interaction between the BODIPY moiety and the gold nanoparticles in **NC1**, **NC2** and **NC4** caused redshifts in the SPR and molecular peaks as compared to their components. However,

NC3 showed a broad absorption spectrum starting at 450 nm and extending up to 800 nm indicating the electronic transitions between the constituents, whereas **NC6** showed two absorption peaks at 443 and 523 nm which were blue-shifted as compared to the individual components. The multi-chromophoric nanocomposite **NC7** evidenced a distinct absorption feature as compared to the individual nanocomposites **NC2** and **NC3**. A broad absorption spectrum was observed for **NC7**, extending from 410 to 650 nm and tailing up to 800 nm (Table 3.4 and Figure 3.17a).

Table 3.4. Photophysical properties of the nanocomposites **NC1-NC4**, **NC6** and **NC7** in water.

System	λ_{abs} (nm)	λ_{em} (nm)	Φ_f
NC1	497, 550	*n.d.*	*n.d.*
NC2	520, 566	*n.d.*	*n.d.*
NC3	450-800	*n.d.*	*n.d.*
NC4	498, 557	*n.d.*	*n.d.*
NC6	443, 523	620	0.13
NC7	458, 518, 550	520	0.12

n.d., Not determined due to low or quenched emission nature of materials.

Further, we studied the emission properties of the nanocomposites. BODIPY molecules **B1-B3** showed a sharp, intense emission whereas a complete quenching of fluorescence was observed for **NC1-NC3**. But, **NC4** showed an emission maximum similar to **B4**, indicating the leaching out of **B4** from **NC4** over time due to its unstable nature (see Section 3.2.9) (Table 3.4 and Figure 3.17b). On the other hand, the multi-chromophoric nanocomposite **NC7** showed a moderately intense emission maximum at 520 nm while the individual nanocomposites, i.e., **NC2** and **NC3**, were found to be non-emissive. The fluorescence quantum yield (Φ_f) of **NC7** was found to be 0.12 (Table 3.4 and Figure 3.17c). Furthermore, **NC6** was observed to be luminescent in nature with a distinct emission maximum at 620 nm (Table 3.4 and Figure 3.17d). The fluorescence quantum yield (Φ_f) of molecule **B6** was found to be very low in acetonitrile whereas **NC6** exhibited a moderately good fluorescence quantum yield of 0.13 in water (Table 3.4).
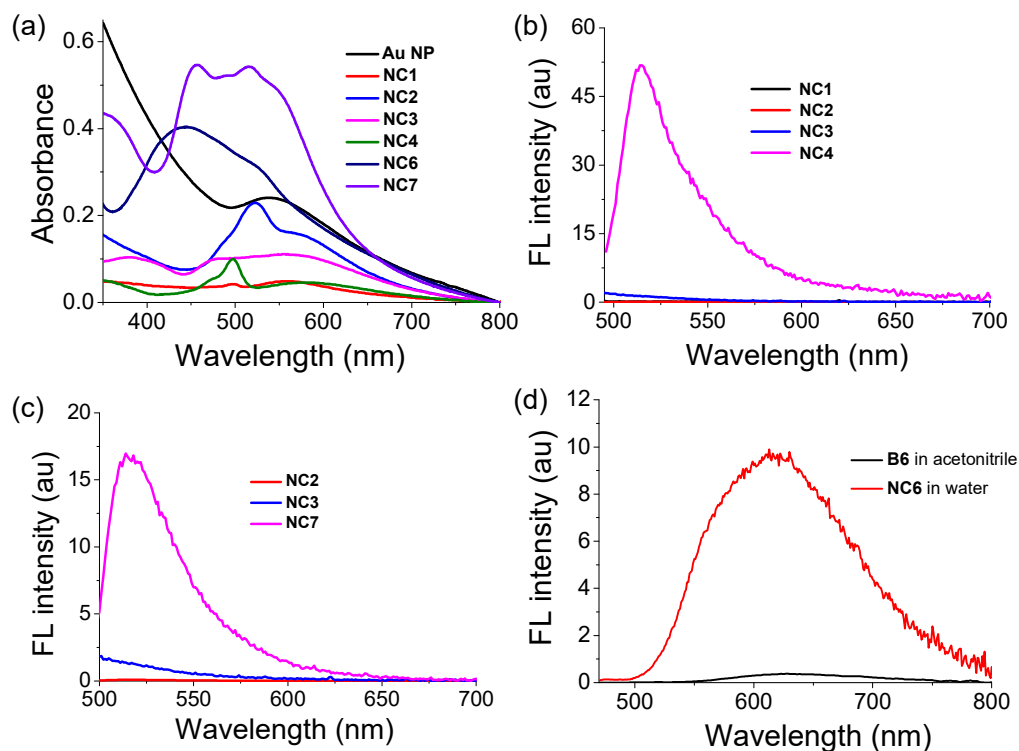
Figure 3.17. UV-Vis absorption spectra of (a) **NC1-NC6**. Fluorescence spectra of (b) **NC1-NC4** and (c) **NC2**, **NC3** and **NC7** in water. (d) Comparison of fluorescence spectra of **B6** in acetonitrile and **NC6** in water. [**NC1-NC4**], 16 µg/mL; [**NC7** and **Au NP**], 12 µg/mL; [**B6**], 16 µM and [**NC6**], 16.6 µg/mL.

3.2.7. Fluorescence Lifetimes.

The fluorescence lifetime of **NC6** and **NC7** were measured by time-correlated single-photon measurements. The lifetime decay for **NC6** in water was observed to bi-exponential with lifetimes of 0.64 ± 0.006 ns (65%) and 2.52 ± 0.01 ns (35%) whereas **ONP6** in water exhibited lifetimes of 0.69 ± 0.008 ns (69%) and 1.89 ± 0.01 ns (31%) (Table 3.5 and Figure 3.18a). However, the lifetime data for molecule **B6** was unreliable due to its low fluorescence intensity. Moreover, the fact that the average lifetime value for **NC6** ($\tau_{ave} = 1.92 \pm 0.01$ ns) was higher than those for **ONP6** ($\tau_{ave} = 1.56 \pm 0.01$ ns) suggested that **NC6** had lesser non-radiative transitions. The lifetime value also suggested that fluorescence in **NC6** in water was caused by efficient plasmon-molecule coupling.

Table 3.5. A comparison of lifetime measurements of **ONP6** and **NC6** in water, BODIPYs **B2** and **B3** in acetonitrile, the organic nanoparticles **ONP2** and the nanocomposites **NC6** and **NC7** in water, and the aggregates of **B2** and **B3** in 90% water-acetonitrile mixture.

Sample	τ (ns)
ONP6	0.69 ± 0.008 ns (69%) and 1.89 ± 0.01 ns (31%)
NC6	0.64 ± 0.006 ns (65%) and 2.52 ± 0.01 ns (35%)
B2	5.85 ± 0.02 ns
B3	1.63 ± 0.01 ns
ONP2	6.42 ± 0.01 ns
NC7	0.21 ± 0.01 ns (14%), 5.12 ± 0.11 ns (69%), and 12.88 ± 0.41 ns (17%)
Aggregates of **B2** and **B3**	6.37 ± 0.01 ns

To understand the origin of fluorescence in multi-chromophoric **NC7**, we compared the fluorescence lifetimes of individual systems, such as the BODIPY molecules **B2** and **B3** in acetonitrile, as well as their organic nanoparticles (**ONP2** and **ONP3**) and nanocomposites (**NC2** and **NC3**) in water with **NC7**. **B2** and **B3** in acetonitrile manifested mono-exponential lifetimes of 5.85 ± 0.02 ns and 1.63 ± 0.01 ns, respectively, as discussed earlier. Likewise, the organic nanoparticles of **B2**, i.e., **ONP2**, exhibited a mono-exponential decay with a lifetime of 6.42 ± 0.01 ns (Table 3.5 and Figure 3.18c). However, the data obtained for organic nanoparticles of **B3**, i.e., **ONP3**, and the nanocomposites **NC2** and **NC3**, were unreliable because the emission of these systems was substantially quenched. Next, we observed a tri-exponential decay for the multi-chromophoric **NC7** with fluorescence lifetimes of 0.21 ± 0.01 ns (14%), 5.12 ± 0.11 ns (69%), and 12.88 ± 0.41 ns (17%) (Table 3.5 and Figure 3.18b). Surprisingly, the lifetime of the major component of **NC7** (5.12 ± 0.11 ns, 69%) was similar to that of **B2** and **ONP2**, implying that the incorporation of **B2** could have caused the emission of **NC7**. Further, FRET between the aggregates of **B2** and **B3** was proposed in the case of **NC7**, where gold nanoparticles served as a supporting matrix to facilitate the FRET process. Furthermore, the fluorescence lifetimes for the mixed aggregates of **B2** and **B3** (6.37 ± 0.01 ns) and **ONP2** (6.42 ± 0.01 ns) were comparable with the major component of **NC7** (5.12 ± 0.11 ns, 69%) thereby confirming the FRET process in **NC7** (Table 3.5).
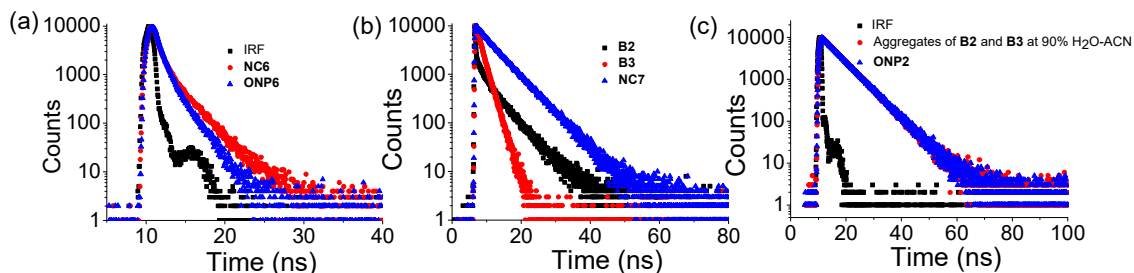
Figure 3.18. Fluorescence lifetime decay profiles of (a) **NC6** (16.6 µg/mL) and **ONP6** (12.2 µg/mL) in water, (b) **B2** (17 µM) and **B3** (12 µM) in acetonitrile, and **NC7** (12 µg/mL) in water and (c) aggregates of **B2** and **B3** in 90% water-acetonitrile mixture, and **ONP2** (8.6 µg/mL) in water. Excitation wavelength, 440 nm.

3.2.8. Environment-Sensitive Photophysical Properties of NC6.

The photophysical properties of **NC6** were observed to be environment-sensitive due to the donor-acceptor nature of the compound **B6**. The absorption and emission spectra of **NC6** were recorded in glycine buffer with pH ranging from 2 to 12. The absorption spectra of **NC6** showed minor changes at different pH, but the emission maximum showed a significant blue shift of 19 nm at pH 2 (Figure 3.19). It is assumed that at pH 2, the N,N-diethylamino group was protonated, which inhibited the intramolecular charge transfer process in **B6**, and resulted in a blue-shifted emission maximum from the locally excited state. The pH-dependent changes in the emission were also visible to the naked eye, wherein a green colour was observed in the case of pH 2, whereas the colour was orange at other pH (Figure 3.20).
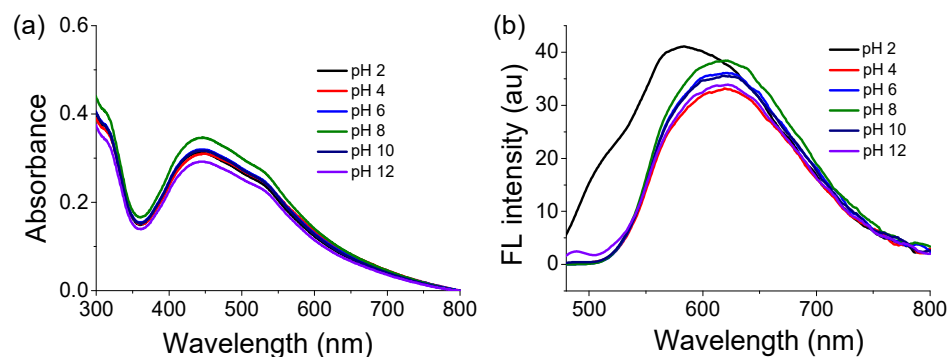

Figure 3.19. UV-Vis absorption and (d) fluorescence spectra of **NC6** (16.6 µg/mL) in glycine buffer (10 mM) at various pH. Excitation wavelength, 450 nm.
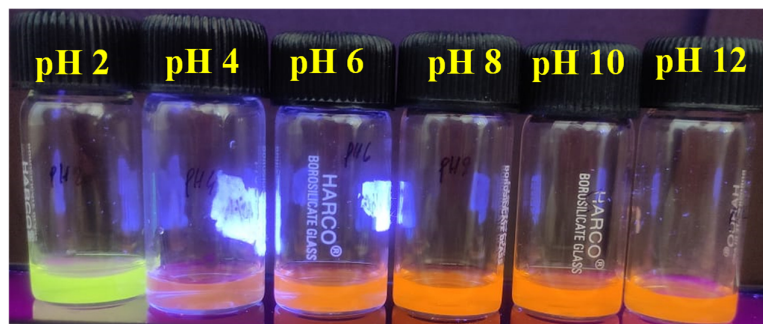
Figure 3.20. Photographs of **NC6** (16.6 μg/mL) at pH 2 to 12 after illuminating with a UV lamp.

3.2.9. Photostability.

After studying the photophysical properties of the nanocomposites, we were interested in exploring their potential application as a photosensitizer for PDT. At the outset, we verified the photostability of various systems by irradiating their aerated solutions. The photostability of the dye molecules, organic nanoparticles and nanocomposites was evaluated by monitoring the changes in the absorption spectra of their solution after irradiation under a Xenon arc lamp for 10 minutes. First, we investigated the photostability of the dye molecules **B1-B6** in acetonitrile. The absorbance of **B3** and **B6** remained unchanged after irradiation, demonstrating their excellent photostability. Under similar conditions, however, the absorbance of **B1**, **B2**, **B4** and **B5** decreased significantly, indicating photobleaching (Figure 3.21 and Table 3.6). We also investigated the photostability of the organic nanoparticles **ONP1-ONP6** in an aqueous solution under the same conditions. We noticed significant changes in the absorbance of **ONP1-ONP3**, **ONP5** and **ONP6**, indicating that the systems undergo photobleaching. **ONP4**, on the other hand, showed no changes in the absorption spectrum after photoirradiation, demonstrating its excellent photostability (Figure 3.22 and Table 3.6).
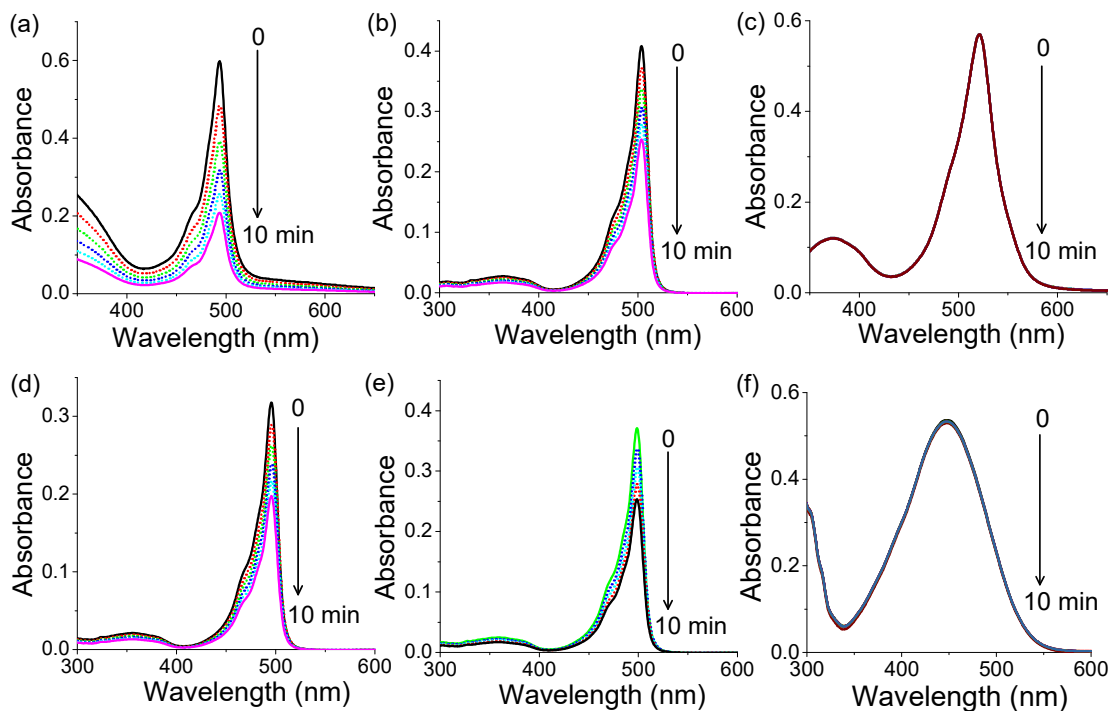
Figure 3.21. Changes in the UV-Vis absorption spectrum of (a-f) **B1-B6** (11, 17, 12, 18, 12 and 20 µM, respectively) in acetonitrile upon irradiation using a Xenon arc lamp.
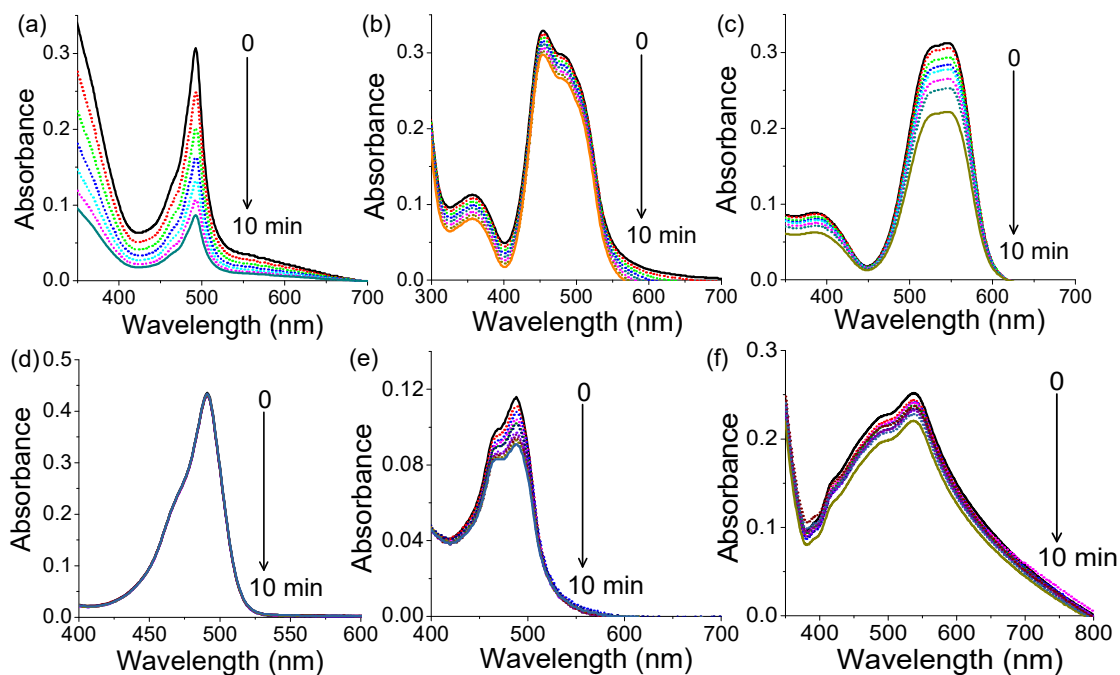

Figure 3.22. Changes in the UV-Vis absorption spectrum of (a-f) **ONP1-ONP6** (9.3, 8.6, 9.2, 19, 12, and 12.2 µg/mL, respectively) in water upon irradiation using a Xenon arc lamp.

Table 3.6. Photostability and photosensitization properties of **B1-B6** in acetonitrile, **ONP1-ONP6** and **NC1-NC4**, **NC6** and **NC7** in water.

System	Photostability	Φ_Δ
B1	No	*n.d.*
B2	No	*n.d.*
B3	Yes	0.62[44]
B4	No	*n.d.*
B5	No	*n.d.*
B6	Yes	*n.d.*
ONP1	No	*n.d.*
ONP2	No	*n.d.*
ONP3	No	*n.d.*
ONP4	Yes	0.28
ONP5	No	*n.d.*
ONP6	No	*n.d.*
Au NP	Yes	0.027[31]
NC1	Yes	0.46
NC2	Yes	0.12
NC3	Yes	0.42
NC4	No	*n.d.*
NC6 at pH 7.4	Yes	0.25
NC6 at pH 10	Yes	0.31
NC7	Yes	0.68

n.d., Not determined due to low or quenched emission nature of materials.

Next, we were intrigued to investigate the photostability of the gold nanoparticles (**Au NP**) and the nanocomposites **NC1-NC4** and **NC6-NC7** in an aqueous solvent under similar conditions. The nanocomposites **NC1-NC3** and **NC7** did not exhibit changes their absorption spectra when exposed to light, confirming their photostability. However, photoirradiation caused a significant increase in the absorption maxima at 498 nm for **NC4**. It is assumed that the bulky phenyl group in the *meso*-position of **B4** caused the photobleaching for **NC4**. Furthermore, when exposed to light, **Au NP** demonstrated excellent photostability (Figure 3.23 and Table 3.6).

Because of its environment sensitive fluorescence properties, we studied the photostability of **NC6** in glycine buffer at pH 2, 4, 6, 7.4, and 10. The absorption maximum of **NC6** was observed to be negligibly affected by irradiation at pH 7.4 and 10, demonstrating the excellent photostability of **NC6** under these conditions. However, the absorbance of **NC6** was found to decrease at pH 2, 4, and 6, indicating photobleaching (Figure 3.24 and Table 3.6). Furthermore, for imaging application, it is desired that **NC6** remain stable in the pH range up to pH 4. So, we tested the stability of **NC6** in the dark for 10 minutes at pH 4 and 7.4. The absorption maximum remained unchanged at pH 4 and 7.4 under these conditions, demonstrating its excellent stability (Figure 3.25).
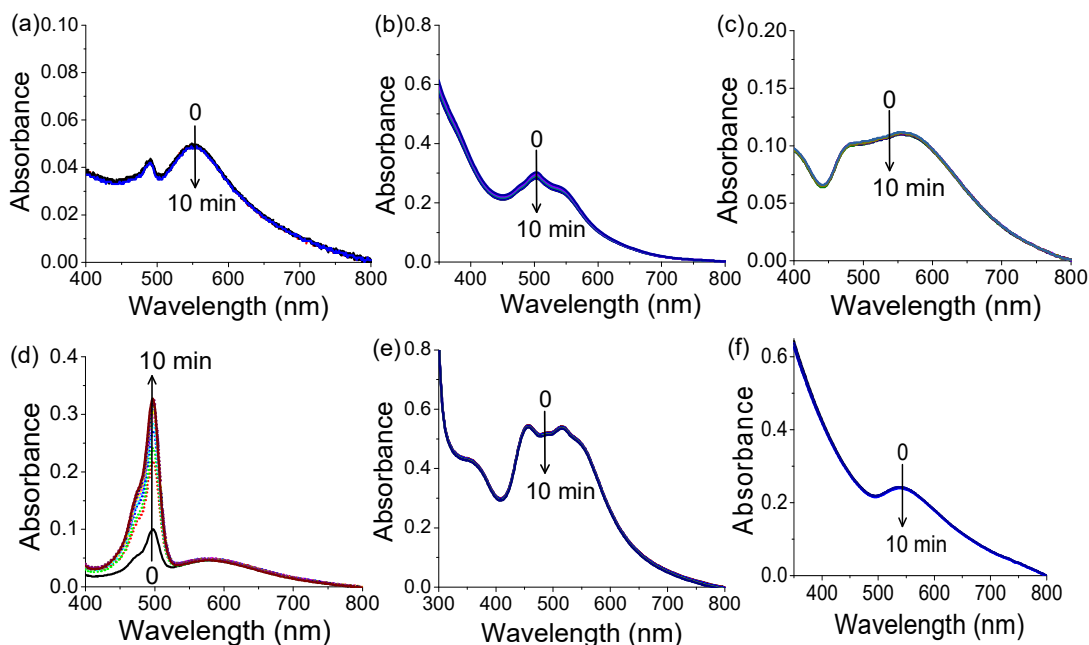

Figure 3.23. Changes in UV-Vis absorption spectrum of (a-d) **NC1-NC4**, (e) **NC7** and (f) **Au NP** in water upon irradiation using a Xenon arc lamp. [**NC1-NC4**], 16 µg/mL and [**NC7** and **Au NP**], 12 µg/mL.
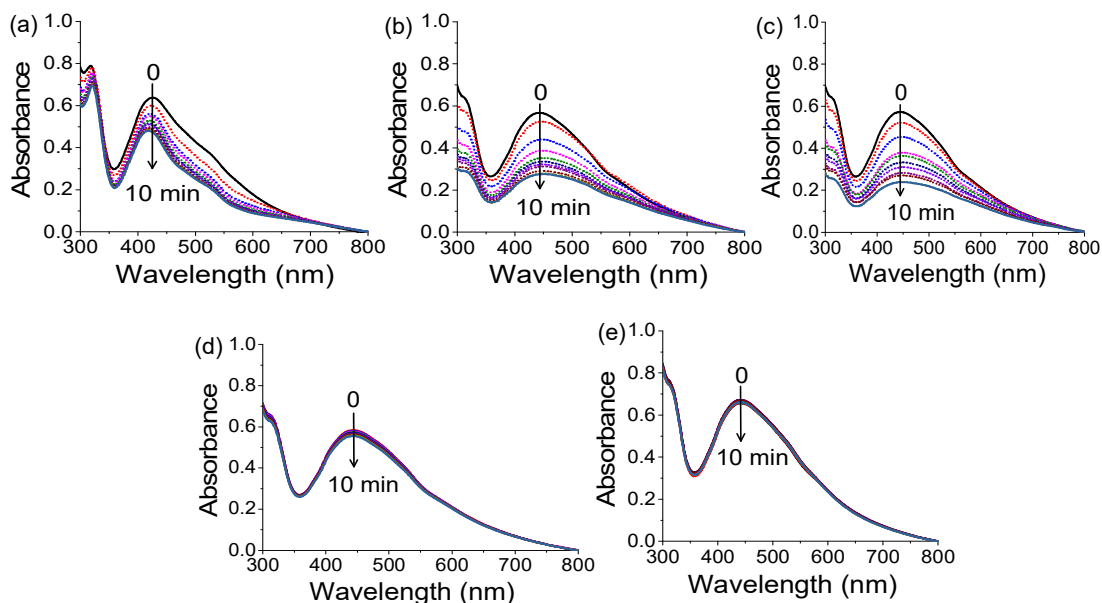
Figure 3.24. Changes in the UV-Vis absorption spectra of **NC6** (16.6 μg/mL) in glycine buffer (10 mM) at pH (a) 2, (b) 4, (c) 6, (d) 7.4 and (e) 10 upon irradiation using a Xenon arc lamp.
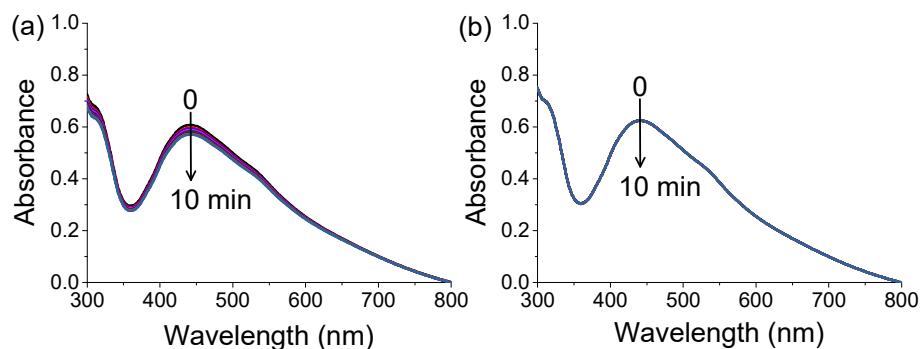

Figure 3.25. Changes in the UV-Vis absorption spectra of **NC6** (16.6 μg/mL) in 10 mM glycine buffer at pH (a) 4 and (b) 7.4 in the dark.

3.2.10. Photosensitization.

After studying the photostability, we were curious to investigate the photosensitization properties of the nanocomposites. The photosensitization properties of the nanocomposites were investigated using 1,3-diphenylisobenzofuran (DPBF), which rapidly reacts with singlet oxygen ($^1O_2$) to form a peroxide that decomposes into 1,2-dibenzoylbenzene (DBB) (Figure 3.26).[45] As the product of this reaction is colourless, it can be monitored with absorption spectroscopy. Aqueous solutions of a mixture of DPBF and the nanocomposites **NC1-NC3** and **NC7** were photo-irradiated using a 450 W Xenon lamp and

the changes in the UV-Vis absorption spectrum were recorded at regular intervals. We observed a decrease in absorbance at 420 nm after irradiation, indicating photooxidation of DPBF (Figure 3.27 and Figure 3.28). The reaction rate differed for each nanocomposite and served as a parameter to assess the efficiency of $^1O_2$ generation. The quantum yield for $^1O_2$ generation (Φ_Δ) was also calculated using methylene blue (**MB**) as a reference standard, and the results are shown in Table 3.6. It is worth noting that the $^1O_2$ quantum yields of **NC1** and **NC3** were relatively high (0.46 and 0.42, respectively) and comparable to that of methylene blue ($\Phi_\Delta = 0.52$)[46] (inset of Figure 3.27). Under similar conditions, **Au NP** was also capable of producing $^1O_2$, but the quantum yield of $^1O_2$ was significantly lower ($\Phi_\Delta = 0.027$).[31] However, the multi-chromophoric nanocomposite **NC7** exhibited the highest $^1O_2$ quantum yield of $\Phi_\Delta = 0.68$ (inset of Figure 3.28 and Table 3.6), whereas the individual nanocomposites **NC2** and **NC3** showed Φ_Δ values of 0.12 and 0.42, respectively. Thus, it can be concluded that incorporation of BODIPY molecules **B1-B3** in gold nanoparticles increases the photostability of the nanocomposites and produces a significant amount of $^1O_2$ as compared to their individual components. It is also important to note that the $^1O_2$ quantum yield was dependent on the chemical structure of the dye molecule. Next, we investigated the photosensitization properties of **NC6** using a 350 W Xenon lamp with a 475 nm cut-off filter in glycine buffer at pH 7.4 and 10. The $^1O_2$ quantum yield of **NC6** was found to be 0.25 and 0.31 at pH 7.4 and 10, respectively, using **MB** as a standard (Figures 3.29a-c, and Table 3.6). It is important to note that under similar conditions in acetonitrile, molecule **B6** was unable to generate $^1O_2$ (Figure 3.29d), and the quantum yield of **Au NP** in $^1O_2$ was found to be very low ($\Phi_\Delta = 0.027$) (Table 3.6). A comparison of the $^1O_2$ generation capability of **B6**, **NC6**, and **Au NP** highlights the importance of plasmon-molecule interactions in modulating the photosensitization property.
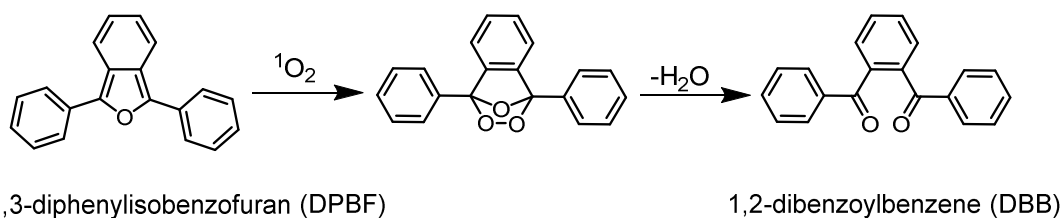

1,3-diphenylisobenzofuran (DPBF)   1,2-dibenzoylbenzene (DBB)

Figure 3.26. Reaction of $^1O_2$ with DPBF.

To confirm the photosensitised generation of $^1O_2$ by the nanocomposites, we carried out control experiments in the absence of light and oxygen under similar conditions. We did

not notice any significant decrease in the absorbance of DPBF at 420 nm under either condition, thereby demonstrating the generation of $^1O_2$ only in the presence of both light and oxygen. Furthermore, we observed negligible changes in the absorbance of DPBF at 420 when irradiated in the presence of sodium azide – a known singlet oxygen quencher,[47] confirming the presence of $^1O_2$ (Figure 3.30). Further, the $^1O_2$ generation of nanocomposites **NC2**, **NC3** and **NC7** was confirmed by NIR luminescence measurement. We observed a luminescence peak at 1280 nm upon irradiation in the presence of **NC2**, **NC3** and **NC7**, confirming $^1O_2$ generation. It is worth noting that the highest peak intensity was observed for **NC7**, followed by **NC3** and **NC2**, which is in line with the $^1O_2$ quantum yield of these for nanocomposites (Figure 3.31).
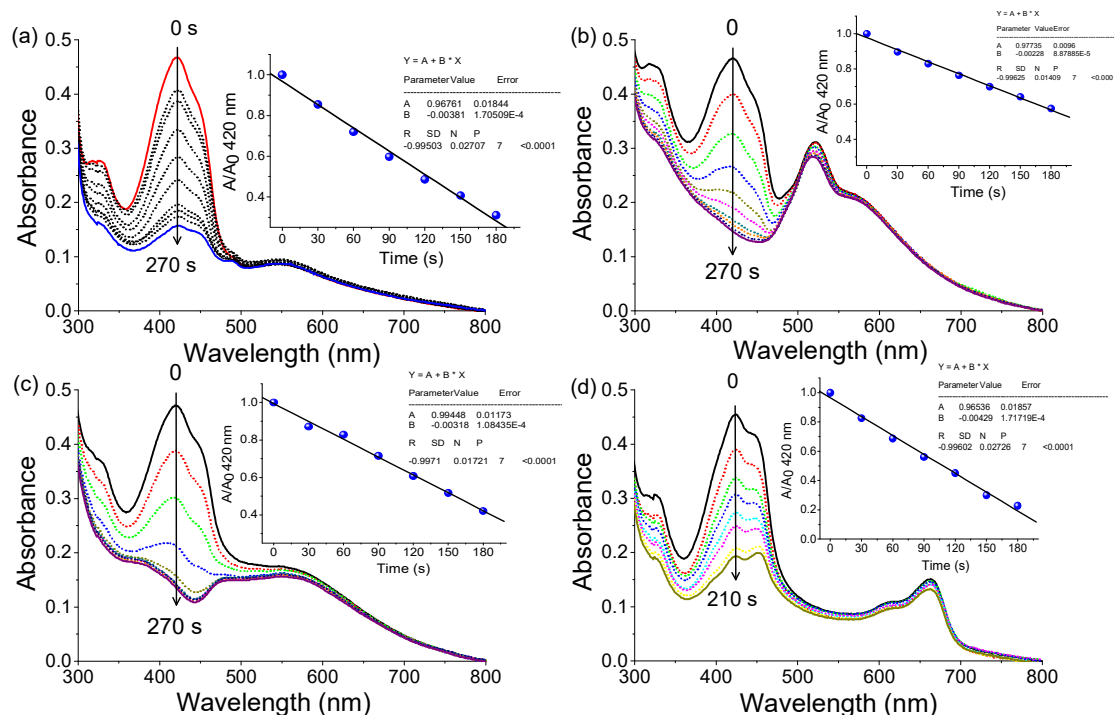

Figure 3.27. Changes in the UV-Vis absorption spectrum of a solution of 1,3-diphenylisobenzofuran (DPBF, 65 μM) and (a-c) **NC1-NC3** (16 μg/mL) and (d) **MB** (16 μg/mL) in 5 % ethanol-water mixture. Insets show the respective curve fitting data for the decrease in the absorbance of DPBF at 420 nm.

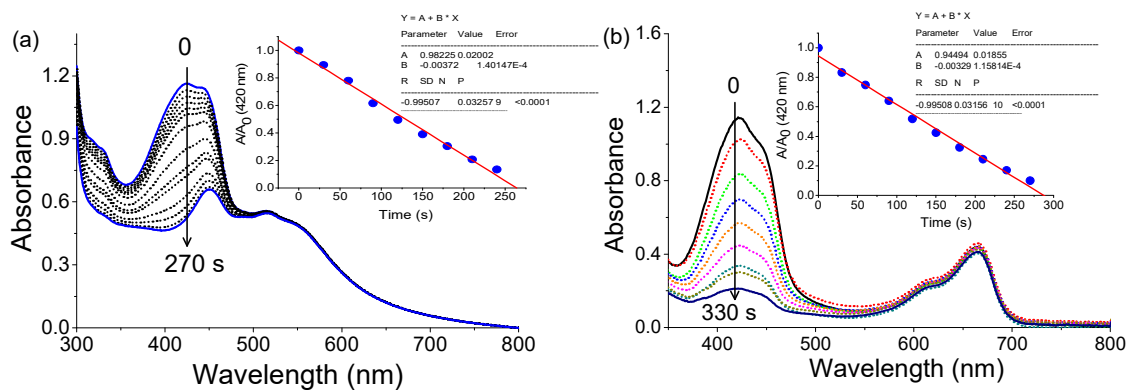**Figure 3.28.** Changes in the UV-Vis absorption spectrum of a mixture of 1,3-diphenylisobenzofuran (DPBF, 96 μM) and (a) **NC7** (12 μg/mL) and (b) **MB** (12 μM) upon irradiation in 20% ethanol-water mixture. Insets show the respective curve fitting data for the decrease in the absorbance of DPBF at 420 nm.
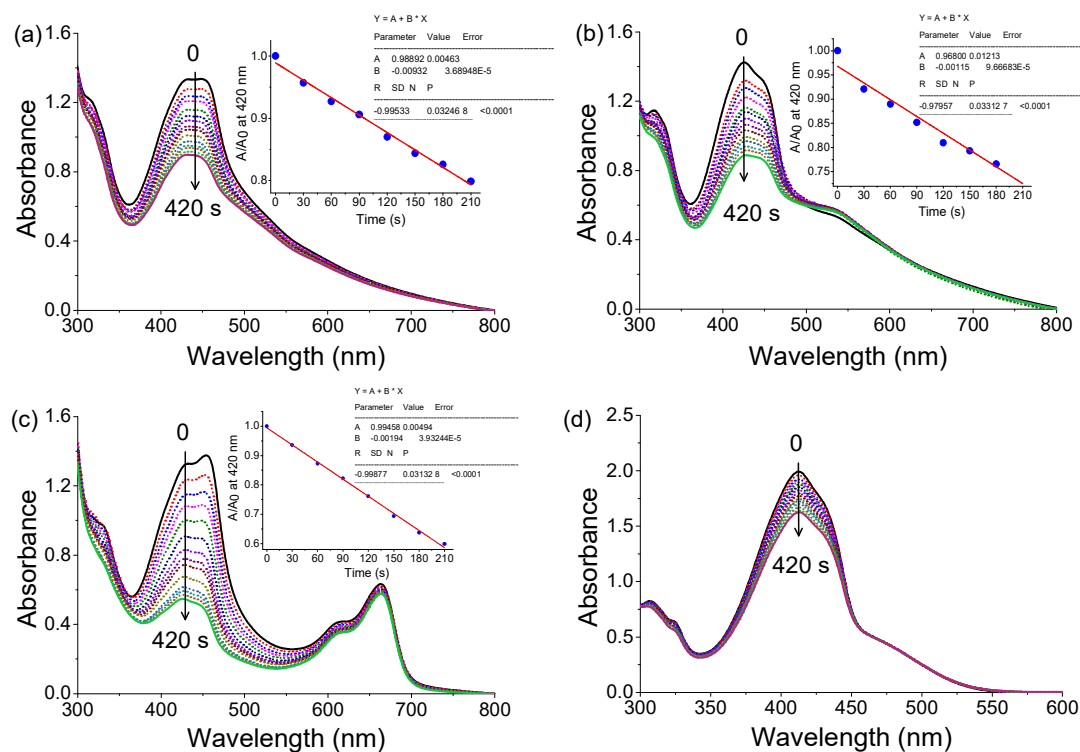

Figure 3.29. Changes in the UV-Vis absorption spectrum of a mixture of 1,3-diphenylisobenzofuran (DPBF, 96 μM) and **NC6** (16.6 μg/mL) upon irradiation in 5% ethanol-glycine buffer (10 mM) at pH (a) 7.4 and (b) 10, (c) **MB** (21 μM) at pH 10 and (d) **B6** (65 μM) in 5% ethanol-acetonitrile. Insets show the respective curve fitting data for the decrease in the absorbance of DPBF at 420 nm.
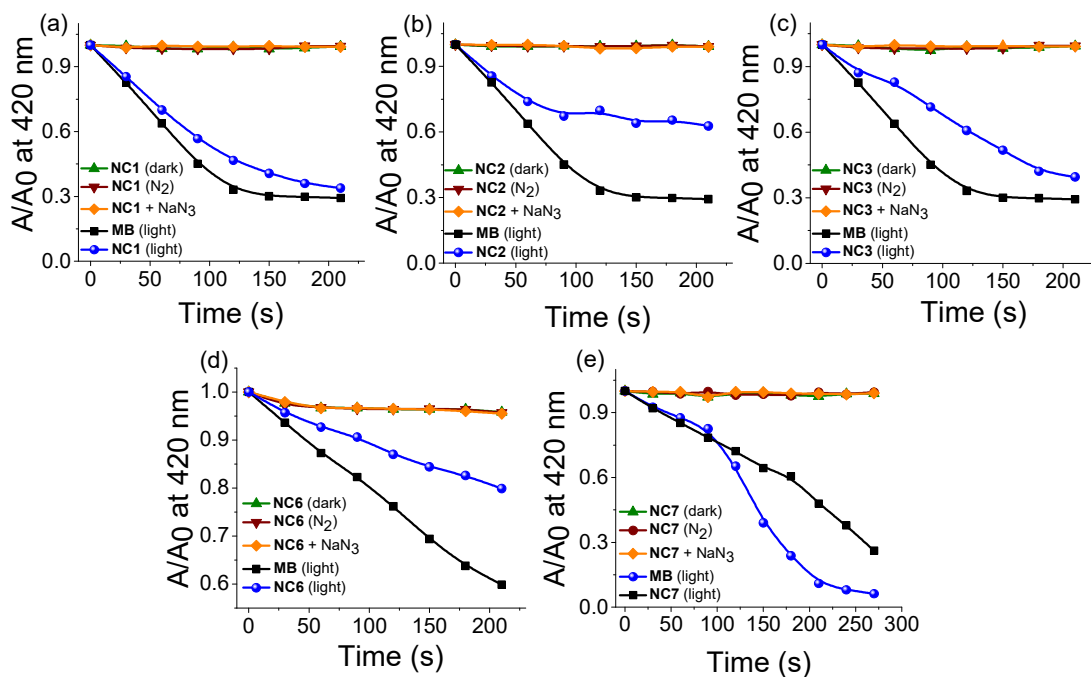
Figure 3.30. The relative changes in absorbance at 420 nm of a solution of DPBF in the presence of methylene blue (**MB**) or the nanocomposites (a-c) **NC1-NC3** in 5% ethanol-water mixture, (d) **NC6** in 5% ethanol-glycine buffer (10 mM) at pH 7.4 and (e) the multi-chromophoric nanocomposite **NC7** in 20 % ethanol-water mixture, respectively under different experimental conditions.
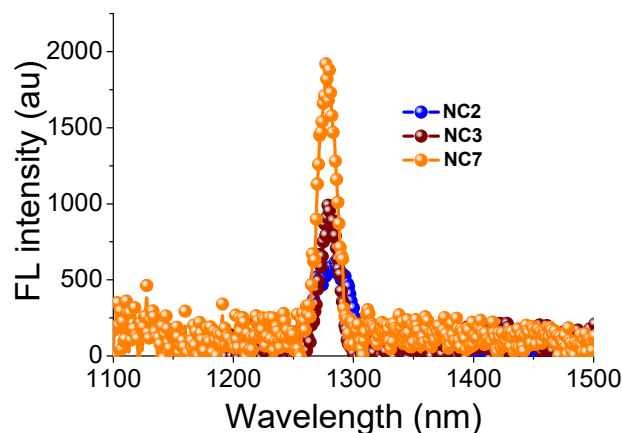

Figure 3.31. Luminescence spectra of **NC2**, **NC3** and **NC7** in water. Excitation wavelength, 377 nm. [**NC2**, **NC3** and **NC7**], 12 μg/mL.

3.3.   Discussion.

We investigated the photophysical properties of a few nanocomposites containing dye molecules and gold nanoparticles. The changes in absorption and emission maxima in acetonitrile-water mixtures is attributed to molecular aggregation of the dye molecules. The

minor shift in the absorption and emission maxima indicates a random aggregation of the BODIPYs **B1** and **B2** whereas a systematic decrease in the absorption and emission maxima of **B5** revealed a controlled aggregation of **B5** (Figures 3.4 and 3.6). The blue shift in absorption maxima and fluorescence quenching, on the other hand, demonstrated the formation of *H*-aggregates for **B3** (Figure 3.5).[48,49] However, one striking finding from the self-assembly experiments was the difference in the spectral features of aggregates containing both **B2** and **B3** as compared to individual aggregates of **B2** and **B3**. In the case of dilute solutions (micromolar concentrations), we observed blue shifts in the absorption maxima, and the spectrum of a mixture of **B2** and **B3** in a 90% water-acetonitrile mixture was reasonably sharp, with a maximum at 500 nm and a bump at 463 nm that may be attributed to the individual aggregates. On the other hand, the absorption spectrum of a concentrated solution (millimolar concentrations) of a 1:1 mixture of **B2** and **B3** in 100% water was broad, with an absorption maximum at 508 nm with a shoulder at 457 nm (Figure 3.32). The difference in the spectral features of a mixture of **B2** and **B3** at different concentrations could be attributed to an environment-dependent self-assembly process. It is assumed that the mixture of **B2** and **B3** formed small, regular aggregates in dilute conditions in 90% water-acetonitrile mixture. In contrast, large, irregular aggregates were formed at higher concentrations in 100% water. DLS measurements also supported the formation of irregular aggregates in 100% water for the mixture of **B2** and **B3** (Figure 3.33). Furthermore, the naphthalidenimine-boron complex **B6** exhibited a red shift in absorption maxima and a sudden increase in emission intensity after 50% water content, indicating aggregation-induced emission (Figure 3.12).
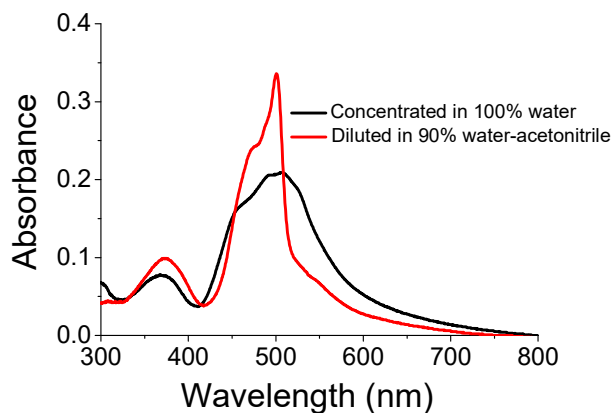

Figure 3.32. UV-Vis absorption spectra of concentrated (millimolar concentration) and dilute solutions (micromolar concentration) of a mixture of **B2** and **B3** in 100% water and 90% water-acetonitrile, respectively.
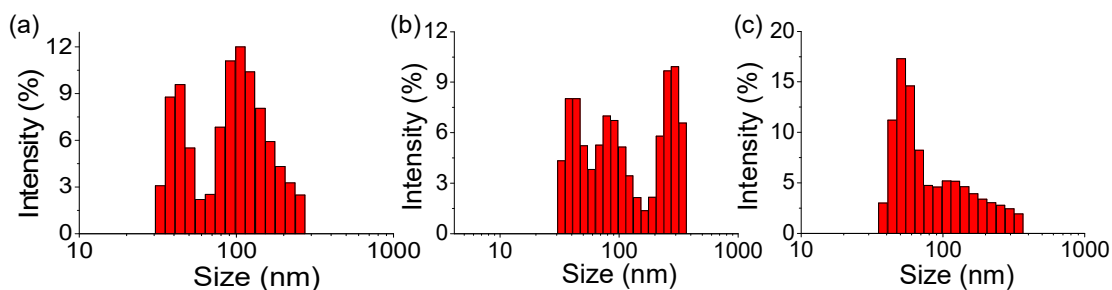
Figure 3.33. Particle size analysis by dynamic light scattering of three different batches of the mixture of **B2** and **B3** in 100% water. The observed average particle sizes were 200 ± 1, 290 ± 1, and 324 ± 1 nm for (a-c), respectively.

It is hypothesized that the increase in the fluorescence intensity in the mixture of aggregates of **B2** and **B3** resulted in a FRET process from the aggregates of **B3** to the aggregates of **B2**, as demonstrated by the emission at 507 nm with a lifetime of 6.37 ± 0.01 ns for a mixture of aggregates of **B2** and **B3** in the 90% water-acetonitrile mixture. This lifetime matched well with the lifetime of **ONP2** of 6.42 ± 0.01 ns (Table 3.5), validating the FRET from aggregates of **B3** to aggregates of **B2**. Significant overlap between the emission spectrum of **B3** aggregates and the absorption spectrum of **B2** aggregates (Figure 3.9) further confirmed the feasibility of the FRET process. Similarly, the existence of energy transfer between the aggregates of **B3** and **B2** was also observed in the transient absorption spectroscopy experiments (Figures 3.10 and 3.11). Notably, the FRET process is favoured only in the aggregated state because of the complementarity between the emission and absorption spectra of the aggregates, thereby signifying the importance of molecular aggregation for the FRET process.

The photophysical properties of organic nanoparticles (**ONPs**) in water showed a blue shift, broadening in the absorption spectra and significantly quenched the fluorescence. However, **ONP6** showed a red shift in absorption maximum and a blue shift in emission maximum with a substantial enhancement in emission. The changes in the absorption and emission spectra of **ONPs** substantiate the importance of the chemical structure of dye molecules for their different aggregation behaviour in water. The optical properties of the nanocomposites were significantly different when compared from those of the chromophores, organic nanoparticles and pristine gold nanoparticles. The spectral features of the nanocomposites were consistent with the hybridized signature of molecular and plasmonic absorptions. For example, **NC1** showed absorption maxima at 500 and 550 nm whereas **B1** and **Au NP** had absorption maxima at 495 and 530 nm. As a result, a red shift in the

absorption maxima of the molecular and plasmonic peaks was observed for **NC1**. Similar differences were observed in the absorption spectra of **NC2-NC4** when compared to their constituents. On the other hand, **NC6** showed a blue shift in the molecular and plasmonic peak maxima as compared to the individual components (Figure 3.34). These results indicate a strong interaction between the dye molecules and gold in the nanocomposites. Furthermore, **NC7** exhibited a broad spectrum from 400 to 800 nm. Surprisingly, the absorption spectrum of **NC7** showed significant differences from the additive spectrum of the individual components, i.e., **ONP2**, **ONP3**, and **Au NP**, indicating strong interactions between the individual components while incorporated in **NC7** (Figure 3.35).
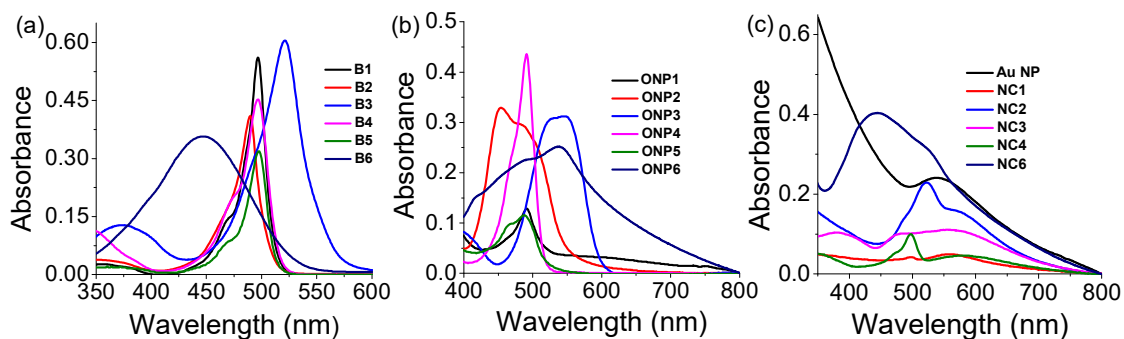

Figure 3.34. A comparison of the UV-Vis absorption spectra of (a) dye molecules **B1-B6**, (b) organic nanoparticles **ONP1-ONP6**, (c) the gold nanoparticles (**Au NP**) and nanocomposites (**NC1-NC4** and **NC6**).
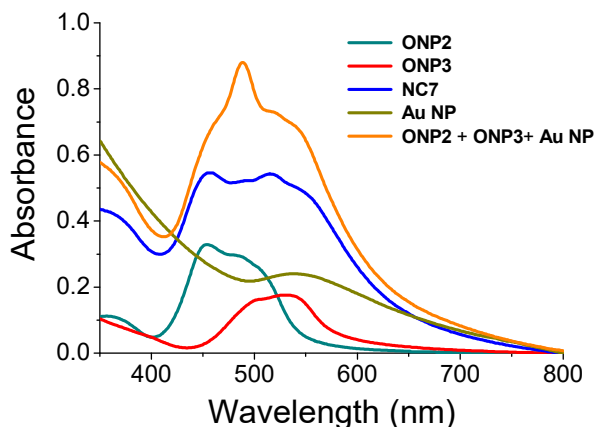

Figure 3.35. A comparison of the UV-Vis absorption spectrum of **NC7** with the individual components **ONP2**, **ONP3**, and **Au NP**, and the additive spectra of **ONP2**, **ONP3**, and **Au NP** in water.

Plasmon-molecule coupling between the dye molecules and gold nanoparticles resulted in the quenching fluorescence of the dye molecule for **NC1-NC3**, whereas **NC6** and

NC7 were found to be fluorescent. Further, an overlap in the absorption of **B6** with gold nanoparticles was minimal, but there was a significant overlap between the fluorescence of **B6** and the absorption of gold nanoparticles resulting in plasmon-enhanced luminescence in the case of **NC6**. In the case of the multi-chromophoric nanocomposite **NC7**, it is inferred that the mixed aggregates of compounds **B2** and **B3** are formed on the surface of gold nanoparticles, thereby facilitating a FRET from the aggregates of **B3** to the aggregates of **B2**.

The photostability and photosensitization properties of nanocomposites were also dependent on the chemical composition of the dye molecules. The sterically bulky BODIPY **B4** induced photo instability to the nanocomposite **NC4**. We noticed that photostable nanocomposites could generate $^1O_2$ in the presence of oxygen and light. The quantum yield of $^1O_2$ in nanocomposites was significantly higher than their individual components, with the multi-chromophoric nanocomposite **NC7** having the highest value of $\Phi_\Delta = 0.68$.

3.4.   Conclusions.

We studied the photophysical properties of dye molecule **B1-B6**, their aggregates, the organic nanoparticles **ONP1-ONP6** and the nanocomposites **NC1-NC7**. BODIPY molecules **B1-B5** exhibited sharp absorption and emission maxima while the naphthalidenimine-boron complex **B6** showed a charge transfer phenomenon from the donor (diethyl)amino group to the acceptor boryl moiety. Aggregation studies in acetonitrile-water mixture revealed changes in absorption and emission maxima for **B1-B3** and **B5**. In tune with the literature reports, **B1, B2**, **B3** and **B5** formed molecular aggregates in aqueous media, and the spectroscopic characteristics indicated that *H*-type aggregates were formed as evidenced by the blue shift in the absorption maxima and quenching in fluorescence. However, a mixture of **B2** and **B3** exhibited blue-shifted absorption maxima while the fluorescence intensity increased as the water content increased from 0 to 90%. It was further confirmed that an increase in fluorescence intensity in the case of the mixed aggregates of **B2** and **B3** was caused by Förster resonance energy transfer (FRET) from aggregates of **B3** to **B2**. A similar type of FRET was proposed for the multi-chromophoric nanocomposite **NC7** on the surface of gold nanoparticles between the aggregates of **B2** and **B3**, thereby making the nanocomposite fluorescent. On the other hand, the naphthalidenimine-boron complex **B6** showed aggregation-induced emission when the water content was increased from 0 to 90%.

The formation of organic nanoparticles (**ONPs**) in water mainly showed a broadening and blue shift in absorption maxima while quenching of fluorescence was observed for BODIPY molecules **B1-B5**. However, a significant red shift in absorption maxima and

enhancement in emission intensity with a blue shifted maximum was noticed for **B6** upon organic nanoparticle formation, resulting in an aggregation-induced emission.

The formation of the nanocomposites caused significant changes in the photophysical properties of its constituents: bathochromic shifts in the absorption maxima of the dye molecules and gold nanoparticles were observed, while the fluorescence of the dye molecules was quenched for all the nanocomposites except **NC6** and **NC7**. Further, the plasmon-enhanced luminescence was observed in the case of **NC6** where the overlap of the absorption of **B6** with gold nanoparticles was minimal. Thus, our findings highlight the importance of spectral overlap between the dye molecule and gold nanoparticles on plasmon-molecule coupling.

We also studied the photostability and photosensitization properties of **B1-B6**, **ONP1-ONP6** and **NC1-NC7**. The chemical composition of the dye molecules significantly affects the photostability and photosensitization of the nanocomposites. **NC4** was observed to unstable upon irradiation while **NC6** exhibited pH depended photostability and photosensitization properties. The $^1O_2$ quantum yield was observed to depend on the chemical composition of the dye molecules, and multi-chromophoric nanocomposite **NC7** was the most efficient photosensitizer.

3.5.   Experimental Section.
3.5.1. General Techniques.

All experiments were conducted at room temperature (25 ± 1 °C) unless otherwise mentioned. The particles were dispersed in Milli Q water before analysis. Absorption spectra were recorded on a Shimadzu UV-2600 UV-vis spectrophotometer in 3 mL quartz cuvettes having a path length of 1 cm. Fluorescence spectra were recorded on a Fluorolog 3-221 fluorimeter equipped with a 450 W Xenon lamp. The fluorescence quantum yields were determined by using optically matched solutions. Rhodamine 6G ($\Phi_f = 0.95$) in ethanol was used as the standard. The fluorescence quantum yields were calculated using equation 3.1,

$$\Phi_f(sample) = \Phi_f(ref) \times \frac{I\,(sample) \times OD\,(ref) \times n^2(sample)}{I\,(ref) \times OD\,(sample) \times n^2(ref)} \qquad (3.1)$$

where I is the integrated intensity, OD is the optical density at the excitation wavelength, n is the refractive index of the solvent, ref. stands for the reference standard. Fluorescence lifetimes were measured on a Fluorolog TCSPC Horiba FL-1057. The fluorescence decay profiles were deconvoluted using IBH data station software V2.1 and minimizing the χ^2 values of the fit to 1 ± 0.1. Photostability and photosensitization experiments were carried out

using a 450 W of 350 W Xenon arc lamp (Oriel instruments) with a 475 nm cut-off filter (Newport Corporation). The changes in absorption spectra after irradiation were recorded on a Shimadzu UV-Vis spectrophotometer in 3 mL quartz cuvettes having a path length of 1 cm.

3.5.2. Femtosecond transient absorption spectroscopy.[50]

We used a Ti: sapphire amplifier system (Astrella, Coherent, 800 nm, 3mJ/pulse energy, ~ 35 fs pulse width, and 1 kHz repetition rate) and Helios Fire pump-probe spectrometer for the ultrafast measurements. The output laser beam was cleaved into the pump (95% of the output) and probe (remaining 5%) beams using two different beam splitters. The required pump wavelength was obtained using Optical Parametric Amplifier (OPerA-SOLO) for the photo-excitation of the sample. A perfect pump-probe delay was maintained by placing a delay stage in the probe beam path. Monochromatic probe light passes through a sapphire crystal generating visible probe pulses. The probe beam passes through sample dispersion and falls upon fiber-coupled CMOS detectors connected with the computer system. The chirping and fitting of the collected TA data was done in surface explorer software.

3.5.3. Aggregation studies in acetonitrile-water mixture.

A stock solution of the dye molecules **B1**-**B3**, **B5** and **B6** in acetonitrile was prepared. Diluted solutions for measurement were then prepared from the stock solution in the cuvette using acetonitrile-water mixtures. The acetonitrile-water fraction was kept constant for all the molecules.

3.5.4. Investigation of pH-responsive property of the nanocomposite NC6.

Glycine buffer (10 mM) in 40 mL was prepared by following a standard method. Stock solutions of **NC6** (16.6 µg/mL) were prepared by varying the pH from 2 to 12 before use. The changes in UV-vis and emission spectra were recorded at different pH in glycine buffer.

3.5.5. Photostability of the various systems under different conditions.

A solution of the dye molecules in acetonitrile were irradiated using a 450 W or 350 W Xenon lamp with a 475 nm cut-off filter. The change in absorption was monitored over 10 minutes with a one-minute time interval. Further, an aqueous solution of the organic nanoparticles or the nanocomposites were irradiated under similar conditions and changes in

absorption spectra were changed recorded. Furthermore, the nanocomposite **NC6** was prepared in glycine buffer (10 mM) at pH 2, 4, 6, 7.4 and 10. The solution was irradiated using a 350 W Xenon lamp with a 475 nm cut-off filter. The change in UV-Vis absorbance of **NC6** was monitored at one-minute intervals over 10 minutes.

3.5.6. Investigation of $^1O_2$ generation of nanocomposites under different conditions.

The solutions of the nanocomposites and methylene blue in water were mixed with a solution of diphenylisobenzofuran (DPBF) in 5% ethanol-water or 20% ethanol-water in a 3 mL cuvette. The solution was irradiated using a 450 W Xenon lamp with a 475 nm cut-off filter. The decrease in absorbance of DPBF at 420 nm was monitored at intervals of 30 seconds. On the other hand, the nanocomposite **NC6** in glycine buffer (30 mM) of pH 7.4 or pH 10 was admixed with the solution of DPBF in 5% ethanol-glycine buffer (30 mM) at the same pH. Then, the change in absorption of DPBF at 420 nm was monitored in the presence of **NC6** after irradiation using a 350 W Xenon lamp with a 475 nm cut-off filter at intervals of 30 seconds.

3.5.7. Determination of $^1O_2$ quantum yield.

The quantum yield of singlet oxygen was estimated using a previously reported method[31] with methylene blue (MB, $\Phi_\Delta = 0.52$) as a reference standard and the following equation 3.2.

$$\Phi_\Delta \text{ (sample)} = \Phi_\Delta \text{ (ref)} \times \frac{m \text{ (sample)} \times F \text{ (ref)}}{m \text{ (ref)} \times F \text{ (sample)}} \qquad (3.2)$$

where m is the slope of the difference in the change in the absorbance of DPBF (at 420 nm) with irradiation time, and F is the absorption correction factor, which is given by $F = 1 - 10^{-OD}$.

3.6. References.

[1]   F. Karimi, S. Soleimanikahnoj, I. Knezevic, *Phys. Rev. B* **2021**, *103*, L161401.

[2]   C.-F. Wang, P. Z. El-Khoury, *J. Phys. Chem. Lett.* **2021**, *12*, 10761–10765.

[3]   W. Zhang, L. Zhang, F. Lu, D. Bai, T. Xue, C. Meng, M. Liu, D. Mao, F. Gao, T. Mei, *Nanoscale* **2020**, *12*, 7045–7050.

[4]   P. Chen, N. T. Tran, X. Wen, Q. Xiong, B. Liedberg, *ACS Sens.* **2017**, *2*, 235–242.

[5]   J.-F. Li, C.-Y. Li, R. F. Aroca, *Chem. Soc. Rev.* **2017**, *46*, 3962–3979.

[6]   A. B. Taylor, P. Zijlstra, *ACS Sensors* **2017**, *2*, 1103–1122.

[7]   T. Vo-Dinh, A. M. Fales, G. D. Griffin, C. G. Khoury, Y. Liu, H. Ngo, S. J. Norton, J. K. Register, H.-N. Wang, H. Yuan, *Nanoscale* **2013**, *5*, 10127–10140.

[8]   M. Shanthil, R. Thomas, R. S. Swathi, K. George Thomas, *J. Phys. Chem. Lett.* **2012**, *3*, 1459–1464.

[9]   E. Fort, S. Grésillon, *J. Phys. D: Appl. Phys.* **2007**, *41*, 013001.

[10] K. Aslan, I. Gryczynski, J. Malicka, E. Matveeva, J. R. Lakowicz, C. D. Geddes, *Curr. Opin. Biotechnol.* **2005**, *16*, 55–62.

[11] C. E. Talley, J. B. Jackson, C. Oubre, N. K. Grady, C. W. Hollars, S. M. Lane, T. R. Huser, P. Nordlander, N. J. Halas, *Nano Lett.* **2005**, *5*, 1569–1574.

[12] J. J. Mock, D. R. Smith, S. Schultz, *Nano Lett.* **2003**, *3*, 485–491.

[13] N. Nath, A. Chilkoti, *Anal. Chem.* **2002**, *74*, 504–509.

[14] Y.-H. Qiu, S.-J. Ding, F. Nan, Q. Wang, K. Chen, Z.-H. Hao, L. Zhou, X. Li, Q.-Q. Wang, *Nanoscale* **2019**, *11*, 22033–22041.

[15] A. J. Wilson, K. A. Willets, *Annual Rev. Anal. Chem.* **2016**, *9*, 27–43.

[16] M. C. di Gregorio, A. Ben Moshe, E. Tirosh, L. Galantini, G. Markovich, *J. Phys. Chem. C* **2015**, *119*, 17111–17116.

[17] Y.-F. Zhang, D.-J. Yang, J.-H. Wang, Y.-L. Wang, S.-J. Ding, L. Zhou, Z.-H. Hao, Q.-Q. Wang, *Nanoscale* **2015**, *7*, 8503–8509.

[18] H. Chen, T. Ming, L. Zhao, F. Wang, L.-D. Sun, J. Wang, C.-H. Yan, *Nano Today* **2010**, *5*, 494–505.

[19] S. Balci, B. Kucukoz, O. Balci, A. Karatay, C. Kocabas, G. Yaglioglu, *ACS Photonics* **2016**, *3*, 2010–2016.

[20] J. Guo, Y. Zhang, L. Shi, Y. Zhu, M. F. Mideksa, K. Hou, W. Zhao, D. Wang, M. Zhao, X. Zhang, J. Lv, J. Zhang, X. Wang, Z. Tang, *J. Am. Chem. Soc.* **2017**, *139*, 17964–17972.

[21] J. Jana, M. Ganguly, T. Pal, *RSC Adv.* **2016**, *6*, 86174–86211.

[22] F. Todisco, S. D'Agostino, M. Esposito, A. I. Fernández-Domínguez, M. De Giorgi, D. Ballarini, L. Dominici, I. Tarantini, M. Cuscuná, F. Della Sala, G. Gigli, D. Sanvitto, *ACS Nano* **2015**, *9*, 9691–9699.

[23] H. Chen, L. Shao, K. C. Woo, J. Wang, H.-Q. Lin, *J. Phys. Chem. C* **2012**, *116*, 14088–14095.

[24] K. L. Kelly, E. Coronado, L. L. Zhao, G. C. Schatz, *J. Phys. Chem. B* **2003**, *107*, 668–677.

[25] B. K. Juluri, M. Lu, Y. B. Zheng, T. J. Huang, L. Jensen, *J. Phys. Chem. C* **2009**, *113*, 18499–18503.

[26] J. F. Lovell, T. W. B. Liu, J. Chen, G. Zheng, *Chem. Rev.* **2010**, *110*, 2839–2857.

[27] M. R. Hamblin, T. Hasan, *Photochem. Photobiol. Sci.* **2004**, *3*, 436–450.

[28] A. Escudero, C. Carrillo-Carrión, M. C. Castillejos, E. Romero-Ben, C. Rosales-Barrios, N. Khiar, *Mater. Chem. Front.* **2021**, *5*, 3788–3812.

[29] M. Lan, S. Zhao, W. Liu, C.-S. Lee, W. Zhang, P. Wang, *Adv. Healthcare Mater.* **2019**, *8*, 1900132.

[30] X. J. Loh, *Mater. Horiz.* **2014**, *1*, 185–195.

[31] P. P. P. Kumar, P. Yadav, A. Shanavas, S. Thurakkal, J. Joseph, P. P. Neelakandan, *Chem. Commun.* **2019**, *55*, 5623–5626.

[32] N. Macia, R. Bresoli-Obach, S. Nonell, B. Heyne, *J. Am. Chem. Soc.* **2019**, *141*, 684–692.

[33] H. Zhang, H. Li, H. Fan, J. Yan, D. Meng, S. Hou, Y. Ji, X. Wu, *Nano Res.* **2018**, *11*, 1456–1469.

[34] B. Hu, X. Cao, K. Nahan, J. Caruso, H. Tang, P. Zhang, *J. Mater. Chem. B* **2014**, *2*, 7073–7081.

[35] Y. Zhang, K. Aslan, M. J. R. Previte, C. D. Geddes, *Proc. Natl. Acad. Sci. U.S.A.* **2008**, *105*, 1798–1802.

[36] G. Ulrich, R. Ziessel, A. Harriman, *Angew. Chem. Int. Ed.* **2008**, *47*, 1184–1201.

[37] A. Loudet, K. Burgess, *Chem. Rev.* **2007**, *107*, 4891–4932.

[38] R. Ziessel, G. Ulrich, A. Harriman, *New J. Chem.* **2007**, *31*, 496–501.

[39] Y. Wu, J. Mack, X. Xiao, Z. Li, Z. Shen, H. Lu, *Chem. Asian J.* **2017**, *12*, 2216–2220.

[40] E. A. Kovrigina, B. Pattengale, C. Xia, A. R. Galiakhmetov, J. Huang, J.-J. P. Kim, E. L. Kovrigin, *Biochemistry* **2016**, *55*, 5973–5976.

[41] T. Gu, T. Ye, J. D. Simon, J. K. Whitesell, M. A. Fox, *J. Phys. Chem. B* **2003**, *107*, 1765–1771.

[42] K. Xue, C. Wang, J. Wang, S. Lv, B. Hao, C. Zhu, B. Z. Tang, *J. Am. Chem. Soc.* **2021**, *143*, 14147–14157.

[43] X. Ma, R. Sun, J. Cheng, J. Liu, F. Gou, H. Xiang, X. Zhou, *J. Chem. Educ.* **2016**, *93*, 345–350.

[44] W. Li, L. Li, H. Xiao, R. Qi, Y. Huang, Z. Xie, X. Jing, H. Zhang, *RSC Adv.* **2013**, *3*, 13417–13421.

[45] Y. You, *Org. Biomol. Chem.* **2018**, *16*, 4044–4060.

[46] F. Wilkinson, W. P. Helman, A. B. Ross, *J. Phys. Chem. Ref. Data* **1993**, *22*, 113.

[47] J. R. Harbour, S. L. Issler, *J. Am. Chem. Soc.* **1982**, *104*, 903–905.

[48] N. K. Allampally, A. Florian, M. J. Mayoral, C. Rest, V. Stepanenko, G. Fernández, *Chem. Eur. J.* **2014**, *20*, 10669–10678.

[49] Y. Tokoro, A. Nagai, Y. Chujo, *Tetrahedron Lett.* **2010**, *51*, 3451–3454.

[50] A. Shukla, G. Kaur, K. J. Babu, N. Ghorai, T. Goswami, A. Kaur, H. N. Ghosh, *J. Phys. Chem. Lett.* **2020**, *11*, 6344–6352.

Chapter 4

Mechanism and Applications

Direction of hot e⁻ migration depends on the chemical structure of dyes
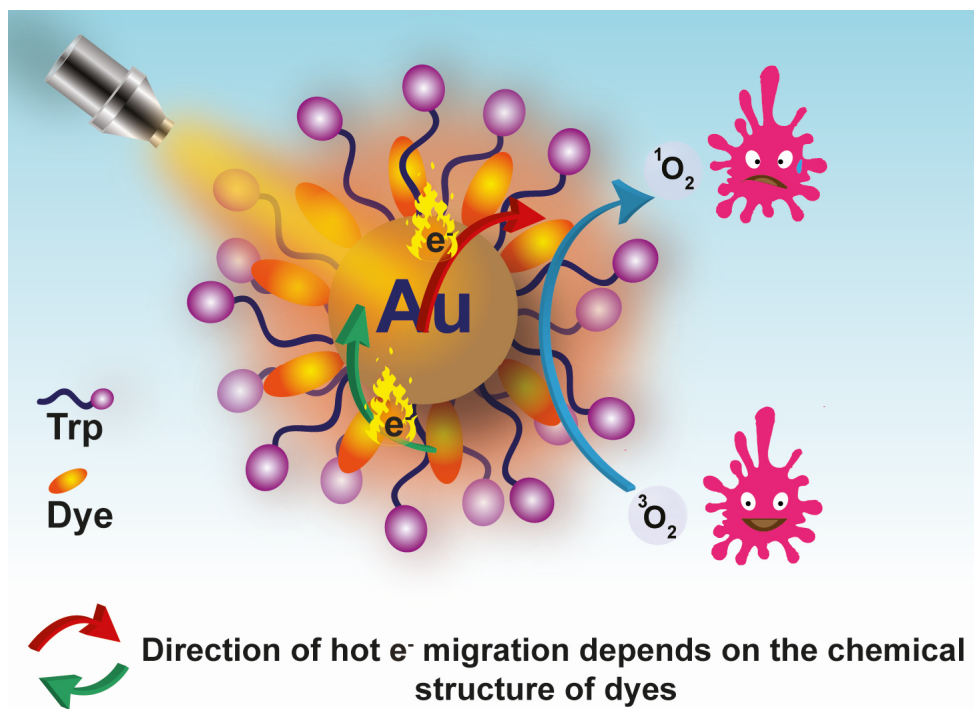
4.1.   Introduction.

Plasmon-molecule coupled systems have rich and intriguing optical properties, which have led to their use in various fields ranging from optoelectronics[1,2] and spectroscopy[3,4] to imaging[5–8] and sensing[4,9]. Plasmon-molecule coupled systems exhibit strong absorption due to the localized surface plasmons and has been shown to promote many photophysical processes such as Raman scattering[10–12], fluorescence[13–15], Förster resonance energy transfer[16], phosphorescence[17], and singlet oxygen ($^1O_2$) production[18–21]. $^1O_2$ is a highly reactive species, the lowest and most stable excited state of molecular oxygen.[22] $^1O_2$ is a widely used chemical reagent and cytotoxic agent.[23] Generally, $^1O_2$ is generated by photosensitization, a process in which a photosensitizer produces $^1O_2$ upon light exposure via energy transfer.[24] Production of photosensitized $^1O_2$ is essential for many applications, including photodynamic therapy (PDT) of cancer[25–28], photodynamic inactivation of micro-organisms[29], photoinduced oxidation[30,31], photodegradation[32], wastewater treatment[33], and fine chemical synthesis[34]. When $^1O_2$ is produced near or within tumour cells and micro-organisms, it can efficiently react with various cellular targets, causing detrimental structural

damage that eventually leads to their inactivation and death.[35] However, most photosensitizers show several drawbacks, including a tendency to aggregate in biological media, poor cellular uptake, and low-to-moderate $^1O_2$ quantum yield.[8] Besides, due to the dark toxicity of heavy atoms such as bromine and iodine, the development of heavy-atom-free photosensitizers is an extensively researched topic. To overcome this shortfall, plasmon-enhanced $^1O_2$ production has been developed recently as a viable method. It occurs as a result of plasmonic coupling between photosensitizers and noble metal nanostructures, which is a promising method for increasing the efficacy of PDT. Nonetheless, the ability of noble metal nanostructures to boost $^1O_2$ production is relatively unexplored. Furthermore, the underlying mechanism of plasmon-enhanced $^1O_2$ generation is still unknown. Many theoretical studies have shown that metal nanostructures facilitate intersystem crossing in the plasmon-molecule hybrid system.[21,36] As a result, these hybrid systems subsequently generate more $^1O_2$ due to the enhanced intersystem crossing and triplet yield.[19,20]

As described in Section 3.2.10 of Chapter 3, a few of the synthesized nanocomposites efficiently photosensitized the generation of $^1O_2$. This chapter describes the elucidation of the mechanism of photosensitized $^1O_2$ generation using ultrafast spectroscopy. Our results show that hot charge carrier migration is the key for the observed photophysical properties and that the direction of hot electron transfer is determined by the chemical composition of the dye molecules, which also played a significant role in the photophysical properties of nanocomposites. Finally, we studied their utility as a cytotoxic and imaging agents against cancer cells due to their luminescence and biocompatibility. Furthermore, due to the environment-dependent luminescence nature of nanocomposite **NC6**, we used it for the selective detection and killing of cancer cells.

4.2. Results.

4.2.1. Transient Absorption Spectroscopy (TA) Studies.

Transient absorption (TA) spectroscopy is widely used to investigate the intrinsic photophysical behaviour of a variety of materials.[37–40] To study the mechanism of the $^1O_2$ generation of nanocomposites and to realize the native photophysical behaviour in this hybrid system, we investigated the excited-state charge carrier dynamics using TA spectroscopy. First, we wanted to see how the chemical structure of the BODIPYs **B1-B3** affected the $^1O_2$ generation efficiency of nanocomposites **NC1-NC3**. In the transient absorption spectra of **B1-B3** in acetonitrile, we observed a strong photoinduced bleach feature peaking around 505, 502, and 518 nm corresponding to the spin allowed π-π* transitions from S_0 to S_1 state[41,42]

(Figures 4.1a-c). The primary channel for the effective production of $^1O_2$ in BODIPYs is the population of triplet states via the singlet-triplet intersystem crossing (ISC) process.[39] However, in the presence of gold nanoparticles, the mechanism of $^1O_2$ generation in gold-BODIPY nanocomposites may differ. This could be due to the ISC process being aided against fast relaxation of S_1 to S_0[43] or the plasmonic photoexcitation induced population increment in oxygen singlet states.[44] In our previous nanosecond transient studies, we observed no signature of triplet state formation for **NC1**.[45] Thus, plasmonic photoexcitation of these systems could be the mechanism of $^1O_2$ generation in gold-BODIPY nanocomposites.

To better understand this, we studied the TA spectra of nanocomposites **NC1-NC3** using 450 nm pump excitation. We noticed that the transient absorption spectra of the nanocomposites **NC1-NC3** were dominated by the gold plasmonic bleach signal at 545 nm, indicating a strong resonance coupling between gold nanoparticles and the molecular entities[41,46] (Figures 4.1d-f). We observed a significantly redshifted plasmonic bleach signal in **NC1-NC3** as compared to the plasmonic bleach signal in gold nanoparticles (**Au NP**), which was observed at 540 nm under the same photoexcitation (Figure 4.2). It is worth noting that a strong photoinduced absorption at 490 nm replaces the BODIPY ground state bleach feature in the spectra of the nanocomposites (Figures 4.1d-f). This could imply a BODIPY to metal charge transfer phenomenon in the nanocomposites. The quenching of the steady-state fluorescence of **B1-B3** incorporated into nanocomposites **NC1-NC3** also supports this interference. It is also well known that the fast relaxation of plasmonic excitations in **Au NP** inhibits the electron transfer process, resulting in low singlet oxygen efficiency. In the case of nanocomposites **NC1-NC3**, it is hypothesized that the longer plasmonic lifetime caused photoexcited electron migration from BODIPY to **Au NP**, allowing a longer time for electron transfer into oxygen singlet states.
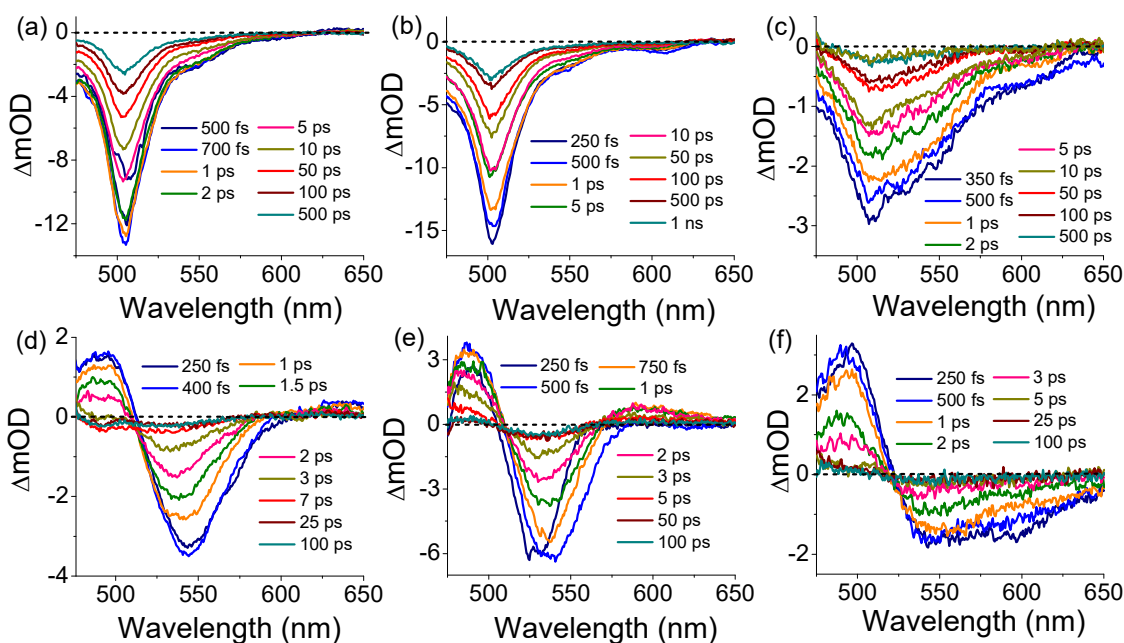
Figure 4.1. Transient absorption spectra of (a-c) the BODIPY molecules **B1-B3** in acetonitrile, and (d-f) the nanocomposites **NC1-NC3** in water as a function of pump-probe delay time for 450 nm photoexcitation and 200 µJ/cm^2 laser fluence. [**B1**], 11 µM; [**B2**], 49 µM; [**B3**], 31 µM and [**NC1-NC3**], 16 µg/mL each.
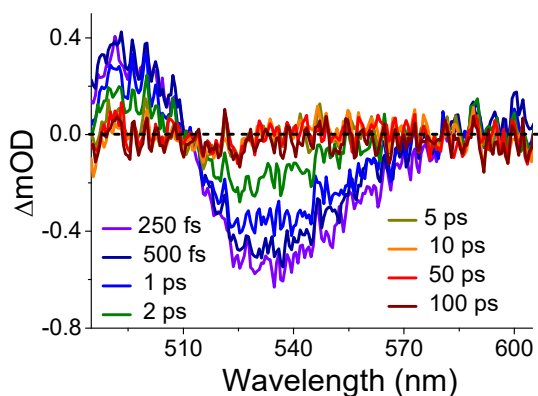

Figure 4.2. Transient absorption spectra of pristine **Au NP (**16 µg/mL) as a function of pump-probe delay time for 450 photoexcitation and 200 µJ/cm^2 laser fluence.

To determine the coupling strength in nanocomposites **NC1-NC3**, we studied the bleach dynamics of pure molecules **B1-B3** in acetonitrile and nanocomposites **NC1-NC3** in water as a function of pump-probe delay time. It was noticed that the growth time of the ground state bleach was longer for **B1** than for **B2** and **B3**, implying a longer relaxation time for **B1** and indicating the possibility of hot electron transfer in **NC1**, which is very unlikely in **NC2** and **NC3**. The slower recovery kinetics of **B1** would favour over **B2** and **B3** for

plasmon-molecule coupling, resulting in efficient electron transfer to gold (Figure 4.3a). We observed a gradual decrease in the growth time of the plasmonic bleach from **NC1** to **NC3**, whereas a rapid rise was observed in the case of **Au NP**. The growth time component of a plasmonic signal was caused by electron-electron scattering in photoexcited hot electron gas before they are thermalized in the SPR state.[47] Thus, an increase or decrease in scattering time would indicate a change in electron population in the metal regime. Our experimental results in Figure 4.3b showed that the electron population in metal excited states followed the order **NC1** > **NC2** > **NC3** > **Au NP**. It is hypothesized that a higher BODIPY interaction probability readily increased plasmon lifetime, resulting in a superior singlet oxygen population. However, the higher singlet oxygen efficiency of **NC3** as compared to **NC2** may be due to the broader plasmonic absorption of **NC3**, as shown in Figure 4.1f. Due to their poor gold-BODIPY interaction, it is also inferred that the heavy atom effect[48] of the **B3** entity contributes to singlet oxygen generation in **NC3** along with the gold-mediated phenomena.
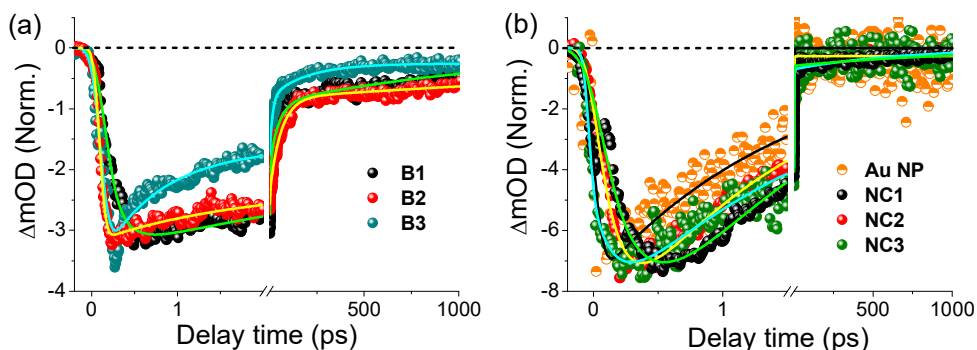
Figure 4.3. Normalized evolution of the transient decay kinetics of (a) **B1-B3** and (b) **NC1-NC3** following plasmon-molecule interactions probed at the bleach maxima after 450 nm photoexcitation. The kinetics of **Au NP** is also plotted as a reference.

Based on our experimental findings, we also propose a simplified scheme for discussing the differentiation of $^1O_2$ generation and photoinduced processes in **NC1** and **NC2** (Figure 4.4). In the presence of gold, photoexcited BODIPY electrons are transferred into metal SPR states or occupy the unfilled *6sp* band with subsequent intra-band relaxation. This would slow down the fast relaxation of plasmonic electrons and increase the gold carrier lifetime, both of which are critical for electron extraction to fill the singlet states of oxygen. The appearance of a molecular bleach signal in the transient spectra of **NC1** after 3 ps indicates the refilling of the S_1 state via back-electron transfer from gold to **B1**. However,

gold hot electron absorption obscures it in the early time scales ($\leq$ 3 ps). But the bleach intensity was very low compared to pure BODIPYs, indicating a low carrier population in the state, preventing back-migration of transferred electrons towards S_1, which helped to populate the singlet state of oxygen. The fast relaxation of photoexcited electrons in the molecular regime makes hot electron transfer minimal for **NC2**. Further, electron transfer would be possible only from near band-edge states to the molecular singlet state of oxygen in **NC2**. According to our experimental results on singlet oxygen efficiency, hot electron transfer is the most effective channel for the delocalization of molecular electrons into gold due to the plasmon-molecule interaction, resulting in a commendable singlet oxygen yield.
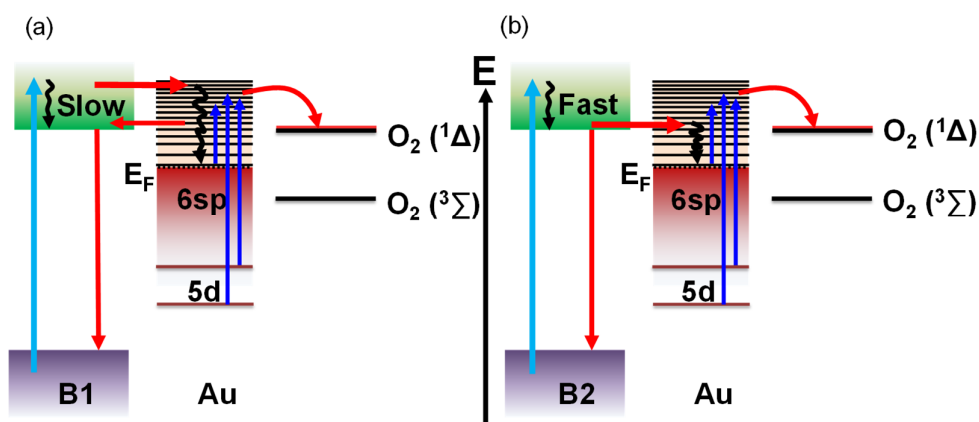
Figure 4.4. Schematic display of the excited state photophysical processes in (a) **NC1** and (b) **NC2** after 450 nm pump excitation resulting in the generation of singlet oxygen.

Following that, we wanted to investigate the mechanism of $^1O_2$ generation in the multi-chromophoric nanocomposites **NC7**, which contained BODIPY **B2** and **B3**. To explore this further, we studied the TA spectra of various systems using a 350 nm pump excitation. The rationale behind using a high-energy 350 nm pump is to examine the TA spectra of organic nanoparticles, which have a steady-state absorbance of around 463 nm and produce a clean, scatter-free spectrum. We observed bleach maxima at 502 and 518 nm in acetonitrile for **B2** and **B3**, respectively (Figure 4.5). However, the spectra of their organic nanoparticles **ONP1** and **ONP2** revealed a significant blue shift and a sharp bleach peak at 463 nm (Figures 4.6a-b). After that, we studied the TA spectra for a mixture of **B2** and **B3** in acetonitrile consisting of two peaks at 502 and 518 nm, attributed to individual bleach peak positions of **B2** and **B3** (Figure 4.7a). This observation indicated that the molecules retained their original signature in the mixture and that no additional property emerged in the system. Intriguingly, the transient absorption spectra of a mixture of **B2** and **B3** in an aqueous medium were

significantly different from those of the mixture in acetonitrile: while the multi-chromophoric organic nanoparticles **ONP7** showed a blue-shifted peak at 463 nm in 100% water (Figure 4.6c), two peaks were observed at 463 and 505 nm in 90% water-acetonitrile mixture (Figure 4.7b). These findings corresponded to the steady-state absorption spectra of the molecules and their aggregates. During the aggregation process, the bleach signal corresponding to molecule **B3** vanished while that of molecule **B2** remained, and a new peak corresponding to molecular aggregates appeared at 463 nm.
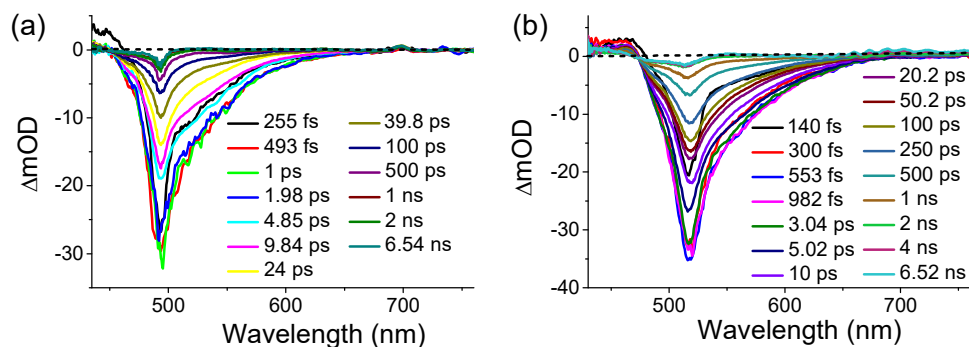
Figure 4.5. Transient absorption spectra of (a) **B2** (49 μM) and (b) **B3** (31 μM) in acetonitrile for 350 nm photoexcitation and 200 μJ/cm^2 laser fluence as a function of pump-probe delay time.
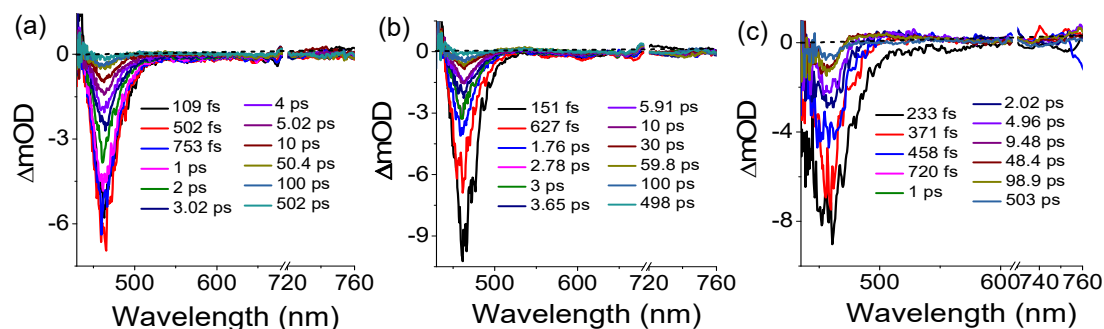
Figure 4.6. Transient absorption spectra of (a) **ONP2** (8.6 μg/mL), (b) **ONP3** (9.2 μg/mL) and multi-chromophoric organic nanoparticles **ONP7** (11.6 μg/mL) in water for 350 nm photoexcitation and 200 μJ/cm^2 laser fluence as a function of pump-probe delay time.

The ultrafast dynamics of nanocomposites **NC2**, **NC3** and **NC7** were then investigated under similar conditions. After photoexcitation at 350 nm, the transient absorption spectra of **Au NP** showed a plasmonic bleach at 549 nm and a broad photoinduced absorption peak at 493 nm (Figure 4.8c). The strong bleach signal was also linked to a wide bleach signal that extended up to 650 nm. The nanocomposite **NC2** showed peaks at 447 and 565 nm, as well as photoinduced absorption peaks at 495 and 639 nm, whereas **NC3** showed

peaks at 463 and 545 nm, as well as photoinduced absorption peaks at 492 and 627 nm (Figures 4.8a-b). The multi-chromophoric composite **NC7**, on the other hand, showed a bleach signal at around 545 nm, a weak bleach at 463 nm, and photoinduced absorption peaks at 493 and 630 nm (Figure 4.7c). After applying a 350 nm pump pulse, significant photoinduced features were observed in both blue and red wings. The plasmonic signal of gold was observed to exhibit a marginal blue shift in the case of **NC7** and a marginal red shift in the case of **NC2**. Eventually, we observed a significant increase in the plasmonic signal intensity of gold in the presence of BODIPY aggregates in **NC2**, **NC3** and **NC7**. Furthermore, we compared the dynamic profiles of the plasmonic bleach maxima of **NC7** to the kinetic profiles of **Au NP**, **NC2**, and **NC3** (Figure 4.9). As compared to **Au NP**, the plasmonic signals for **NC3** and **NC7** decayed much slower, indicating enhanced charge carrier separation in the nanocomposites. As a result, the highest hot electron transfer from BODIPY aggregates of **B2** and **B3** to gold in **NC7** occurred, resulting in high $^1O_2$ generation.
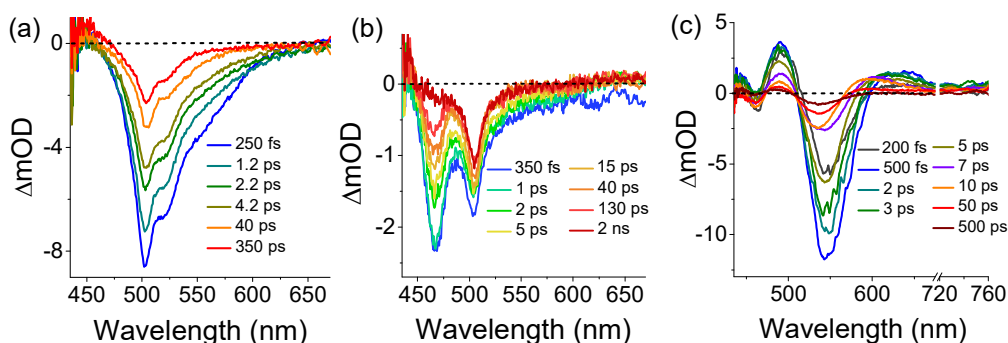

Figure 4.7. Transient absorption spectra of a mixture of **B2** (21 μM) and **B3** (14 μM) in (a) acetonitrile and (b) 90% acetonitrile-water and (c) the nanocomposite **NC7** (12 μg/mL) in water for 350 nm photoexcitation and 200 μJ/cm^2 laser fluence as a function of pump-probe delay time.
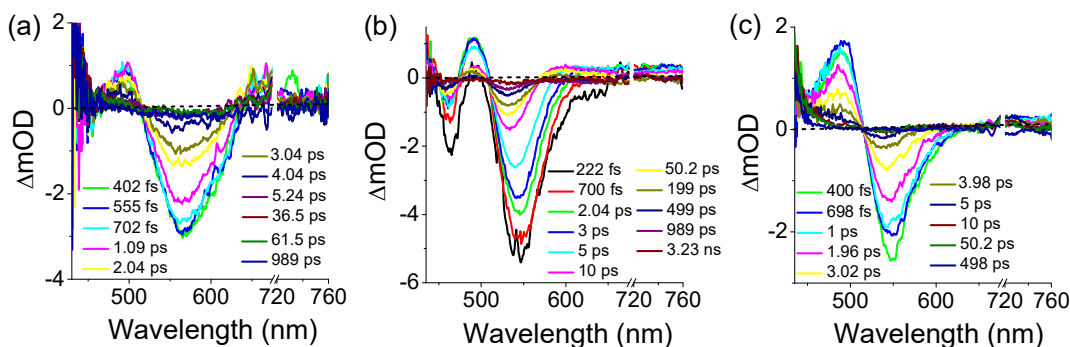

Figure 4.8. Transient absorption spectra of (a) **NC2**, (b) **NC3** and (c) **Au NP** in water for 350 nm photo-excitation and 200 μJ/cm^2 laser fluence as a function of pump-probe delay time. [**NC2**, **NC3** and **Au NP**], 12 μg/mL.
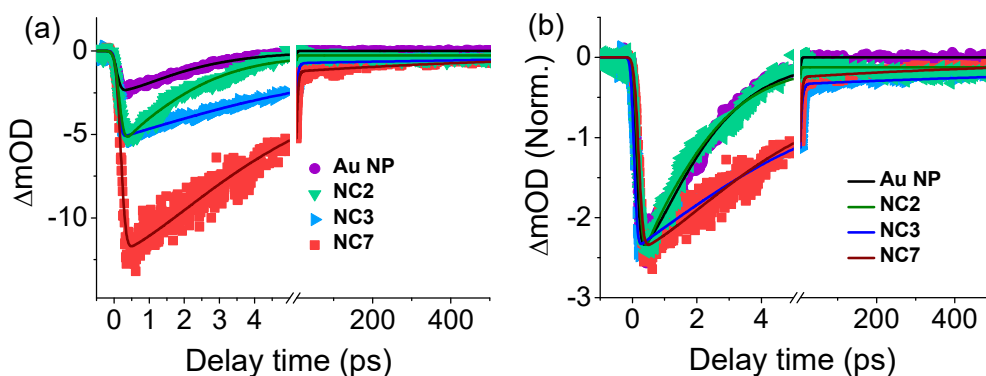
Figure 4.9. (a) Evolution and (b) normalized evolution of the transient decay kinetics in the nanocomposites **NC2**, **NC3** and **NC7** following plasmon-molecule interactions probed at the bleach maxima. The kinetics of **Au NP** is also plotted as a reference.

Next, we studied the TA spectra of **B6**, **ONP6**, and **NC6** using 360 nm pump pulses to understand the photophysical properties of **NC6**. We observed one positive peak at 525 nm and one negative peak around 630 nm in the TA spectra of **B6**, which can be attributed to photoinduced absorption and stimulated emission (SE) bleach, respectively (Figure 4.10a). However, a bleach signal at 540 nm was observed for **ONP6**, which corresponded to the steady-state absorption maximum. Furthermore, the red regime of the spectra of **ONP6** was dominated by a photoinduced absorption feature, which was observed to reduce the SE bleach signal at 630 nm (Figure 4.10b). It is inferred that this could be the effect of molecular aggregation upon organic nanoparticle formation. On the other hand, we observed two negative peaks at 555 and 630 nm and a positive peak along with a photoinduced absorption peak of 490 nm for **NC6** (Figure 4.10c). The bleach at 555 nm could be attributed to the surface plasmon resonance of gold nanoparticles, which was observed in the case of **Au NP** around 560 nm (Figure 4.10d). It is important to note that the TA spectra of **NC6** showed a minor blue shift in the bleach and a significant decrease in signal intensity when compared to **Au NP**. Further, we noticed a bleach around 630 nm in the TA spectrum of **NC6**, which is the signature of the SE signal corresponding to molecule **B6**. This implies that both the molecule and the gold plasmons significantly contributed to the **NC6** transient signal. Furthermore, we studied the dynamic profiles of **NC6** and **Au NP** at their corresponding bleach maxima (Figures 4.11a-b). It is clear that the dynamic profile of **NC6** has been significantly altered when compared to **Au NP**. The **NC6** signal decays much faster than the **Au NP** signal. The extremely fast kinetics of **NC6** could be due to a low charge carrier population in **NC6**, indicating a charge transfer phenomenon from the gold nanoparticles to the molecule.

Moreover, we also compared the dynamic profiles of **B6**, **ONP6**, and **NC6** at the bleach maxima at 630 nm, which shows the dramatic evolution of the SE signal from pure molecule **B6** to molecular aggregate **ONP6** and then to nanocomposite **NC6** (Figure 4.11c). The negative signal in **B6** was changed entirely to a positive signal in **ONP6**, as **B6** was aggregated upon forming the organic nanoparticles. However, in the presence of gold nanoparticles, the negative feature reappeared in its original position, even though the molecule is still aggregated in **NC6**. This could be due to an increased charge carrier population in the molecular singlet state of **NC6** in the presence of the gold nanoparticle, thereby increasing the luminescence. Furthermore, it is proposed that increasing the charge carrier population at the LUMO level would significantly increase the likelihood of intersystem crossing (ISC) and singlet-triplet electron transfer, facilitating singlet oxygen generation in **NC6**.
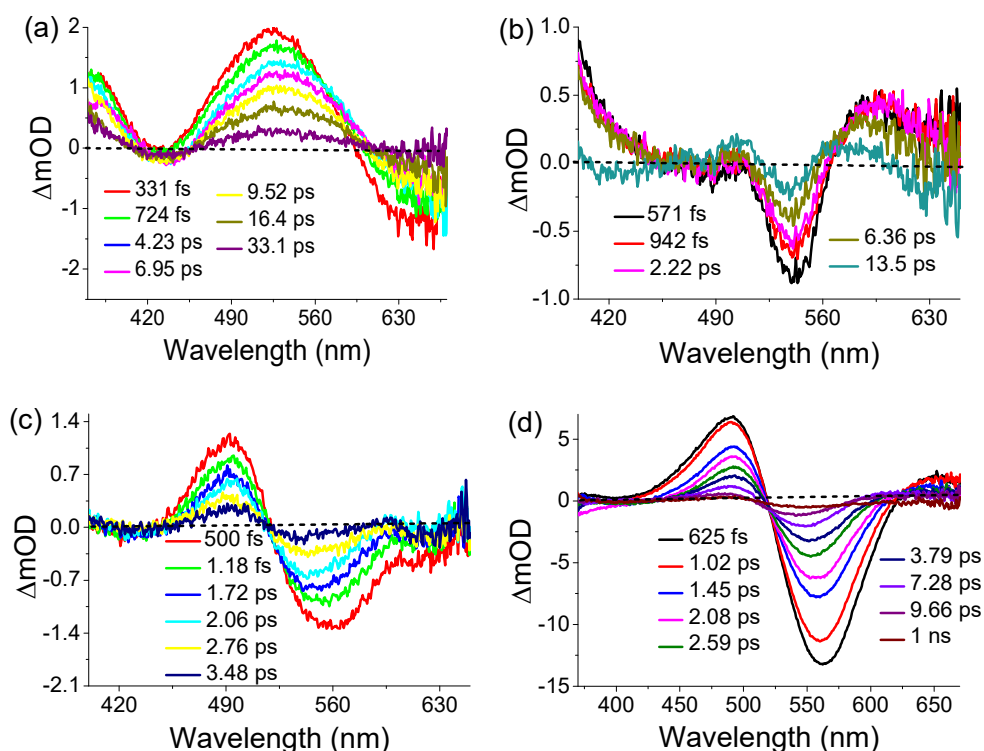

Figure 4.10. Transient absorption spectra of (a) **B6** (18 μM) in acetonitrile, (b) **ONP6** (12 μg/mL), (c) **NC6** (12 μg/mL) and (d) **Au NP** (24 μg/mL) in water for 360 nm photoexcitation in a wide range of pump-probe delay probed in a broad wavelength regime.
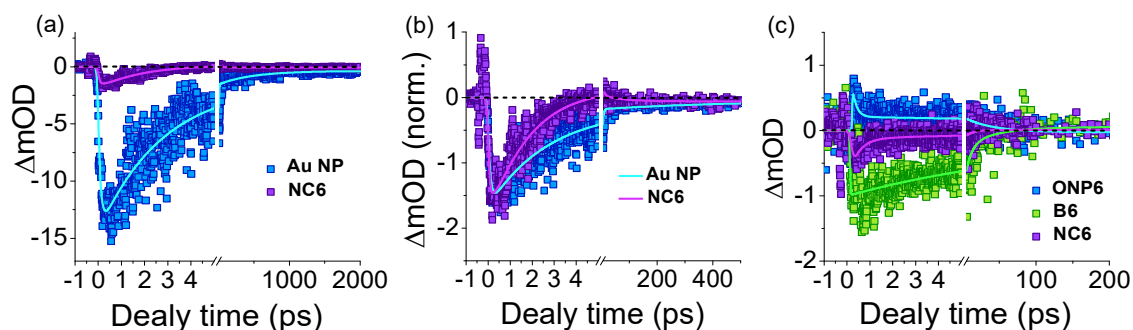
Figure 4.11. (a) Evolution and (b) normalized evolution of the transient decay kinetics of **NC6** and **Au NP** at 555 and 560 nm bleach maxima and (c) a comparison of the kinetics of molecule **B6**, **ONP6**, and **NC6** at 630 nm bleach maxima.

4.2.2. Photobiological Studies.

After establishing the mechanism of photophysical processes in the nanocomposites, we were interested in evaluating their potential for biological applications. The first step in this direction was to see if they were biocompatible. A preliminary screening was performed against toxin-sensitive HUVEC cells to confirm the biocompatibility of the nanocomposites **NC2**, **NC3** and **NC7**. The viability of cells in the presence of various concentrations of **NC2**, **NC3** and **NC7** indicated their biocompatibility. The cell viability assay revealed that more than 80% of cells are viable in the dark at up to 10 µg/mL concentrations (Figure 4.12a). Next, we tested the effectiveness of **NC3** and **NC7** in serving as PDT agents at the same concentration. C6 glioma cells with internalized nanocomposites **NC3** or **NC7** were exposed to white light to demonstrate their efficacy as a PDT agent. Then, the intracellular Reactive Oxygen Species (ROS) generation was investigated using a non-fluorescent 2,7-dichlorofluorescein diacetate (DCFDA) dye as a probe. DCFDA is oxidized in the presence of ROS to yield a green fluorescent derivative, 2,7-dichlorofluorescein (DCF). After 24 hours of incubation with the nanocomposite, the cells were exposed to white light from a LED for 20 minutes. We experimented with identical conditions in the absence of light as a control. As shown in Figure 4.12b, in the presence of light, 10 µg/mL of **NC3** and **NC7** generated ~254 % and ~274% intracellular ROS over untreated C6 glioma cells. In contrast, these treated groups were also found to generate intracellular ROS (~164% and ~185%, respectively) under dark conditions.

In vitro phototoxicity of the three nanocomposites (**NC2**, **NC3** and **NC7**) was further tested at various concentrations ranging from 2.5 to 40 µg/ mL in the presence and absence of white LED light. The dose-dependent toxicity of the nanocomposites against glioma cells

(Figure 4.12c) showed cell viability ranging ~50 to ~65% beyond 5 µg/mL concentration for both **NC3** and **NC7** under dark. Now, considering that the molecule **B3** is the common entity present in both **NC3** and **NC7**, the dose-dependent effect of its free form was assessed against cancer cells (Figure 4.13). It was found that cell viability significantly decreased beyond 0.75 µg/mL with a marginal rise in intracellular ROS with increasing concentration. Due to the non-covalent interaction between **Au NP** and **B3**, the intracellular release of the latter is warranted and could be linked to the dark toxicity. However, pronounced phototoxicity was observed following white light irradiation with cell viability of ~25% for both **NC3** and **NC7** at 10 µg/mL (Figure 4.12d). Thus, **NC3** and **NC7** could serve as potential candidates for PDT.
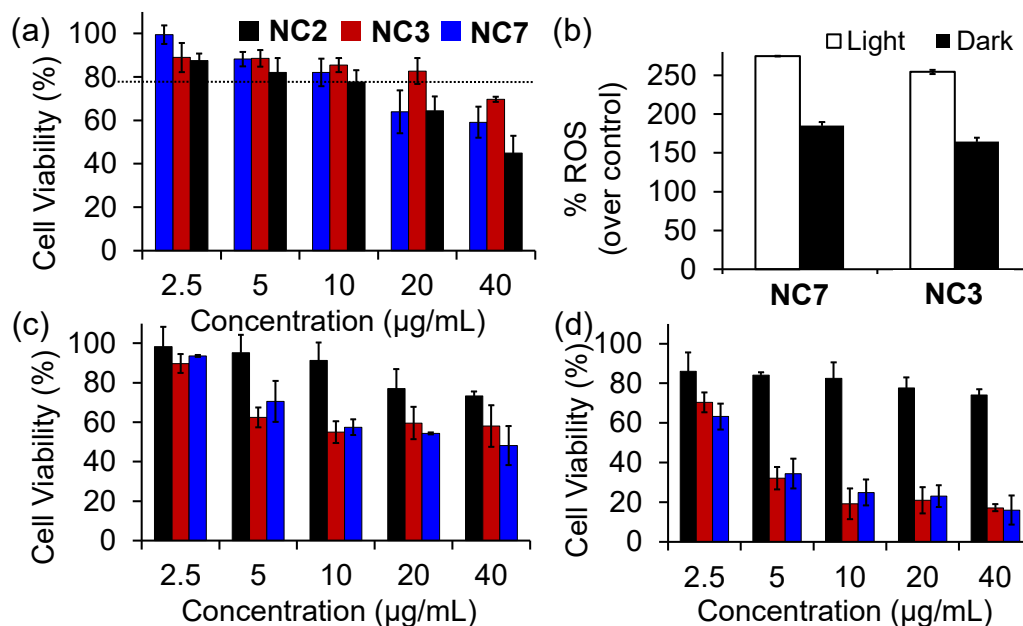

Figure 4.12. (a) Dose-dependent biocompatibility of nanocomposites **NC2**, **NC3** and **NC7** with human umbilical cord endothelial cells (HUVECs) under dark conditions. (b) Percentage intracellular ROS generated with **NC3** and **NC7**. Dose-dependent toxicity of the nanocomposites **NC2**, **NC3** and **NC7** under (c) dark and (d) light conditions.
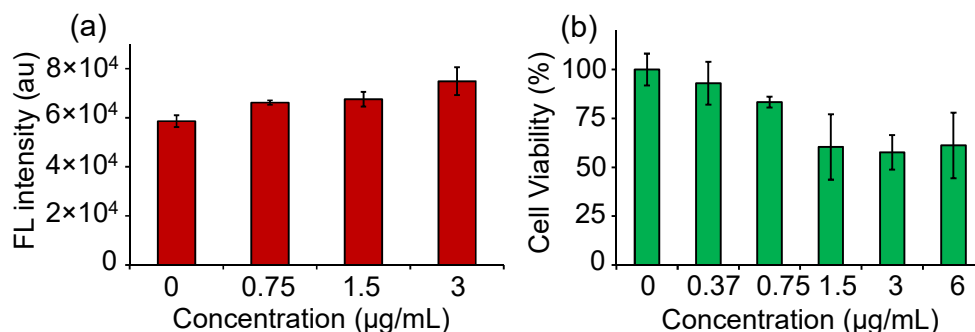
Figure 4.13. Dose-dependent effect of **B3** on (a) intracellular ROS generation and (b) viability of C6 cells.

Further, we were interested in studying the mechanism of PDT, which may involve cell arrest at a specific checkpoint in the cell cycle. So, we examined the effect of nanocomposites **NC2**, **NC3** and **NC7** on cell cycle perturbations in the presence and absence of light for C6 cancer cells, as shown in Figure 4.14. Nanocomposites **NC3** and **NC7** in the presence of light blocked the entry of cells into the G2/M phase due to mitotic arrest in the S-phase. Consequently, these photo-damaged cells could not complete the cycle, leading to the commencement of apoptosis. The cells harbouring G2/M DNA were found to be ~7.3% and ~2.9% in **NC3** and **NC7** treated cells, respectively, as compared to 19.5% in the control. Further, the percentage of the apoptotic population due to phototoxicity of **NC3** and **NC7** was investigated. In tune with the observation of toxicity in both dark and light conditions, **NC2** and **NC3** showed necrotic populations in dark conditions (Figure 4.15). In the presence of light, they predominantly induced the cells into early (~10%) and late (~90%) apoptosis. Prior reports show that elevated intracellular ROS leads to oxidative stress followed by necrosis and apoptosis. While both **NC3** and **NC7** were phototoxic to glioma C6 cells, **NC7** was further evaluated as a tracer using confocal microscopy due to its pronounced fluorescence. **NC7** showed concentration-dependent accumulation of the nanocomposite with significant green and weak red emissions when excited at 488 nm and 561 nm, respectively (Figure 4.16). No evident emission was observed in both regions from cells treated with **NC3** and untreated control. Thus, **NC7** could induce PDT-induced cancer cell death at concentrations as low as 10 μg/mL and allow intracellular fluorescent labelling at higher concentrations (100 μg/mL). Further, concentration-dependent internalization of **NC7** was confirmed by quantifying intracellular gold content with inductively coupled plasma-mass

spectrometry (ICP-MS) analysis (Figure 4.17). These findings further validated the cellular uptake depicted by confocal microscopy.

Furthermore, the cytotoxic assessment of nanocomposites (**NC3** and **NC7**) was performed by the Live/Dead assay by examining cells under confocal microscopy after incubation with 10 µg/mL of nanocomposite and subsequent incubation with fluorescent markers that differentiate between live and dead cells. To substantiate the phototoxic nature of **NC3** and **NC7**, C6 cancer cells were treated with fluorescein diacetate (FDA) to stain metabolically active cells with the intact plasma membrane and propidium iodide (PI) to stain the nucleus of damaged membrane cells. We observed that ~99% of cells treated with **NC3** and **NC7** followed by white light exposure sustained membrane damage as depicted by their PI uptake. However, with dark treatment, more than 70% of cells were alive (Figure 4.18).
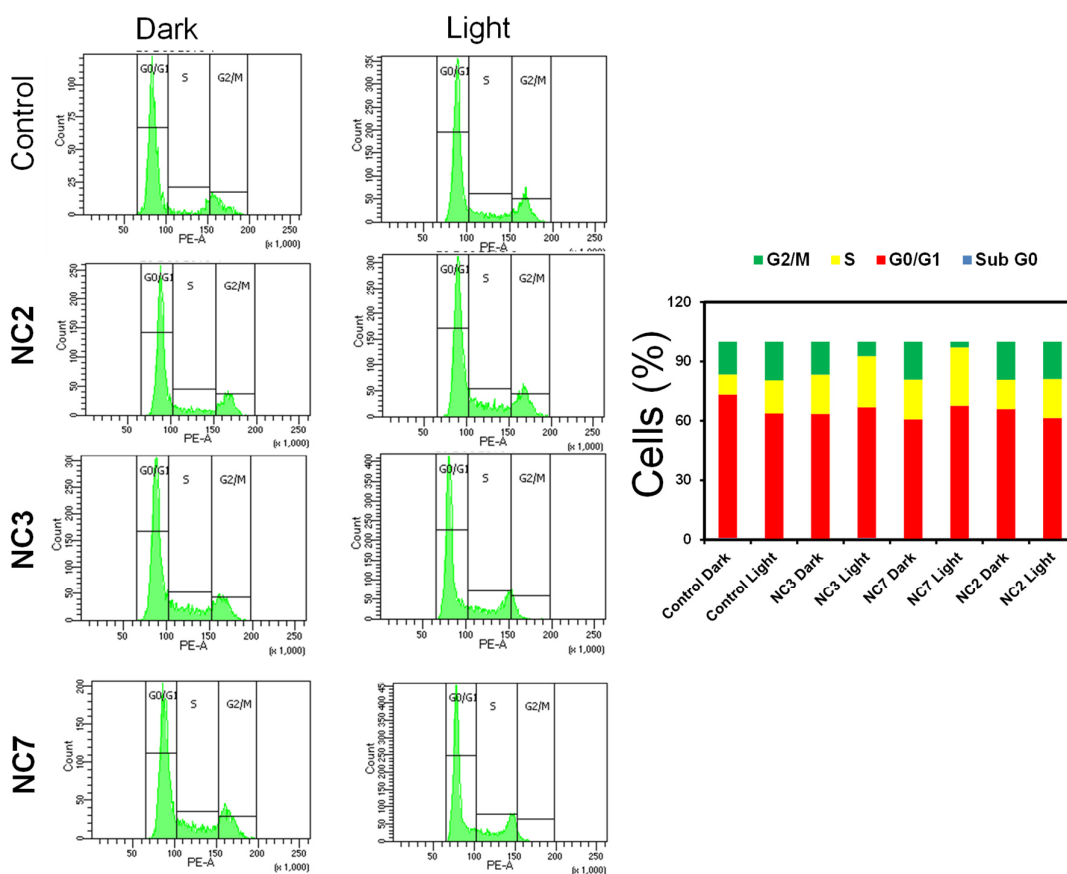

Figure 4.14. Cell cycle analysis of **NC2**, **NC3**, and **NC7** treated C6 cells under light and dark conditions. [**NC2**, **NC3** and **NC7**], 10 µg/mL.
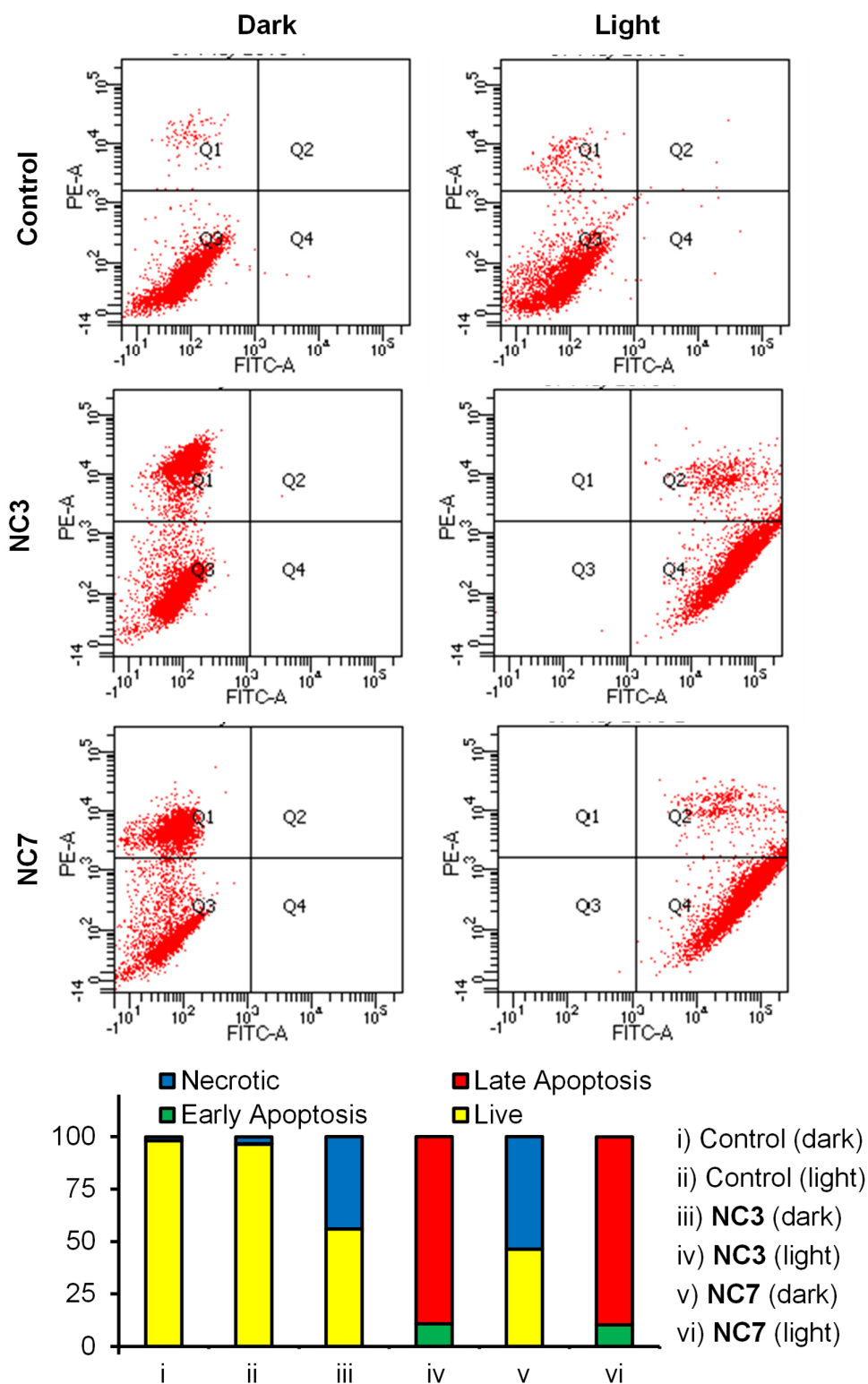
Figure 4.15. Percentage necrotic and apoptotic population of **NC3** (10 μg/mL) and **NC7** (10 μg/mL) treated C6 cells under dark and light conditions.
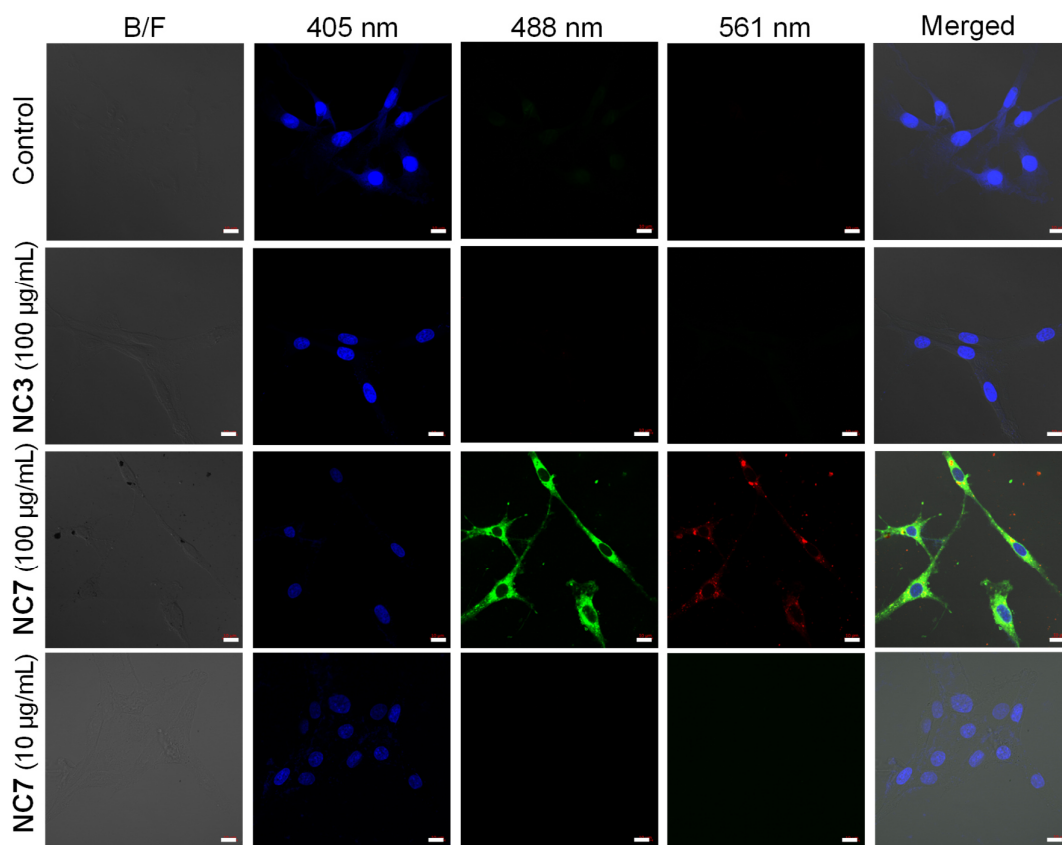
Figure 4.16. Confocal laser scanning microscopy images of **NC3** and **NC7** treated C6 glioma cells. B/F are bright-field images; 405, 488, and 561 nm are the wavelengths of the laser used to excite the nanocomposites. The scale bar is 10 μm.
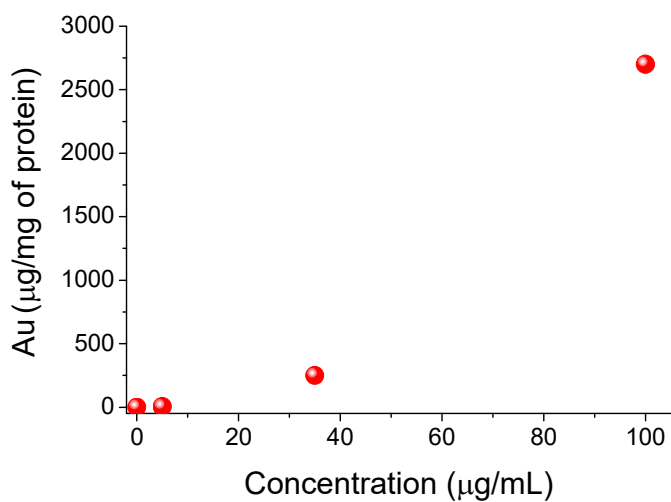

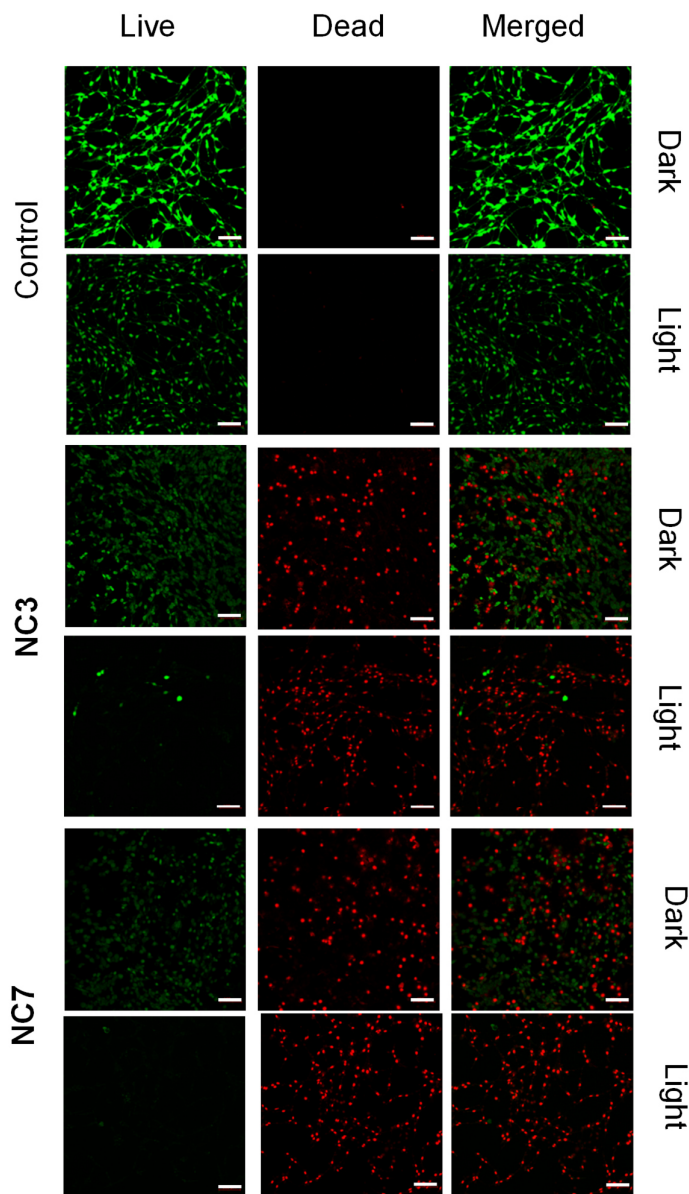**Figure 4.17.** Cellular uptake analysis of **NC7** quantified by ICP-MS.

Figure 4.18. Live/dead cell staining assay **NC3** (10 µg/mL), **NC7** (10 µg/mL) to assess the cell viability post PDT effect. The green channel depicts live cells and the red channel depicts compromised/dead cells. The scale bar is 100 µm.

Next, we studied the PDT activity of **NC6**. We investigated its biocompatibility with normal L929 fibroblast cells. Even at higher concentrations, **NC6** demonstrated excellent biocompatibility, with >70% of cells viable at a concentration of 200 µg/mL (Figure 4.19a). Next, we studied the phototoxic effect of **NC6** against C6 glioma cells. So, we conducted a dose-dependent cytotoxicity experiment of **NC6** against C6 glioma cells in the dark and with an incandescent white LED light irradiation. At a concentration of 200 µg/mL of **NC6**, ~60%

of cells were observed to be viable in the dark whereas after 60 min of irradiation, only 30% of the cells were viable (Figure 4.19b). Thus, when exposed to white light, **NC6** showed a significant increase in phototoxicity against C6 glioma cells, implying that **NC6** could be a candidate for PDT. Furthermore, because of its environment-sensitive luminescence, we used confocal microscopy to test the effectiveness of **NC6** as a tracer for site-selective accumulation. **NC6** was found in the cytoplasm of cancerous and normal cells, as evidenced by emission in the green and red channels. We only observed the accumulation and significantly intense green emission via the green channel in the case of C6 glioma cell lines due to the acidic nature of the cancer cells, whereas the accumulation was observed as green and red emission via both green and red channels in the case of L929 normal cell lines (Figure 4.20). Furthermore, the fluorescence intensity in both cell lines was quantified using the software Zen 3.5. The percentage intensity of the green channel was more than 20 times greater than that of the red channel in the C6 cell line, whereas it was three times greater in the L929 cell line (Figure 4.21). These findings show that **NC6** can be used as a fluorescent intracellular labelling agent to differentiate between normal and cancer cells.
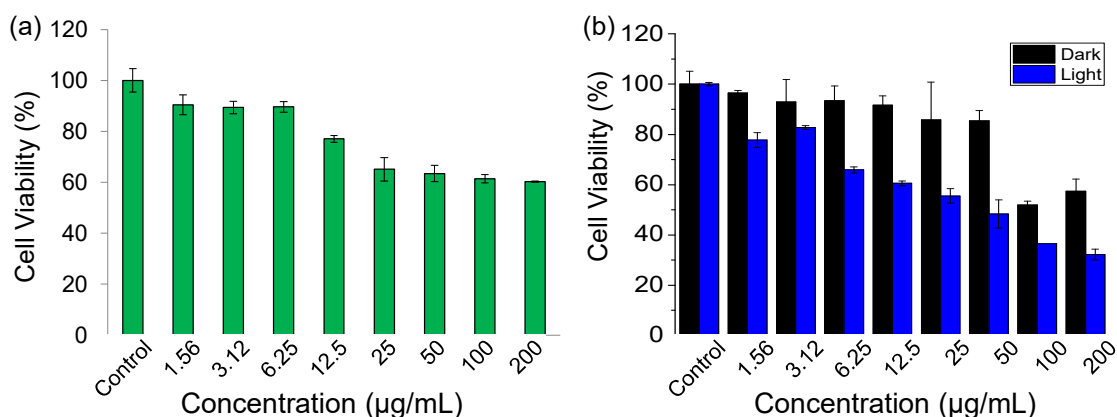

Figure 4.19. Cell viability assessment of the nanocomposite **NC6** against (a) L929 mouse fibroblast cells and (b) C6 cancer cells under dark and light irradiation using 36 W white LED at various concentrations.
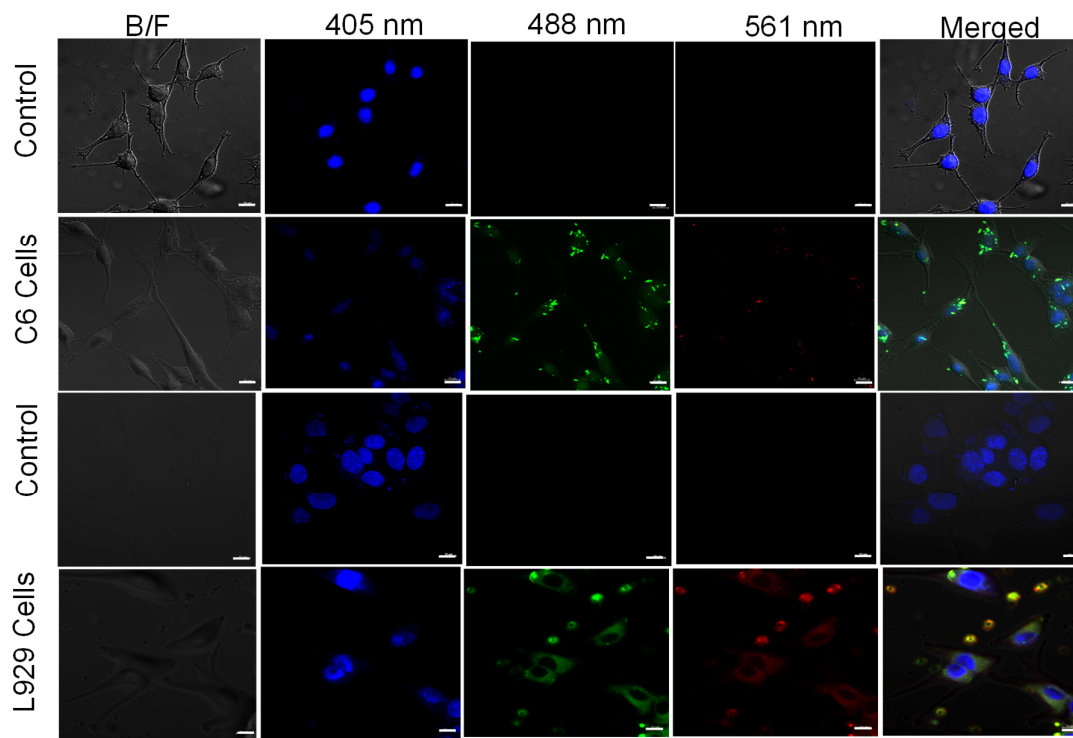
Figure 4.20. Confocal laser scanning microscopic images of **NC6** (5 µg/mL) treated C6 glioma cells and L929 normal cells upon 12 hours of incubation. B/F are bright field images; 405, 488 and 561 nm denote the wavelength of the laser used to excite the nanocomposite. The scale bar is 10 µm.
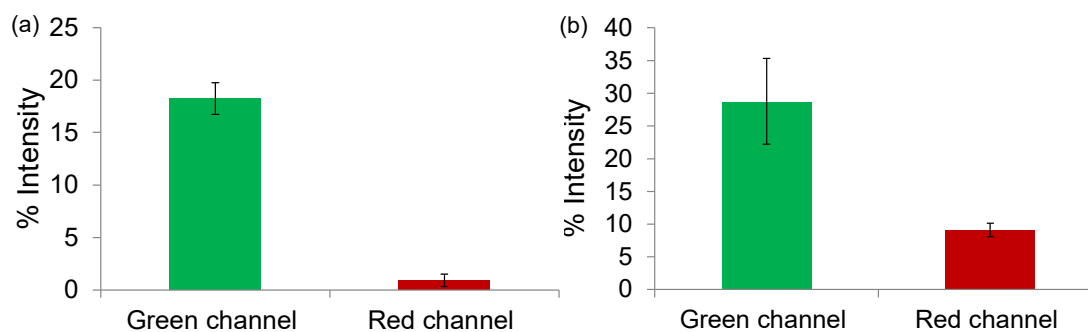

Figure 4.21. Cell viability assessment of the nanocomposite **NC6** against C6 cancer cells under (a) dark and (b) light irradiation using 36 W white LED at various concentrations.

4.3.   Discussion.

We used ultrafast spectroscopy to investigate the possible mechanisms of $^1O_2$ generation in nanocomposites. Generally, a plasmonic signal is produced by the collective oscillation of metal (e.g., gold) *6sp* electrons near their Fermi level and is known as the surface plasmon resonance (SPR).[47] This plasmon-mediated feature is controlled by

electron-electron scattering before being thermalized, followed by relaxation toward the ground state via phonon-phonon and electron-phonon scattering.[49] In transient spectroscopy, the electron-electron scattering process dictates the rise time component of a plasmonic bleach, while phonon-phonon and electron-phonon scattering rates dominate the decay time scales.[49,50] Thermalization of coherent hot electrons in SPR states occurs at 100 fs for pristine gold nanoparticles.[51] In line with these findings, we discovered that the rise of the gold plasmonic bleach was very fast (100 fs) in **Au NP**.

Similarly, ultrafast TA spectroscopy was used to explain the photophysics of nanocomposites and to visualize the behaviour of photoexcited charge carriers in the femtosecond time scale. The nanocomposites showed hybrid nature in their TA spectra, comprising a dominant plasmonic signature, photoinduced absorption peak, and an aggregated molecular signature. Further, we investigated the role of charge carrier separation in increasing singlet oxygen generation in the gold-BODIPY composite systems **NC1-NC3**. A significant increase in the plasmonic bleach signal intensity and subsequent red shift was observed for **NC1-NC3**. A comparison of the dynamic profiles of the plasmonic bleach in **NC1-NC3** and **Au NP** revealed that the time scales for electron-electron and electron-phonon scattering were found to be much higher in nanocomposites than that of corresponding pristine gold nanoparticles in the order **NC1** > **NC2** > **NC3** > **Au NP** (Figure 4.3). As a result, photoexcited electrons in the molecular system were transferred to the gold moiety, increasing the hot carrier population in the metallic system and thus increasing $^1O_2$ generation in **NC1-NC3** upon plasmonic photoexcitation. Eventually, the system with more charge carriers produced more amount of $^1O_2$. Moreover, the $^1O_2$ quantum yield of **NC3** was found to be higher than **NC2** due to the heavy atom effect of BODIPY **B3**.

Furthermore, in the case of the multi-chromophoric nanocomposite **NC7**, it is claimed that the mixed aggregates of BODIPY **B2** and **B3** are formed on the surface of gold nanoparticles, thereby facilitating a FRET from the aggregates of **B3** to the aggregates of **B2**. FRET, being a dipole-dipole interaction in the excited state, competes with electron transfer from BODIPY to gold and imparts fluorescence to **NC7** (Figure 4.22). Further, the presence of aggregates of BODIPYs of **B2** and **B3** has a substantial effect on the plasmonic properties of gold. It is inferred that the bleach signature of **NC7** is plasmonic and strongly modified in the presence of **B2** and **B3** aggregates. The extremely slow decay dynamics also suggest that the photoinduced bleach signal in **NC7** is a hybrid gold-molecule system rather than a pure plasmonic form (Figure 4.9). Again, the significant increase in positive features indicates an increased charge carrier population in the multi-chromophoric system **NC7**, as these positive

signals are expressions of hot electron absorption in the system. The hot carrier signal intensity was found to be the highest in **NC7** (Figure 4.23). These observations would be possible only if charge carriers in the system were extensively delocalized. The bleach at 463 nm is similar to the typical bleach signature of BODIPY molecule aggregates but with a much lower signal intensity. Previously, gold and silver nanoparticles embedded with molecular *J*-aggregates demonstrated similar transient behaviour.[52] An increase in the plasmonic lifetime is thought to aid in the efficient extraction of electrons toward oxygen singlet states, resulting in an enhancement in the singlet oxygen generation efficiency for **NC7** (Φ_Δ = 0.68) when compared to **NC3** (Φ_Δ = 0.42), **NC2** (Φ_Δ = 0.12) or **Au NP**. In the case of **NC7**, electron transfer probability is significantly increased (a two-fold increase in plasmonic bleach intensity) due to stronger coupling between gold nanoparticles and aggregates of **B2** and **B3**, resulting in a significant increase in singlet oxygen generation efficiency. Furthermore, plasma-enhanced formation of triplet states in chromophores could be an additional pathway that boosts singlet oxygen generation in **NC7**. This is supported by the observation of a long-lifetime species in **NC7** with a lifetime of 12.88 ± 0.41 ns (section 3.2.7 of Chapter 3). The strong interaction of molecular aggregates of **B2** and **B3** and gold nanoparticles leads to extensive charge separation in **NC7** and improves singlet oxygen generation efficiency.
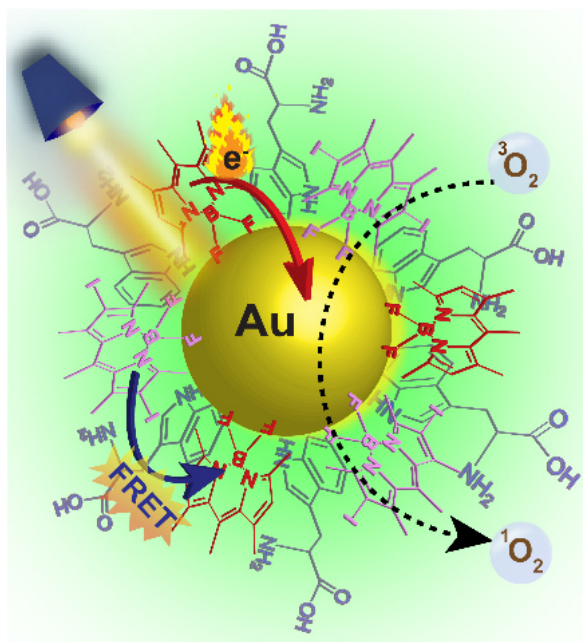

Figure 4.22. Schematic representation of **NC7** and the simultaneous FRET and electron transfer from BODIPY aggregates to gold resulting in fluorescence and singlet oxygen generation. BODIPY aggregates are represented using one molecule to improve visibility.
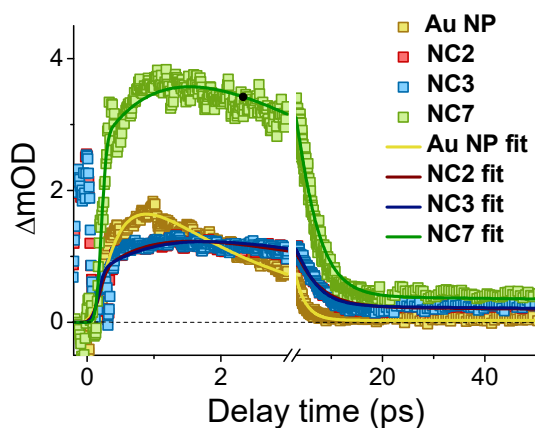
Figure 4.23. Transient decay profiles at 493 nm for **Au NP**, **NC2**, **NC3** and **NC7**.

Following that, we employed ultrafast TA spectroscopy to investigate the behaviour of photoexcited charge carriers on the femtosecond time scale in **NC6**. Previously, we observed that photoexcited electrons in the molecular system were transferred to the gold moiety, increasing the hot carrier population in the metallic system for gold-BODIPY nanocomposites. The situation was entirely different in **NC6**, where we used the stimuli-responsive naphthalidenimine-boron complex **B6**. The charge carrier dynamics of the plasmonic bleach were much faster in the presence of **B6**, implying electron transfer from gold to the molecule. Furthermore, a significant decrease in the intensity of the plasmonic bleach signal indicates that hot electrons are being transferred from gold to molecule at an ultrafast time scale. Moreover, the dynamics of **NC6** were found to be very fast as compared to **Au NP**. When the dynamic profiles of the plasmonic bleach in **Au NP** and **NC6** are compared, the time scales for electron-electron and electron-phonon scattering in **NC6** were found to be much shorter (Figure 4.11). This substantiates the electronic migration from gold to the molecule. Moreover, transient spectra of **NC6** were composed of both plasmonic and molecular signatures, i.e., plasmonic bleach at 555 nm and SE signal at 630 nm. It is worth noting that the SE signature was missing in the aggregated state of the molecule, i.e., **ONP6**, where a strong photoinduced absorption was observed (Figure 4.10). Thus, the reappearance of the SE signature in **NC6** indicates that charge carriers on the edge of singlet excited states have been enhanced. Furthermore, it is hypothesized that the increment in the charge carriers at the edge of the molecular singlet state of **B6** endorsed intersystem crossing and aided the generation of singlet oxygen in **NC6**.

Preliminary photobiological studies revealed that the nanocomposites **NC3**, **NC6** and **NC7** have the potential to serve as efficient PDT agents against C6 glioma cancer cell lines

when exposed to white LED light. Even though the singlet oxygen quantum yield of **NC7** was significantly higher than that of **NC3**, the PDT activities of both were comparable. We attribute this to a similar quantity of intracellular ROS generated by both under white light irradiation. The mechanism of cancer cell death indicated that it occurred via the apoptosis and necrosis pathways in **NC3** and **NC7**. Further, owing to the fluorescence properties and moderately long lifetimes, **NC7** may be considered superior to **NC3** with utilization as a cellular nanotracer. The pH-responsive luminescence property and $^1O_2$ generation of **NC6** were used as an intracellular tracer for differentiating and selective killing cancer cells over normal cells.

4.4. Conclusion.

Ultrafast spectroscopy was used to investigate the excited charge carrier dynamics in nanocomposites in order to better understand their mechanism of $^1O_2$ generation. These studies revealed that the hot electron migration from BODIPY (**B1-B3** or mixture **B2** and **B3**) to gold nanoparticles was observed in **NC1-NC3** and **NC7**. Further, the nanocomposites showed an enhancement in the plasmonic lifetime than the pristine gold nanoparticles, increasing the $^1O_2$ generation upon plasmonic photoexcitation. The higher the plasmonic lifetime, the more charge transfer from molecule to gold nanoparticles with the highest $^1O_2$ quantum yield in the case of **NC7**. In contrast, a reversal of hot electron migration from gold to molecule **B6** was observed for **NC6**, resulting in increased luminescence due to the fast photorelaxation process. Moreover, it was assumed that increased charge carrier population to the molecular LUMO level facilitated singlet to triplet electron transfer, resulting in efficient $^1O_2$ generation by **NC6**. Photobiological studies showed that the nanocomposites **NC3** and **NC7** could generate ROS under cellular conditions and induce cell death in glioma cells upon light irradiation through necrosis and apoptosis. However, because of its luminescence, **NC7** was chosen as the intracellular tracker agent over **NC3**. Because of the pH-dependent luminescence switching and photosensitization properties, nanocomposite **NC6** was used to detect and kill cancerous cells over normal cells.

4.5. Experimental Section.

4.5.1. Materials.

L929 mouse fibroblast and glioblastoma C6 cells were obtained from National Centre for Cell Sciences, Pune, India. Human umbilical vein endothelial cells (HUVECs) (Cat. No. 2517A) and endothelial growth medium (Cat. No. 3162) were purchased from Lonza. 2,7-

Dichlorofluorescein diacetate (DCFDA), fluorescein diacetate (FDA), bisbenzimide (Hoechst 33342) and propidium iodide (PI) were from Sigma-Aldrich. 3-(4,5-Dimethylthiazol-2-yl)-2,5-diphenyltetrazolium bromide (MTT), Dulbecco's Modified Eagle Medium (DMEM) containing 10 % fetal bovine serum (FBS) and 1% v/v penicillin-streptomycin solution were purchased from HiMedia.

4.5.2. Femtosecond transient absorption spectroscopy.[53]

We used a Ti: sapphire amplifier system (Astrella, Coherent, 800 nm, 3mJ/pulse energy, ~ 35 fs pulse width, and 1 kHz repetition rate) and Helios Fire pump-probe spectrometer for the ultrafast measurements. The output laser beam was cleaved into the pump (95% of the output) and probe (remaining 5%) beams using two different beam splitters. The required pump wavelength was obtained using Optical Parametric Amplifier (OPerA-SOLO) for the photoexcitation of the sample. A perfect pump-probe delay was maintained by placing a delay stage in the probe beam path. Monochromatic probe light passes through a sapphire crystal generating visible probe pulses. The probe beam passes through sample dispersion and falls upon fiber-coupled CMOS detectors connected with the computer system. The chirping and fitting of the collected TA data was done in surface explorer software.

4.5.3. Cell culture.

L929 mouse fibroblast, glioblastoma C6 cells and Human umbilical vein endothelial cells (HUVECs) were cultured and maintained in Dulbecco's modified Eagle's medium (DMEM) supplemented with 10% fetal bovine serum (FBS) and 1% antibiotics antimycotic solution at 37 OC in a humidified incubator containing 5% CO_2.

4.5.4. *In vitro* biocompatibility.[54,55]

The biocompatibility of **NC2**, **NC3**, and **NC7** was evaluated using an MTT assay against HUVEC cells, whereas **NC6** was assessed against L929 mouse fibroblast cells. 200 µL of cells were seeded in a 96-well flat culture plate at a density of 2.5×10^4 cells per well and cultured for 24 h at 37 °C under 5% CO_2. To analyse biocompatibility, different concentrations of **NC2**, **NC3**, and **NC7** (0-40 µg/mL) and **NC6** (0-200 µg/mL) were added to the cells in triplicate and incubated for 48 hours. The cells were washed with prewarmed 1X PBS thrice to remove traces of the sample. 20 µL MTT solutions (5 mg/mL in PBS) diluted with 180 µL media were added to the wells and incubated for 4 hours, after which the plates

were centrifuged at 1500 rpm for 5 min at room temperature. 150 µL DMSO was added to each well to dissolve the formazan crystals, and all the wells were aspirated well before taking absorbance. The absorbance of the suspension was measured at 570 nm on an ELISA reader. The cell viability was calculated using the following equation 4.1.

$$Cell\ Viability\ (\%) = \frac{Absorbance\ of\ the\ treated\ cells}{Absorbance\ of\ the\ control\ cells} \times 100 \qquad (4.1)$$

4.5.5. *In vitro* ROS Assay.[54,55]

In vitro ROS was measured using 2,7-dichlorofluorescein diacetate (DCFDA), a non-fluorescent dye that can readily diffuse into cells and cleave by the intracellular esterases to form 2,7-dichlorofluorescein (DCF) by the ROS generated in cells. C6 cells were incubated with **NC3** and **NC7** for 24 hours and then exposed to white light from a LED for 20 minutes. Cells treated with gold nanoparticle alone were taken as control. After 24 hours, cells were washed with Hank's buffer and incubated with DCFDA (50 µg in 2mL serum-free media) for 1 hour. Then the cells were rewashed with Hank's buffer to remove any excess dye. Then the cells were treated with lysis buffer (0.1M Tris HCl containing 1% Tween 20). The supernatant of lysed cells was evaluated for fluorescence intensity. ROS amounts directly correlate with the excitation wavelength of 488 nm and emission wavelength of 535 nm, respectively.

4.5.6. *In vitro* photodynamic therapy.[54,55]

Different concentrations of **NC2**, **NC3**, **NC6** and **NC7** were tested against C6 using the MTT assay. Cells were seeded at 2.5×10^4 cells per well in a 96-well flat culture plate at 37 °C under 5% CO_2 for 24 hours. The cells were then treated with different concentrations of **NC2**, **NC3**, and **NC7** (0-40 µg/mL, each) and **NC6** (0-200 µg/mL) prepared in media the following day. After 24 hours, the cells were exposed to white light for 20 minutes for **NC2**, **NC3**, **NC7**, and **NC6**, and then incubated for 24 hours in the CO_2 humidified incubator. The cells were washed with prewarmed PBS buffer thrice to remove traces of the sample. 20 µL MTT (5 mg/mL in PBS buffer) diluted with 180 µL media was added to the wells and incubated for 4 hours. After 4 hours, the plates were centrifuged at 1500 rpm for 5 minutes at room temperature. 150 µL DMSO was added to each well to dissolve the formazan crystals and all the wells were aspirated well before taking absorbance. The absorbance of the suspension was measured at 570 nm on a microplate reader. The cell viability was calculated using the same equation 4.2.

4.5.7. Cellular uptake study.[54,55]

C6 glioblastoma cells were seeded at a density of 5×10^4 cells in a 35 mm Petri dish on a coverslip, and **NC3** (100 µg/mL) and **NC7** (10 and 100 µg/mL) were added to it after 24 hours. Further, C6 glioblastoma cells and L929 cells were seeded at a density of 1×10^4 cells in a 35 mm Petri dish on a coverslip, and **NC6** (5 µg/mL) was added after 24 hours. The next day, the cells were washed with PBS and fixed with 3.7% paraformaldehyde, followed by staining with Hoechst 33342. The coverslips were mounted on a glass slide and allowed to air dry and observed under Zeiss confocal microscope.

Further, the amount of gold internalized by C6 cells was quantified using ICP-MS to determine the intracellular concentration of **NC7**. Briefly, the cells were incubated with different concentrations of **NC7** for 24 hrs. Before harvesting, the cells were washed thrice to remove unbound nanoparticles. The cells were digested with ICP grade 35% HNO_3, followed by heating at 50 °C until the colour of the solution became transparent. Next, the solution was allowed to cool and diluted with 9 mL of Milli-Q water before analysis.

4.5.8. Live/Dead cell staining assay.[54,55]

Fluorescein diacetate (FDA)/propidium iodide (PI) staining was used to determine the number of viable and nonviable cells. 5×10^4 cells were seeded in a 35 mm Petri dish and treated with **NC3** and **NC7** followed by a similar method as described above, followed by white light exposure.

4.5.9. Annexin V apoptosis assay.[54,55]

Apoptosis detection was performed using the Annexin V FITC and PI, Apoptosis Detection Kit (Invitrogen). C6 cells were seeded at a density of 1×10^5 cells and treated with **NC3** and **NC7**, followed by white light exposure. Post-treatment, the cells were harvested and washed with PBS. The cell pellet was resuspended in 1X- Annexin V binding buffer, followed by staining with Annexin V and PI for 15 minutes at room temperature in the dark. The distribution of cell population in different quadrants was analysed with quadrant statistics. The lower left quadrant depicts the percentage of viable cells, the lower right quadrant depicts the early apoptotic population, the upper right quadrant depicts late-apoptotic cells and the upper left quadrant represents the percentage of necrotic cells.

4.5.10. Cell cycle analysis.[54,55]

PI/RNase staining solution was used to determine the distribution of cells in different phases based on the DNA content of the cells by flow cytometry analysis. Briefly, C6 cells were seeded into a 35 mm Petri dish at a cell density of 1×10^5 cells, followed by treatment with **NC2**, **NC3**, and **NC7**, followed by treatment with white light. Before fixation, cells were harvested and washed with PBS. According to the manufacturer's protocol, the fixed cells were incubated with 0.5 mL of PI/ RNase staining solution for 20 min in the dark at room temperature. The samples were analysed using a 488/532 nm bandpass filter under a flow cytometer.

4.6. References.

[1] J. H. Han, D. Kim, T.-W. Lee, Y. Jeon, H. S. Lee, K. C. Choi, *ACS Photonics* **2018**, *5*, 3322–3330.

[2] Z. Li, A. W. Clark, J. M. Cooper, *ACS Nano* **2016**, *10*, 492–498.

[3] K. Wonner, M. V. Evers, K. Tschulik, *J. Am. Chem. Soc.* **2018**, *140*, 12658–12661.

[4] S. Laing, L. E. Jamieson, K. Faulds, D. Graham, *Nat. Rev. Chem.* **2017**, *1*, 1–19.

[5] Y. Liu, Z. Yang, X. Huang, G. Yu, S. Wang, Z. Zhou, Z. Shen, W. Fan, Y. Liu, M. Davisson, H. Kalish, G. Niu, Z. Nie, X. Chen, *ACS Nano* **2018**, *12*, 8129–8137.

[6] J. Reguera, D. J. de Aberasturi, M. Henriksen-Lacey, J. Langer, A. Espinosa, B. Szczupak, C. Wilhelm, L. M. Liz-Marzán, *Nanoscale* **2017**, *9*, 9467–9480.

[7] K. Wang, L. Shangguan, Y. Liu, L. Jiang, F. Zhang, Y. Wei, Y. Zhang, Z. Qi, K. Wang, S. Liu, *Anal. Chem.* **2017**, *89*, 7262–7268.

[8] J. F. Lovell, T. W. B. Liu, J. Chen, G. Zheng, *Chem. Rev.* **2010**, *110*, 2839–2857.

[9] A. B. Taylor, P. Zijlstra, *ACS Sensors* **2017**, *2*, 1103–1122.

[10] H. Chen, Z. Cheng, X. Zhou, R. Wang, F. Yu, *Anal. Chem.* **2022**, *94*, 143–164.

[11] M. F. Cardinal, E. V. Ende, R. A. Hackler, M. O. McAnally, P. C. Stair, G. C. Schatz, R. P. V. Duyne, *Chem. Soc. Rev.* **2017**, *46*, 3886–3903.

[12] C. E. Talley, J. B. Jackson, C. Oubre, N. K. Grady, C. W. Hollars, S. M. Lane, T. R. Huser, P. Nordlander, N. J. Halas, *Nano Lett.* **2005**, *5*, 1569–1574.

[13] T. Ming, H. Chen, R. Jiang, Q. Li, J. Wang, *J. Phys. Chem. Lett.* **2012**, *3*, 191–202.

[14] P. Anger, P. Bharadwaj, L. Novotny, *Phys. Rev. Lett.* **2006**, *96*, 113002.

[15] K. Aslan, I. Gryczynski, J. Malicka, E. Matveeva, J. R. Lakowicz, C. D. Geddes, *Curr. Opin. Biotechnol.* **2005**, *16*, 55–62.

[16] M. Lessard-Viger, M. Rioux, L. Rainville, D. Boudreau, *Nano Lett.* **2009**, *9*, 3066–3071.

[17] Y. Zhang, K. Aslan, M. J. R. Previte, S. N. Malyn, C. D. Geddes, *J. Phys. Chem. B* **2006**, *110*, 25108–25114.

[18] N. Macia, R. Bresoli-Obach, S. Nonell, B. Heyne, *J. Am. Chem. Soc.* **2019**, *141*, 684–692.

[19] H. Zhang, H. Li, H. Fan, J. Yan, D. Meng, S. Hou, Y. Ji, X. Wu, *Nano Res.* **2018**, *11*, 1456–1469.

[20] B. Hu, X. Cao, K. Nahan, J. Caruso, H. Tang, P. Zhang, *J. Mater. Chem. B* **2014**, *2*, 7073–7081.

[21] Y. Zhang, K. Aslan, M. J. R. Previte, C. D. Geddes, *Proc. Natl. Acad. Sci. U.S.A.* **2008**, *105*, 1798–1802.

[22] P. R. Ogilby, *Chem. Soc. Rev.* **2010**, *39*, 3181–3209.

[23] M. C. DeRosa, R. J. Crutchley, *Coord. Chem. Rev.* **2002**, *233–234*, 351–371.

[24] J. Dang, H. He, D. Chen, L. Yin, *Biomater. Sci.* **2017**, *5*, 1500–1511.

[25] A. Escudero, C. Carrillo-Carrión, M. C. Castillejos, E. Romero-Ben, C. Rosales-Barrios, N. Khiar, *Mater. Chem. Front.* **2021**, *5*, 3788–3812.

[26] M. Lan, S. Zhao, W. Liu, C.-S. Lee, W. Zhang, P. Wang, *Adv. Healthcare Mater.* **2019**, *8*, 1900132.

[27] P. G. Calavia, G. Bruce, L. Pérez-García, D. A. Russell, *Photochem. Photobiol. Sci.* **2018**, *17*, 1534–1552.

[28] X. Li, S. Kolemen, J. Yoon, E. U. Akkaya, *Adv. Funct. Mater.* **2017**, *27*, 1604053.

[29] Y. Guo, S. Rogelj, P. Zhang, *Nanotechnology* **2010**, *21*, 065102.

[30] A. Manfrin, N. Borduas-Dedekind, K. Lau, K. McNeill, *J. Org. Chem.* **2019**, *84*, 2439–2447.

[31] D. Han, Z. Bao, H. Xing, Y. Yang, Q. Ren, Z. Zhang, *Nanoscale* **2017**, *9*, 6026–6032.

[32] C. Chen, W. Ma, J. Zhao, *Chem. Soc. Rev.* **2010**, *39*, 4206–4219.

[33] R. Gerdes, D. Wöhrle, W. Spiller, G. Schneider, G. Schnurpfeil, G. Schulz-Ekloff, *J. Photochem. Photobiol., A* **1997**, *111*, 65–74.

[34] P. Esser, B. Pohlmann, H.-D. Scharf, *Angew. Chem. Int. Ed.* **1994**, *33*, 2009–2023.

[35] M. P. Brynildsen, J. A. Winkler, C. S. Spina, I. C. MacDonald, J. J. Collins, *Nat. Biotechnol.* **2013**, *31*, 160–165.

[36] Y. Zhang, K. Aslan, M. J. R. Previte, C. D. Geddes, *J. Fluoresc.* **2007**, *17*, 345–349.

[37] W. Hu, P. N. Prasad, W. Huang, *Acc. Chem. Res.* **2021**, *54*, 697–706.

[38] M. Maiuri, M. Garavelli, G. Cerullo, *J. Am. Chem. Soc.* **2020**, *142*, 3–15.

[39] X. Miao, W. Hu, T. He, H. Tao, Q. Wang, R. Chen, L. Jin, H. Zhao, X. Lu, Q. Fan, W. Huang, *Chem. Sci.* **2019**, *10*, 3096–3102.

[40] C. Jin, E. Y. Ma, O. Karni, E. C. Regan, F. Wang, T. F. Heinz, *Nature Nanotech.* **2018**, *13*, 994–1003.

[41] F. M. Dumanoğulları, Y. Tutel, B. Küçüköz, G. Sevinç, A. Karatay, H. Yılmaz, M. Hayvali, A. Elmali, *J. Photochem. Photobiol., A* **2019**, *373*, 116–121.

[42] W. Wu, H. Guo, W. Wu, S. Ji, J. Zhao, *J. Org. Chem.* **2011**, *76*, 7056–7064.

[43] B. C. D. Simone, G. Mazzone, W. Sang-aroon, T. Marino, N. Russo, E. Sicilia, *Phys. Chem. Chem. Phys.* **2019**, *21*, 3446–3452.

[44] S. J. Chadwick, D. Salah, P. M. Livesey, M. Brust, M. Volk, *J. Phys. Chem. C* **2016**, *120*, 10647–10657.

[45] P. P. P. Kumar, P. Yadav, A. Shanavas, S. Thurakkal, J. Joseph, P. P. Neelakandan, *Chem. Commun.* **2019**, *55*, 5623–5626.

[46] H. Chen, L. Shao, K. C. Woo, J. Wang, H.-Q. Lin, *J. Phys. Chem. C* **2012**, *116*, 14088–14095.

[47] G. V. Hartland, *Chem. Rev.* **2011**, *111*, 3858–3887.

[48] X.-F. Zhang, X. Yang, *J. Phys. Chem. B* **2013**, *117*, 5533–5539.

[49] J. Hodak, I. Martini, G. V. Hartland, *Chem. Phys. Lett.* **1998**, *284*, 135–141.

[50] R. Krahne, G. Morello, A. Figuerola, C. George, S. Deka, L. Manna, *Phys. Rep.* **2011**, *501*, 75–221.

[51] J. H. Hodak, A. Henglein, G. V. Hartland, *J. Phys. Chem. B* **2000**, *104*, 9954–9965.

[52] G. P. Wiederrecht, G. A. Wurtz, J. Hranisavljevic, *Nano Lett.* **2004**, *4*, 2121–2125.

[53] A. Shukla, G. Kaur, K. J. Babu, N. Ghorai, T. Goswami, A. Kaur, H. N. Ghosh, *J. Phys. Chem. Lett.* **2020**, *11*, 6344–6352.

[54] P. Yadav, Mimansa, K. Kailasam, A. Shanavas, *ACS Appl. Bio Mater.* **2022**, *5*, 1169–1178.

[55] P. Yadav, C. Zhang, A. K. Whittaker, K. Kailasam, A. Shanavas, *ACS Biomater. Sci. Eng.* **2019**, *5*, 6590–6601.

List of Publications

1) Hot Electron Migration from Gold Nanoparticle to an Organic Molecule Enhances Luminescence and Photosensitization Properties of a pH Activatable Plasmon-Molecule Coupled Nanocomposite. **A. Rahman**, T. Goswami, N. Tyagi, H. N. Ghosh*, P. P. Neelakandan*, *J. Photochem. Photobiol. A: Chemistry* **2022**, *432*, 114067.

2) Gold-BODIPY Nanoparticles with Luminescence and Photosensitization Properties for Photodynamic Therapy and Cell Imaging. **A. Rahman**,[†] P. P. P. Kumar,[†] P. Yadav,[†] T. Goswami,[†] A. Shanavas,* H. N. Ghosh,* and P. P. Neelakandan*, *ACS Appl. Nano Mater*. **2022**, *5*, 6532-6542.

3) Fine-Tuning Plasmon-Molecule Interactions in Gold-BODIPY Nanocomposites: The Role of Chemical Structure and Noncovalent Interactions. P. P. P. Kumar,[†] **A. Rahman**,[†] T. Goswami, H. N. Ghosh*, P. P. Neelakandan*, *ChemPlusChem* **2021**, *86*, 87-94.

4) Synthesis and Anti-Proliferative Activity of a Triazole-Fused Thymidine Analogue. **A. Rahman**, P. Sharma,[†] N. Kaur,[†] A. Shanavas*, and P. P. Neelakandan*, *ChemistrySelect* **2020**, *5*, 5473-5478.

5) Gold-BODIPY Nanocomposite deposited on Thin Film: Efficient degradation of Pesticides and Water Pollutants. H. Jangra, **A. Rahman**, P. P. Neelakandan*, (to be communicated).

6) Multi-stimuli Responsive Fluorescence Switching of Positional Isomers of Naphthalidenimine-Boron Complex. K. Naim, **A. Rahman**, S. C. Sahoo, P. P. Neelakandan* (to be communicated).

† Equal contribution

Workshop and Conferences Attended

1) "Plasmon-Molecule Coupling Modulates Photophysical Properties of Dye-loaded Gold Nanoparticles", an oral presented at the *2nd Research Scholars Day (RSD) at Institute of Nano Science and Technology*, INST Mohali, India on 31st March and 1st April, 2022.

2) "Simultaneous FRET and Plasmon-Molecule Interactions in a Multi-chromophoric Gold-BODIPY Nanocomposite", a poster presented at the *NanoDay@INST-2021at Institute of Nano Science and Technology*, INST Mohali, India on 31st December, 2021.

3) "Role of supramolecular interactions in fine tuning plasmon-molecule interactions in Au-BODIPY nanocomposites", a poster presented at the *International Conference on Nano Science and Technology (ICONSAT-2020) at Biswa Bangla Convention Centre*, Kolkata, India on 5th-7th March, 2020.

4) "Novel Nucleoside and Nucleic Acid Analogues based on Thymidine for Therapeutic Applications", a poster presented at the *1st CRIKC Chemistry Symposium (CCS 2019)*, IISER Mohali, India on 2nd and 3rd November, 2019.

5) Participated in the *MHRD-Global Initiative of Academic Networks (GIAN) Course on "DNA Nanoarchitecture"* at Jamia Millia Islamia University, Delhi, India from 20th to 28th February, 2017.

Permissions from Journals for reuse of content in Thesis

CCC
RightsLink

Surface plasmon-driven photocatalysis in ambient, aqueous and high-vacuum monitored by SERS and TERS

Author: Zhenglong Zhang,Ping Xu,Xianzhong Yang,Wenjie Liang,Mengtao Sun
Publication: Journal of Photochemistry and Photobiology C: Photochemistry Reviews
Publisher: Elsevier
Date: June 2016

Order Completed

Thank you for your order.

This Agreement between Mr. Atikur Rahman ("You") and Elsevier ("Elsevier") consists of your license details and the terms and conditions provided by Elsevier and Copyright Clearance Center.

Your confirmation email will contain your order number for future reference.

License Number	5352040305929	🖶 Printable Details
License date	Jul 18, 2022	

☑ Licensed Content

Licensed Content Publisher	Elsevier
Licensed Content Publication	Journal of Photochemistry and Photobiology C: Photochemistry Reviews
Licensed Content Title	Surface plasmon-driven photocatalysis in ambient, aqueous and high-vacuum monitored by SERS and TERS
Licensed Content Author	Zhenglong Zhang,Ping Xu,Xianzhong Yang,Wenjie Liang,Mengtao Sun
Licensed Content Date	Jun 1, 2016
Licensed Content Volume	27
Licensed Content Issue	n/a
Licensed Content Pages	13

📋 Order Details

Type of Use	reuse in a thesis/dissertation
Portion	figures/tables/illustrations
Number of figures/tables/illustrations	1
Format	both print and electronic
Are you the author of this Elsevier article?	No
Will you be translating?	No

📄 About Your Work

Title	Modulating Photophysical Properties of Dye-loaded Gold Nanoparticles through Plasmon-molecule Coupling
Institution name	Inst Mohali
Expected presentation date	Dec 2022

📁 Additional Data

Portions	Fig.1

📍 Requestor Location

Requestor Location	Mr. Atikur Rahman
Sector-81
SAS Nagar
Mohali
Mohali, 140306
India
Attn: Institute of Nano Science and Technology

🖩 Tax Details

Publisher Tax ID	GB 494 6272 12

$ Price

Total	0.00 USD

Total: 0.00 USD

CLOSE WINDOW   ORDER MORE

CCC
RightsLink

Plasmon–molecule interactions

Author:
Huanjun Chen,Tian Ming,Lei Zhao,Feng Wang,Ling-Dong Sun,Jianfang Wang,Chun-Hua Yan
Publication: Nano Today
Publisher: Elsevier
Date: 2010

Copyright © 2010 Elsevier Ltd. All rights reserved.

Order Completed

Thank you for your order.

This Agreement between Mr. Atikur Rahman ("You") and Elsevier ("Elsevier") consists of your license details and the terms and conditions provided by Elsevier and Copyright Clearance Center.

Your confirmation email will contain your order number for future reference.

License Number	5352040746159	🖨 Printable Details
License date	Jul 18, 2022	

☑ Licensed Content

Licensed Content Publisher	Elsevier
Licensed Content Publication	Nano Today
Licensed Content Title	Plasmon–molecule interactions
Licensed Content Author	Huanjun Chen,Tian Ming,Lei Zhao,Feng Wang,Ling-Dong Sun,Jianfang Wang,Chun-Hua Yan
Licensed Content Date	Jan 1, 2010
Licensed Content Volume	5
Licensed Content Issue	5
Licensed Content Pages	12

📋 Order Details

Type of Use	reuse in a thesis/dissertation
Portion	figures/tables/illustrations
Number of figures/tables/illustrations	4
Format	both print and electronic
Are you the author of this Elsevier article?	No
Will you be translating?	No

📄 About Your Work

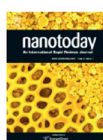|	
Title	Modulating Photophysical Properties of Dye-loaded Gold Nanoparticles through Plasmon-molecule Coupling
Institution name	Inst Mohali
Expected presentation date	Dec 2022

📁 Additional Data

Portions	1

📍 Requestor Location

Requestor Location	Mr. Atikur Rahman
Sector-81
SAS Nagar
Mohali
Mohali, 140306
India
Attn: Institute of Nano Science and Technology

📋 Tax Details

Publisher Tax ID	GB 494 6272 12

$ Price

Total	0.00 USD

Total: 0.00 USD

CLOSE WINDOW   ORDER MORE

🏠 Home   ❓ Help ⌄   📞 Live Chat   👤 Atikur Rahman ⌄

Gold and Silver Nanoparticles in Sensing and Imaging: Sensitivity of Plasmon Response to Size, Shape, and Metal Composition

ACS Publications
Most Trusted. Most Cited. Most Read.

Author: Kyeong-Seok Lee, Mostafa A. El-Sayed

Publication: The Journal of Physical Chemistry B

Publisher: American Chemical Society

Date: Oct 1, 2006

Copyright © 2006, American Chemical Society

PERMISSION/LICENSE IS GRANTED FOR YOUR ORDER AT NO CHARGE

This type of permission/license, instead of the standard Terms and Conditions, is sent to you because no fee is being charged for your order. Please note the following:

- Permission is granted for your request in both print and electronic formats, and translations.
- If figures and/or tables were requested, they may be adapted or used in part.
- Please print this page for your records and send a copy of it to your publisher/graduate school.
- Appropriate credit for the requested material should be given as follows: "Reprinted (adapted) with permission from {COMPLETE REFERENCE CITATION}. Copyright {YEAR} American Chemical Society." Insert appropriate information in place of the capitalized words.
- One-time permission is granted only for the use specified in your RightsLink request. No additional uses are granted (such as derivative works or other editions). For any uses, please submit a new request.

If credit is given to another source for the material you requested from RightsLink, permission must be obtained from that source.

BACK   CLOSE WINDOW

🏠 Home   ❓ Help ⌄   📞 Live Chat   👤 Atikur Rahman ⌄

Shape- and Size-Dependent Refractive Index Sensitivity of Gold Nanoparticles

ACS Publications
Most Trusted. Most Cited. Most Read.

Author: Huanjun Chen, Xiaoshan Kou, Zhi Yang, et al

Publication: Langmuir

Publisher: American Chemical Society

Date: May 1, 2008

Copyright © 2008, American Chemical Society

PERMISSION/LICENSE IS GRANTED FOR YOUR ORDER AT NO CHARGE

This type of permission/license, instead of the standard Terms and Conditions, is sent to you because no fee is being charged for your order. Please note the following:

- Permission is granted for your request in both print and electronic formats, and translations.
- If figures and/or tables were requested, they may be adapted or used in part.
- Please print this page for your records and send a copy of it to your publisher/graduate school.
- Appropriate credit for the requested material should be given as follows: "Reprinted (adapted) with permission from {COMPLETE REFERENCE CITATION}. Copyright {YEAR} American Chemical Society." Insert appropriate information in place of the capitalized words.
- One-time permission is granted only for the use specified in your RightsLink request. No additional uses are granted (such as derivative works or other editions). For any uses, please submit a new request.

If credit is given to another source for the material you requested from RightsLink, permission must be obtained from that source.

BACK   CLOSE WINDOW

Home   Help ∨   Email Support   Sign in   Create Account

Coherent Coupling of Molecular Excitons to Electronic Polarizations of Noble Metal Nanoparticles

ACS Publications
Most Trusted. Most Cited. Most Read.

Author: Gary P. Wiederrecht, Gregory A. Wurtz, Jasmina Hranisavljevic

Publication: Nano Letters

Publisher: American Chemical Society

Date: Nov 1, 2004

Copyright © 2004, American Chemical Society

Home   Help ∨   Email Support   Sign in   Create Account

Plexcitonic Nanoparticles: Plasmon–Exciton Coupling in Nanoshell–J-Aggregate Complexes

ACS Publications
Most Trusted. Most Cited. Most Read.

Author: Nche T. Fofang, Tae-Ho Park, Oara Neumann, et al

Publication: Nano Letters

Publisher: American Chemical Society

Date: Oct 1, 2008

Copyright © 2008, American Chemical Society

CCC
RightsLink

Coupling between Molecular and Plasmonic Resonances in Freestanding Dye–Gold Nanorod Hybrid Nanostructures

ACS Publications
Most Trusted. Most Cited. Most Read.

Author: Weihai Ni, Zhi Yang, Huanjun Chen, et al

Publication: Journal of the American Chemical Society

Publisher: American Chemical Society

Date: May 1, 2008

Copyright © 2008, American Chemical Society

PERMISSION/LICENSE IS GRANTED FOR YOUR ORDER AT NO CHARGE

This type of permission/license, instead of the standard Terms and Conditions, is sent to you because no fee is being charged for your order. Please note the following:

- Permission is granted for your request in both print and electronic formats, and translations.
- If figures and/or tables were requested, they may be adapted or used in part.
- Please print this page for your records and send a copy of it to your publisher/graduate school.
- Appropriate credit for the requested material should be given as follows: "Reprinted (adapted) with permission from {COMPLETE REFERENCE CITATION}. Copyright {YEAR} American Chemical Society." Insert appropriate information in place of the capitalized words.
- One-time permission is granted only for the use specified in your RightsLink request. No additional uses are granted (such as derivative works or other editions). For any uses, please submit a new request.

If credit is given to another source for the material you requested from RightsLink, permission must be obtained from that source.

BACK   CLOSE WINDOW

CCC
RightsLink

Plexcitons: The Role of Oscillator Strengths and Spectral Widths in Determining Strong Coupling

ACS Publications
Most Trusted. Most Cited. Most Read.

Author: Reshmi Thomas, Anoop Thomas, Saranya Pullanchery, et al

Publication: ACS Nano

Publisher: American Chemical Society

Date: Jan 1, 2018

Copyright © 2018, American Chemical Society

PERMISSION/LICENSE IS GRANTED FOR YOUR ORDER AT NO CHARGE

This type of permission/license, instead of the standard Terms and Conditions, is sent to you because no fee is being charged for your order. Please note the following:

- Permission is granted for your request in both print and electronic formats, and translations.
- If figures and/or tables were requested, they may be adapted or used in part.
- Please print this page for your records and send a copy of it to your publisher/graduate school.
- Appropriate credit for the requested material should be given as follows: "Reprinted (adapted) with permission from {COMPLETE REFERENCE CITATION}. Copyright {YEAR} American Chemical Society." Insert appropriate information in place of the capitalized words.
- One-time permission is granted only for the use specified in your RightsLink request. No additional uses are granted (such as derivative works or other editions). For any uses, please submit a new request.

If credit is given to another source for the material you requested from RightsLink, permission must be obtained from that source.

BACK   CLOSE WINDOW

Rightslink® by Copyright Clearance Center

CCC
RightsLink

Strong Polarization Dependence of Plasmon-Enhanced Fluorescence on Single Gold Nanorods

Author: Tian Ming, Lei Zhao, Zhi Yang, et al

Publication: Nano Letters

Publisher: American Chemical Society

Date: Nov 1, 2009

Copyright © 2009, American Chemical Society

PERMISSION/LICENSE IS GRANTED FOR YOUR ORDER AT NO CHARGE

This type of permission/license, instead of the standard Terms and Conditions, is sent to you because no fee is being charged for your order. Please note the following:

- Permission is granted for your request in both print and electronic formats, and translations.
- If figures and/or tables were requested, they may be adapted or used in part.
- Please print this page for your records and send a copy of it to your publisher/graduate school.
- Appropriate credit for the requested material should be given as follows: "Reprinted (adapted) with permission from {COMPLETE REFERENCE CITATION}. Copyright {YEAR} American Chemical Society." Insert appropriate information in place of the capitalized words.
- One-time permission is granted only for the use specified in your RightsLink request. No additional uses are granted (such as derivative works or other editions). For any uses, please submit a new request.

If credit is given to another source for the material you requested from RightsLink, permission must be obtained from that source.

BACK   CLOSE WINDOW

Rightslink® by Copyright Clearance Center

CCC
RightsLink

Gold–BODIPY Nanoparticles with Luminescence and Photosensitization Properties for Photodynamic Therapy and Cell Imaging

Author:
Atikur Rahman, Panangattukara Prabhakaran Praveen Kumar, Pranjali Yadav, et al

Publication: ACS Applied Nano Materials

Publisher: American Chemical Society

Date: May 1, 2022

Copyright © 2022, American Chemical Society

PERMISSION/LICENSE IS GRANTED FOR YOUR ORDER AT NO CHARGE

This type of permission/license, instead of the standard Terms and Conditions, is sent to you because no fee is being charged for your order. Please note the following:

- Permission is granted for your request in both print and electronic formats, and translations.
- If figures and/or tables were requested, they may be adapted or used in part.
- Please print this page for your records and send a copy of it to your publisher/graduate school.
- Appropriate credit for the requested material should be given as follows: "Reprinted (adapted) with permission from {COMPLETE REFERENCE CITATION}. Copyright {YEAR} American Chemical Society." Insert appropriate information in place of the capitalized words.
- One-time permission is granted only for the use specified in your RightsLink request. No additional uses are granted (such as derivative works or other editions). For any uses, please submit a new request.

If credit is given to another source for the material you requested from RightsLink, permission must be obtained from that source.

BACK   CLOSE WINDOW

SPRINGER NATURE

Large single-molecule fluorescence enhancements produced by a bowtie nanoantenna

Author: Anika Kinkhabwala et al

Publication: Nature Photonics

Publisher: Springer Nature

Date: Oct 18, 2009

Copyright © 2009, Nature Publishing Group

Order Completed

Thank you for your order.

This Agreement between Mr. Atikur Rahman ("You") and Springer Nature ("Springer Nature") consists of your license details and the terms and conditions provided by Springer Nature and Copyright Clearance Center.

Your confirmation email will contain your order number for future reference.

License Number	5352320260211	🖨 Printable Details
License date	Jul 19, 2022	

☑ Licensed Content

Licensed Content Publisher	Springer Nature
Licensed Content Publication	Nature Photonics
Licensed Content Title	Large single-molecule fluorescence enhancements produced by a bowtie nanoantenna
Licensed Content Author	Anika Kinkhabwala et al
Licensed Content Date	Oct 18, 2009

🗐 Order Details

Type of Use	Thesis/Dissertation
Requestor type	non-commercial (non-profit)
Format	print and electronic
Portion	figures/tables/illustrations
Number of figures/tables/illustrations	1
High-res required	no
Will you be translating?	no
Circulation/distribution	1 - 29
Author of this Springer Nature content	no

📄 About Your Work

Title	Modulating Photophysical Properties of Dye-loaded Gold Nanoparticles through Plasmon-molecule Coupling
Institution name	Inst Mohali
Expected presentation date	Dec 2022

📁 Additional Data

Portions	1

📍 Requestor Location

Requestor Location	Mr. Atikur Rahman Sector-81 SAS Nagar Mohali Mohali, 140306 India Attn: Institute of Nano Science and Technology

🗐 Tax Details

$ Price

Total	0.00 USD

Total: 0.00 USD

CLOSE WINDOW   ORDER MORE

CCC
RightsLink

Thousand-fold Enhancement of Single-Molecule Fluorescence Near a Single Gold Nanorod

Author: Haifeng Yuan, Saumyakanti Khatua, Peter Zijlstra, et al

Publication: Angewandte Chemie International Edition

Publisher: John Wiley and Sons

Date: Dec 6, 2012

Copyright © 2013 WILEY-VCH Verlag GmbH & Co. KGaA, Weinheim

Order Completed

Thank you for your order.

This Agreement between Mr. Atikur Rahman ("You") and John Wiley and Sons ("John Wiley and Sons") consists of your license details and the terms and conditions provided by John Wiley and Sons and Copyright Clearance Center.

Your confirmation email will contain your order number for future reference.

License Number	5352320757350	🖨 Printable Details
License date	Jul 19, 2022	

☑ Licensed Content

Licensed Content Publisher	John Wiley and Sons
Licensed Content Publication	Angewandte Chemie International Edition
Licensed Content Title	Thousand-fold Enhancement of Single-Molecule Fluorescence Near a Single Gold Nanorod
Licensed Content Author	Haifeng Yuan, Saumyakanti Khatua, Peter Zijlstra, et al
Licensed Content Date	Dec 6, 2012
Licensed Content Volume	52
Licensed Content Issue	4
Licensed Content Pages	5

📋 Order Details

Type of use	Dissertation/Thesis
Requestor type	University/Academic
Format	Print and electronic
Portion	Figure/table
Number of figures/tables	1
Will you be translating?	No

📄 About Your Work

Title	Modulating Photophysical Properties of Dye-loaded Gold Nanoparticles through Plasmon-molecule Coupling
Institution name	Inst Mohali
Expected presentation date	Dec 2022

📁 Additional Data

Portions	1

📍 Requestor Location

Requestor Location	Mr. Atikur Rahman Sector-81 SAS Nagar Mohali Mohali, 140306 India Attn: Institute of Nano Science and Technology

🖥 Tax Details

Publisher Tax ID	EU826007151

$ Price

Total	0.00 USD

Would you like to purchase the full text of this article? If so, please continue on to the content ordering system located here: Purchase PDF
If you click on the buttons below or close this window, you will not be able to return to the content ordering system.

Total: 0.00 USD

CLOSE WINDOW   ORDER MORE

Quantitative super-resolution imaging uncovers reactivity patterns on single nanocatalysts

SPRINGER NATURE

Author: Xiaochun Zhou et al
Publication: Nature Nanotechnology
Publisher: Springer Nature
Date: Feb 19, 2012

Copyright © 2012, Nature Publishing Group

Order Completed

Thank you for your order.

This Agreement between Mr. Atikur Rahman ("You") and Springer Nature ("Springer Nature") consists of your license details and the terms and conditions provided by Springer Nature and Copyright Clearance Center.

Your confirmation email will contain your order number for future reference.

License Number	5352320943602	🖨 Printable Details
License date	Jul 19, 2022	

✓ Licensed Content

Licensed Content Publisher	Springer Nature
Licensed Content Publication	Nature Nanotechnology
Licensed Content Title	Quantitative super-resolution imaging uncovers reactivity patterns on single nanocatalysts
Licensed Content Author	Xiaochun Zhou et al
Licensed Content Date	Feb 19, 2012

📋 Order Details

Type of Use	Thesis/Dissertation
Requestor type	non-commercial (non-profit)
Format	print and electronic
Portion	figures/tables/illustrations
Number of figures/tables/illustrations	1
High-res required	no
Will you be translating?	no
Circulation/distribution	1 - 29
Author of this Springer Nature content	no

📄 About Your Work

Title	Modulating Photophysical Properties of Dye-loaded Gold Nanoparticles through Plasmon-molecule Coupling
Institution name	Inst Mohali
Expected presentation date	Dec 2022

📁 Additional Data

Portions	1

📍 Requestor Location

Requestor Location	Mr. Atikur Rahman Sector-81 SAS Nagar Mohali Mohali, 140306 India Attn: Institute of Nano Science and Technology

📑 Tax Details

💲 Price

Total	0.00 USD

Total: 0.00 USD

CLOSE WINDOW   ORDER MORE

CCC | Marketplace™

Order Number: 1248774
Order Date: 19 Jul 2022

Payment Information

Atikur Rahman
atikur.ph16238@inst.ac.in
Payment method: Invoice

Billing Address:
Mr. Atikur Rahman
Sector-81
SAS Nagar
Mohali
Mohali, 140306
India

+91 8791788951
atikur.ph16238@inst.ac.in

Customer Location:
Mr. Atikur Rahman
Sector-81
SAS Nagar
Mohali
Mohali, 140306
India

Order Details

1. Chemical communications : Chem comm

Article: A three-component supramolecular nanocomposite as a heavy-atom-free photosensitizer.

Billing Status: Open

Order License ID	1248774-1	**Type of use**	Republish in a thesis/dissertation
Order detail status	Completed		
ISSN	1359-7345	**Publisher**	THE SOCIETY,
		Portion	Chart/graph/table/figure

0.00 USD
Republication Permission

LICENSED CONTENT

Publication Title	Chemical communications : Chem comm	**Publication Type**	Journal
		Start Page	5623
Article Title	A three-component supramolecular nanocomposite as a heavy-atom-free photosensitizer.	**End Page**	5626
		Issue	39
		Volume	55
Author/Editor	ROYAL SOCIETY OF CHEMISTRY (GREAT BRITAIN)	**URL**	http://www.rsc.org/Publishing/Journals/cc/Article.asp?Type=CurrentIssue
Date	01/01/1996		
Language	English		
Country	United Kingdom of Great Britain and Northern Ireland		
Rightsholder	Royal Society of Chemistry		

REQUEST DETAILS

Portion Type	Chart/graph/table/figure	**Distribution**	Worldwide
		Translation	Original language of publication
Number of charts / graphs / tables / figures requested	5	**Copies for the disabled?**	No
Format (select all that apply)	Print, Electronic	**Minor editing privileges?**	Yes
Who will republish the content?	Academic institution	**Incidental promotional use?**	No
Duration of Use	Life of current edition	**Currency**	USD
Lifetime Unit Quantity	Up to 499		
Rights Requested	Main product		

NEW WORK DETAILS

Title	Modulating Photophysical Properties of Dye-loaded Gold Nanoparticles through Plasmon-molecule Coupling	**Institution name**	INST Mohali
		Expected presentation date	2022-12-01
Instructor name	Prakash P. Neelakandan		

ADDITIONAL DETAILS

|	
The requesting person / organization to appear on the license	Atikur Rahman

REUSE CONTENT DETAILS

Title, description or numeric reference of the portion(s)	S10, S11, S12, S13, S14	**Title of the article/chapter the portion is from**	A three-component supramolecular nanocomposite as a heavy-atom-free photosensitizer.
Editor of portion(s)	Joseph, Joshy; Neelakandan, Prakash P; Praveen Kumar, P. P.; Shanavas, Asifkhan; THURAKKAL, SHAMEEL; Yadav, pranjali	**Author of portion(s)**	Joseph, Joshy; Neelakandan, Prakash P; Praveen Kumar, P. P.; Shanavas, Asifkhan; THURAKKAL, SHAMEEL; Yadav, pranjali
Volume of serial or monograph	55		
Page or page range of portion	5623-5626	**Issue, if republishing an article from a serial**	39
		Publication date of portion	2019-05-09

Total Items: 1	Subtotal:	0.00 USD
	Order Total:	**0.00 USD**

Marketplace Order General Terms and Conditions

Home   Help ∨   Live Chat   Atikur Rahman ∨
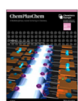
Fine-Tuning Plasmon-Molecule Interactions in Gold-BODIPY Nanocomposites: The Role of Chemical Structure and Noncovalent Interactions

Author: P. P. Praveen Kumar, Atikur Rahman, Tanmay Goswami, et al

Publication: CHEMPLUSCHEM

Publisher: John Wiley and Sons

Date: Oct 15, 2020

© 2020 Wiley-VCH GmbH

Order Completed

Thank you for your order.

This Agreement between Mr. Atikur Rahman ("You") and John Wiley and Sons ("John Wiley and Sons") consists of your license details and the terms and conditions provided by John Wiley and Sons and Copyright Clearance Center.

Your confirmation email will contain your order number for future reference.

🖶 Printable Details

License Number	5352031071677
License date	Jul 18, 2022

☑ Licensed Content

Licensed Content Publisher	John Wiley and Sons
Licensed Content Publication	CHEMPLUSCHEM
Licensed Content Title	Fine-Tuning Plasmon-Molecule Interactions in Gold-BODIPY Nanocomposites: The Role of Chemical Structure and Noncovalent Interactions
Licensed Content Author	P. P. Praveen Kumar, Atikur Rahman, Tanmay Goswami, et al
Licensed Content Date	Oct 15, 2020
Licensed Content Volume	86
Licensed Content Issue	1
Licensed Content Pages	8

📑 Order Details

Type of use	Dissertation/Thesis
Requestor type	Author of this Wiley article
Format	Print and electronic
Portion	Full article
Will you be translating?	No

📄 About Your Work

Title	Modulating Photophysical Properties of Dye-loaded Gold Nanoparticles through Plasmon-molecule Coupling
Institution name	Inst Mohali
Expected presentation date	Dec 2022

📁 Additional Data

📍 Requestor Location

Requestor Location	Mr. Atikur Rahman Sector-81 SAS Nagar Mohali Mohali, 140306 India Attn: Institute of Nano Science and Technology

📑 Tax Details

Publisher Tax ID	EU826007151

$ Price

Total	0.00 USD

Would you like to purchase the full text of this article? If so, please continue on to the content ordering system located here: Purchase PDF
If you click on the buttons below or close this window, you will not be able to return to the content ordering system.

Total: 0.00 USD

CLOSE WINDOW   ORDER MORE

Hot electron migration from gold nanoparticle to an organic molecule enhances luminescence and photosensitization properties of a pH activatable plasmon-molecule coupled nanocomposite

Author:
Atikur Rahman,Tanmay Goswami,Nidhi Tyagi,Hirendra N. Ghosh,Prakash P. Neelakandan

Publication: Journal of Photochemistry and Photobiology A: Chemistry

Publisher: Elsevier

Date: 1 November 2022

© 2022 Elsevier B.V. All rights reserved.

Journal Author Rights

BACK   CLOSE WINDOW